Measurement of Top-Quark Pair Production Cross Sections and Calibration of the Top-Quark Monte-Carlo Mass using LHC Run I Proton-Proton Collision Data at $\sqrt{s} = 7$ and 8 TeV with the CMS Experiment.

Dissertation

zur Erlangung des Doktorgrades
des Departments Physik
der Universität Hamburg

vorgelegt von
Jan Kieseler
aus Hamburg

Hamburg
2015

Gutachter der Dissertation: Dr. Katerina Lipka
Prof. Dr. Sven-Olaf Moch
Prof. Dr. Zhiqing Zhang

Gutachter der Disputation: PD Dr. Olaf Behnke
Prof. Dr. Elisabetta Gallo
Prof. Dr. Caren Hagner
Dr. Katerina Lipka
Prof. Dr. Sven-Olaf Moch

Vorsitzende des Prüfungsausschusses: Prof. Dr. Caren Hagner

Datum der Disputation: 14. Dezember 2015

Vorsitzende des Promotionsausschusses: Prof. Dr. Jan Louis

Leiter des Fachbereichs Physik: Prof. Dr. Peter Hauschildt

Dekan der Fakultär für Mathematik,
Informatik und Naturwissenschaften: Prof. Dr. Heinrich Graener

Abstract

In this thesis, measurements of the production cross sections for top-quark pairs and the determination of the top-quark mass are presented. Dileptonic decays of top-quark pairs ($\mathrm{t\bar{t}}$) with two opposite-charged lepton (electron and muon) candidates in the final state are considered. The studied data samples are collected in proton-proton collisions at the CERN Large Hadron Collider with the CMS detector and correspond to integrated luminosities of $5.0\,\mathrm{fb}^{-1}$ and $19.7\,\mathrm{fb}^{-1}$ at center-of-mass energies of $\sqrt{s} = 7\,\mathrm{TeV}$ and $\sqrt{s} = 8\,\mathrm{TeV}$, respectively. The cross sections, $\sigma_{\mathrm{t\bar{t}}}$, are measured in the fiducial detector volume (visible phase space), defined by the kinematics of the top-quark decay products, and are extrapolated to the full phase space. The visible cross sections are extracted in a simultaneous binned-likelihood fit to multi-differential distributions of final-state observables, categorized according to the multiplicity of jets associated to b quarks (b jets) and other jets in each event. The fit is performed with emphasis on a consistent treatment of correlations between systematic uncertainties and taking into account features of the $\mathrm{t\bar{t}}$ event topology. By comparison with predictions from the Standard Model at next-to-next-to leading order (NNLO) accuracy, the top-quark pole mass, m_t^{pole}, is extracted from the measured cross sections for different state-of-the-art PDF sets.

Furthermore, the top-quark mass parameter used in Monte-Carlo simulations, m_t^{MC}, is determined using the distribution of the invariant mass of a lepton candidate and the leading b jet in the event, $\mathrm{m_{lb}}$. Being defined by the kinematics of the top-quark decay, this observable is unaffected by the description of the top-quark production mechanism. Events are selected from the data collected at $\sqrt{s} = 8\,\mathrm{TeV}$ that contain at least two jets and one b jet in addition to the lepton candidate pair. A novel technique is presented, in which fixed-order calculations in quantum chromodynamics (QCD) are employed to determine the top-quark mass from the shape of the measured $\mathrm{m_{lb}}$ distribution.

The analysis is extended to a simultaneous fit of the $\mathrm{t\bar{t}}$ production cross sections and m_t^{MC}, including the $\mathrm{m_{lb}}$ distribution to increase the sensitivity to m_t^{MC}. The resulting $\mathrm{t\bar{t}}$ production cross sections at $\sqrt{s} = 7$ and $8\,\mathrm{TeV}$ do not depend on assumptions on m_t^{MC} and are the most precise ones obtained with the CMS experiment. The extracted m_t^{MC} reaches an unprecedented precision for a single measurement of m_t^{MC} in the dileptonic decay channel. The measured $\sigma_{\mathrm{t\bar{t}}}$ are further used to determine m_t^{pole} and the $\overline{\mathrm{MS}}$ mass, $m_t^{\overline{\mathrm{MS}}}$, at up to NNLO QCD. The extracted $m_t^{\overline{\mathrm{MS}}}$ exhibits a better perturbative convergence and is converted to the pole mass, $m_t^{\mathrm{p,conv}}$, using recent calculations at 4-loop QCD. For the first time, the direct relation of m_t^{MC} to $m_t^{\overline{\mathrm{MS}}}$, m_t^{pole}, and $m_t^{\mathrm{p,conv}}$ is quantified experimentally at the highest available precision.

Zusammenfassung

In dieser Arbeit werden Messungen der Produktionswirkungsquerschnitte für Topquarkpaare und die Bestimmung der Topquarkmasse beschrieben. Dileptonische Zerfälle von Topquarkpaaren ($\mathrm{t\bar{t}}$) mit zwei entgegengesetzt geladenen Leptonkandidaten (Elektronen und Muonen) im Endzustand werden untersucht. Die untersuchten Datensätze sind von dem CMS Experiment am CERN Large Hadron Collider aufgenommen worden und entsprechen einer integrierten Luminosität von $5.0\,\mathrm{fb}^{-1}$ bei einer Schwerpunktsenergie von $\sqrt{s} = 7\,\mathrm{TeV}$ und $19.7\,\mathrm{fb}^{-1}$ bei $\sqrt{s} = 8\,\mathrm{TeV}$. Die Wirkungsquerschnitte, $\sigma_{\mathrm{t\bar{t}}}$, werden innerhalb der Detektorakzeptanz gemessen, die definiert ist durch die kinematischen Eigenschaften der Zerfallsprodukte des $\mathrm{t\bar{t}}$-Systems, und in einem zweiten Schritt in den vollen Phasenraum extrapoliert. Die Messung basiert auf einem simultanen Likelihood-Fit von differentiellen Verteilungen im beobachteten Endzustand. Diese sind kategorisiert in Bezug auf die Multiplizität von Jets, die mit einem b-Quark assoziiert sind (b-Jets), und die Anzahl der übrigen Jets. Innerhalb des Fits werden Korrelationen zwischen systematischen Unsicherheiten und die erwartete Topologie von $\mathrm{t\bar{t}}$-Zerfällen besonders berücksichtigt. Durch Vergleich der Ergebnisse mit Vorhersagen der Quantenchromodynamic (QCD) mit einer Genauigkeit zu „nächst-zu-nächst-zu-führender Ordnung" (NNLO) wird die Topquark-Polmasse, m_t^{pole}, bestimmt. Dies geschieht für verschiedene, neue PDF-Sets.

Desweiteren wird die Topquarkmasse, die in Monte-Carlo Simulationen genutzt wird, m_t^{MC}, aus der Verteilung der invarianten Masse $\mathrm{m_{lb}}$ bestimmt. Diese setzt sich aus einem Leptonkandidaten und einem b-Jet zusammen. Da diese Verteilung durch den Zerfall der Topquarks bestimmt wird, bleibt sie unbeeinflusst durch die Beschreibung des $\mathrm{t\bar{t}}$ Produktionsmechanismusses. Ereignisse bei einer Energie von $\sqrt{s} = 8\,\mathrm{TeV}$ werden selektiert, die zusätzlich zum Leptonenpaar mindestens zwei Jets und mindestens einen b-Jet enthalten. Es wird außerdem eine neue Methode eingeführt, die es erlaubt Vorhersagen der QCD in einer festen Ordnung in Störungstheorie zu nutzen, um die Topquarkmasse zu bestimmen. Für diese Bestimmung wird die normierte $\mathrm{m_{lb}}$-Verteilung herangezogen.

Der Fitmethode wird erweitert um $\sigma_{\mathrm{t\bar{t}}}$ und m_t^{MC} simultan zu bestimmen. Dabei wird die $\mathrm{m_{lb}}$ Verteilung benutzt um die Sensitivität auf m_t^{MC} zu erhöhen. Infolgedessen werden $\sigma_{\mathrm{t\bar{t}}}$ bei $\sqrt{s} = 7$ und $8\,\mathrm{TeV}$ zum ersten Mal bestimmt ohne eine Abhängigkeit von m_t^{MC} aufzuweisen. Das Ergebnis für letztere zeichnet sich durch die höchste Genauigkeit aus, die bisher in einer Einzelmessung im dileptonischen Zerfallskanal erreicht wurde. Die extrahierten Wirkungsquerschnitte stellen deren präziseste Messung mit dem CMS Detektor dar und werden genutzt um sowohl m_t^{pole} als auch die $\overline{\mathrm{MS}}$-Masse, $m_t^{\overline{\mathrm{MS}}}$, durch Vergleich mit Vorhersagen bis zu NNLO QCD zu bestimmen. Die gemessene $m_t^{\overline{\mathrm{MS}}}$ zeigt ein besseres Konvergenzverhalten in Bezug auf die Störungsreihe und wird basierend auf neuen QCD-Korrekturen mit 4-Schleifen-Genauigkeit in die Polmasse, $m_t^{\mathrm{p,conv}}$, umgerechnet. Zum ersten mal wird konsistent der Bezug zwischen m_t^{MC} und sowohl der Pol- als auch der $\overline{\mathrm{MS}}$-Masse experimentell hergestellt.

Contents

Chapter 1

Introduction

Particle physics studies the fundamental components of matter and their interactions. Within the last decades impressive advancements in this field have been achieved. The variety of physics phenomena are explained in terms of fundamental interactions between elementary particles. All of them, except the gravitational force, are combined into the Standard Model (SM) of particle physics, describing the building blocks of matter. It comprises leptons and quarks which build up matter, and gauge bosons, which mediate the exchange forces between them. Combinations of two or three quarks, held together by gluons, create hadrons, thereby defining their properties.

The SM has been successfully tested over the past 30 years. Very recently, at the Large Hadron Collider (LHC) experiments at CERN, experimental evidence has been found for a Higgs boson with a mass of around 125 GeV [1,2], which was the last missing building block of the SM. However, the SM cannot explain particular features of our universe, such as the origin of dark matter and the predominance of matter over antimatter. Therefore, it is believed that the SM is only an effective description of the structure of matter up to a certain energy scale and that there must be a truly fundamental underlying theory. Most of the extensions of the theory that have been proposed to solve the shortcomings of the SM have a common feature: they predict the existence of new physics phenomena not considered by the SM at the TeV scale. Nevertheless, no evidence of such phenomena has yet been observed.

Within the SM, the top quark is the heaviest fundamental particle. Due to its large mass, the top quark decays very rapidly (within $5 \cdot 10^{-25}$ s), before hadronizing, and is thus the only quark that gives direct access to its properties such as spin and charge. With its large mass, the top quark has a uniquely strong coupling to the Higgs boson. Thus, the top quark is believed to play a special role in the electroweak symmetry breaking. Various scenarios of physics beyond the SM expect the top quark to couple to new particles. Furthermore, SM top quark processes are a dominant background to many searches for physics beyond the SM. It is crucial to understand the production mechanisms and properties of the top quark to the highest possible precision. Apart from this, the description of final states of all processes at hadron colliders such as the LHC relies on Quantum Chromodynamics (QCD), describing the interaction of colliding partons and subsequently produced hadrons. The exceptional properties of the top quark offer unique possibilities to test QCD as well as predictions from the electroweak theory.

The top quark was discovered at the Tevatron proton-antiproton collider in 1995 at a center-of-mass energy ($\sqrt{s}$) of 1.8 TeV [3,4]. Although some of its properties and interactions have been measured very precisely as reviewed in [5], others suffer from the relatively low rate of top quarks produced at the Tevatron. At the LHC, which is in operation since 2009, protons collide with protons at $\sqrt{s} = 7\,\text{TeV}$ (2010-2011) and 8 TeV (2012), and since June 2015, also 13 TeV. These high collision energies allow for a large production rate for top quarks. In consequence, several million of top-quark pairs have been produced at the LHC, around 100 times more than at the Tevatron. This allows to perform precise measurements of the top-quark production and properties, challenging the accuracy of the theoretical predictions, potentially constraining QCD parameters, and opening the possibility to search for new physics by studying deviations of the top-quark properties from the SM expectation.

The top-quark mass, m_t, is one of the fundamental parameters of the SM. Its value significantly affects predictions for many observables either directly or via radiative corrections. As a consequence, the measured top-quark mass is one of the crucial inputs to electroweak precision fits, which enable comparisons between experimental results and predictions within and beyond the SM. Furthermore, together with the Higgs-boson mass, it has critical implications on the stability of the electroweak vacuum when extrapolating the SM to high energy scales [6, 7]. The top-quark mass has been determined with remarkable precision: the current world average is $173.34 \pm 0.76\,\mathrm{GeV}$[1] [8], determined by combining results from the Tevatron and the LHC. However, these *direct* measurements rely on the relation between the top-quark mass and the respective experimental observable, e.g. the reconstructed invariant mass of the top-quark decay products. This relation is derived from Monte Carlo (MC) simulations. Hence, the direct measurements determine the top-quark mass parameter implemented in this simulation, m_t^{MC}, that is most compatible with the data. It is important to understand how to interpret the experimental result in terms of well-defined theory parameters used in QCD and electroweak calculations. In calculations beyond leading order (LO), the top-quark mass depends on the renormalization scheme [9], e.g. the *pole* or $\overline{MS}$ scheme. The relation between m_t^{MC} and these mass parameters is of particular relevance since the uncertainty on the measured m_t^{MC} parameter has become smaller than the uncertainty on its theoretical interpretation, which is of the order of 1 GeV [10]. Therefore, a calibration of m_t^{MC} to a theoretically well-defined top-quark mass is necessary and an important aspect of this thesis.

The top-quark mass can be extracted by confronting a measured observable with its prediction, e.g. the inclusive top-quark pair ($t\bar{t}$) production cross section ($\sigma_{t\bar{t}}$) [11–13], calculated beyond LO QCD in a well-defined top-quark mass scheme. Studies of $\mathrm{t\bar{t}}$ production have been performed on a variety of production and decay channels in the recent years by the LHC and Tevatron experiments. So far, all these results are consistent with predictions from the SM at next-to-next-to leading order ($NNLO$) with a precision of about 4% [14], depending on the dominant production mechanism and the center-of-mass energy. Reaching a similar or lower uncertainty in measurements at hadron colliders is experimentally challenging.

Compared to previous precision analyses of $\sigma_{\mathrm{t\bar{t}}}$ [12, 15, 16], the measurements presented in this thesis bring the following improvements. The full data sample recorded by the Compact Muon Solenoid (CMS) experiment at the LHC in the years 2011-2012 is analyzed, corresponding to two center-of-mass energies, 7 and 8 TeV. An innovative cross section extraction method is employed: a simultaneous fit of the $\mathrm{t\bar{t}}$ production cross sections at $\sqrt{s} = 7$ and 8 TeV is performed, with emphasis on a consistent treatment of correlations regarding simulation modeling and detector uncertainties. The cross sections are measured in the visible phase space, defined by the detector fiducial volume, and extrapolated to the full phase space. With total uncertainties of 3.6% (7 TeV) and 3.8%

---

[1] Throughout this thesis $c = \hbar = 1$ applies.

(8 TeV), the measurements presented in this thesis constitute the most precise determinations of $\sigma_{\mathrm{t\bar{t}}}$ with the CMS detector and are competitive with recent results published by the ATLAS collaboration [12]. These precise results are used to determine the top-quark pole mass through comparison with recent calculations.

Alternatively, differential $\mathrm{t\bar{t}}$ production cross sections are studied, aiming for the determination of m_t in a well-defined scheme. These measurements can improve the precision compared to the results from $\sigma_{\mathrm{t\bar{t}}}$ if the chosen observable is particular sensitive to m_t or not affected by certain systematic uncertainties. Already long before the first start-up of the LHC, it was proposed to employ the invariant mass of lepton and b jet (m_{lb}) in dileptonic $\mathrm{t\bar{t}}$ events as such an observable [17]. It has been noted that the distribution is under good theoretical control up to next-to-leading order (NLO) QCD over the entire range that is relevant for measurements of m_t [9, 18, 19]. In this thesis, a novel technique is presented to relate such fixed-order calculations to the distribution observed in data and extract the top-quark mass. The method is applied to predictions of the $\mathrm{t\bar{t}}$ production cross section as a function of $\mathrm{m_{lb}}$ calculated with MCFM [20] and the resulting distribution is compared to the observation in data at $\sqrt{s} = 8$ TeV.

Finally, a simultaneous fit of m_t^{MC} and $\sigma_{\mathrm{t\bar{t}}}$ at $\sqrt{s} = 7$ and 8 TeV is performed, profiting from the individual studies of these parameters. In consequence, the production cross sections are determined for the first time without prior assumptions on m_t^{MC}. The extracted $\sigma_{\mathrm{t\bar{t}}}$ are employed to determine the top-quark mass in well-defined renormalization schemes with unprecedented precision. The simultaneously determined m_t^{MC} parameter not only represents the by far most precise single measurement of m_t^{MC} in dileptonic $\mathrm{t\bar{t}}$ events, but also provides a consistent treatment of correlations between the extracted $\sigma_{\mathrm{t\bar{t}}}$ and m_t^{MC}, and as a consequence between the extracted well-defined top-quark mass parameters and m_t^{MC}. Thus, this measurement represents the first experimental calibration of the m_t^{MC} parameter to these mass parameters.

This thesis is organized as follows: The SM is introduced in Chapter 2 with particular focus on the top quark, its production, decay and the interpretation of its mass. Furthermore, the MC generators and detector modeling used in the analyses are discussed. In Chapter 3, the LHC machine, the CMS detector, and the data employed in this thesis are described. The event reconstruction and selection are reviewed in Chapter 4, which also comprises a description of data-driven corrections applied to the simulation. The simultaneous fitting technique to extract $\sigma_{\mathrm{t\bar{t}}}$ at 7 and 8 TeV is presented and validated in Chapter 5, together with a description of the sources of systematic uncertainties. The resulting visible and total cross sections are also discussed there. Chapter 6 is dedicated to the extraction of the top-quark mass from the measured $\sigma_{\mathrm{t\bar{t}}}$ and the $\mathrm{m_{lb}}$ distribution. The simultaneous fit of $\sigma_{\mathrm{t\bar{t}}}$ at 7 and 8 TeV and m_t^{MC} is described in Chapter 7, as well as the determination of the theoretically well-defined top-quark masses and the calibration of m_t^{MC}. The summary and conclusions are discussed in Chapter 8.

Frequently used terms and expressions

Throughout this thesis, the term "uncertainties on A due to variations of x and y are added in quadrature" is defined in the following way: let the variation increasing A due to a variation of κ be $\Delta_{\kappa,+}$ and the term decreasing A $\Delta_{\kappa,-}$. Then, both uncertainties are added to the total asymmetric uncertainty on A, $\Delta_{A,\pm}$, as:

$$\Delta^2_{A,+} = \Delta^2_{x,+} + \Delta^2_{y,+} \tag{1.1}$$

$$\Delta^2_{A,-} = \Delta^2_{x,-} + \Delta^2_{y,-} \tag{1.2}$$

The term "the difference in quadrature between A and B is C" refers to the following operation:

$$C^2 = |A^2 - B^2|. \tag{1.3}$$

Chapter 2

Top Quark Production and Decay in Proton-Proton Collisions

The properties of the top quark are important parameters of the SM and determine the precision of our understanding of nature to a wide extent. Top quarks are produced at high rates in proton-proton collisions at high center-of-mass energies and their properties can be studied to high precision. In the following, the theoretical basis for understanding the top quark production and its properties are discussed.

2.1 The Standard Model of fundamental particles and their interactions

The SM of particle physics is based on a quantum field theory of the strong, weak and the electromagnetic interactions [21]. The elementary particles of the SM are categorized in 12 fermions comprising six *flavors* of quarks and six leptons as illustrated in Figure 2.1. The interactions between these fermions are mediated by a set of gauge bosons: gluons mediate the strong, photons the electromagnetic and the W^+, W^-, and Z bosons the weak interaction. Quarks participate in all three fundamental interactions. The charged e, μ and τ leptons are subject to electromagnetic and weak interactions, while the neutrinos experience weak interactions only. To each fermion corresponds an antiparticle with quantum numbers equal in magnitude but of opposite sign.

The interactions among particles described by a quantum field theory have the effect of modifying masses and interaction strengths. This means that, when masses and scattering amplitudes are measured, the *bare* mass and coupling parameters of the theory are still not known [22]. Measured and bare parameters are related through *renormalization.* The criterion for a theory to be renormalizable is given by a demand for *local gauge invariance* [23].

The electromagnetic interaction of charged particles is described by Quantum Electrodynamics (QED). QED is a relativistic quantum field theory emerging from the principle of local gauge invariance. The requirement of local gauge invariance with respect to space-time dependend transformations represented by the $U(1)$ group results in the massless field A_μ, which can be identified as the photon field.

The weak interaction is mediated by three massive gauge bosons: the neutral Z and the charged W^+ and W^- bosons. At low energies, the high masses of the gauge bosons reduce the effective strength of the interaction although the coupling itself is of the order of the electromagnetic coupling. An example for a weak interaction at low energies is the β decay. Weak eigenstates and mass eigenstates are not necessarily the same. Weak eigenstates can consist of a superposition of different mass (or strong) eigenstates in both

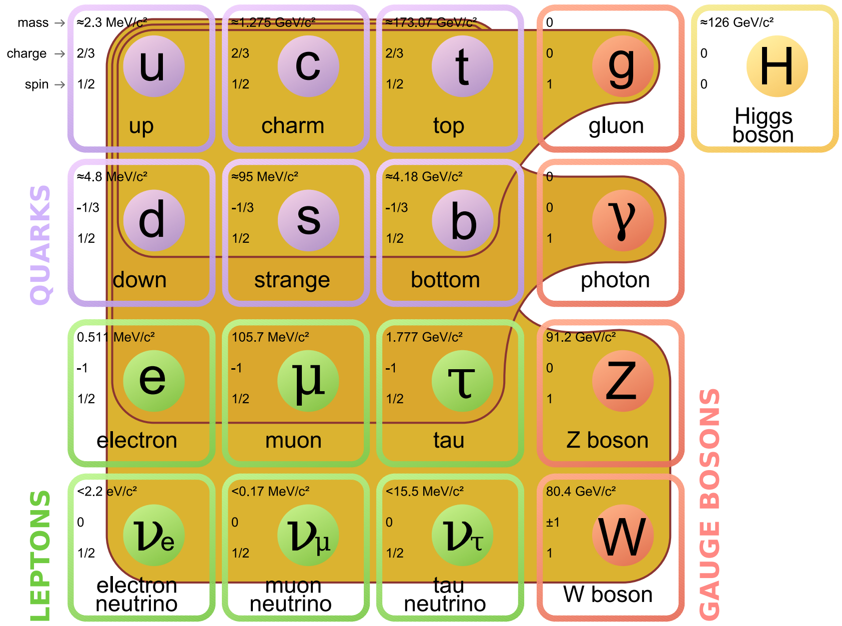

Figure 2.1: All fundamental particles of the Standard Model including their masses, charges and spins. The first three columns represent three generations of fermions, the fourth and fifth column depict bosons. Interactions between the gauge bosons (red) and fermions are indicated by light circlings [24].

the lepton and the quark sector. In the lepton sector this results in neutrino oscillations, for the quarks in quark-generation changing weak interactions mediated by $W^{\pm}$ bosons. The transition probability for the quarks is described by the Cabibbo-Kobayashi-Maskawa (CKM) matrix [25]:

$$\begin{pmatrix} d' \\ s' \\ b' \end{pmatrix} = \begin{pmatrix} V_{ud} & V_{us} & V_{ub} \\ V_{cd} & V_{cs} & V_{cb} \\ V_{td} & V_{ts} & V_{tb} \end{pmatrix} \begin{pmatrix} d \\ s \\ b \end{pmatrix} \tag{2.1}$$

The weak eigenstates d', s' and b' are superpositions of the strong eigenstates d, s, and b. In the SM, the CKM matrix is unitary. Through a complex phase in the matrix, it can describe the observed violation [26,27] of the charge-parity symmetry within the SM. Given the well measured values of the first rows of the matrix, the observation of three generations, and the unitarity requirement, V_{tb} is almost 1 and $V_{td} \approx V_{ts} \approx 0$. Measurements of V_{tb} itself with and without the unitarity assumption result in $|V_{tb}| = 0.998{\pm}0.041$ or $|V_{tb}| > 0.92$ at 95% confidence level (CL), respectively [28]. The probability P_{bW} for the decay of top quarks to b quarks is given as

$$P_{bW} = \frac{|V_{tb}|^2}{|V_{tb}|^2 + |V_{ts}|^2 + |V_{td}|^2}. \tag{2.2}$$

Therefore, top quarks decay almost exclusively into a b quark and a $W^{\pm}$ boson.

The weak and the electromagnetic force can be described by a unified theory of electroweak (EWK) interactions [29,30]. Each fermion is expressed as a right-handed singlet, and a left-handed isospin doublet[1]. The left-handed isospin doublets are written as

$$\begin{pmatrix} u \\ d' \end{pmatrix}_L, \begin{pmatrix} c \\ s' \end{pmatrix}_L, \begin{pmatrix} t \\ b' \end{pmatrix}_L, \begin{pmatrix} \nu_e \\ e \end{pmatrix}_L, \begin{pmatrix} \nu_\mu \\ \mu \end{pmatrix}_L, \begin{pmatrix} \nu_\tau \\ \tau \end{pmatrix}_L.$$

A $U(1)_Y$ and $SU(2)_L$ transformation is introduced. The fields $W_\mu^{(1,2,3)}$ couple to left-handed isospin doublets via the isospin operators $T^{(1,2,3)}$, and the field B_μ couples to left and right-handed particles via the hypercharge operator Y. The left-handed doublets are eigenstates to the T^3 operator with the eigenvalues of $\pm 1/2$. The hypercharge Y relates to the operators for charge, Q, and the third projection of the isospin T^3 as $Q = T^3 + Y/2$. The $W^\pm$ boson fields can be written as ladder operators $\mathrm{W}^\pm \propto W_\mu^1 \mp iW_\mu^2$ which flip the eigenvalue of T^3. Orthogonal superpositions of the W_μ^3 field and the B_μ field result in the A_μ and the Z_μ boson fields:

$$A_\mu = W_\mu^3 \cos\theta_W - B_\mu \sin\theta_W \tag{2.3}$$

$$Z_\mu = W_\mu^3 \cos\theta_W + B_\mu \sin\theta_W \tag{2.4}$$

The mixing angle θ_W is a free parameter and can be determined experimentally. The manifestation of the EWK unification was measured [31, 32] at the HERA accelerator in deep-inelastic electron-proton scattering (DIS). In the measurement of DIS cross sections of neutral current (NC) and charged current (CC) processes as a function of momentum transfer Q^2, as illustrated in Figure 2.2, it was shown that the cross sections of interactions mediated by a photon or Z boson and the ones mediated by $\mathrm{W}^\pm$ bosons become similar for scales Q^2 above the W mass.

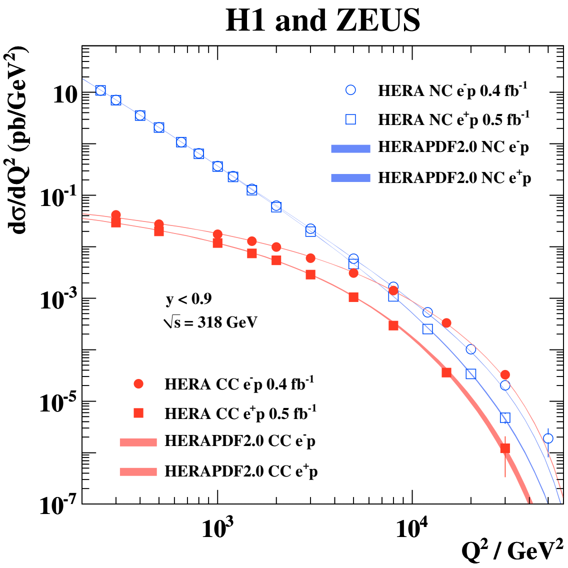

Figure 2.2: Combined HERA neutral currect (NC) and charged current (CC) e$^-$-p and e$^+$-p cross sections as a function of momentum transfer Q^2 together with predictions from HERAPDF2.0 NLO. The bands represent the total uncertainty on the predictions [32].

---

[1] Anti-fermions are expressed as right-handed doublets and left-handed singlets and are implied in the following.

In order to preserve the $SU(2)_L \otimes U(1)_Y$ gauge symmetry, all particles are required to be massless, which contradicts the experimental measurements. The question of particle mass can be solved by introducing an additional $SU(2)_L \otimes U(1)_Y$ gauge invariant field Φ (the Higgs field [33]) in the SM Lagrangian as

$$\mathcal{L}_H = (\partial_\kappa \Phi)^\dagger (\partial^\kappa \Phi) - \mu^2 \Phi^\dagger \Phi - \lambda (\Phi^\dagger \Phi)^2. \tag{2.5}$$

The Lagrangian $\mathcal{L}_H$ respects local $SU(2)_L \otimes U(1)_Y$ gauge invariance and can provide a non-zero vacuum expectation value $v = -\mu^2/\lambda$. The latter can be expressed in terms of the Fermi coupling constant G_F, measured precisely from muon decays as $v = \sqrt{2^{1/2} G_F} = 246$ GeV [34]. This relation becomes apparent when a particular ground state is chosen. The EWK symmetry is broken and the Higgs field can be expressed as the doublet

$$\Phi_0 = 1/\sqrt{2} \begin{pmatrix} 0 \\ v + H \end{pmatrix}_L , \tag{2.6}$$

with H being the real field with zero vacuum expectation value. The symmetry breaking leads to three degrees of freedom that correspond to zero-energy excitations along the ground-state surface. These allow the $W_\mu^{(1,2,3)}$ fields to acquire mass proportional to v, and therefore lead to a relation to G_F, with $G_F \propto 1/m_W^2$. In the same way the $W_\mu^{(1,2,3)}$ fields acquire mass in this mechanism, they couple to the Higgs boson (the non-zero-energy excitation along H). On the other hand, the chosen ground state remains invariant under charge transformations and therefore leaves the photon massless and without direct coupling to the Higgs boson. The T^3=1/2 (T^3=−1/2) fermions can acquire mass and coupling to the Higgs boson through Yukawa coupling, expressed as interaction terms to Φ (its gauge transformation). Although this mechanism preserves the local gauge symmetry, a coupling parameter $g_i \propto m_i$ has to be introduced for each fermion i. The values of these parameters can not be derived from basic principles and have to be measured.

The strong interaction is described by quantum chromodynamics, based on the $SU(3)_C$ gauge group. There are three strong-charge eigenstates, the colours, named red, green and blue and their corresponding anticolors. Owing to the group structure with 8 generators there are 8 gluon fields carrying colour themselves, which mediate the strong force and interact amongst each other. The strong coupling constant α_s, which quantifies the coupling to the colour charge, depends on the momentum transfer Q^2 of the interaction and the number of quark flavors with mass lower than Q^2. At low Q^2, corresponding to large interaction distances, α_s becomes very large due to the gluon self-coupling, while at high Q^2, α_s becomes very small (asymptotic freedom). In consequence, the energy needed to separate two quarks increases with their distance until it is energetically more beneficial to produce an additional quark-antiquark pair (confinement). This results in *hadronization*, a process where colorless hadrons are created: baryons (3-quark combinations) and mesons (2-quark combinations).

2.2 Phenomenology at the LHC

The LHC is a proton-proton (pp) collider. Protons are compound baryons consisting of *partons* (quarks and gluons), which can be expressed in terms of parton density functions (PDFs), $f_{i,j}(x_i, \mu_F^2)$. Those PDFs represent the probability for a parton i to carry a momentum fraction x_i of the proton momentum at a *factorization* scale μ_F^2.

The PDFs are experimentally determined from structure function measurements in DIS experiments at HERA [35], with additional constraints provided by neutrino-nucleon scattering [36], LHC [37], and Tevatron measurements. The x-dependence of the parton distributions is not yet calculable in perturbative QCD and has to be parametrized at a certain scale $Q_0 = \mu_{F,0}$. The dependence on Q is described by the DGLAP evolution equations [38–43]. The resulting PDFs depend on the order in which the perturbative QCD calculation is performed, the assumptions about the parametrization, and the treatment of heavy quarks [44].

The calculation of the production cross section, σ, for any SM process can be factorized by a convolution of *long-distance* contributions such as the proton structure and *short-distance* terms such as the hard parton-parton interaction [45]. The hard interaction refers to the interaction between the partons of the colliding protons. The kinematics of the hard interaction are then described by the effective center-of-mass energy $\hat{s} = \tau \cdot s = x_1 \cdot x_2 \cdot s$ and the proton momentum fractions x_1 and x_2, such that σ can be calculated as:

$$\sigma(s) = \sum_{i,j} \int_{\tau_0}^{1} \frac{d\tau}{\tau} \cdot \frac{dL_{ij}(\mu_F^2)}{d\tau} \cdot \hat{s} \cdot \hat{\sigma}_{ij}\left(\alpha_s(\mu_R^2)\right). \tag{2.7}$$

Here, $\hat{\sigma}_{ij}\left(\alpha_s(\mu_R^2)\right)$ represents the cross section of a strong parton-parton interaction described by matrix elements (*ME*). These can be calculated through a perturbative expansion in α_S to a certain order at the *renormalization* scale μ_R^2. The term

$$\tau \cdot \frac{dL_{ij}}{d\tau} \propto \int_{0}^{1} dx_1 dx_2 \left(x_1 f_i(x_1, \mu_F^2) \cdot x_2 f_j(x_2, \mu_F^2)\right) + (1 \leftrightarrow 2)\delta(\tau - x_1 x_2) \tag{2.8}$$

represents the parton luminosity and involves the description of the proton structure by the PDFs. The PDFs of both interacting protons enter multiplicatively into the the calculation of the process cross section. Therefore, a precise knowledge of the PDFs is of particular importance for cross-section predictions [44].

2.2.1 Parton showers and underlying event

To be able to compare theoretical predictions to an experimental observation, not only a prediction of its production cross section is necessary. Further production and decay of particles have to be modeled, in particular the emission of additional partons. This corresponds to higher-order corrections to the perturbative series and could be predicted by including the corresponding ME. Currently, these can only be calculated up to a certain order, which is by far insufficient to describe all observed radiation. Instead, the corrections from these long-distance contributions are accounted for by phenomenological *parton shower (PS)* models, where the perturbation series consisting of terms such as $\alpha_S^n \ln^m(Q^2)$ and $\alpha_S^n \ln^m(1/x)$ is rearranged through evolution equations (e.g. DGLAP) and only single logarithmic terms are used for further calculations, referred to as *leading-log* (*LL*) approximation. The solution of this evolution can be rewritten with the help of the *Sudakov form factor*, which indicates the probability of evolving from a higher scale to a lower scale without the emission of a gluon greater than a given value [46]. Based on this form factor, the PS models initial- (*ISR*) and final-state radiation (*FSR*) by restricting the phase space to an ordered parton cascade. The ordering depends on the specific model and, while fixed order calculations explicitly account for color coherence, the color-flow is modeled by the PS only approximately. The initial state showering evolves from the scale of the hard process backwards to the initial partons described by the PDF. During final state showering, the energy scale decreases until an infrared cut-off is reached, where non-perturbative models have to be taken into account for the modeling of subsequent hadronization. The Sudakov form factor depends on this cut-off, the hard scale of the process, the parton type and its momentum fraction, and the resolution scale for the emission. All parameters used to configure the PS are tuned to measurements and are referred to as *tune*.

Not only radiation resulting from the inital and final state of the hard interaction process contributes to the observed final states. Also, other contributions from soft parton radiation, multiple parton scattering (*MPI*), and interaction with the proton remnants can emerge and modify the event topology. These effects summarized as *underlying event* (*UE*) comprise perturbative and non-perturbative contributions.

2.3 The top quark

The top quark is the heaviest particle of the SM and was discovered 1995 at the Tevatron [47]. Due to its high mass, it is the only quark that decays before hadronization and therefore offers unique possibilities to study bare-quark properties. These properties are crucial in calculations in the SM and beyond. As a direct consequence of the spontaneous EWK symmetry breaking, the high mass of the top quark gives rise to large radiative corrections to the electroweak coupling at low energies and has a direct impact on the Higgs sector and on extrapolations of the SM up to high scales.

The top quark is likely to be the most sensitive probe of the EWK symmetry breaking [48]. Hence, it also plays a special role in many extensions of the SM. These theories often provide possible scenarios to solve the hierarchy problem of the SM, the large discrepancy between the EWK and the Planck scale, for which the contribution from the coupling between the top quark and the Higgs boson is important. Thus, it is natural to assume that new physics might reveal itself through measurements of top-quark properties that can be affected by e.g. models beyond the SM aiming for a dynamical explanation of EWK symmetry breaking such as Topcolor Assisted technicolor theories [49], or by a top quark partner of similar mass in supersymmetric or composite Higgs scenarios [50]. Also a heavy Z' boson in Topcolor or Kaluza-Klein theories would be visible as an excess in the $\mathrm{t\bar{t}}$ invariant mass spectrum and would change the event kinematics [51], and the charge asymmetry in $\mathrm{t\bar{t}}$ production can give insights to non-SM boson exchange.

The leading-order diagrams for the production of $\mathrm{t\bar{t}}$ pairs are shown in Figure 2.4. The required energy to produce a $\mathrm{t\bar{t}}$ pair is at least double the top-quark mass. At $\sqrt{s} = 7$ and 8 TeV, the gluon-gluon luminosity is higher than the quark luminosity at the corresponding partonic momentum fractions. Therefore 90% of the $\mathrm{t\bar{t}}$ pairs at the LHC are produced by gluon-gluon fusion. The production cross sections for top quarks as a function of $\sqrt{s}$ is illustrated in Figure 2.3. It is orders of magnitude smaller than for many other SM processes, e.g. b-quark or heavy gauge-boson production.

In the SM, top quarks decay via weak interaction almost exclusively into a W boson and a b quark as illustrated in Figure 2.5. The W boson subsequently decays either into a lepton and its corresponding neutrino or into a pair of quarks. This decay determines the nomenclature of the $\mathrm{t\bar{t}}$ decay channels (dileptonic, semi-leptonic, and full-hadronic).

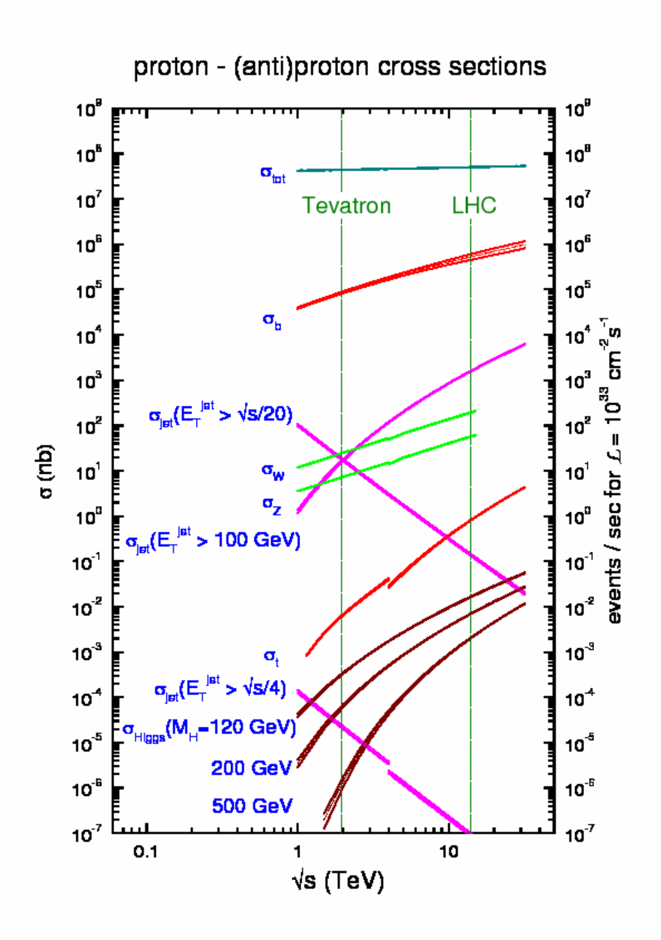

Figure 2.3: Cross section expectations for selected standard model processes as functions of the center of mass energy, $\sqrt{s}$. The dashed vertical lines mark the center-of-mass-energy at the Tevatron at 1.96 TeV and at the LHC at 14 TeV, respectively. For $\sqrt{s} <$ 4 TeV the cross sections for proton-antiproton collisions are shown and for $\sqrt{s} >$ 4 TeV for proton-proton collisions [52].

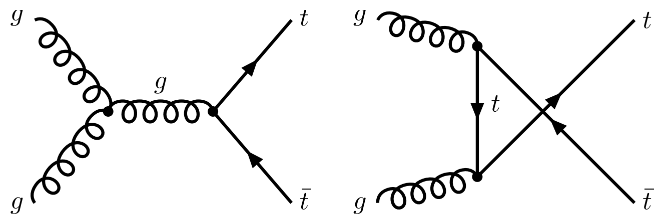

(a) gg fusion s-channel (b) gg fusion u-channel

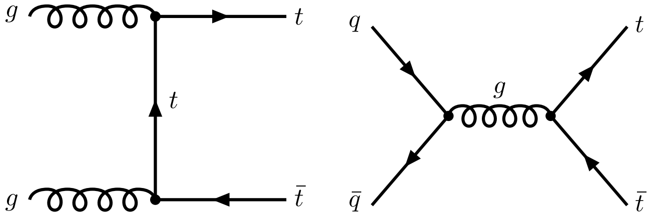

(c) gg fusion t-channel (d) $q\bar{q}$ annihilation

Figure 2.4: Feynman diagrams for top-quark pair production at leading order.

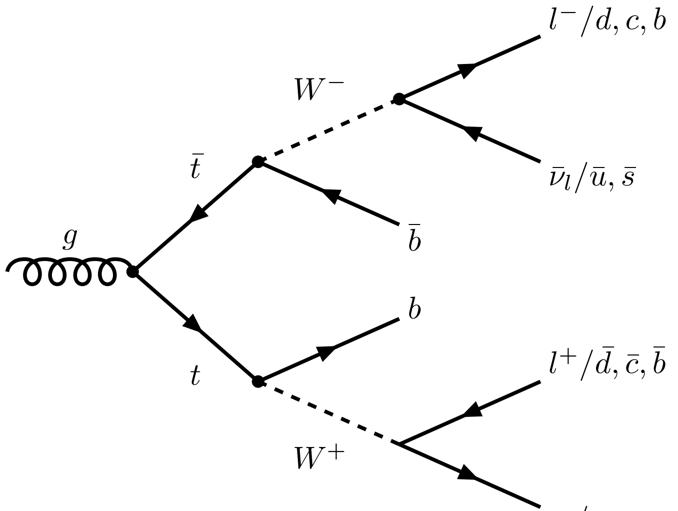

Figure 2.5: Diagram for the decay of a top-quark pair at tree level.

The contribution of the dileptonic $\mathrm{t\bar{t}}$ decay is about 10%, whereas semi-leptonic and full-hadronic channels contribute to about 45%, each.

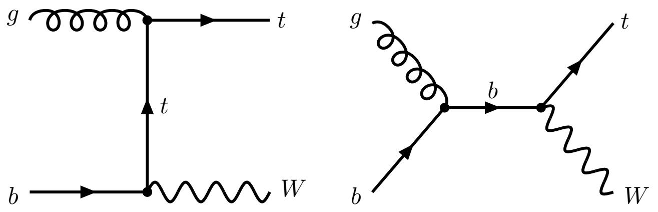

(a) Associated tW production t-channel

(b) Associated tW production s-channel

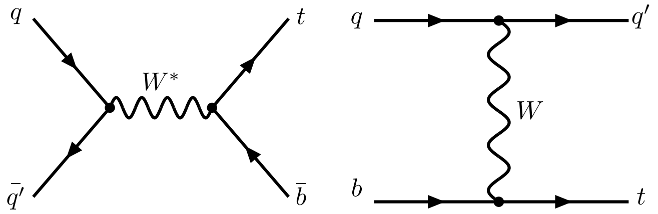

(c) tq production s-channel

(d) tq production t-channel

Figure 2.6: Feynman diagrams for single top-quark production at leading order.

In addition to $\mathrm{t\bar{t}}$ production, also single top-quark production via electroweak interaction is possible. The leading-order diagrams are shown in Figure 2.6. At NLO, a clear separation of single top-quark and $\mathrm{t\bar{t}}$ production is challenging since the reaction $gg \to$ WbWb enters NLO corrections to associated tW production [53]. Due to the same final states (WbWb), these contributions interfere with the $\mathrm{t\bar{t}}$ production, especially those for a resonant top-quark propagator (doubly-resonant), but can be separated such that associated tW production can be considered as a well-defined process [54].

In fixed-order calculations, interference can be decreased e.g. by excluding the resonant region where the invariant mass of Wb is close to the top-quark mass or by imposing a transverse-momentum (p_T) veto on additional b quarks [55]. A fully inclusive approach is to subtract the $\mathrm{t\bar{t}}$ contributions multiplied by the $t \to Wb$ branching ratio at the level of squared amplitudes [56].

If inital- and final-state parton showers are present, these approaches cannot be applied directly. Instead, two schemes are introduced: the diagram removal (DR) method, where doubly-resonant diagrams are removed from the calculation, and the diagram subtraction (DS) method that cancels $\mathrm{t\bar{t}}$ contributions locally by implementing a subtraction term [55]. Although the DR method violates gauge invariance, the impact of its gauge dependence can safely be neglected in numerical studies.

2.3.1 The top-quark mass

Although the top quark acquires its mass due to the Higgs mechanism, the value of its mass cannot be calculated within the SM and has to be determined experimentally. In QCD, quark masses are simply parameters of the Lagrangian. They appear in theory predictions and, as such, they are subject to the definition of a renormalization scheme once quantum corrections beyond LO are included [23, 57]. In consequence, self-energy corrections $\Sigma(m_0)$ to the bare mass m_o have to be considered. Their divergencies are absorbed by the renormalization procedure in a specific scheme s, that corresponds to a choice of the mass parameter m^{s} and a reexpression of $\Sigma \to \Sigma'$ such that

$$m_0 = m^s + \delta m, \quad \Sigma'(m^s) = \Sigma(m^s) - \delta m \tag{2.9}$$

and m^s and Σ' become finite. Although the choice of the scheme is a purely technical, it can become a very important practical issue, because one scheme may result in a perturbative expansion that converges better than another [10, 57].

One scheme choice for the quark mass renormalization is the pole mass (m_t^{pole}). It is based on the idea that fermions appear as asymptotic states and corresponds to the real part of the fermion propagator pole including all self-energy corrections. Conceptually, this corresponds to measuring its mass in isolation, i.e. without any external interaction. This is only possible for colorless, stable particles. Therefore, the concept of a quark pole mass has intrinsic theoretical limitations owing to the fact that quarks are colored objects subject to confinement [48]. While the pole mass is well-defined to every fixed order k in perturbation theory, it cannot be defined to all orders ($k \to \infty$) [58].

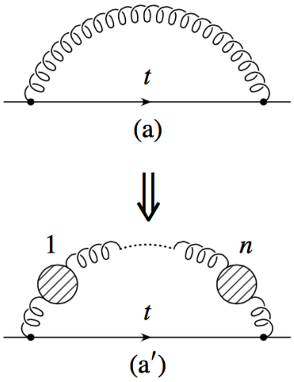

Figure 2.7: Diagrams contributing to the top-quark self-energy at leading order in α_S (a) and when summing to all orders in the gluon propagator by inserting n vacuum polarization subdiagrams (a') [59].

For example, when inserting n vacuum polarization subdiagrams into the gluon propagator in the one-loop self-energy diagram as shown in Figure 2.7, *renormalons* arise [59, 60]. The results can be expressed as an expansion in α_S with coefficients c_n. For $n \to \infty$, c_n grows factorically and leads to a divergent series [61–63]. However, the series can be truncated, which leads to an irreducible uncertainty of at least $\mathcal{O}(\Lambda_{QCD})$ [64, 65].

Alternatively, a short-distance definition, e.g. the modified minimal subtraction ($\overline{\text{MS}}$) scheme, can be used for the renormalization. A short-distance mass, such as the $\overline{\text{MS}}$ mass can in principle be measured with arbitrary accuracy [59]. Here, only the ultraviolet divergent (short distance) terms (and constants) are subtracted to achieve a finite expression for m^s. These terms depend on the renormalization scale μ, and therefore lead to a *running* mass $m_t^{\overline{\text{MS}}}(\mu)$[2]. The perturbative series for total $\mathrm{t\bar{t}}$ cross sections con-

---

[2] Throughout this thesis, $m_t^{\overline{\text{MS}}}$ corresponds to $m_t^{\overline{\text{MS}}}(\mu = m_t^{\overline{\text{MS}}})$.

verges significantly faster if expressed in terms of $m_t^{\overline{\mathrm{MS}}}$ rather than m_t^{pole} [57]. For every observable that has been analyzed in sufficient detail to make this comparison, the same conclusion has been reached [10].

As alternative renormalization schemes, all short distance masses can be related to the pole mass through a perturbative series[3]. To any order k, it is given for the $\overline{\mathrm{MS}}$ mass as [58]:

$$m_t^{\mathrm{pole}}(k) = m_t^{\overline{\mathrm{MS}}}(\mu) \cdot \left[1 + \sum_{n=1}^{k} c_n \left(\frac{\mu}{m_t^{\overline{\mathrm{MS}}}} \right) \alpha_S^n(\mu) \right] . \tag{2.10}$$

The coefficients c_n are calculated to 4 loops (α_S^4) in QCD [66]. The perturbation series in terms of $c_n \alpha_S^n(m_t)$ has a reasonable behavior for the top quark, while already for the b quark, the term for $n = 4$ is almost as large as the term for $n = 3$ [66].

Further, the *MSR* [67, 68] scheme can be chosen, where self-energy corrections from scales larger than R are absorbed into the mass $m_t^{\mathrm{MSR}}(R)$ and R is a continuous parameter that can interpolate between the $\overline{\mathrm{MS}}$ and pole mass schemes.

A determination of the top-quark mass in either scheme is possible from the mass dependence of any observable which is precisely measured and, at the same time, theoretically predicted beyond the leading order (LO) approximation in QCD perturbation theory [6].

The currently most precise measurements of the top-quark mass are performed in pp and $p\bar{p}$ collisions and employ final-state properties [69–72]. These *direct* measurements reconstruct the top-quark mass from its measured decay products. For this purpose, *Monte-Carlo* (*MC*) simulations are used to relate the measured observable to a top quark mass. Beneath the hard-interaction calculations, these simulations also contain contributions from ISR, FSR and UE modeled by parton showers, which correspond to LL approximations. To some extent, MC predictions are therefore always based on heuristic modeling, which does not allow a precise definition of the mass scheme [10]. Even though measurements of the top quark MC mass (m_t^{MC}) as a function of kinematic event variables [69] promise to be a useful method to improve the understanding of its interpretation [9], the m_t^{MC} parameter can not be interpreted directly as a mass in a well-defined scheme. However, studies suggest that m_t^{MC} can be translated to a theoretically well defined short-distance mass definition (m_t^{MSR}) at a low scale R [67]:

$$m_t^{\mathrm{MC}} = m_t^{\mathrm{MSR}}(3^{+6}_{-2}\,\mathrm{GeV}) \tag{2.11}$$

and that the difference to m_t^{pole} should be of the order of 1 GeV [10] or even below [73]. Nevertheless, further studies to relate m_t^{MC} to a theoretically well-defined top-quark mass have to be performed.

The aim of *alternative* measurements (in contrast to direct measurements) is to determine a well-defined top-quark mass. At the Tevatron and the LHC these measurements are performed by employing the mass dependence of the inclusive $\mathrm{t\bar{t}}$ production cross section [11–13] or based on the kinematics of the top-quark pair system in association with an additional jet [74, 75]. These observables are measured and compared to fixed-order predictions in a well-defined top-quark mass scheme in a second step. Also endpoints of kinematic distributions can be related to the top-quark mass analytically using the narrow-width approximation (*NWA*) and allow to measure a top mass that does not rely

---

[3] To all orders, this series shows the divergent behavior discussed before. However, it is well-defined for a fixed order in perturbation theory.

on MC simulation and is therefore not using the MC mass [9, 76]. The alternative measurements, however, do not reach the precision of direct measurements. A determination of a running top-quark mass with a precision of about 100 MeV could be achieved at a future linear e^+e^- collider together with the strong coupling constant in a scan of the center-of-mass energy at the $\mathrm{t\bar{t}}$ production threshold [77–79].

2.4 Theory predictions for top-quark production

The inclusive cross section for $\mathrm{t\bar{t}}$ production in hadronic collisions is calculated to NNLO for all production channels: the all-fermionic modes ($q\bar{q}$, qq', $q\bar{q}'$, $qq \rightarrow \mathrm{t\bar{t}} + X$) [80, 81], the reaction $q\mathrm{g} \rightarrow \mathrm{t\bar{t}} + X$ [82], and the gluon-fusion process $\mathrm{gg} \rightarrow \mathrm{t\bar{t}} + X$ [14]. At energies near production threshold, soft gluon radiation leads to large logarithmic terms. These are resummed at next-to-next-to-leading-log (NNLL). The theoretical uncertainty of this calculation due to yet uncalculated higher order corrections is evaluated by independent variations of the factorization and renormalization scale by a factor of 2. This variation is restricted by $0.5 \leq \mu_F/\mu_R \leq 2$ and amounts to an uncertainty on the cross-section of about 4%. The NNLO+NNLL calculations are implemented in the TOP++ program [14, 80–85], that allows to calculate the $\mathrm{t\bar{t}}$ production cross section for different choices of PDF sets, renormalization and factorization scales, α_S, and m_t^{pole} values. In addition, the dependence of the $\mathrm{t\bar{t}}$ production cross section on $m_t^{\overline{\mathrm{MS}}}$ can be evaluated with HATHOR [86, 87] employing calculations [14, 80–82] at NNLO accuracy and EWK corrections based on Ref. [88–90]. A similar precision is provided by predictions for the production cross section of single top quarks in association with a W-boson calculated at approximate NNLO [91]. The prediction employs NLO calculations with soft-gluon resummation in NNLL, performed by determining the two-loop soft anomalous dimension for two massive quarks, and then using these results in the limit when only one quark, the top quark, is massive [92].

The comparison of QCD predictions with the data and a multitude of phenomenological analyses of interest require to have precise predictions not only for the inclusive production cross section, but also at differential level [93]. While exact NLO calculations for differential $\mathrm{t\bar{t}}$ cross sections are available [20, 94–96], full NNLO calculations are only performed for a limited set of observables [97]. By using threshold resummation methods one can derive approximate formulas at NNLO for other differential distributions, in which the cross sections are expanded in terms of the logarithmic enhanced contributions (appearing as positive distributions), and can therefore be written at various degrees of logarithmic accuracy [93, 98–105].

Differential cross sections as a function of a variety of observables can be calculated with MCFM [20]. It is a parton-level event integrator which gives results for a series of processes, some including subsequent decays, as in case of the top quark. The latter is treated as being on-shell and therefore, the amplitudes for top-quark pair production and single-top-quark production can be factorized into the product of an amplitude for production and an amplitude for decay [19]. The calculation of production and decay includes real and virtual QCD corrections at NLO, keeping the full dependence on the b-quark mass and retaining all spin correlations [18, 19, 106]. Since it is performed completely differential, properties of the decay products are predicted up to the particles emerging from the subsequent W-boson decays.

2.5 Monte-Carlo simulation

Monte-Carlo generators are employed to simulate not only the hard interaction but also the subsequent decays up to stable particles. This is done on an event-by-event basis where a random generator produces each event statistically distributed according to the cross-section predictions based on the implemented model. To avoid statistical fluctuations, the *MC samples* used here typically comprise 5–10 times more events than expected in the data. The expected number of events, N_{exp}, is given by the product of the predicted production cross section of the process and a machine parameter constant, the *luminosity*, discussed further in Chapter 3.1. For comparison with the measured event yields, the contributions from each MC sample are normalized to N_{exp}. Each event is generated in several steps. First, the MEs for the hard scattering process are calculated. In a second step, ISR and FSR are modeled by parton shower programs that also incorporate phenomenological models for the hadronization and the UE, where proton remnants interact with the final state. The particles generated by the parton shower attain the momentum in the direction of the source parton and form *jets*. Finally, the interaction of the generated particles with the detector material is simulated.

In the following, the specific event generators used in the analyses are described. Subsequently, the simulation of the $\mathrm{t\bar{t}}$ signal process and of contributions from other processes are discussed.

PYTHIA 6.426 [107] is a general-purpose MC event generator for processes within and beyond the SM. It combines analytical results from LO matrix elements with phenomenological models to describe the PS and the hadronization based on the Lund String model. In addition, UE effects from proton and beam remnants are modeled. Different tunes for the UE, the PS and the hadronization models can be chosen. For the analyses presented here, the *Z2* [108] and the *Z2** tunes [109] are employed for the central MC simulation and all calculations are performed based on the PDF set CTEQ6L [110]. Variations of the UE modeling are evaluated using different Perugia 2011 (P11) tunes [111]: the *mpiHi* and the *Tevatron* tunes, which generate a larger or lower fraction of underlying event activity compared to the central tune, respectively. In addition, the P11 *noCR* tune is employed to study effects of CR between the final state and the UE. Polarization effects in the decay of τ leptons are modeled with TAUOLA [112] that is closely interfaced to PYTHIA. TAUOLA offers the possibility to take into account effects of spin, EWK corrections or of new physics and incorporates a substantial amount of specific results from distinct τ-lepton measurements.

MADGRAPH 5.1.4.8 [113] is a generator for matrix elements on tree-level for pp and $p\bar{p}$ collisions. In case of $\mathrm{t\bar{t}}$ production, up to three additional partons are generated on ME level. The MADGRAPH MC samples used here employ the CTEQ6L PDF set. Further top-quark decays are simulated using MADSPIN 2.0.0.beta4 [114], that allows to decay narrow resonances while preserving both spin correlations and finite width effects to a good accuracy. The factorization and renormalization scales are set to the combined hard scattering scale $Q^2 = m_t^2 + \sum_i p_{\mathrm{T}}(i)$ with i being an additional generated parton. For the simulation of hadronization and parton showering MADGRAPH with MADSPIN is interfaced to PYTHIA (in the following MADGRAPH+PYTHIA). To avoid double counting due to radiation generated by the showering and matrix element, an energy threshold (*ME-PS matching scale*) is introduced that assigns each jet production to a distinct generator. The matching is performed based on the *MLM* approach described in Ref. [115].

POWHEG [116–120] incorporates NLO ME calculations and passes on interactions to parton showering generators ranked by their hardness. Therefore, it employs a different approach to avoid a double counting. The hardest emission is generated with a Sudakov form factor modified with the NLO contributions, and subsequent emissions are generated according to the standard algorithm of the parton shower program [116], here PYTHIA. Two versions are employed: POWHEG 1.0 r1380, and POWHEG 2.0 using the PDF set CTEQ6M [110].

In the following, the processes relevant for the analyses presented in this work are discussed. The production of $\mathrm{t\bar{t}}$ pairs is considered the *signal* process. For this process, the central simulation is performed with MADGRAPH+PYTHIA using the Z2* tune. Dedicated MC samples are produced to estimate the effect of variations of modeling parameters (*modeling uncertainties*): possible higher-order contributions are estimated by variations of the Q^2 scale by a factor of 2 up and down. This scale variation is propagated to the PS. The ME-PS matching threshold is varied from a central value of 20 GeV to 10 GeV and 40 GeV. P11 tunes (mpiHi, Tevatron, and noCR) are employed for variations of the UE modeling. The nominal m_t^{MC} value used in the signal simulation is 172.5 GeV. Depending on the analysis purpose, m_t^{MC} is varied up to ±6 GeV. In addition to the signal process simulation with MADGRAPH+PYTHIA, POWHEG 2.0 interfaced with PYTHIA is employed to study the effect of the ME generator choice. The configuration parameters for the signal simulation of POWHEG 2.0, MADGRAPH, and MADSPIN can be found in Appendix A. All $\mathrm{t\bar{t}}$ MC samples are normalized to the predicted cross section for $\mathrm{t\bar{t}}$ production $\sigma_{\mathrm{t\bar{t}}}$ at NNLO+NNLL [14].

The analyses are performed in the dileptonic $\mathrm{t\bar{t}}$ decay channel. Contributions from other decay channels are not considered signal and referred to as *$t\bar{t}$ background* (*$t\bar{t}\,bg$*). Other *background* processes with signatures that mimic the $\mathrm{t\bar{t}}$ decay contribute to the analyses and are discussed in the following.

The production of single-top-quarks in association with a W boson (tW) is simulated for variations of $m_t^{\mathrm{MC}} = 172.5 \pm 6\,\mathrm{GeV}$ using POWHEG 1 interfaced with PYTHIA using the Z2* tune and normalized to the cross-section prediction at approximate NNLO [91]. The dependence of this prediction on m_t^{pole} is calculated with HATHOR. For all remaining background processes, the Z2* tune is employed for $\sqrt{s} = 8\,\mathrm{TeV}$, and the Z2 tune for $\sqrt{s} = 7\,\mathrm{TeV}$. The production of $\mathrm{t\bar{t}}$ in association with heavy vector bosons ($t\bar{t}\,V$) is simulated using MADGRAPH+PYTHIA and normalized to their predicted production cross sections at NLO [121,122]. Predictions by MADGRAPH+PYTHIA are also employed for Drell-Yan (DY) processes and production of a W-boson in association with jets (*W+jets*), both normalized to the corresponding cross section predicted by FEWZ 3.1 [123]. Diboson (VV) production as well as multijet-production (*QCD*) events are simulated with PYTHIA.The former is normalized to the cross section predicted at NLO using MCFM, the latter is normalized to cross section predictions at LO from PYTHIA. The simulation of QCD events is enriched with e or μ by requiring a generated muon with p_{T} above 15 GeV or leptonic decays of the produced hadrons. In particular cases, contributions from QCD and W+jets processes are treated together as *non-W/Z* contribution.

The interaction of the generated particles with the material of different detector components is modeled with GEANT4 [124,125]. This software includes a model of the CMS detector geometry and detector materials including all subdetectors, magnetic fields, electronic systems and supporting structures. The generated particles are fed through a simulation of bremsstrahlung, showering in calorimeters, and multiple scattering. The information about the quantities of each generated particle is preserved and can be addressed at a later stage of the analysis. As a result, the full response of all detector subsystems to each generated event is simulated.

Within the CMS Collaboration, the production of MC samples is organized centrally. However, particular MC samples were generated specifically for the analyses presented here. The $\mathrm{t\bar{t}}$ signal simulations for $\sqrt{s} = 7\,\mathrm{TeV}$ including Q^2, and ME-PS matching scale and m_t^{MC} variations were configured and tested privately before submitting them to central production. The simulation of tW processes at $\sqrt{s} = 7\,\mathrm{TeV}$ for different m_t^{MC} choices was configured and carried out completely independent of the central production.

Chapter 3

The LHC and the CMS Experiment

3.1 The Large Hadron Collider

The LHC [126] is a proton-proton ring collider[1] with a circumference of 27 km designed for $\sqrt{s} = 14$ TeV located at CERN (European Organization for Nuclear Research) near Geneva, Switzerland. During its first running period (*Run 1*) from 2010 until 2012, it was operating at $\sqrt{s} = 7$ TeV and 8 TeV for pp collisions.

Two proton beams running in opposite direction are led in bunches in two evacuated beam pipes by helium-cooled superconducting magnets with a field up to 4.16 T. The proton bunches are accelerated in steps: hydrogen atoms are first stripped of their electrons, split and accelerated to 50 MeV in a linear accelerator. Boosters and synchrotrons then accelerate the protons to an energy of 450 GeV before they are injected in the LHC beam pipes. There, acceleration up to the final beam energy takes place.

The beams are focused and collide at 4 interaction points, where the experiments are located: ALICE (A Large Ion Collider Experiment), ATLAS (A Toroidal LHC ApparatuS), CMS (Compact Muon Solenoid), and LHCb (Large Hadron Collider beauty experiment). The LHCb detector is designed for studies of heavy-flavor physics and CP violation. It covers a horizontal angle of 10 to 300 mrad and a vertical angle of 250 mrad with respect to the beam line, where heavy flavor c and b mesons are predominantly produced. The ALICE experiment is optimized to measure high track multiplicities in heavy ion collisions. Being technically a part of the CMS experiment, the TOTEM experiment is build to perform measurements of the total pp cross section and diffraction. At the interaction points of the two multi-purpose experiments, CMS and ATLAS, the beams are focused to a profile of 16.7 μm diameter and collide with a crossing angle of 285 μrad and a rate of $\mathcal{O}(40$ MHz).

The expected event rate $\mathrm{d}N_k/\mathrm{d}t$ of a certain process k is connected with its cross section σ_k through the instantaneous luminosity of the machine. It depends on the number of bunches, N_b, the number of protons per bunch, N_i, in beam i, the revolution frequency, ν, and the beam profile area, A, at the collision point:

$$\mathcal{L} = \frac{N_b \cdot N_i \cdot N_j \cdot \nu}{A}, \quad \frac{\mathrm{d}N_k}{\mathrm{d}t} = \mathcal{L}(t) \cdot \sigma_k. \tag{3.1}$$

During Run 1, the luminosity increased gradually as illustrated in Figure 3.1, such that to the total integrated luminosity delivered by the LHC amounts to 6.1 fb^{-1} at $\sqrt{s} = 7\,\mathrm{TeV}$ and 23.3 fb^{-1} at $\sqrt{s} = 8\,\mathrm{TeV}$. The luminosity recorded by each experiment is determined separately. Its measurement with the CMS detector is described in Section 3.2.6.

---

[1] It is also a heavy ion collider which is not part of this work.

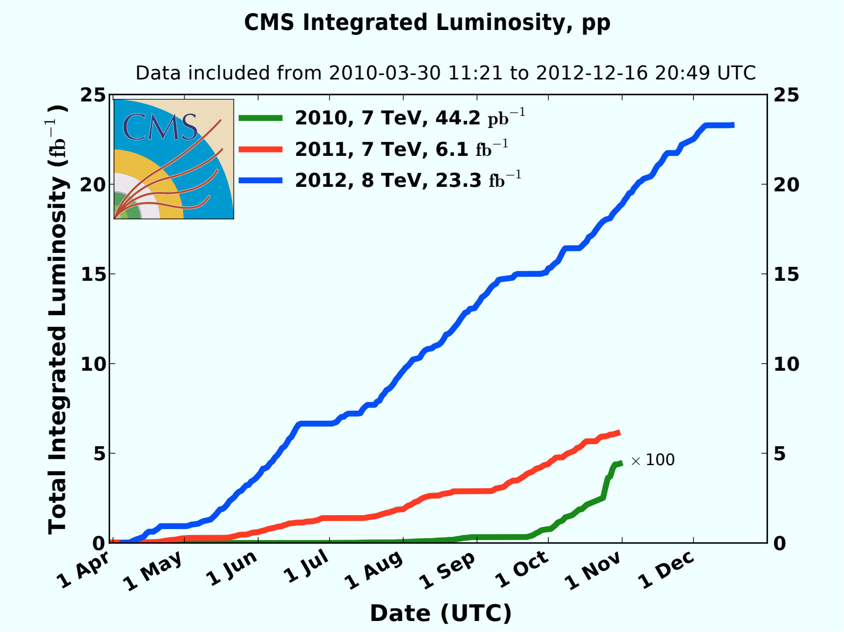

Figure 3.1: Luminosity delivered by the LHC as a function of time for the data-taking periods 2010-2012 [127].

3.2 The Compact Muon Solenoid

The CMS experiment is one of the two general-purpose detectors at the LHC, which is located about 100 m underground at one of the LHC interaction points. Its design, as shown in Figure 3.2, is radially symmetric along the beam pipe and consists of several subdetector-layers.

The origin of the CMS coordinate system is the interaction point at the center of the detector [128]. The x-axis points to the middle of the LHC ring, the y-axis upwards and the z-axis along the beamline in anti-clockwise direction. The polar angle θ is measured with respect to the z-axis and the pseudorapidity η is defined as $\eta = \ln\left(tan(\theta/2)\right)$. The azimuthal angle ϕ is measured in the x–y plane with respect to the x-axis. Angular distances in ϕ and η between objects emerging from the center of the detector are described by $\Delta\mathrm{R} \equiv \sqrt{(\Delta\eta)^2 + (\Delta\phi)^2}$, the distance to the interaction point in $x-y$-plane is defined as $\rho = \sqrt{x^2 + y^2}$.

A homogeneous magnetic field of 3.8 T is produced by a solenoid coil of 12.5 m length and a diameter of 6 m. Inside the coil, starting from the interaction point, the tracking system is surrounded by the main calorimeters. The muon system outside the coil is embedded in the iron yoke, which returns the magnetic flux. The endcaps close the coils orifices and show the same layers of sub-detectors.

In the following, the detector components particularly important for the analyses performed in this thesis are described.

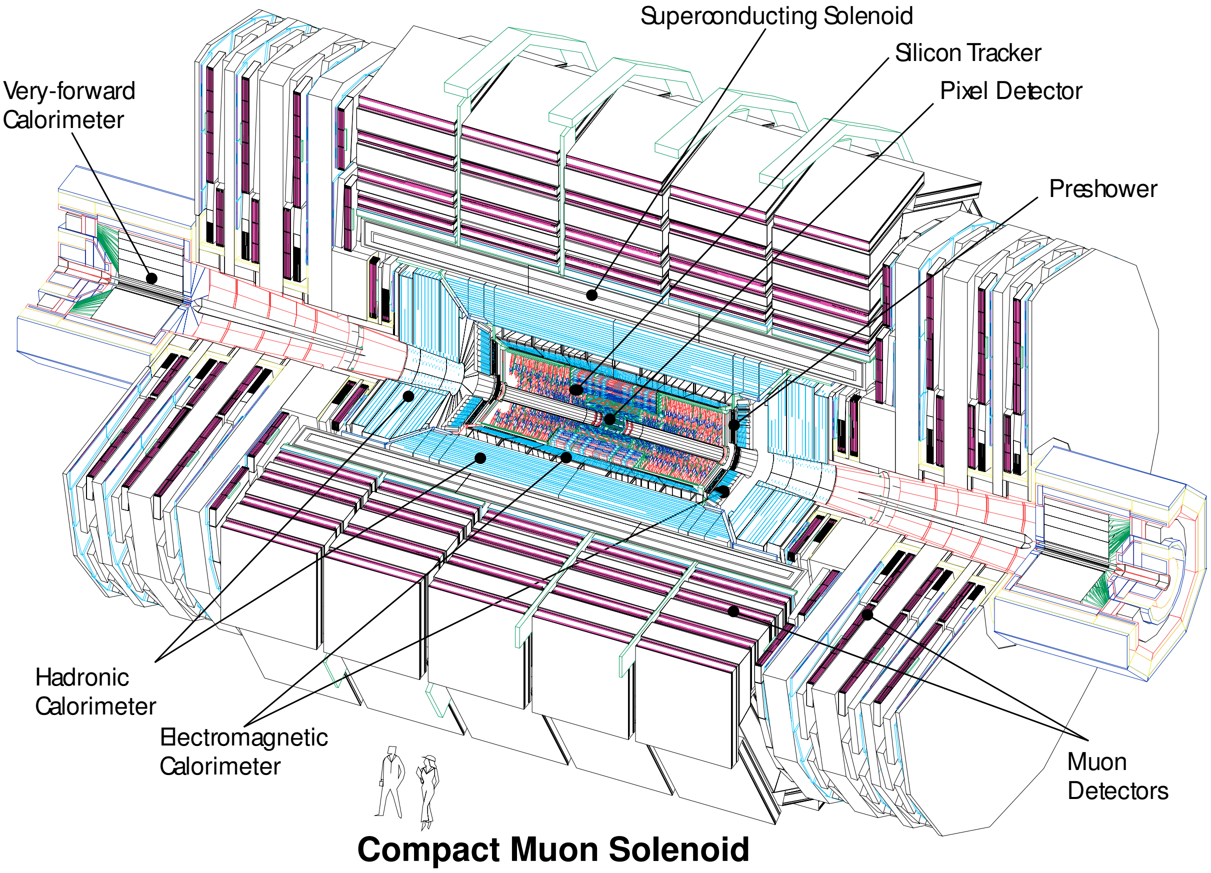

Figure 3.2: The CMS detector with its main components [129].

3.2.1 Tracker

The CMS tracker is placed on a carbon-fibre frame and cooled down to –20 ^{o}C. It is divided into an inner pixel detector and an outer strip detector for the reconstruction of trajectories and charge measurements.

Both tracker parts, which are illustrated in Figure 3.3, are based on semi-conductive silicon diodes with embedded readout chips and cover an angular acceptance of $|\eta| < 2.5$. They provide a fine granularity and fast readout to cope with high track multiplicities and a high bunch crossing rate.

The inner pixel detector consists of three cylindrical layers of sensors, which are located at a radial distance of 4.4 cm, 7.3 cm, and 10.2 cm, and layers in the $x - y$ plane at $|z| =$ 34.5 cm and 46.5 cm. In total 66 million pixels, distributed over a total area of about $1\,\text{m}^2$, result in a $\rho - \phi$ resolution of $\approx 10\,\mu$m and a resolution in z of $\approx 20\,\mu$m.

The outer strip detector is divided into four parts as shown in Figure 3.3: the Tracker Inner Barrel (TIB), the Tracker Outer Barrel (TOB), the Tracker Inner Disks (TID) and the Tracker Endcap (TEC). The barrel parts are located in the $\rho - \phi$ plane, the disk and endcap parts in the $x - y$ plane. Strips are used to collect the electrons or holes produced by charged particles passing the diode material. The first two layers of each part and the fifth layer of the TEC incorporate *stereo* modules, which provide a measurement not only in $r - \phi$, but also in $r - z$. Two strip sensors are superimposed with an angle of 100 mrad to form a stereo module.

So called *ghost* hits occur if two particles cross a module at the same time but at different points where the stripes from the layers of a module overlap. The resulting ambiguity has to be resolved in the reconstruction process using pixel detector information. The tracker stripes are distributed over an area of approximately 200 m^2 and are read out in 9.6 million channels. The resolution is of the order of 20 μm to 50 μm in $\rho - \phi$ and 500 μm in z.

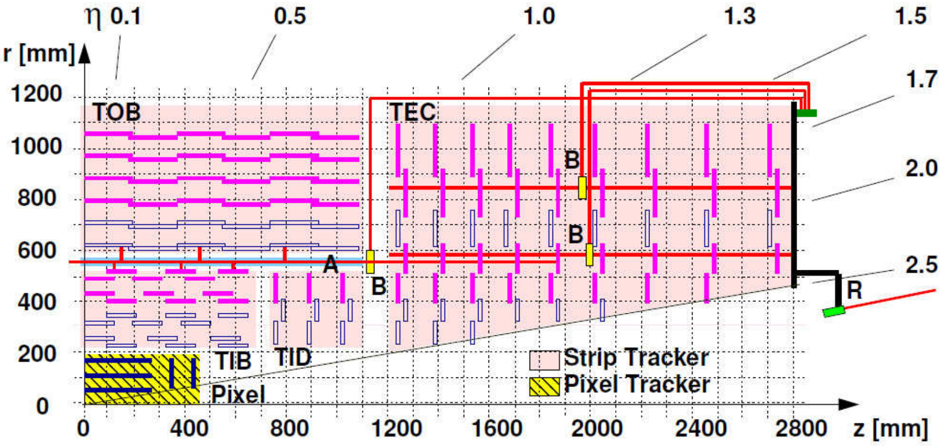

Figure 3.3: Drawing of a quadrant of the inner tracker of CMS in the $r - z$ plane. The pixel detector, the tracker inner barrel (TIB), outer barrel (TOB), inner disks (TID), and endcaps (TEC) are shown [130].

3.2.2 Electromagnetic calorimeter

The electromagnetic calorimeter (ECAL) covers two regions in $|\eta|$. The barrel calorimeter measures energies for the region $1.479 > |\eta|$ and the endcap calorimeter for $1.479 < |\eta| < 3.0$ as illustrated in Figure 3.4. Both are crystal calorimeters made out of tungstate ($PbWO_4$) which acts as scintillator and absorber simultaneously. Each of in total 75848 crystals covers an angle of $0.0174^o \times$ 0.0174 in $\phi \times \eta$. The material allows for a high granularity due to a short Moliere radius of 2.2 cm and a fast response, such that 80% of the light is emitted within 25 ns.

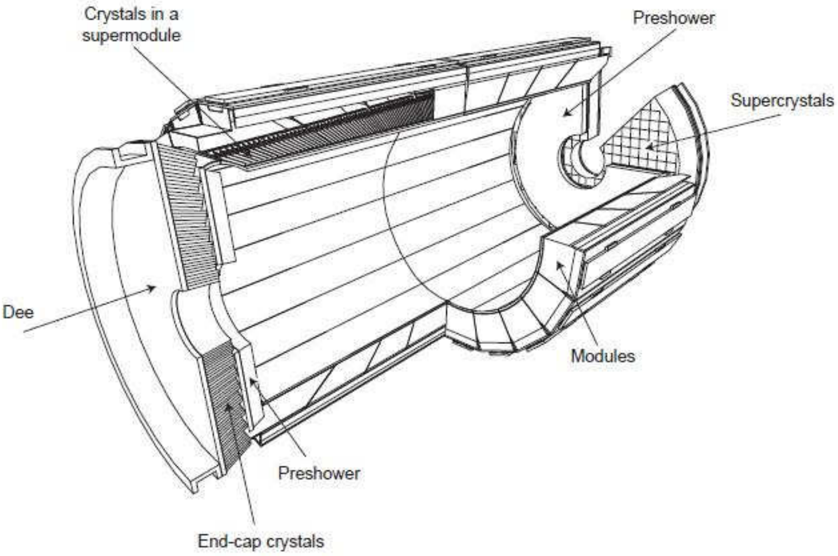

Figure 3.4: Schematic view of the electromagnetic crystal calorimeter of CMS [131].

The length of the barrel and endcap crystals is 22 cm and 23 cm, respectively, corresponding to a radiation length of about $25 \cdot X_0 = 25 \cdot 0.89\,\text{cm}$. The emitted light is detected by photodiodes in the barrel part and by phototriodes in the endcaps. The crystals, as well as the photodiodes are cooled down and held at a temperature of $18\,^o$C to ensure a constant sensitivity. Pre-shower detectors are placed in front of the endcap ECAL modules in the region $1.653 < |\eta| < 2.6$. These are sampling calorimeters which consist of layers of altering scintillator and showering material. The preshower detectors identify neutral pions and improve the position resolution of the showers with their inbuilt silicon strip sensors. The relative resolution of the ECAL depends on the energy deposit E and is approximately given by:

$$\frac{\Delta(E)}{E} = \frac{2.\%}{\sqrt{E/GeV}} \oplus \frac{12\%}{E/GeV} \oplus 0.3\% \tag{3.2}$$

Here, the first term is a stochastic term, the second describes noise from electronics and the third constant term describes leakages, non-uniformities, and non-linearities in the response.

3.2.3 Hadronic calorimeter

The hadronic calorimeter is divided into four subsystems as shown in Figure 3.5. These are all sampling calorimeters: the hadronic barrel calorimeter (HB), the hadronic endcap calorimeter (HE), the outer hadronic calorimeter (HO), and the forward hadronic calorimeter (HF).

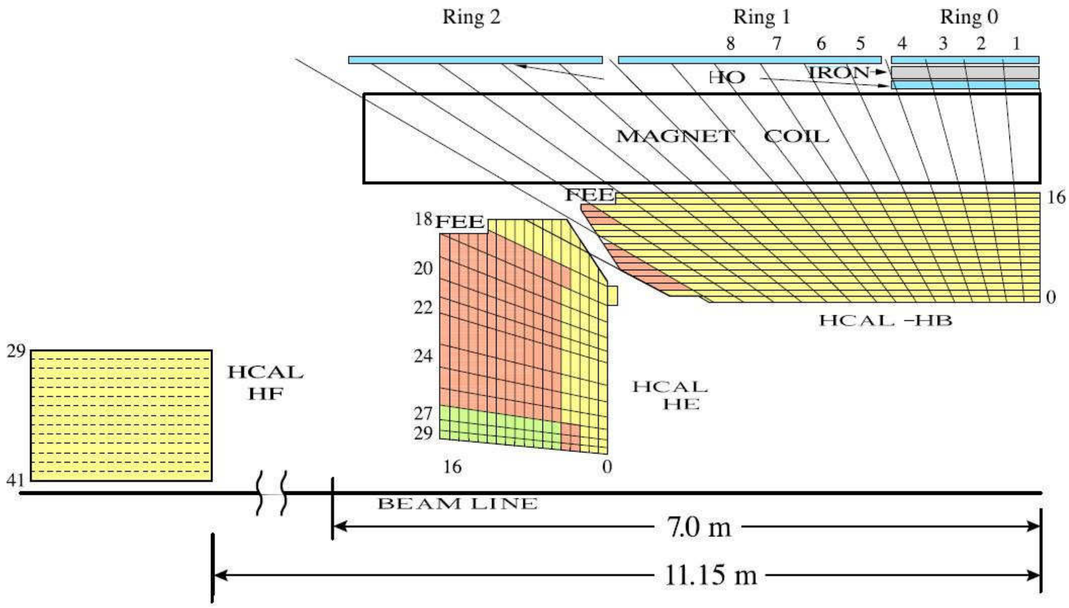

Figure 3.5: Structure of a quadrant of the CMS hadronic calorimeter in the $y - z$ plane with the hadronic barrel (HB), the hadronic endcap (HE), the hadronic forward (HF) and the hadronic outer calorimeter (HO) [132].

The HB covers the range of $|\eta| < 1.4$ and consists of segments (*towers*) incorporating 15 layers of alternating absorber and scintillator. Each of these 2304 towers is enclosed in stainless steel and covers an angle of $0.087^o \times 0.087$ in $\phi - \eta$. The thickness increases from 5.85 interaction lenghts in the central region to about 10 at $|\eta| = 1.3$. The scintillator light is lead though wave-shifting fibres to multi-channel hybrid photodiodes.

The HO, which is located outside the solenoid coil, increases the total thickness of the hadronic calorimeters in the barrel region to above 10 interaction lengths and follows the segmentation geometry of the HB.

The HE covers the range of $1.3 < |\eta| < 3.0$. Its tower size increases with respect to η up to $\Delta\eta = 0.35$ and $\Delta\phi = 0.175$. Each HB and HE tower matches 5×5 ECAL segments.

The HF is positioned 11.2 m away from the interaction point in z and covers the range of $3.0 < |\eta| < 5.0$. In contrast to all other HCAL parts, it incorporates steel as absorber and quartz fibres as scintillator material. Both materials have good radiation hardness, needed since most of the collisions at the LHC result in soft scattering interactions in this spatial region. The energy resolution of the hadronic calorimeter follows Equation 3.3 with $a = 0.847 \pm 0.016$, $b = 0.074 \pm 0.008$ for HE and HB, and $a = 1.98$, $b = 0.09$ for the HF [132]. This part of the HCAL is not used in this thesis.

$$\frac{\Delta(E)}{E} = \frac{a}{\sqrt{E/GeV}} \oplus b \tag{3.3}$$

3.2.4 Muon system

The most outer part of the detector is the muon system. It is embedded in the iron yoke to return the magnetic flux. The magnetic field in the return yoke is 2 T. The muon detectors illustrated in Figure 3.6 consist of the following gas detectors: resistive plate chambers (RPC) and drift tubes (DT) for the barrel region and cathode strip chambers (CSC) in the endcap region.

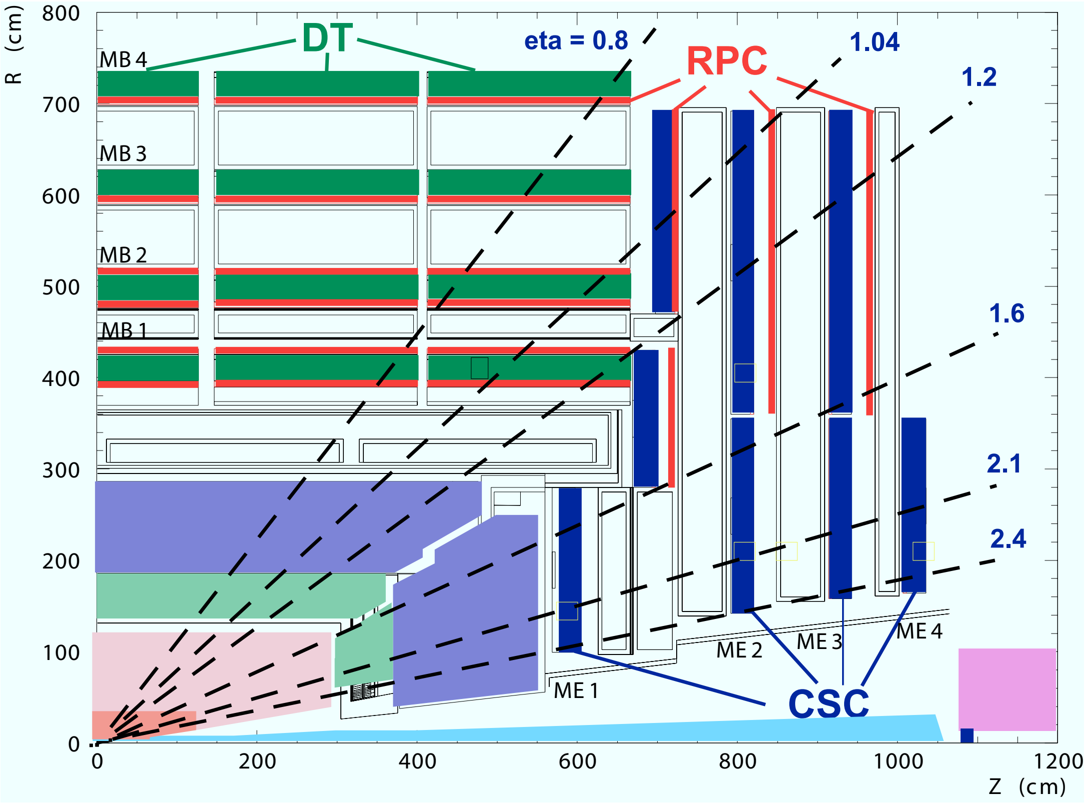

Figure 3.6: Quadrant of the CMS muon detector system consisting of Drift Tubes (DT) in the barrel and Cathode Strip Chambers (CSC) in the endcaps, and attached to both Resistive Plate Chambers (RPC) [128].

The gas gap in the RPCs is enclosed by two parallel phenolic resin plates with large electrical resistance and a distance of a few millimeters coated by conductive paint [133]. This graphite paint forms the electrodes, which induce the electric field. Insulated from the electrodes, aluminum stripes are coupled to the readout electronics. The CMS RPCs are operated in avalanche mode, meaning that no local discharges are induced by crossing particles. This increases the read-out speed to cope with the LHC interaction rate. The RPCs provide a time resolution of about 1 ns and are used mainly for trigger purposes.

Four layers of drift tubes at $\rho = 4.0\,\mathrm{m}$, $4.9\,\mathrm{m}$, $5.9\,\mathrm{m}$, and $7.0\,\mathrm{m}$ are located in the barrel region. The drift tubes have a rectangular profile with a maximum drift distance of 2.1 cm. Drift tubes are collected in so-called *stations MB1 – MB4*, having a resolution of $\approx 100\,\mu\mathrm{m}$.

In the endcaps four disks of CSCs (*ME1 – ME4*) provide track information. A total of 36 chambers are combined with an RPC at the inner side to form one disk for the ME2, ME3, and ME4 stations and have a spatial resolution of about $200\,\mu\mathrm{m}$. The ME1 station consists of 18 chambers and achieves a resolution of about 100 μm. The CSC signals can be used for triggering purposes, due to the fast detector response.

3.2.5 Trigger

At the full design luminosity, the LHC has a bunch crossing rate of 40 MHz. To record the information delivered by the detector systems, the event rate must be reduced to approximately 100 Hz. This is achieved by a trigger system [131], which decides during data taking which events to record and which to reject. It consists of the hardware-based Level-1 (*L1*) trigger and the software-based High Level Trigger (*HLT*).

The L1 trigger is built of programmable electronics and reduces the event rate by a factor of about 1000. It is divided in local, regional and global subsystems, as illustrated in Figure 3.7. During a decision time of less then 1 μs the full event information is stored in a memory. The decision process starts from an event in a local detector subsystem, such as a hit pattern in a muon chamber or energy deposits in a calorimeter tower. In a second step, the information of the chambers or towers is combined *regionally* to build *primitive* trigger objects. These are transferred from all regions of the detector to the Global Muon and Calorimeter Triggers ranked by energy, momentum and quality. The highest rank objects are then passed on to the Global Trigger, which rejects or accepts the event.

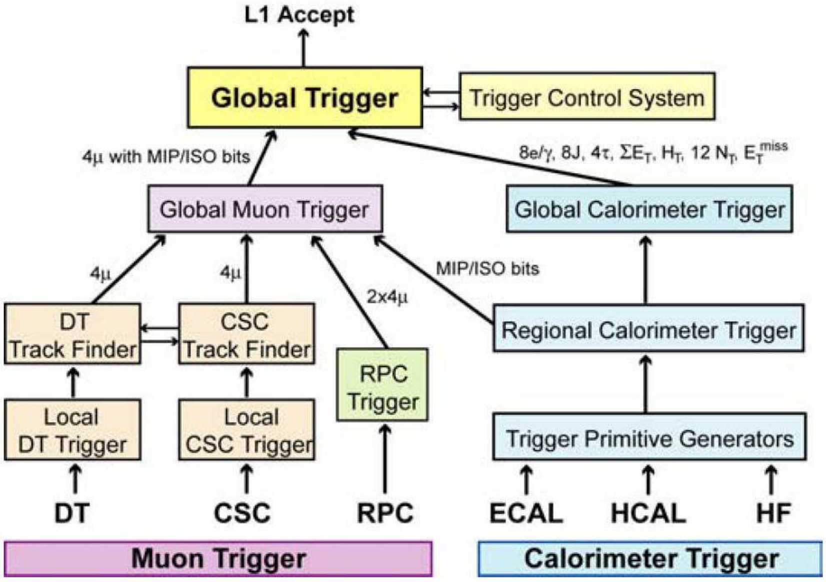

Figure 3.7: Structure of the Level-1 CMS Trigger [131].

Is the event accepted, the full event information from the memory pipeline is transferred to the High Level Trigger. The HLT is run on a computing farm with $\mathcal{O}(1000)$ processors and reduces the event rate from $\approx$ 100 kHz to $\approx$ 100 Hz before it is finally recorded. It takes a decision based on software algorithms, which perform a fast reconstruction of physics objects. The reconstruction starts at *regions of interest* marked by the L1 Trigger and adds gradually more information from other detector subsystems e.g. from the tracker to construct *trigger objects*. The HLT is organized in *trigger paths*, corresponding to a sequence of requirements. If at one step the event does not fulfill the requirements of any path, the event is rejected. If an event is accepted by a path (the trigger *fired*), the event is recorded.

3.2.6 Luminosity determination

An accurate determination of the instantaneous and the (integrated) total luminosity $L = \int \mathcal{L} \mathrm{d}t$ is crucial for most of the physics measurements at the LHC. The most precise measurements are performed using the Pixel Cluster Counting method [134]. The relation between the instantaneous luminosity, $\mathcal{L}$, the average number of active clusters in the pixel detector per event, $\langle n \rangle$, the corresponding visible cross section, σ_{vis}, and the beam revolution frequency, ν, can be expressed as:

$$\mathcal{L} = \nu \langle n \rangle / \sigma_{vis}. \tag{3.4}$$

The instantaneous luminosity can be expressed in terms of several beam parameters [135]:

$$\mathcal{L} = \nu N_1 N_2 K(\vec{v}_1, \vec{v}_2) \int \rho_1(\vec{r} - \Delta\vec{r}) \rho_2(\vec{r}, t) \mathrm{d}^3\vec{r} \mathrm{d}t \tag{3.5}$$

Here, $K(\vec{v}_1, \vec{v}_2)$ is the kinetic factor depending on the beam velocities, $\Delta\vec{r} = (\Delta x, \Delta y, 0)$ the nominal separation between the two beams in transverse plane, and $\rho(\vec{r}, t)$ the charge density function. The product of the protons populating the beam, $N_1 N_2$, is measured using Fast Beam Current Transformers (FBCT) and Direct Current Current Transformers (DCCT). The DCCT are designed to be insensitive to the time structure of the beam. Two FBCTs, one per ring, give a measure of the individual bunch charges. Assuming Gaussian shapes for the charge densities, the equation can be integrated and expressed as

$$\mathcal{L}(\Delta x, \Delta y) = \frac{\nu N_1 N_2}{2\pi \Sigma_x \Sigma_y} \exp\left(-\Delta x^2/(2\Sigma_x^2) - \Delta y^2/(2\Sigma_y^2)\right). \tag{3.6}$$

The effective overlap area of the colliding beams, e.g. $\Sigma_x \Sigma_y$, is obtained using Van der Meer luminosity calibration scans [136]. The beam profile is measured by recording the relative interaction rate as a function of the transverse beam separation along horizontal and vertical planes. The functional forms that describe the measured beam shapes allow to define a relation between the width of the rate profile and $\Sigma_{y,x}$.

During a scan, the number of active clusters $\langle n \rangle$ peaks at $\Delta x, \Delta y = 0$ and σ_{vis} can be extracted with high accuracy by combining Equations 3.4 and 3.6:

$$\sigma_{vis} = \frac{2\pi \Sigma_x \Sigma_y \langle n \rangle (\Delta x, \Delta y = 0)}{N_1 N_2}. \tag{3.7}$$

This allows to monitor the luminosity during data taking based on Equation 3.4. The necessary measurement of $\langle n \rangle$ is performed in zero-bias events [137] that are recorded without further requirements on the bunch crossing.

The amount of data recorded by the CMS experiment and employed in the analyses presented here corresponds to luminosities of 5049 pb^{-1} in 2011 at $\sqrt{s} = 7\,\mathrm{TeV}$ and 19664 pb^{-1} in 2012 at $\sqrt{s} = 8\,\mathrm{TeV}$ [134, 135] with an uncertainty of 2.2% and 2.6%, respectively. The data at $\sqrt{s} = 7\,\mathrm{TeV}$ is further divided into two run periods corresponding to a luminosity of $2310\,\mathrm{pb}^{-1}$ (*Run2011A*) and $2740\,\mathrm{pb}^{-1}$ (*Run2011B*). At

$\sqrt{s} = 8\,\mathrm{TeV}$, four run periods corresponding to a luminosity of $890\,\mathrm{pb}^{-1}$ (*Run2012A*), $4430\,\mathrm{pb}^{-1}$ (*Run2012B*), $7030\,\mathrm{pb}^{-1}$ (*Run2012C*), and $7270\,\mathrm{pb}^{-1}$ (*Run2012D*) are employed.

Chapter 4

Event Reconstruction and Selection

The detector responses are subject to the reconstruction procedure, common for data and simulation. The signature of different particles in the detector is schematically shown in Figure 4.1. The magnetic field bends the tracks of the charged particles corresponding to their charge and their momentum. Neutral particles are neither affected by the magnetic field nor leave hits in the tracker. Muons pass all subsystems including the iron return yoke with the inbuilt muon chambers. Charged and neutral hadrons deposit their energy mainly in the HCAL, electrons and photons in the ECAL only. Based on this information, the detector response is interpreted by reconstruction algorithms.

Simulations are used to describe the response of the detector systems to physics processes. The quality of these simulations is carefully monitored by detailed comparison to the measured detector response and the remaining deficits are corrected using data-driven methods. The corrections are applied either to the measured physical observable or assigned as weights on an event-by-event basis.

The physics analyses rely on proper reconstruction of the *physics objects*, which, in the case of the decay channel under investigation, are muons and electrons, accompanied by jets and neutrinos in the final state. The latter are not detected directly by the detector but reconstructed based on the energy balance in the event. For the remaining physics objects, a precise reconstruction of tracks and interaction vertices is crucial, both described in Section 4.1. In the subsequent Section 4.2, the *particle-flow* algorithms are discussed, which combine information of subdetector systems of the CMS experiment to identify the physics objects. In Section 4.3, additional quality criteria imposed on these objects and on each event considered for analysis are presented, together with the corresponding data-driven corrections applied. Furthermore, the triggers used in the event recording are studied in Section 4.4.

4.1 Track and vertex reconstruction

The track reconstruction is composed of several logical steps [128]. First, individual hits in the tracker are clustered since a particle passing through a tracker layer may result in more than one individual hit, in particular in layers with fine granularity. The clustering starts with those hits that provide a high signal-to-noise ratio (*SNR*) and subsequently adds adjacent hits with lower SNR.

Next, a seed is generated to provide the initial trajectory for the track reconstruction based on triplets or pairs of clusters in the tracker. For pairs, further constraints from the beam-spot position are taken into account. The pixel detector is well suited for this purpose due to its fine resolution. The initial track estimate is extrapolated to the next most compatible cluster in outer layers, and its parameters are recalculated, until no more

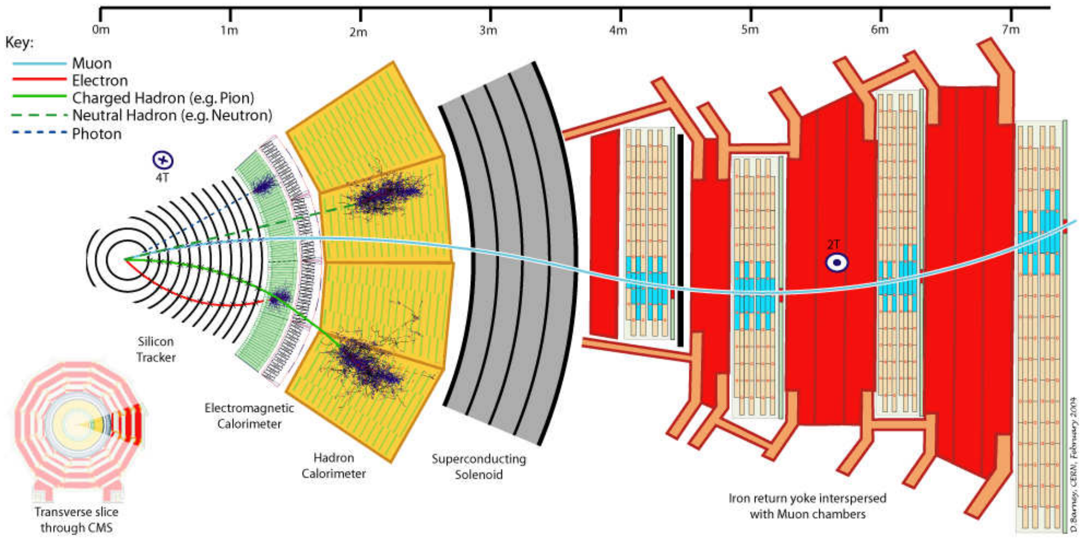

Figure 4.1: Signatures of different particles in the CMS detector in the ρ-ϕ plane [138].

compatible clusters can be found. From all reconstructed track candidates, only the best ones with respect their goodness of fit (normalized χ^2) are kept. The associated clusters are removed for the next iteration of track finding. Up to 6 iterations are performed, each with more relaxed requirements on the seeds, to find low-momentum tracks or tracks displaced with respect to the pixel detector.

High quality tracks with a *transverse impact parameter*[1] with respect to the beam-spot below 5 cm, associated hits in at least 2 pixel layers and at least 3 pixel or strip layers in addition, and a normalized $\chi^2 < 20$ are selected to reconstruct primary interaction vertices. The selected tracks are clustered on the basis of their z-coordinates at their point of closest approach to the center of the beam-spot using a deterministic annealing algorithm [139] as described in Ref. [140].

For each track associated to a resulting vertex candidate, a weight w_i between 0 and 1 is assigned to describe the probability of belonging to the vertex. Vertices reconstructed with at least $\sum_i w_i - 3 > 4$ and within $|z| < 24$ cm and $|\rho| < 2$ cm are considered primary vertex candidates. The vertex with maximum scalar sum of the associated tracks p_T is considered the primary vertex, with p_T being the transverse momentum of the track. This vertex is used as the reference for all relevant objects in the event.

On average 6 (14) primary vertex candidates are reconstructed at $\sqrt{s} = 7$ (8) TeV, as shown in Figure 4.2. The number of multiple pp interactions in each bunch crossing (*pileup*), N_PU, follows the Poisson distribution. The mean of this Poisson distribution, $< N_\mathrm{PU} >$, can be obtained from measurements [134,135,141] of the instantaneous luminosity per bunch crossing, $\mathcal{L}$, the total inelastic pp cross section, σ_tot, and the beam revolution frequency, ν, as [142, 143]

$$< N_\mathrm{PU} >= \frac{\mathcal{L} \cdot \sigma_\mathrm{tot}}{\nu}. \tag{4.1}$$

The simulation of the number of proton-proton interactions per event, $N_\mathrm{PU}^\mathrm{sim}$, is based on a-priori assumptions on the LHC run conditions and does not correspond to the measured distribution. Therefore, a weight w_PU is assigned to each simulated event.

---

[1] The transverse impact parameter of a track is defined as the distance of closest approach to the reference point in r-ϕ plane.

It is determined from the simulated and calculated pileup distributions with in total $n_{\mathrm{sim}}(N_{\mathrm{PU}}^{\mathrm{sim}})$ and $n(N_{\mathrm{PU}})$ events, respectively:

$$w_{\mathrm{PU}}(N_{\mathrm{PU}}^{\mathrm{sim}}) = \frac{n(N_{\mathrm{PU}}^{\mathrm{sim}})}{n_{\mathrm{sim}}(N_{\mathrm{PU}}^{\mathrm{sim}})} \cdot \frac{\sum_j n_{\mathrm{sim}}(j)}{\sum_k n(k)}. \tag{4.2}$$

After the correction, the vertex multiplicity distributions, shown in Figure 4.2, are well described by the simulation.

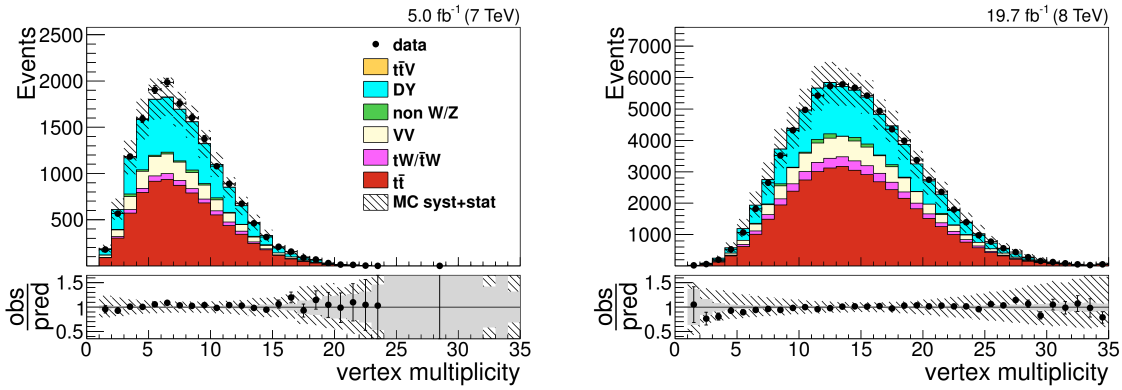

Figure 4.2: Reconstructed vertex multiplicity for $\sqrt{s} = 7\,\mathrm{TeV}$ (left) and $\sqrt{s} = 8\,\mathrm{TeV}$ (right). The hatched bands correspond to statistical and systematic uncertainties (discussed in Section 5.2) added in quadrature. The lower panels depict the ratio of observed and predicted yields. Here, the statistical uncertainty on the simulated yields is indicated by a gray shaded band. All events are required to fulfill the dilepton selection defined in Section 4.3.

4.2 Particle-flow event reconstruction

The particle-flow (*PF*) event algorithm [144,145] reconstructs and identifies each individual particle with an optimized combination of information from the various elements of the CMS detector [146]. The particles are identified as charged hadron, neutral hadron, muon, electron, and photon candidates.

The reconstruction procedure associates the reconstructed tracks and vertices to distinct energy deposits in the calorimeters. The energy deposits are clustered using a specific algorithm that has been developed for PF [144]. The tracks are extrapolated to the calorimeters and clusters compatible in ΔR are *linked* to the track. In the following PF candidate reconstruction, the candidates with the most distinct signature are reconstructed first, and the associated information (tracks and energy deposits) are removed from further processing.

Tracks linked to the tracker and the muon chambers and to typical energy deposits in the ECAL of 0.5 GeV and the HCAL of 3 GeV are reconstructed as PF muon candidates. A track associated to an energy deposit in the ECAL, which shows tangent tracks linked to ECAL deposits (identified as bremsstrahlung photon candidates), is assigned to a PF electron candidate. The remaining tracks are reconstructed as charged hadron candidates, if their track momentum and the associated energy deposit in the calorimeters are compatible. If the clustered energy exceeds the track momentum significantly, a neutral particle candidate is created. The latter can be a neutral hadron or a photon candidate depending on the fraction of energy deposed in the HCAL. In the same way, either photon or neutral hadron candidates are created from the remaining calorimeter clusters in the last step of the PF candidate reconstruction. All particle candidates not associated to the primary vertex are not taken into account for further event selection.

4.3 Event and object selection

The analyses presented here employ the dileptonic $\mathrm{t\bar{t}}$ decay channel. In particular, final states with one electron and one muon are considered. These leptons are expected to have a large momentum, to be produced in the primary interaction, and to be isolated with respect to other particles from ISR/FSR or the top-quark decay. Therefore, events considered for analysis are required to contain an opposite charged lepton candidate pair. Opposite-charged $\mathrm{e}^{\pm}\mathrm{e}^{\mp}$,$\mathrm{e}^{\pm}\mu^{\mp}$, and $\mu^{\pm}\mu^{\mp}$ candidates are paired. For events with more than one pair, the pair with the largest scalar sum of p_{T} is selected. Events are rejected if this pair does not consist of an electron and a muon candidate. The individual kinematic and quality criteria imposed on the lepton candidates, derived from further aspects of the $\mathrm{t\bar{t}}$ signature, are discussed in the following section. The pairs invariant mass, m_{ll}, distribution is shown in Figure 4.3 and is required to exceed 20 GeV to suppress contamination from QCD processes. This selection will be referred to as *dilepton selection*.

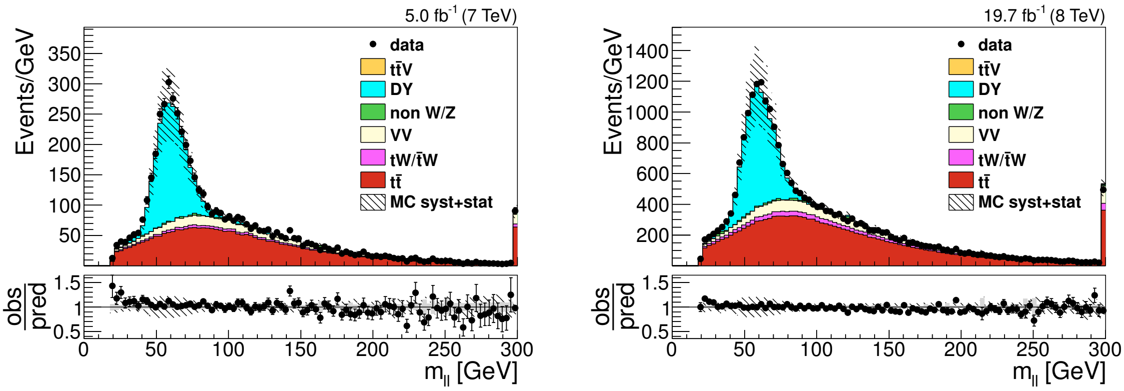

Figure 4.3: Invariant mass m_{ll} of the selected lepton candidate pair for $\sqrt{s} = 7\,\mathrm{TeV}$ (left) and $\sqrt{s} = 8\,\mathrm{TeV}$ (right). The hatched bands correspond to statistical and systematic uncertainties (discussed in Section 5.2) added in quadrature. The lower panels depict the ratio of observed and predicted yields. Here, the statistical uncertainty on the simulated yields is indicated by a gray shaded band.

4.3.1 Lepton candidates

Electron and muon candidates are required to have $p_{\mathrm{T}} > 20\,\mathrm{GeV}$ and $|\eta| < 2.4$, such that the candidates energies exceed the trigger thresholds discussed in Section 4.4, and hat the associated tracks can be reconstructed within the CMS tracker. Furthermore, lepton candidates are required to fulfill the isolation condition $I_{\mathrm{rel}} < 0.1$ (electrons) and $I_{\mathrm{rel}} < 0.12$ (muons), where I_{rel} is defined for a lepton candidate with transverse momentum

$p_{\mathrm{T},l}$ as:

$$I_{\mathrm{rel}} = \frac{1}{p_{\mathrm{T},l}} \left[\sum_{\text{charged hadr}} p_{\mathrm{T}} + \max\left(0, \sum_{\text{neutral hadr}} p_{\mathrm{T}} + \sum_{\text{photon}} p_{\mathrm{T}} - C_{\mathrm{PU}} \right) \right] . \tag{4.3}$$

Here, the transverse energy deposits p_{T} from charged hadron, neutral hadron, and photon candidates in a cone ΔR around the lepton candidate are considered. The cone is chosen as $\Delta \mathrm{R} = 0.4$ for muon and $\Delta \mathrm{R} = 0.3$ for electron candidates and the isolation values are corrected for pileup effects by the term C_{PU}. The latter quantifies the average energy deposits from pileup events within ΔR, determined technically different for electron [147] and muon [148] candidates.

Each electron candidate is required to have a transverse impact parameter, d_0, with respect to the primary vertex smaller than 0.02 cm. Converted photons and candidates with missing hits in their associated tracks are removed, to further decrease the contribution from mis-identified photons. For the final electron identification, a *multivariate analysis* (*MVA*) technique[2] is employed that combines information from the electron tracks, track quality criteria, geometrical and energy matching of ECAL deposits to tracks, and shower shapes within the ECAL [147]. The MVA returns a *discriminator* with a value between 0 and 1, describing how well the requirements are fulfilled by the electron candidate. Candidates with a discriminator value of at least 0.9 are selected providing a high selection purity.

Muon candidates are also selected with high purity by imposing the following quality criteria on their tracks: each track has to be reconstructed in both the muon system and the tracker, the combined track fit is required to have a normalized $\chi^2 < 10$. The track must be associated to at least one valid hit in the muon chambers, 6 tracker layers, and the inner pixel detector. Muon candidates are excluded if their tracks cannot be matched to at least one muon station, their transverse impact parameter is larger than 0.2 cm or their distance d_z in z exceeds 0.5 cm with respect to the primary vertex.

Lepton identification and selection efficiencies

The efficiencies to identify an isolated electron or muon candidate are determined from data. The method exploits the clean signature of $\mathrm{Z} \to \ell^+\ell^-$ decays and takes into account a possible presence of background processes in the selected event sample. The measurement is performed using a *tag-and-probe* technique, where one *tag* lepton candidate is required to select the event recorded by single-lepton triggers. The tag lepton candidate passes stringent selection criteria. In addition to the requirements given above, the tag lepton candidate has to be associated to the corresponding trigger object and must have a $p_{\mathrm{T}} > 30\,\mathrm{GeV}$. Tag muon candidates are reconstructed with $|\eta| < 2.1$, tag electron candidates within $|\eta| < 0.8$. The latter requirement is loosened to $|\eta| < 2.4$ for data at $\sqrt{s} = 7\,\mathrm{TeV}$ to increase statistics.

A second (*probe*) lepton is used to determine the efficiency. Probe electron candidates are reconstructed by the PF algorithm without imposing further quality criteria[3]. Probe muon candidates are represented by a track. If an opposite charged tag and probe pair can

---

[2] An MVA identifies well reconstructed physics objects (or a signal process) based on a set of probability distributions. These are derived from the simulation of its input observables.

[3] The efficiencies to reconstruct electron candidates without imposing further quality criteria is well described by the simulation [147].

be associated to a $Z \to \ell^+\ell^-$ decay by its invariant mass value ($76\,\mathrm{GeV} < m_{ll} < 106\,\mathrm{GeV}$), the efficiency is extracted from the fraction of probes that passes the requirements imposed for physics analysis. The quality criteria are studied in 2 steps: first, the identification efficiency is determined and in a second step, the isolation requirement is applied.

The efficiencies are determined as a function of $|\eta|$ and p_T of the lepton candidates. Details on the efficiency determination for muon candidates at $\sqrt{s} = 7\,\mathrm{TeV}$ and electron candidates at $\sqrt{s} = 7$ and $8\,\mathrm{TeV}$ are compiled in Ref. [149]. More information on muon candidate selection efficiencies at $\sqrt{s} = 8\,\mathrm{TeV}$ can be found in Ref. [150]. The lepton selection efficiencies depend on the topology of the underlying physics process. In particular the isolation efficiency is affected by the amount of hadronic activity in the event, higher for $\mathrm{t\bar{t}}$ processes than for $Z \to \ell^+\ell^-$ decays. Therefore, the efficiencies measured in data, ϵ^data, are used to correct small deficits of the simulated efficiencies instead of applying them directly to the simulation. For this purpose, the corresponding efficiency in simulation ϵ^MC is determined from $Z \to \ell^+\ell^-$ events using the same procedure employed for data, such that common effects due to the event topology or the methodology cancel in the resulting scale factors $\mathrm{SF} = \epsilon^\mathrm{data}/\epsilon^\mathrm{MC}$, which are applied as weights per lepton candidate to the simulation.

Lepton energy calibration

The energies of the lepton candidates are calibrated as a function of η and p_T using the invariant-mass spectrum of Z-boson decays, following a procedure described in Ref. [151]. For electrons candidates, also decays of J/ψ and Υ-mesons are employed [147].

The description of the data after the calibration is studied in $Z \to \ell^+\ell^-$ candidate events with $\ell = \mathrm{e}, \mu$, respectively. These are selected by dedicated *dilepton triggers*, HLT algorithms designed to record events with two electron or muon candidates. The dilepton selection is applied, with the modification of requiring a same-flavour lepton candidate pair. The energy response is studied for the endcap and barrel region independently by requiring both leptons to be either within $|\eta| < 1.5$ or $2.4 > |\eta| > 1.5$. The invariant mass of the muon-candidate pair, $m_{\mu\mu}$, is very well described by the simulation at both $\sqrt{s}$ and does not require further corrections, as shown in Figure 4.4 for $\sqrt{s} = 7\,\mathrm{TeV}$. Small discrepancies between data and simulation are visible in the invariant mass of electron candidates, m_ee at both $\sqrt{s}$.

Therefore, an additional scale factor, $c_e(|\eta|)$, for the momenta of simulated electron candidates is derived by fitting the innermost Z-peak with a Gaussian, illustrated in Figure 4.4 for $\sqrt{s} = 7\,\mathrm{TeV}$. The relation between the simulated p^MC and the measured peak position p^data directly corresponds to $c_e = p^\mathrm{data}/p^\mathrm{MC}$. All results for c_e are listed in Table 4.1.

	$c_e - 1$	
$\sqrt{s}$	$\lvert\eta\rvert < 1.5$	$1.5 \leq \lvert\eta\rvert < 2.4$
7 TeV	$3.84 \cdot 10^{-3}$	$3.45 \cdot 10^{-3}$
8 TeV	$2.63 \cdot 10^{-3}$	$1.87 \cdot 10^{-3}$

Table 4.1: Additional energy correction factors $c_e - 1$ for electron candidates in the barrel ($|\eta| < 1.5$) and the endcap regions ($1.5 \leq |\eta| < 2.4$) for the simulation at $\sqrt{s} = 7$ and $8\,\mathrm{TeV}$.

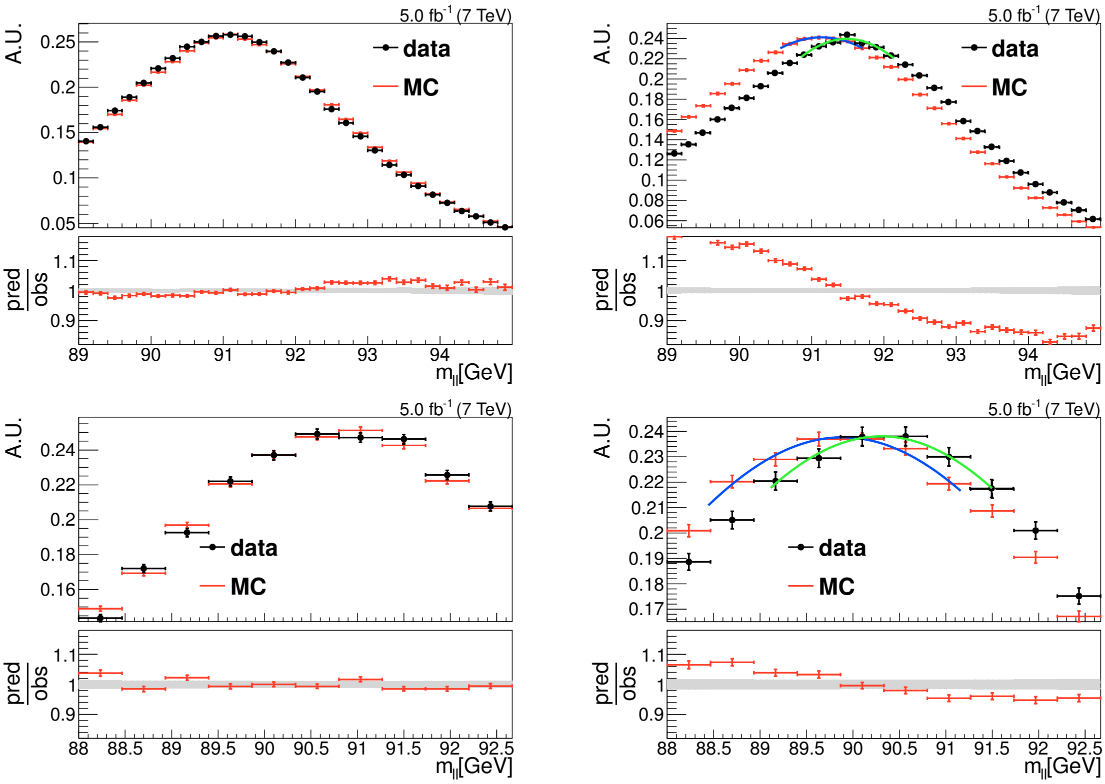

Figure 4.4: Invariant mass of muon (left) and electron (right) candidate pairs without additional lepton energy corrections at $\sqrt{s} = 7\,\text{TeV}$ normalized to 1. The upper row shows the barrel region ($|\eta| \leq 1.5$), the lower row the endcap region ($2.4 > |\eta| > 1.5$). The green (blue) line corresponds to a Gaussian fitted to the data (simulation). The statistical uncertainties are indicated by error bars. The lower panel depicts the ratio of predicted and observed yields. Here, the statistical uncertainty on the data is indicated by a gray shaded band.

After applying these additional electron-candidate energy corrections, the discrepancy between simulation and data is significantly reduced as shown in Figure 4.5. The absolute peak positions do not exactly correspond to the Z-boson mass. However, for all analyses presented in this work, the absolute reconstructed energies do not affect the final results as long as all effects are properly modeled by the simulation.

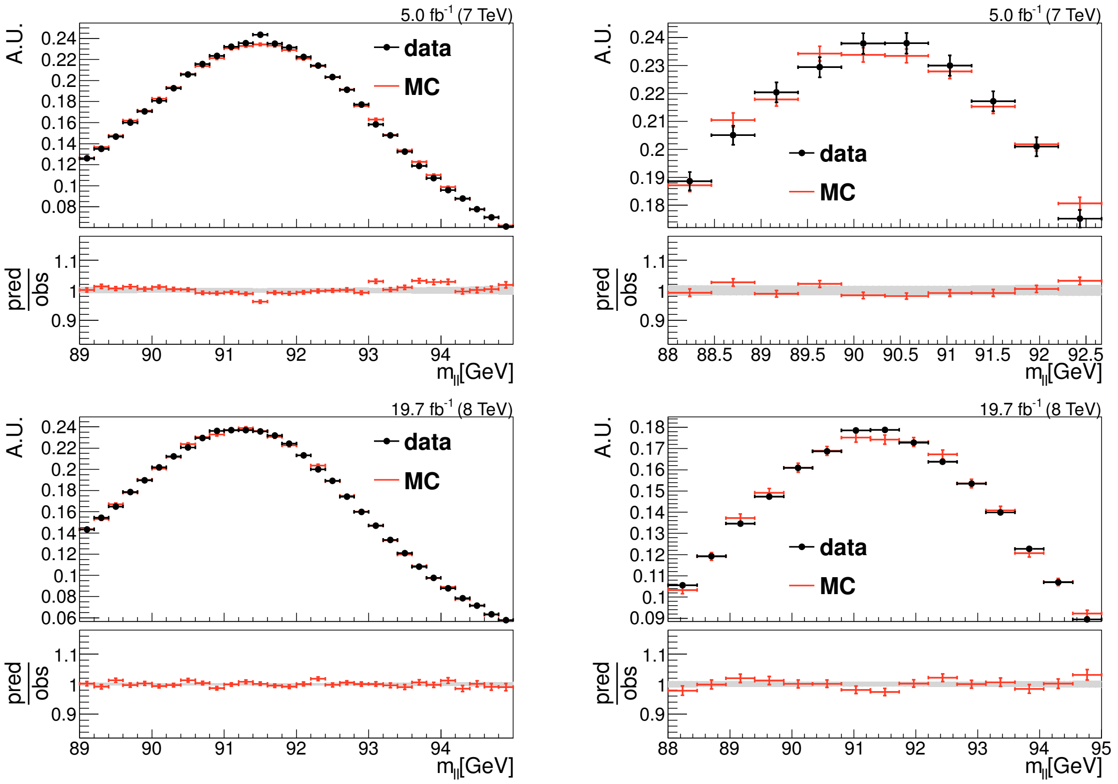

Figure 4.5: Invariant mass of electron candidate pairs with additional lepton energy corrections at $\sqrt{s} = 7\,\text{TeV}$ (top) and $\sqrt{s} = 8\,\text{TeV}$ (bottom) normalized to 1. The left column shows the barrel region ($|\eta| \leq 1.5$), the right column the endcap region ($2.4 > |\eta| > 1.5$). The statistical uncertainties are indicated by error bars. The lower panels depict the ratio of predicted and observed yields. Here, the statistical uncertainty on the data is indicated by a gray shaded band.

.

4.3.2 Jets

The hadronic jets are reconstructed using the *anti-kt* [152] algorithm, aiming at a determination of the original parton energy before hadronization. The result does not depend on soft radiation and is not influenced by collinear splitting.

The algorithm merges a particle i with transverse momentum $p_\mathrm{T}(i)$ to a particle or jet j with transverse momentum $p_\mathrm{T}(j)$ upon a following condition on the distance parameter:

$$d_{ij} = \min\left(p_\mathrm{T}(i)^{-2}, p_\mathrm{T}(j)^{-2}\right) \frac{\Delta\mathrm{R}(i,j)}{R} < p_\mathrm{T}(i)^{-2} \,. \tag{4.4}$$

The input for the jet clustering are the candidates reconstructed by the PF algorithms. The *jet cone* R is chosen as $R = 0.5$. All resulting jets are required to have $p_\mathrm{T} > 30\,\mathrm{GeV}$ and $|\eta| < 2.4$. The jet has to be composed of neutral, charged electromagnetic, and hadronic particle candidates. If the fraction of one of these categories exceeds 0.99, the jet is rejected, as well as if it overlaps with a selected lepton candidate within $\Delta\mathrm{R} < 0.5$.

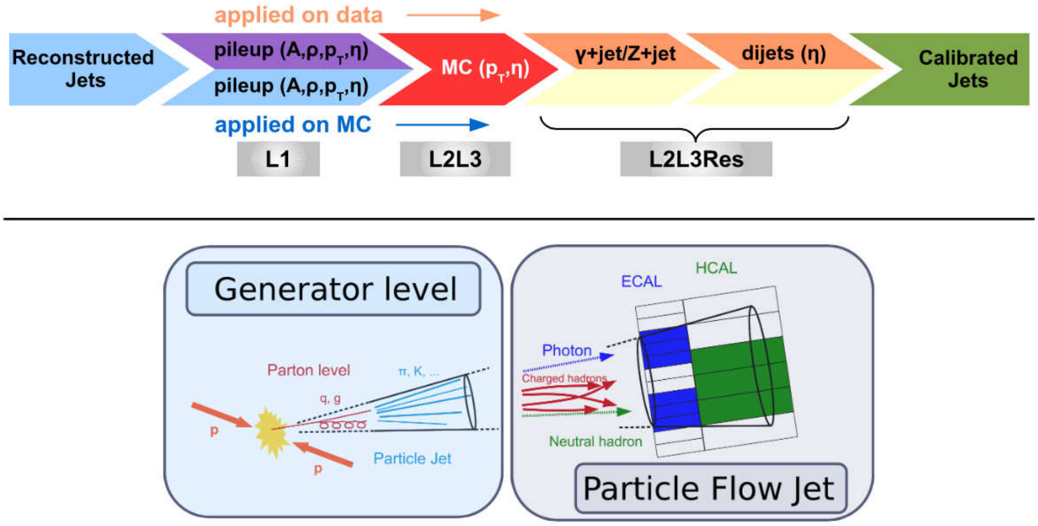

Figure 4.6: Top: sketch of the factorized approach to jet-energy corrections adopted by CMS, subsequently correcting for offset energy due to pileup (L1), response dependencies as a function of p_T ant η derived from simulations (L2L3), and residual corrections from data-driven methods (L2L3Res). Bottom: sketch of a true-particle ("generator level") jet used as reference for the energy corrections and a reconstructed PF jet [153].

.

The jet energy scale (*JES*) is calibrated to relate the energy measured for the reconstructed jet to the energy of a corresponding *true-particle jet* [154]. A true-particle jet is composed by clustering stable generated particles. The corrections are factorized as illustrated in Figure 4.6.

The electronic noise or pileup-induced responses in the detectors introduce offsets in the measured energy. These are subtracted in a first step (*L1*) based on the average energy density in the event ρ, the jet area A, and the jet p_T and η [154]. In the second step (*L2L3*), the energy of the reconstructed jet is calibrated to the true-particle jet as a function of p_T and η using simulation. These corrections are verified in data using dijet, photon+jet and Z+jets processes, and additional corrections (*L2L3Res*) are applied to compensate for any mismatch between MC and data [146].

Data-driven corrections for the jet energy resolution (*JER*) are derived based on momentum conservation in the transverse plane of dijet events [154, 155]. They are applied to the simulation by increasing or decreasing the energy difference between the reconstructed jet and its associated true-particle jet.

Indentification of b jets

Jets that arise from the hadronization of b quarks (*b jets*) are present in many physics processes, such as the decay of top quarks, of the Higgs boson, and of various new particles predicted by supersymmetric models [156]. The ability to accurately identify b jets is crucial in reducing the otherwise overwhelming contribution from different background processes. The algorithms to identify (*tag*) these jets exploit the long lifetime and large mass of b-flavored hadrons, expressed in a significant displacement of the secondary vertex in events containing b-quarks as illustrated in Figure 4.7.

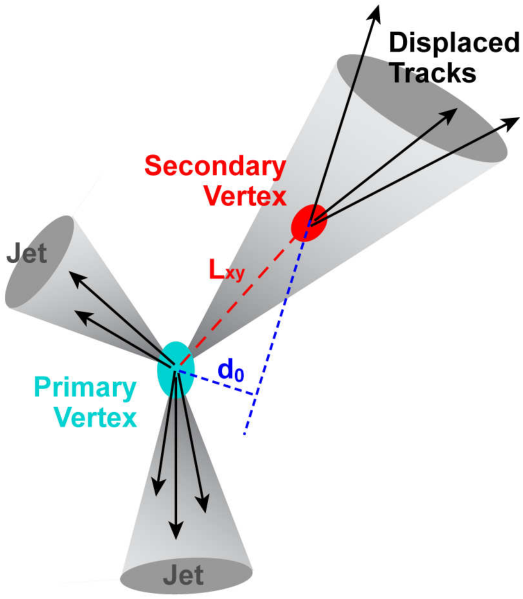

Figure 4.7: Illustration of a secondary vertex displaced with a distance of L_{xy} in x-y-plane with respect to the primary vertex. The transverse impact parameter of one track is indicated by d_0 [157].

Properties of these secondary vertices and track-based lifetime information are used to build a likelihood-based discriminator to distinguish between jets from b-quarks and those from charm or light quarks and gluons [158]. However, only a fraction of reconstructed jets that originate in a b quark are identified as b jets, described by the *b-tagging efficiency*. The fraction of reconstructed jets associated to a light true-particle jet and therefore wrongly identified as b jet is quantified by the *mistag probability*. Three *working points* are defined that require different minimal discriminator values: a *loose* working point with 10% mistag probability, a *medium* working point with 1% mistag probability, and a *tight* working point with 0.1% mistag probability, corresponding to about 80%, 65%, and 50% b-tagging efficiency, respectively.

In order to correct the b-tagging efficiency and mistag probability in the simulation, data-driven techniques are used. These employ QCD-multijet processes and are described in Ref. [158].

For the simulation, the b tagging efficiencies, ϵ^{MC}, are derived using generator information. Per-jet scale factors for the simulation are calculated as a function of the jet p_{T} and η by comparing to the corresponding efficiency measured in data. The scale factors are applied to the simulation using a statistical *random tagging* technique [159], that corrects the number of selected b jets. For a scale factor $SF < 1$, a fraction of $(1 - SF)$ of previously b-tagged jets are considered light jets. If the $SF > 1$, a fraction of $(1 - SF)/(1 - 1/\epsilon^{\mathrm{MC}})$ non b-tagged jets are considered b jets. The same procedure is employed for light jets and the corresponding mistag probabilities.

4.4 Trigger selection and efficiencies

For the analyses presented in this thesis, several dilepton HLT paths that require an electron and a muon candidate are combined with a logical **OR** to increase the efficiency. All paths comprise lepton candidate identification algorithms that employ information from the muon system, the tracker, and the calorimeters. A p_{T} threshold is imposed on the identified lepton candidates. For data at $\sqrt{s} = 7\,\mathrm{TeV}$, a trigger with symmetric p_{T} threshold of $10\,\mathrm{GeV}$ is combined with triggers with asymmetric p_{T} thresholds of $p_{\mathrm{T}} > 8\,\mathrm{GeV}$ for the electron candidate and $p_{\mathrm{T}} > 17\,\mathrm{GeV}$ for the muon candidate or vice versa. Triggers with the same asymmetric threshold are also used at $\sqrt{s} = 8\,\mathrm{TeV}$. A detailed list of the dilepton HLT paths employed in the analyses is given in Appendix B.

The efficiencies of these combinations of HLT paths are determined using a set of weakly correlated monitoring triggers to select the events without requiring information of the trigger under study. HLT algorithms that require missing transverse energy ($\not{E}_T$), a transverse p_{T} imbalance in the event due to undetected particles e.g. neutrinos, are well suited for this purpose. The efficiency of the dilepton triggers depends on the requirements imposed on the lepton candidates. Therefore, all events that enter the trigger analysis are required to pass the dilepton selection as described Section 4.3.1. In consequence, the selected event sample is enriched with dileptonic $\mathrm{t\bar{t}}$ events that are recorded based on $\not{E}_T$.

Four categories of events are defined: the total number of events that pass the dilepton selection, N_{ll}, the number of events that additionally pass the dilepton trigger, n_{dil}, the monitoring trigger requirements, n_{MET}, and both trigger requirements, $n_{\mathrm{MET+dil}}$. In the ideal case, the $\not{E}_T$ and dilepton triggers are uncorrelated and the dilepton trigger efficiency is given as

$$\epsilon_{\mathrm{dil}} = \frac{n_{\mathrm{MET+dil}}}{n_{\mathrm{MET}}}\,. \tag{4.5}$$

The correlations are studied using simulation. Here, events can be selected without imposing a-priori trigger requirements and N_{ll} can be determined. Therefore, the following simulated efficiencies are determined: the true dilepton trigger efficiency $\epsilon_{\mathrm{dil}}^{\mathrm{MC,true}} = n_{\mathrm{dil}}/N_{ll}$, the true $\not{E}_T$ trigger efficiency, $\epsilon_{\mathrm{MET}}^{\mathrm{MC,true}} = n_{\mathrm{MET}}/N_{ll}$, and the efficiency of selecting events that fulfill both requirements at the same time, $\epsilon_{\mathrm{MET+dil}}^{\mathrm{MC,true}} = n_{\mathrm{MET+dil}}/N_{ll}$. A correlation indicator α is defined as:

$$\alpha = \frac{\epsilon_{\mathrm{dil}}^{\mathrm{MC,true}} \cdot \epsilon_{\mathrm{MET}}^{\mathrm{MC,true}}}{\epsilon_{\mathrm{MET+dil}}^{\mathrm{MC,true}}}\,. \tag{4.6}$$

For fully uncorrelated triggers, the efficiencies factorize such that α becomes 1. A variety of $\not{E}_T$ triggers with different $\not{E}_T$ thresholds that range from 45 GeV to 400 GeV is studied. Paths which require additionally the presence of a central jet or a photon candidate are also considered to increase the number of selected events. A combination of 13 (50) $\not{E}_T$ triggers is chosen for $\sqrt{s} = 7$ (8) TeV, resulting in $N_{ll} = 1659$ (9416) selected dilepton events. A detailed list of HLT paths is given in Appendix B. For each chosen trigger path, α is consistent with 1, as well as for the combination of all of them with $\alpha = 1.000$ at $\sqrt{s} = 7\,\text{TeV}$ and $\alpha = 0.999$ at $\sqrt{s} = 8\,\text{TeV}$.

In addition, $\not{E}_T$ triggers with large *prescale* factors $p > 4$ are excluded to avoid large statistical fluctuations. A prescale factor p limits the bandwidth of an HLT path by recording only a fixed fraction $1/p$ of the events that meet the trigger condition. For each selected event, the trigger with the lowest p is chosen and its prescale factor is used as an additional weight for the event.

Prescales and the availability of the $\not{E}_T$ triggers are run-dependent. Thus, the prescale factors are evaluated on an event-by-event basis and the trigger efficiencies are determined separately for different run ranges (listed in Section 3.2.6). The results are combined, weighted by their luminosity fraction.

The trigger efficiencies are derived for data and $\mathrm{t\bar{t}}$ signal simulation following Equation 4.5, and scale factors $SF = \epsilon_{\text{dil}}/\epsilon_{\text{dil}}^{\text{MC}}$ are calculated as a function of lepton-candidate kinematics. A systematic uncertainty of 1% is assigned to the scale factors based on comparisons to complementary approaches to determine the trigger efficiencies [160]. As shown in Figure 4.8, the scale factors are constant with respect to the lepton candidate p_{T}. However, the scale factors show a slight dependence on the lepton candidate η, in particular at $\sqrt{s} = 8\,\text{TeV}$. To account for this dependence, the scale factors are derived double-differentially as a function of $|\eta|$ of the electron and the muon candidates.

The method described here was extended to measure the *dielectron* and *dimuon* HLT paths that require two electron candidates or two muon candidates with varying p_{T} thresholds and identification criteria. The results are documented in Ref. [149] and dedicated studies were performed for validation of the official dimuon trigger corrections provided by the CMS Collaboration [160]. The method was also employed for publications other than the ones presented in this work. For each analysis, the set of required dilepton and $\not{E}_T$ triggers and the lepton-candidate reconstruction and selection was adapted accordingly. The publications include top-quark analyses, such as the first measurement of the inclusive $\mathrm{t\bar{t}}$ production cross section at $\sqrt{s} = 8\,\text{TeV}$ [15] and $\sqrt{s} = 13\,\text{TeV}$ [161] with the CMS experiment, measurements of differential $\mathrm{t\bar{t}}$ production cross sections at $\sqrt{s} = 8\,\text{TeV}$ [162, 163] and their first measurement at $\sqrt{s} = 13\,\text{TeV}$ [164], as well as the first observation of associated tW production [165]. In addition, the scale factors were derived for searches for the associated production of the Higgs boson with a top-quark pair [166].

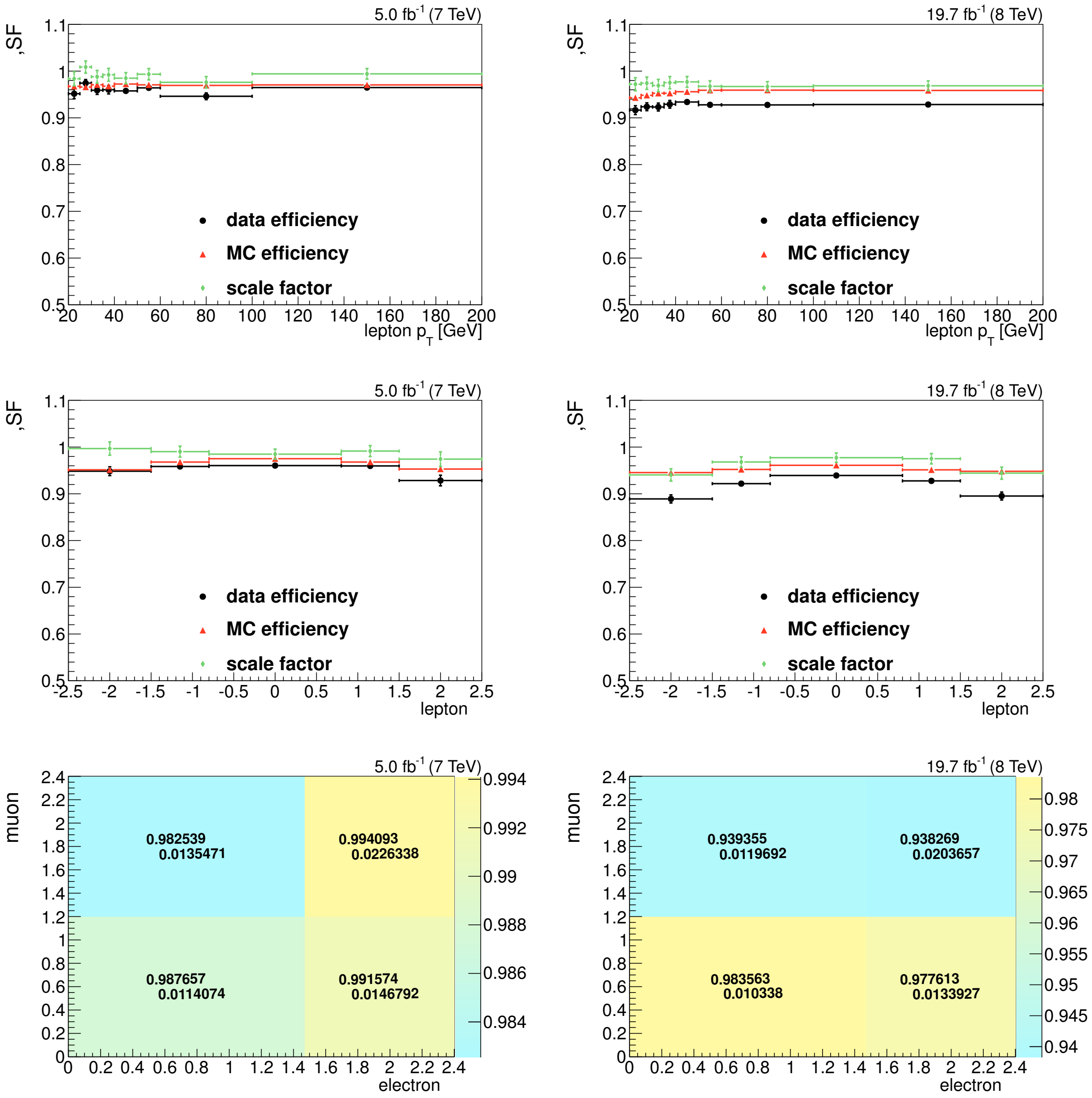

Figure 4.8: Trigger efficiency in data and $\mathrm{t\bar{t}}$ signal simulation and resulting scale factors as a function of the lepton candidate p_{T} (top) and lepton candidate η (middle) for $\sqrt{s} = 7\,\mathrm{TeV}$ (left) and $\sqrt{s} = 8\,\mathrm{TeV}$ (right). The bottom row shows the trigger scale factor as a function of η of the muon and electron candidate. The uncertainties on the scale factors correspond to the statistical and systematic uncertainty added in quadrature.

4.5 Overview of selection requirements

The selection criteria applied to the events considered for analysis and the requirements on the lepton candidates and jets are summarized in Table 4.2.

General event selection	
triggers	$e(p_{\mathrm{T}} \geq 8\,\mathrm{GeV}) + \mu(p_{\mathrm{T}} \geq 17\,\mathrm{GeV})$ **OR** $e(p_{\mathrm{T}} \geq 17\,\mathrm{GeV}) + \mu(p_{\mathrm{T}} \geq 8\,\mathrm{GeV})$
$e^{\pm}\mu^{\mp}$ candidate pairs	$\geq$ 1
$m_{e\mu}$	$\geq$ 20 GeV
Electron candidate selection	
p_{T}	$\geq$ 20 GeV
$\lvert\eta\rvert$	$\leq$ 2.4
relative isolation ($\Delta\mathrm{R} = 0.3$)	$\leq$ 0.1
d_0	$\leq$ 0.02 cm
Rejection of converted photons	applied
MVA discriminator value	$\geq$ 0.9
Muon candidate selection	
p_{T}	$\geq$ 20 GeV
$\lvert\eta\rvert$	$\leq$ 2.4
relative isolation ($\Delta\mathrm{R} = 0.4$)	$\leq$ 0.12
d_0	$\leq$ 0.2 cm
d_z	$\leq$ 0.5 cm
normalized χ^2	$\leq$ 10
hits in muon chambers	$\geq$ 1
hits in tracker layers	$\geq$ 6
hits in pixel detector	$\geq$ 1
matched to muon stations	$\geq$ 1
Jet selection	
p_{T}	$\geq$ 30 GeV
$\lvert\eta\rvert$	$\leq$ 2.4

Table 4.2: Overview of event selection and physics object identification requirements. Details are discussed in Sections 4.3 and 4.4. The identification of b jets is also described there.

Chapter 5

Measurement of the Top-Quark Pair Production Cross Section

In this chapter, the measurement of the $\mathrm{t\bar{t}}$ production cross sections $\sigma_{\mathrm{t\bar{t}}}$ at $\sqrt{s} = 7\,\mathrm{TeV}$ and $\sqrt{s} = 8\,\mathrm{TeV}$ is presented. The cross section for $\mathrm{t\bar{t}}$ production, $\sigma_{\mathrm{t\bar{t}}}$, is determined from the number of reconstructed signal events, N^{sig}, the integrated luminosity, L, and the total efficiency for reconstructing and selecting a $\mathrm{t\bar{t}}$ event, ϵ^{tot}, as:

$$\sigma_{\mathrm{t\bar{t}}} = \frac{N^{\mathrm{sig}}}{L \cdot \epsilon^{\mathrm{tot}}}. \tag{5.1}$$

The measurement is performed in the *visible phase space*, defined as the kinematic region of the decay products from the $\mathrm{t\bar{t}}$ system that can be measured by the detector. The requirement of a visible phase space avoids the extrapolation of the cross sections to unmeasured kinematic ranges. In this analysis, the visible phase space definition follows the selection of lepton candidates as described in Section 4.3.1. The *visible cross section*, $\sigma_{\mathrm{t\bar{t},vis}}$, is defined for events containing an $\mathrm{e}^{\pm}\mu^{\mp}$ pair that originates from the decay of the W bosons. Both leptons are required to fulfill the kinematic criteria $p_{\mathrm{T}} > 20\,\mathrm{GeV}$ and $|\eta| < 2.4$. Intermediate leptonic τ decays are included.

The fraction of $\mathrm{t\bar{t}}$ events that satisfies this condition defines the *acceptance* $A_{\mathrm{e}\mu}$. It is determined from the $\mathrm{t\bar{t}}$ signal MC simulation and relates the visible cross section to the *inclusive* $\mathrm{t\bar{t}}$ production cross section, $\sigma_{\mathrm{t\bar{t}}}$, as

$$\sigma_{\mathrm{t\bar{t}}} = \frac{\sigma_{\mathrm{t\bar{t},vis}}}{A_{\mathrm{e}\mu}}. \tag{5.2}$$

The acceptance, $A_{\mathrm{e}\mu}$, also includes the leptonic branching ratio of W-boson decays corresponding to 10.86% [167]. The acceptance and the reconstruction efficiency of the lepton candidate pair, $\epsilon_{\mathrm{e}\mu}$, determine the total efficiency:

$$\epsilon^{\mathrm{tot}} = A_{\mathrm{e}\mu} \cdot \epsilon_{\mathrm{e}\mu}. \tag{5.3}$$

The extraction of the visible cross section is described in Section 5.1, details on uncertainties are discussed in Sections 5.2 and 5.3. The resulting visible cross sections are presented in Section 5.4, and their extrapolation to the full phase space is described in Section 5.5. The ratio of the production cross sections at $\sqrt{s} = 7$ and $8\,\mathrm{TeV}$ is determined in Section 5.6. Validation procedures of the method are discussed in Section 5.7.

5.1 Extraction technique

The visible $\mathrm{t\bar{t}}$ production cross sections are extracted using a *binned likelihood fit* to *multi-differential* final state distributions, defined in this section. The fit is based on events that fulfill the dilepton selection described in Chapter 4. The kinematics of the selected lepton candidates are shown in Figures 5.1 and 5.2. Within the uncertainties (discussed in Section 5.2), the simulation provides a good description of the data. In most of the previous measurements of the $t\bar{t}$ production cross sections at the LHC [12, 15, 16, 168] the contribution from background processes is reduced by imposing requirements on the number of reconstructed jets or b jets. However, these requirements typically result in a significant uncertainties due to the jet modeling. Here, the likelihood fit is performed on final-state distributions that provide constraints for the contribution from background processes and jet-modeling parameters simultaneously.

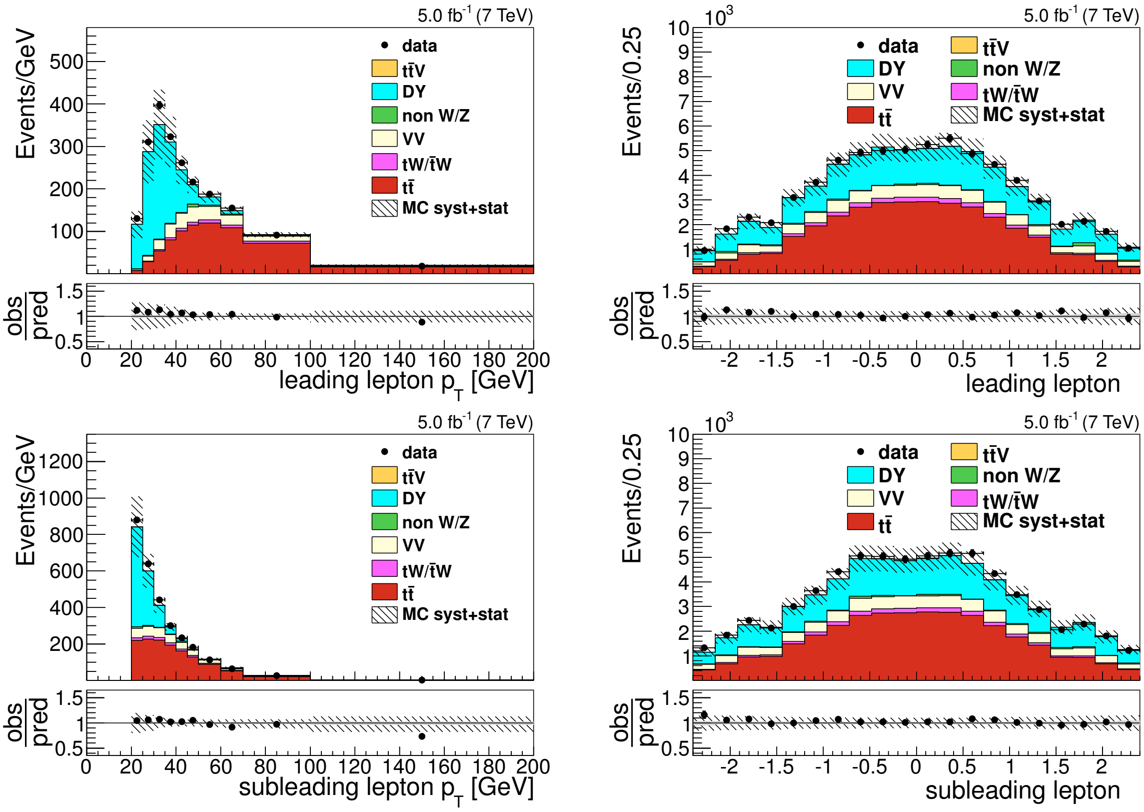

Figure 5.1: Distributions of p_T (left) and η (right) of the leading (top) and subleading (bottom) lepton, after the dilepton selection for the data at $\sqrt{s} = 7\,\mathrm{TeV}$. The hatched bands correspond to statistical and systematic uncertainties (discussed in Section 5.2) added in quadrature. The lower panels depict the ratio of observed and predicted yields. Here, the very small contribution to the uncertainty from MC statistics is indicated by gray shaded bands.

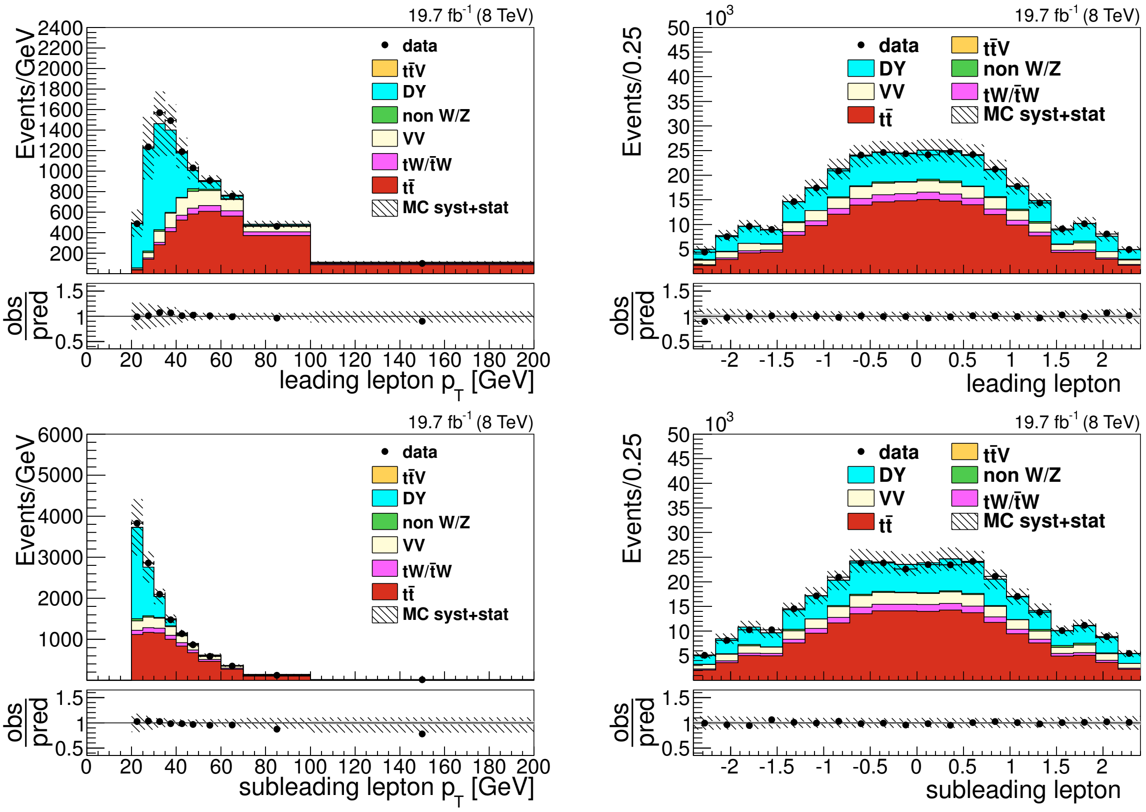

Figure 5.2: Distributions of p_T (left) and η (right) of the leading (top) and subleading (bottom) lepton, after the dilepton selection for the data at $\sqrt{s} = 8\,\mathrm{TeV}$. The hatched bands correspond to statistical and systematic uncertainties (discussed in Section 5.2) added in quadrature. The lower panels depict the ratio of observed and predicted yields. Here, the very small contribution to the uncertainty from MC statistics is indicated by gray shaded bands.

5.1.1 Template fit

In order to disentangle the contributions from signal and background processes, *templates* are constructed using simulation. Signal- and background-process templates have a different shape with respect to a chosen observable, for which *bins* are defined, corresponding to an interval in the observable and each containing a certain number of simulated (expected) and observed events. An example of a binned signal template derived from simulation is shown in Figure 5.3.

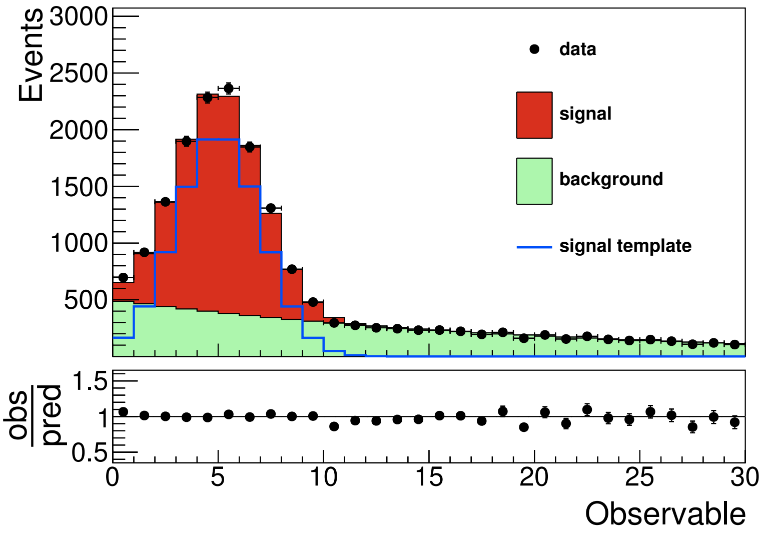

Figure 5.3: Illustration of a distribution of signal and background processes with respect to an observable. The blue line shows the signal template extracted from simulation.

The number of expected events not only depends on the normalization of signal and background processes but also on all systematic uncertainties from detector and process modeling, here generalized as nuisance parameters $\vec{\lambda}$. For each quantity expressed in terms of $\vec{\lambda}$ (e.g. the expected event yield in a bin), the dependence of a parameter λ_m is modeled by a second order polynomial that is constructed from evaluating the quantity at three values $\lambda_m = 0, 1, -1$, representing the ± 1 sigma variations of the corresponding uncertainty. For sources of uncertainties where only one variation is performed, e.g. when comparing two ME calculations, a linear function is chosen and λ_m ranges from 0 to 1.

A likelihood function that describes the compatibility of expected and observed events is defined based on Poisson statistics as:

$$L_H = \prod_i \exp(-\mu_i)\frac{\mu_i^{n_i}}{n_i!} \cdot \Xi(\vec{\lambda}), \tag{5.4}$$

with n_i being the number of observed events in bin i, μ_i the number of expected events, and Ξ a term to introduce additional constraints on the nuisance parameters discussed in detail in Section 5.2. The expectation value, μ_i, is composed of the expected number of signal events, $s_i(\sigma_{\mathrm{t\bar{t}},\mathrm{vis}}, \vec{\lambda})$, and the contributions $b_{l,i}(\vec{\lambda})$ from each background process l as

$$\mu_i = s_i(\sigma_{\mathrm{t\bar{t}},\mathrm{vis}}, \vec{\lambda}) + \sum_l b_{l,i}(\vec{\lambda})\,. \tag{5.5}$$

The dependence of μ_i on all nuisance parameters offers the additional possibility to constrain these parameters from data, given sufficient statistics. These constraints increase with the sensitivity of a distribution on particular nuisance parameters. A suitable distribution for the template fit is the b-jet multiplicity, shown in Figure 5.4. For the cross-section analysis, the tight b-tagging working point is employed. The contribution from the signal process increases with the b-jet multiplicity. Therefore, the distribution has significantly different template shapes for signal and background contributions. In addition the b-jet multiplicity contribution from signal and background processes is affected by the jet modeling. Thus, the distribution provides constraints on jet-related uncertainties.

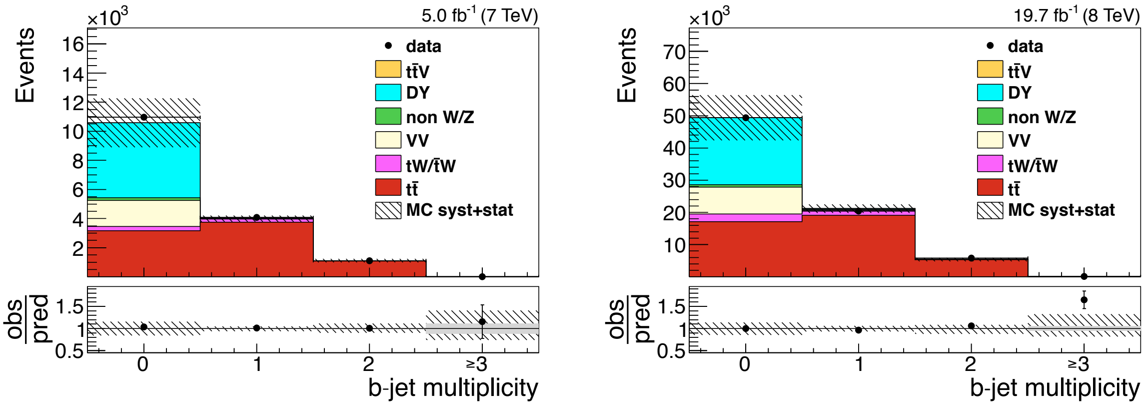

Figure 5.4: Distribution of the b-jet multiplicity after the dilepton selection at $\sqrt{s} = 7\,\text{TeV}$ (left) and $\sqrt{s} = 8\,\text{TeV}$ (right). The hatched bands correspond to statistical and systematic uncertainties (discussed in Section 5.2) added in quadrature. The lower panels depict the ratio of observed and predicted yields. Here, the statistical uncertainty on the simulated yields is indicated by a gray shaded band.

5.1.2 Signal yield parameterization

The b-jet multiplicity distribution provides further advantages owing to the $\mathrm{t\bar{t}}$ event topology. The probability of reconstructing one b jet from the $\mathrm{t\bar{t}}$ decay is almost independent of the probability of reconstructing the other b jet. Under this assumption binomial statistics apply and the probability ξ_i of selecting i b jets can be expressed as [12]:

$$\xi_1 = 2\epsilon_b(1 - C_b\epsilon_b) \text{ and} \tag{5.6}$$

$$\xi_2 = C_b\epsilon_b^2. \tag{5.7}$$

Here, ϵ_b is the total selection efficiency for a b jet. It comprises the probabilities that a jet is reconstructed within the kinematic acceptance region and is identified as a b jet. The factor C_b accounts for small correlations between the reconstruction of both b jets. It is given as $C_b = 4s_{\mathrm{e}\mu}s_2/(s_1 + 2s_2)^2$, with s_i being the number of signal events in b-jet multiplicity bin i and $s_{\mathrm{e}\mu}$ the number of signal events after the dilepton selection. A third relation is introduced to describe the probability of reconstructing 0 or > 2 b jets:

$$\xi_0 = 1 - \xi_1 - \xi_2. \tag{5.8}$$

The number of signal events in each category can then be expressed in terms of luminosity, L, the visible $\mathrm{t\bar{t}}$ production cross section, $\sigma_{\mathrm{t\bar{t}},\mathrm{vis}}$, the probabilities ξ_i, and the efficiency of the dilepton selection, $\epsilon_{\mathrm{e}\mu}$:

$$s_i = L\ \sigma_{\mathrm{t\bar{t}},\mathrm{vis}} \cdot \epsilon_{\mathrm{e}\mu} \cdot \xi_i. \tag{5.9}$$

The quantities $\epsilon_{\mathrm{e}\mu}$, C_b, and ϵ_b are determined from the signal simulation and expressed in terms of $\vec{\lambda}$, such that Equation 5.9 becomes:

$$s_i = L\ \sigma_{\mathrm{t\bar{t}},\mathrm{vis}} \cdot \epsilon_{\mathrm{e}\mu}(\vec{\lambda}) \cdot \xi_i(\vec{\lambda}). \tag{5.10}$$

In consequence, the terms ξ_i introduce non-linear dependencies on the nuisance parameters, in particular for those related to jet modeling. Therefore, possible mismodeling due to linear approximations is avoided.

The sensitivity of the fit can be further improved by defining subcategories. Each b-jet multiplicity bin i is split into categories of j additional non b-tagged jets (*additional jets*). For the cases with 1,2, or ≥ 3 additional jets, the fit is performed in bins of the p_T of the least energetic additional jet. For the categories without additional jets, the total event yield within this category is used in the likelihood function. The resulting multi-differential distributions (*fit distributions*) are shown in Figures 5.5 and 5.6. For each displayed contribution, a template is created. With increasing b-jet and additional-jet multiplicity, the contribution from background processes decreases. In particular the contributions from DY and VV events is dominant for $i = 0$ and $j = 0$, single-top (tW) processes populate mainly the 1 b-jet category. The contributions from QCD, W+jets, and $\mathrm{t\bar{t}bg}$ processes are discussed in the following.

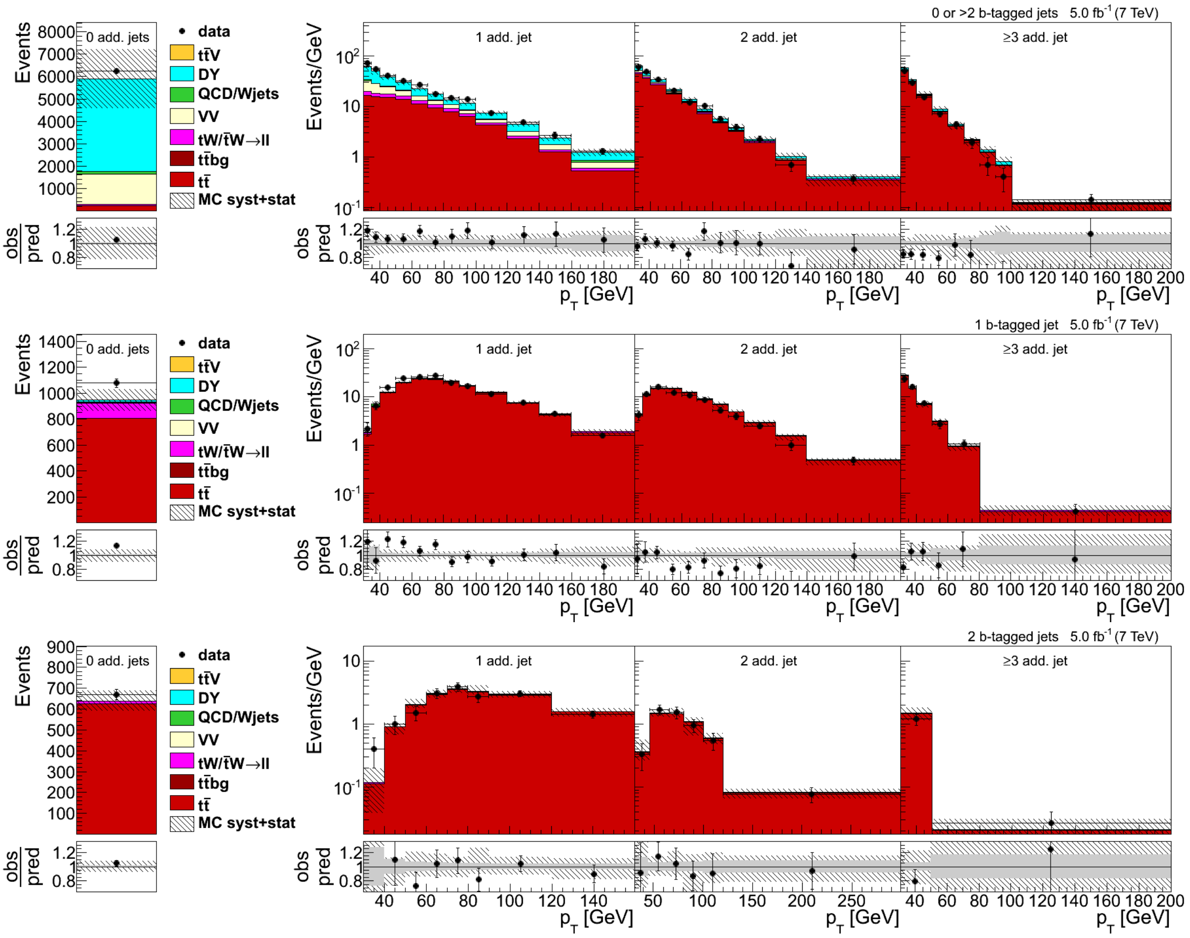

Figure 5.5: Left: total event yield for zero non-b-tagged jets (additional jets). Right: p_{T} of the least energetic additional jet in the event for events with one, two, and at least three additional jets. Shown are events with zero or more than two (top row), one (middle row), and two (bottom row) b-tagged jets at $\sqrt{s} = 7\,\mathrm{TeV}$. The hatched bands correspond to statistical and systematic uncertainties added in quadrature. The lower panels depict the ratio of observed and predicted yields. Here, the statistical uncertainty on the simulated yields is indicated by a gray shaded band.

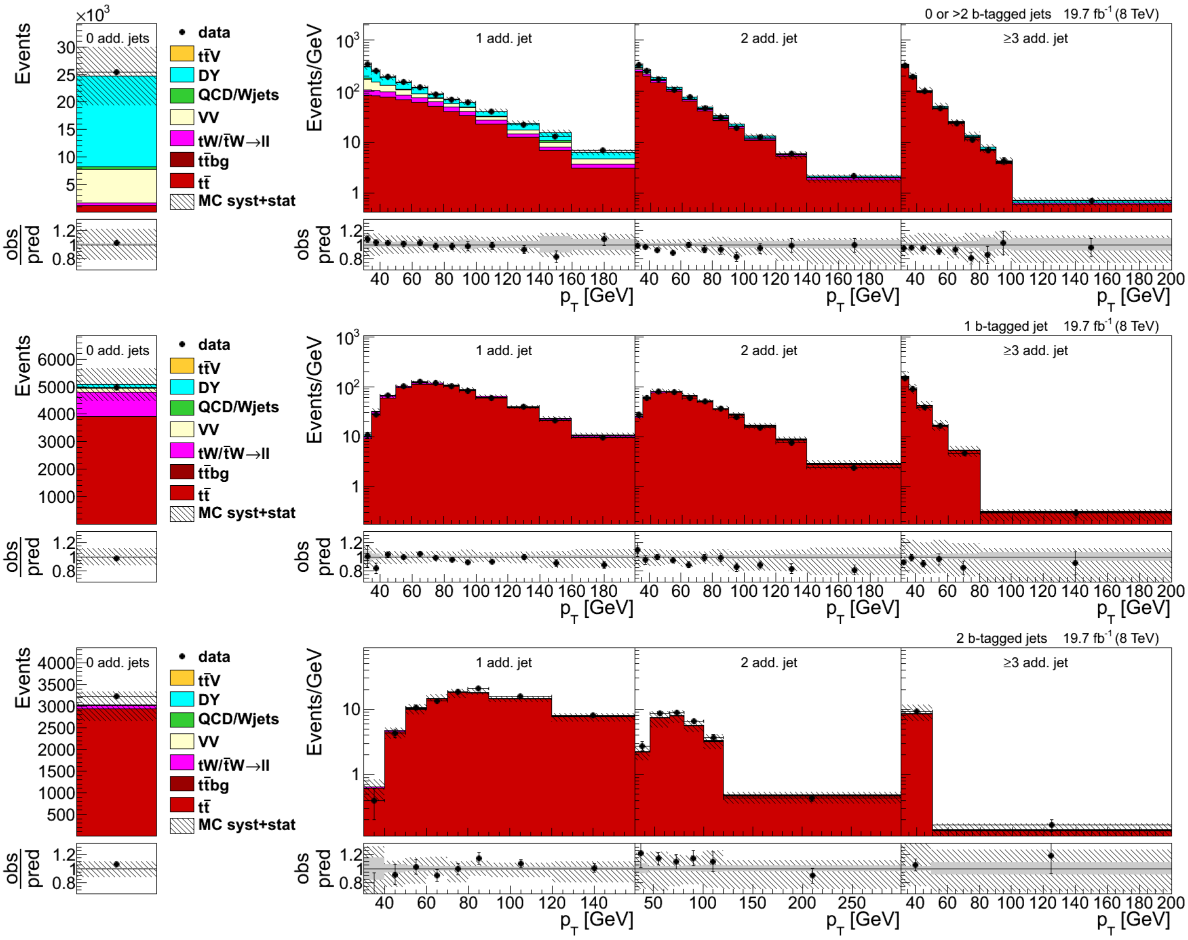

Figure 5.6: Left: total event yield for zero non-b-tagged jets (additional jets). Right: p_{T} of the least energetic additional jet in the event for events with one, two, and at least three additional jets. Shown are events with zero or more than two (top row), one (middle row), and two (bottom row) b-tagged jets at $\sqrt{s} = 8\,\mathrm{TeV}$. The hatched bands correspond to statistical and systematic uncertainties added in quadrature. The lower panels depict the ratio of observed and predicted yields. Here, the statistical uncertainty on the simulated yields is indicated by a gray shaded band.

5.1.3 Contributions from misidentified lepton candidates

The requirements imposed on the lepton candidates result in a high-purity data sample. The contributions from background processes where at least one lepton candidate is misidentified are estimated from simulation to be about 1%. This comprises contributions from QCD-multijet and W+jets processes, and also from $\mathrm{t\bar{t}bg}$ where at least one W boson (or subsequent τ) decays hadronically. The contribution from $\mathrm{t\bar{t}bg}$ processes amounts to 0.13% (0.17%) of all selected events at $\sqrt{s} = 7$ (8) TeV. Its template differs significantly from the $\mathrm{t\bar{t}}$ signal template as shown in Figure 5.7 for $\sqrt{s} = 8$ TeV, since higher additional jet and lower b jet multiplicities are populated. Therefore, both contributions can be distinguished well.

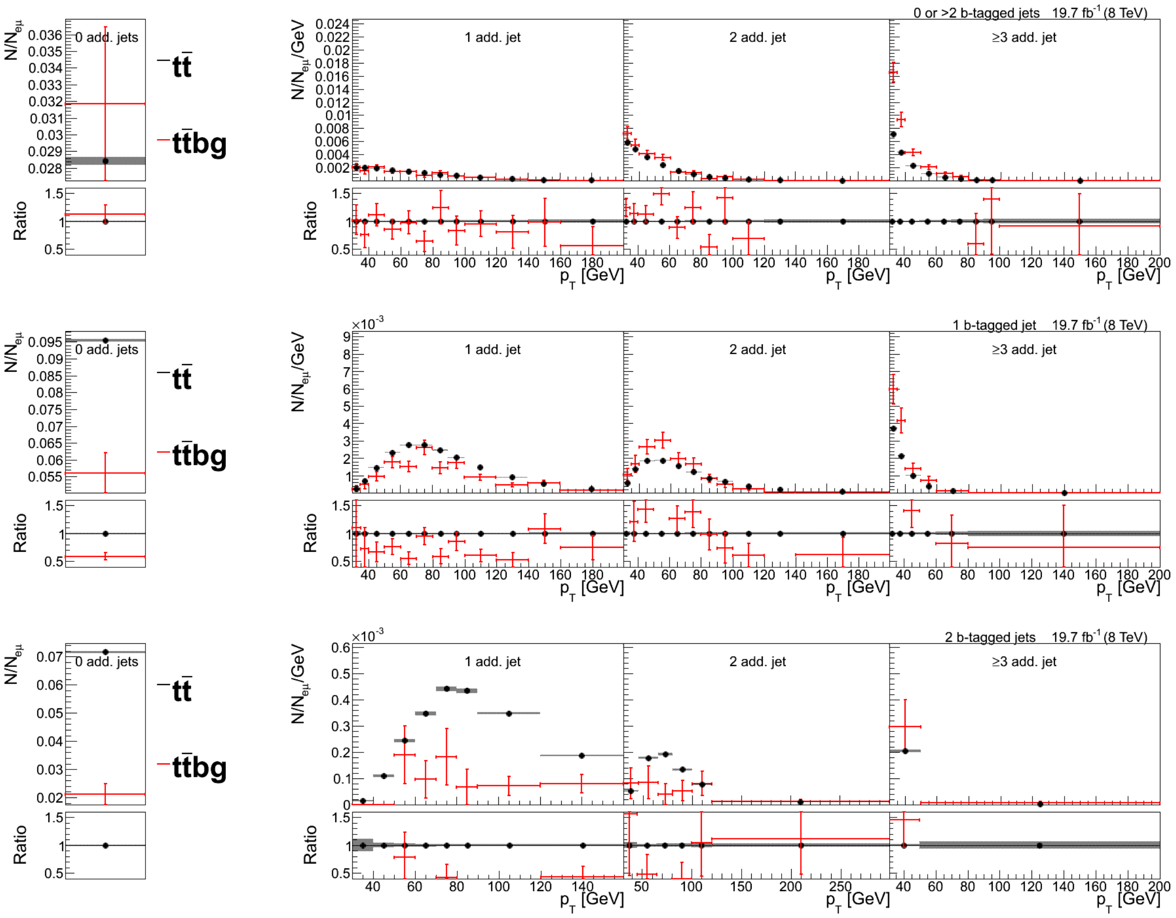

Figure 5.7: Comparison of the template shapes for the contribution from the $\mathrm{t\bar{t}}$ signal and $\mathrm{t\bar{t}}$ processes with non-dileptonic decay ($\mathrm{t\bar{t}bg}$). Left: total event yield for zero non-b-tagged jets (additional jets). Right: p_{T} of the least energetic additional jet in the event for events with one, two, and at least three additional jets. Shown are events with zero or more than two (top row), one (middle row), and two (bottom row) b-tagged jets at $\sqrt{s} = 8$ TeV. Each simulated contribution is normalized to the total number of selected dilepton events $N_{e\mu}$. The error bars and shaded bands indicate the statistical uncertainties on the simulated events yields. The lower panels depict the ratio of the $\mathrm{t\bar{t}bg}$ contribution and the $\mathrm{t\bar{t}}$ signal contribution.

As shown in Figure 5.5 and 5.6, a single template is employed for contributions from

QCD and W+jets processes, assuming that their template shapes agree. This assumption is proved as follows: both contributions are enhanced by inverting the isolation requirement on the lepton candidates, since the available number of events in the MC simulation of QCD processes does not allow to visualize the template shapes. The effect of statistical fluctuations in the simulation is studied in Section 5.7. With the adapted selection, the shapes of both contributions can be compared as shown in Figure 5.8. The category with 2 b jets does not contribute and is not displayed. Within the statistical uncertainties, both shapes agree well. The agreement is assumed to be independent of the isolation criterion. To avoid large statistical fluctuations, the contribution from QCD processes is assumed to be entirely modeled by the template for W+jets processes. Its normalization is scaled by a factor of 1.5 corresponding to the expected signal yields for both processes after the dilepton selection.

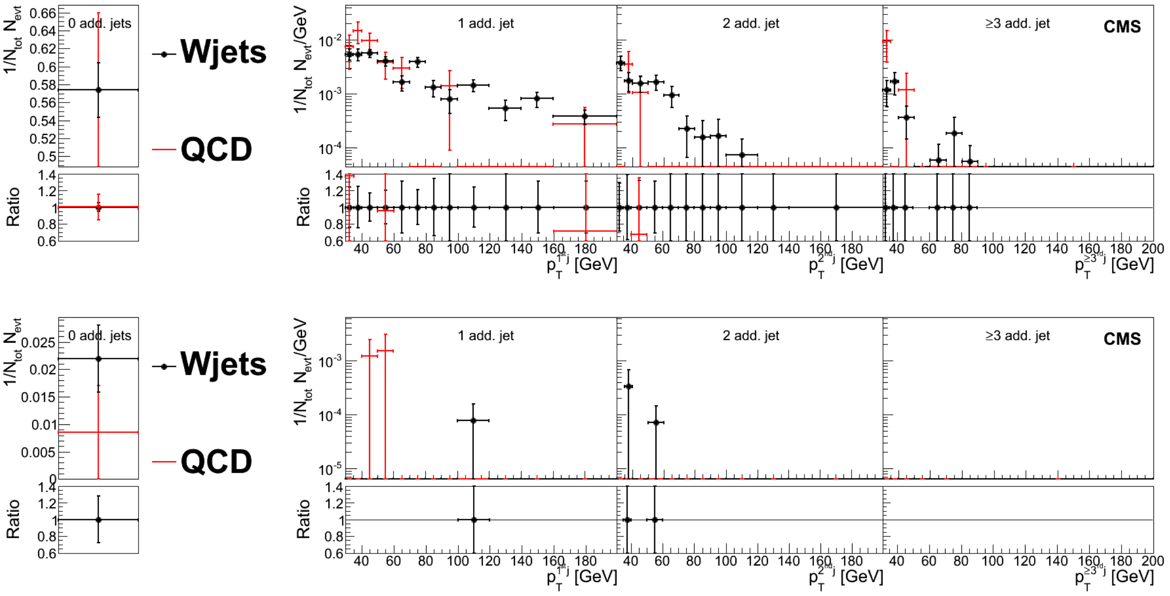

Figure 5.8: Comparison of the contributions from QCD and W+jets processes – each normalized to the total number of selected dilepton events. Left: total event yield for zero non-b-tagged jets (additional jets). Right: p_T of the least energetic additional jet in the event for events with one, two, and at least three additional jets. Shown are events with zero or more than two (top row), and one (bottom row) b-tagged jet at $\sqrt{s} = 8$ TeV. The error bars indicate statistical uncertainties on the simulated events yields. The lower panels depict the ratio of the QCD contribution and the W+jets contribution.

5.2 Systematic uncertainties and prior correlations

The measurement of the $t\bar{t}$ production cross section is affected by systematic uncertainties arising from detector effects and from theoretical assumptions. Each source is evaluated individually by the corresponding variations in the simulation or by varying the correction factors applied to the simulation within their estimated uncertainties. These variations are represented as nuisance parameters and fitted together with the cross sections.

Depending on the prior knowledge of the nuisance parameter, different *priors* $P_m(\lambda_m)$ are assigned to the uncertainties and are expressed as terms in $\Xi(\vec{\lambda})$, the nuisance term in the likelihood given in Equation 5.4:

$$\Xi(\vec{\lambda}) = \prod_m P_m(\lambda_m). \tag{5.11}$$

For each P_m, a Gaussian $G(\lambda_m)$ prior, *box* prior $B(\lambda_m)$ or a *floating* prior $F(\lambda_m)$ is chosen and defined as:

$$\begin{aligned} G(\lambda_m) &= \exp\left(\frac{-\lambda_m^2}{2}\right) && (5.12)\\ B(\lambda_m) &= 1 \text{ if } |\lambda_m| < 1, \;\text{ otherwise } 0 && (5.13)\\ F(\lambda_m) &= 1 \;\forall\; \lambda_m. && (5.14) \end{aligned}$$

The Gaussian prior describes the assumption of an optimal central value and gradually decreases the probability for increasing difference of λ_m to the central choice $\lambda_m = 0$. The box prior restricts the parameter to its ±1 sigma variation without imposing further constraints on an optimal central value, while the floating prior corresponds to no prior knowledge on λ_m.

Particular systematic uncertainties can be either highly correlated between $\sqrt{s} = 7\,\text{TeV}$ and $\sqrt{s} = 8\,\text{TeV}$ or completely decoupled, see next section for details. The degree of correlation between two uncertainties is expressed by the correlation coefficient ρ. A fully correlated uncertainty ($\rho = 1$) is introduced as a single nuisance parameter in the fit, a fully uncorrelated uncertainty ($\rho = 0$) as two independent nuisance parameters. For a partially correlated uncertainty ($0 < \rho < 1$), its variation is split into a fully correlated fraction ρ and an uncorrelated fraction $\sqrt{1-\rho^2}$. These correlations are discussed in the following for experimental uncertainties from detector effects and uncertainties due to the modeling of physics processes. In general, lower correlation coefficients result in a larger uncertainty on the extracted cross sections.

5.2.1 Experimental Uncertainties

All uncertainties arising from detector effects are introduced as nuisance parameters with Gaussian priors, since the data-driven corrections provide a distinct central value. If not mentioned otherwise, all variations are performed in the same discrete kinematic regions the corrections are derived in.

The uncertainties on the dilepton trigger (**trigger**) and lepton identification efficiencies (**lepton ID/iso**) are estimated by varying the data-to-simulation SFs within their uncertainties, which are typically of the order of 1-2%. The momentum calibration of electron (**electron energy scale**) or muon (**muon energy scale**) candidates is varied globally by 0.15% and 0.3%, respectively (see Section 4.3.1). Variations of the lepton identification, isolation and their energy calibration are strongly correlated between $\sqrt{s} = 7$ and $8\,\text{TeV}$ since the same methods are used to derive them and the remaining uncorrelated components are due to the statistical uncertainties from independent data and MC samples. The same applies to uncertainties due to trigger scale factors. In this case, the statistical uncertainty on the scale factors has a larger contribution and a lower correlation coefficient is chosen. In general, different choices of correlations of trigger and lepton uncertainties have no significant impact on the cross-section results.

The **jet energy resolution** is varied depending on the jets $|\eta|$: ±2.5%, ±4%, and ±5%, for $|\eta| < 1.7$, $1.7 < |\eta| < 2.3$, and $|\eta| > 2.3$, respectively [154, 155]. The same JER corrections are employed for simulation at $\sqrt{s} = 7\,\text{TeV}$ and $\sqrt{s} = 8\,\text{TeV}$. To account for possible small differences between the data-taking periods, the correlation factor is chosen as 0.9.

For the determination of the p_{T} and η-dependent JES correction factors, 27 individual sources of uncertainties are considered. One group of sources, the JES uncertainties due to pileup modeling (**JES-pileup**) are not derived in a consistent way at $\sqrt{s} = 7$ and $8\,\text{TeV}$ and therefore assumed to be uncorrelated. Uncertainties related to the simulation based extrapolation procedures (**JES-extr**), described in Ref. [154], are fully correlated. The remaining uncertainty sources are uncorrelated and grouped as **JES-uncorr**.

The b-tagging scale factors depend on the jet p_{T} and are varied simultaneously for all p_{T}. Twenty individual components are considered, describing the uncertainties due to the process modeling, e.g. from ISR/FSR or B-hadron fragmentation, uncertainties due to detector effects (JES, JER, PU), uncertainties on the methods to extract the SF, and their statistical uncertainty. The process modeling and the methods to derive the scale factors are fully consistent between $\sqrt{s} = 7$ and $8\,\text{TeV}$ and thus the corresponding uncertainties are correlated. The components connected to JER, and PU are varied together with the corresponding uncertainty, and are not listed individually. The component related to the JES (**b-tag (JES)**) can not be associated with a particular JES uncertainty source and is therefore varied independently. Since most of these sources are uncorrelated, a correlation factor of 0.2 is assigned. The statistical uncertainty on the b-tagging scale factors (**b-tag (stat)**) is fully uncorrelated. Variations of the **mistag** scale factors are performed within their uncertainties. These are mostly correlated except for statistical effects and differences in the tracking between the running periods with $\sqrt{s} = 7$ and $8\,\text{TeV}$. A correlation coefficient of 0.8 is assigned.

The uncertainties on the **luminosity** determination at $\sqrt{s} = 7\,\text{TeV}$ and $\sqrt{s} = 8\,\text{TeV}$ are 2.2% and 2.6%, respectively [134, 135]. A variation within these uncertainties does not only change the value assumed for s_i in Equation 5.10, but also affects the normalization of the contribution from background processes. The uncertainties on the integrated luminosity are assumed to be uncorrelated, following Ref. [169]. A different assumption changes neither the central cross-section values nor their individual uncertainties.

The event weights that are applied to the simulation to correct the vertex multiplicity are derived using the total inelastic proton-proton cross section. The uncertainty due to **pileup** is determined by varying these cross sections within their uncertainty, ±8% at $\sqrt{s} = 7\,\text{TeV}$ and ±5% at $\sqrt{s} = 8\,\text{TeV}$, respectively, and by re-evaluating the event weights [134, 135, 141].

All uncertainties on the detector modeling are also propagated to the simulated contributions from **background** processes. In addition, a variation of 30% on the normalization is applied to each contribution. In particular for the dominant contributions from single top quark and DY events, this variation covers well the uncertainty arising from the predicted cross section with 11% [91] and 5% [123], respectively. To account for possible deficits in the simulation of the heavy flavor content in DY events, the corresponding normalization parameter is varied independently for each b-jet category. With the exception of small variations in the PS tune, the simulation of background processes is performed consistently at $\sqrt{s} = 7\,\text{TeV}$ and $\sqrt{s} = 8\,\text{TeV}$. Therefore, a correlation coefficient of 0.9 is assigned, also accounting for small differences due to statistical fluctuations.

5.2.2 Modeling uncertainties

The modeling of the $\mathrm{t\bar{t}}$ signal events is an important ingredient for the measurement. If not mentioned otherwise, a box prior is chosen for each nuisance parameter corresponding to a variation of a modeling parameter, since the majority of these parameters have no preferred central value.

The Q^2 and ME-PS matching scales are varied by a factor of 2 up and down. The choice of the ME generator (**ME generator**) is studied by comparing the nominal $\mathrm{t\bar{t}}$ signal simulation, MadGraph+pythia, to powheg interfaced with pythia.

The uncertainty due to the **b-fragmentation tune** is evaluated by varying the Bowler-Lund b-fragmentation function in the Z2* tune to agree with the measurements of the x_B parameter by ALEPH [170] and DELPHI [171]. The fraction of B-hadrons decaying to ν (**B-hadron ν decay fraction**) significantly affects the energy of the reconstructed b jet. Hence, this fraction is varied within the uncertainties from combined measurements [167]. The **JES: flavor** uncertainty comprises the variations in jet-energy response with respect to different hadronization models: the Lund fragmentation model (pythia) and the cluster fragmentation (herwig ++). The individual components describing gluon, c-, b-, and light-quark responses are added linearly. Since the nominal JES corrections are derived for pythia with the Z2* tune, a Gaussian prior is chosen for the nuisance parameters corresponding to b-fragmentation modeling and JES: flavor. The uncertainties due to the B-hadron ν-decay fraction, b-fragmentation modeling, and JES: flavor are summarized as **hadronization** uncertainty.

Differential cross section measurements suggest a softer top-quark p_T (p_T^t) spectrum than predicted by the MadGraph simulation [162]. To account for this effect the difference between the result obtained with the nominal simulation and using the MadGraph prediction weighted to describe the measured p_T^t spectrum is taken as a systematic uncertainty (**top p_T**). This variation has a significant influence on the jet p_T spectra as shown in Figure 5.9 for $\sqrt{s} = 8\,\mathrm{TeV}$, where the jet momenta decrease with softer p_T^t.

Variations of the **underlying event** tune are studied by comparing varied P11 tunes, the mpiHi and the Tevatron tune, to the standard P11 tune (as defined in Chapter 2). The effect of **color reconnection** is studied with a dedicated P11 tune (noCR) without color reconnection. Relative differences with respect to the standard P11 tune are propagated to the nominal $\mathrm{t\bar{t}}$ signal simulation.

The uncertainty from the choice of PDFs (**PDF**) is determined by reweighting the simulation according to the 52 CT10 [172] error PDF sets at 90% CL. Relative variations with respect to the default eigenvector are propagated to the signal simulation. For PDF variations, prior assumptions are modeled by a Gaussian.

All modeling uncertainties are energy independent and hence fully correlated for the simulations at $\sqrt{s} = 7$ and $8\,\mathrm{TeV}$. The correlation coefficients for experimental and modeling uncertainties are summarized in Table 5.1.

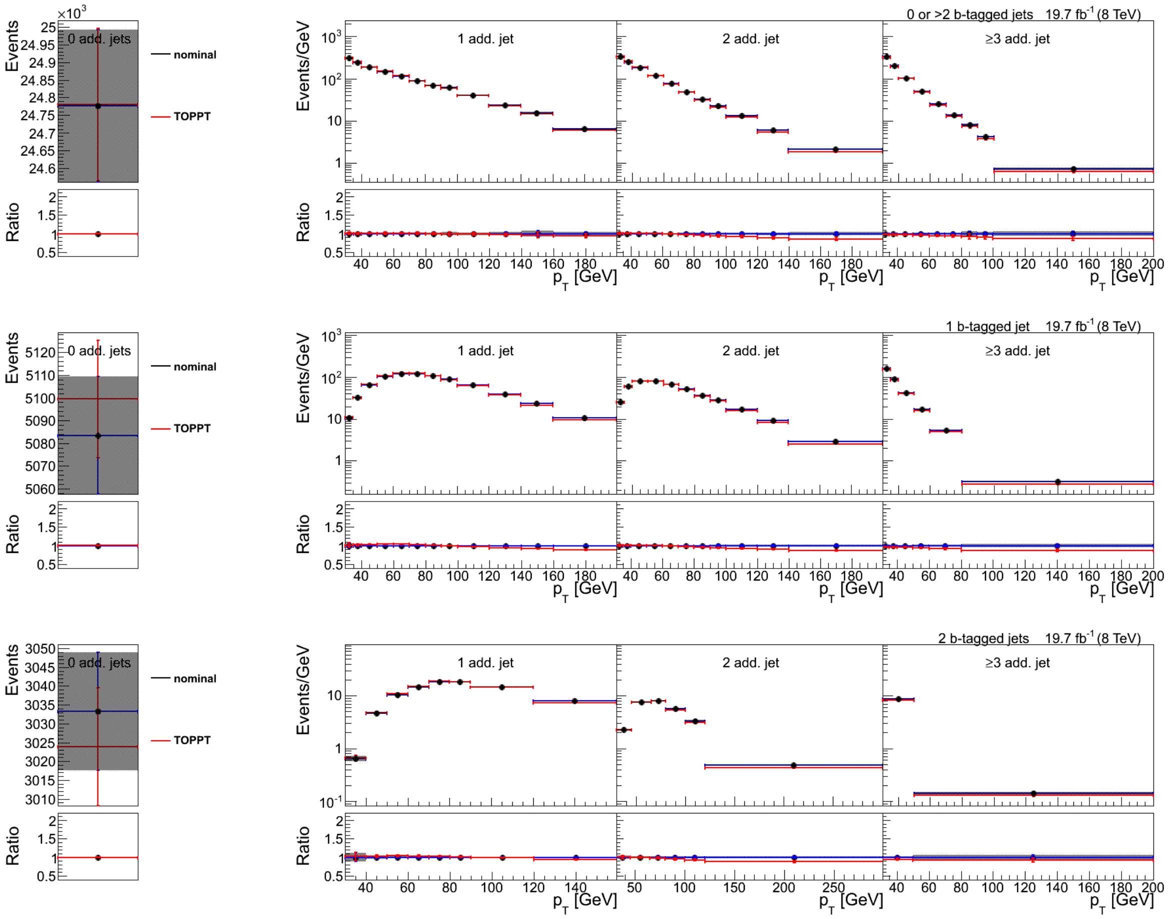

Figure 5.9: Predicted event yields for the nominal simulation and applying the top-quark p_{T} reweighting. Left: total event yield for zero non-b-tagged jets (additional jets). Right: p_{T} of the least energetic additional jet in the event for events with one, two, and at least three additional jets. Shown are events with zero or more than two (top row), one (middle row), and two (bottom row) b-tagged jets at $\sqrt{s} = 8\,\mathrm{TeV}$. The statistical uncertainties on the prediction are indicated by error bars and shaded bands. The lower panels depict the ratio of the reweighted and nominal prediction.

Uncertainty source	correlation(7 TeV, 8 TeV)
trigger	0.8
lepton ID/iso	0.9
muon energy scale	0.9
electron energy scale	0.9
jet energy resolution	0.9
JES-pileup	0
JES-extr	1
JES-uncorr	0
b-tag (stat)	0
b-tag (JES)	0.2
b-tag (other)	1
mistag	0.8
luminosity	0
pileup	0.5
each background	0.9
Q^2 scale	1
ME-PS matching	1
ME generator	1
B-hadron ν decay fraction	1
b-fragmentation tune	1
JES: Flavor	1
top p_{T}	1
color reconnection	1
underlying event	1
PDF	1

Table 5.1: Assumed correlations between systematic uncertainties at $\sqrt{s} = 7\,\mathrm{TeV}$ and $\sqrt{s} = 8\,\mathrm{TeV}$. The table is divided into three parts corresponding to the experimental uncertainties, the background contribution, and modeling uncertainties.

5.3 Fitted parameters and posterior correlations

In total 146 nuisance parameters are fitted simultaneously together with the visible cross sections at $\sqrt{s} = 7\,\text{TeV}$ ($\sigma_{\text{t}\bar{\text{t}},\text{vis}}$ ($7\,\text{TeV}$)) and $\sqrt{s} = 8\,\text{TeV}$ ($\sigma_{\text{t}\bar{\text{t}},\text{vis}}$ ($8\,\text{TeV}$)). The fit is performed with MINUIT [173] by minimization of the term

$$-2 \ln L_H \left(\sigma_{\text{t}\bar{\text{t}},\text{vis}}(7\,\text{TeV}), \sigma_{\text{t}\bar{\text{t}},\text{vis}}(8\,\text{TeV}), \vec{\lambda} \right) \tag{5.15}$$

with L_H being the likelihood defined in Equation 5.4.

For each parameter λ_m the fit gives a *best-fit* value λ_m^0, preferred by the data. The difference with respect to the initial value of $\lambda_m = 0$ is defined as *pull*. Variations from λ_m^0 are constrained by the data to $\lambda_m^0 \pm c_m$. Within the constraints c_m, the pulls for all nuisance parameters are compatible with 1 sigma of the prior uncertainties.

As expected, constraints from the data are particularly strong for variations of the b-tagging and mistag scale factors as well as for the b-fragmentation tune, the ME-PS matching and Q^2 scales and top p_{T}. These variations are constrained between 10% to 40% with respect their pre-fit 1 sigma variation. A full list of pulls and constraints is given in Appendix C.

If a variation of two independent nuisance parameters λ_m and λ_n results in similar changes in the predicted yields both parameters will be correlated after the fit, quantified by the correlation coefficient $-1 \leq \rho_{mn} \leq 1$. The parameter with the strongest *post-fit* correlations to other parameters is corresponding to variations of top p_{T}. It is correlated with the parameters describing the b-fragmentation tune, PDF variations and the ME generator choice, since these all affect the jet energies significantly. Also contributions from background processes that provide a similar shape (DY and diboson events) lead to strong correlations between the respective normalization parameters. For a full table of correlation coefficients, see Appendix C.

The fitted distributions are shown in Figures 5.10 and 5.11. Compared to Figures 5.5 and 5.6, which show the same distributions before the fit, the description of the data by the simulation improves, while the total uncertainty on the prediction decreases significantly. This remaining total uncertainty on the expected event yield μ in each bin of the fitted distributions is calculated using error propagation from the correlation coefficients ρ_{mn}, the best fit values λ_m^0, and the constraints c_m:

$$\mu^{\pm} = \sum_m \sum_n \rho_{mn} \cdot \mu(\lambda_m^0 \pm c_m) \cdot \mu(\lambda_n^0 \pm c_n). \tag{5.16}$$

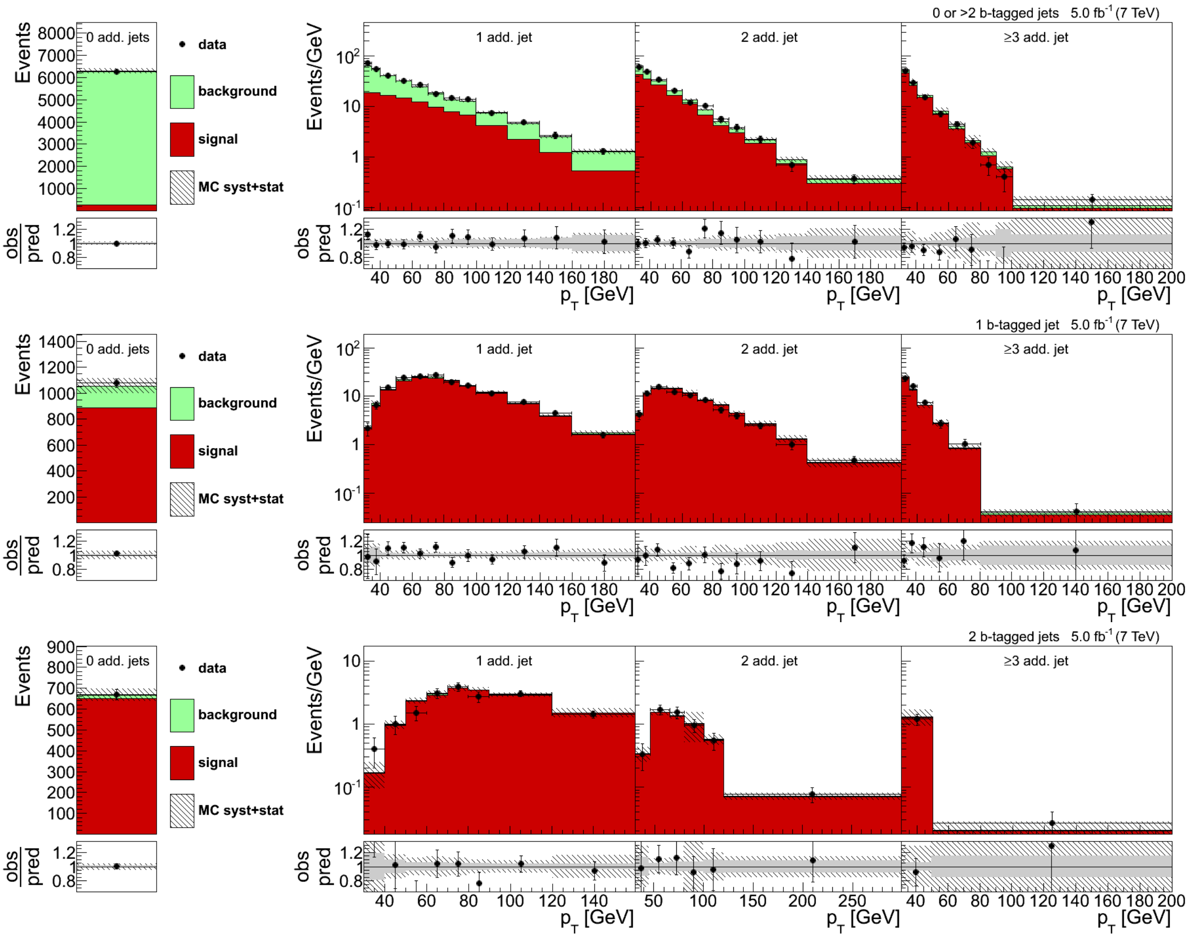

Figure 5.10: Fitted distributions. Left: total event yield for zero non-b-tagged jets (additional jets). Right: p_{T} of the least energetic additional jet in the event for events with one, two, and at least three additional jets. Shown are events with zero or more than two (top row), one (middle row), and two (bottom row) b-tagged jets at $\sqrt{s} = 7\,\mathrm{TeV}$. The hatched bands correspond to statistical and systematic uncertainties added in quadrature. The lower panels depict the ratio of observed and predicted yields. Here, the statistical uncertainty on the simulated yields is indicated by a gray shaded band.

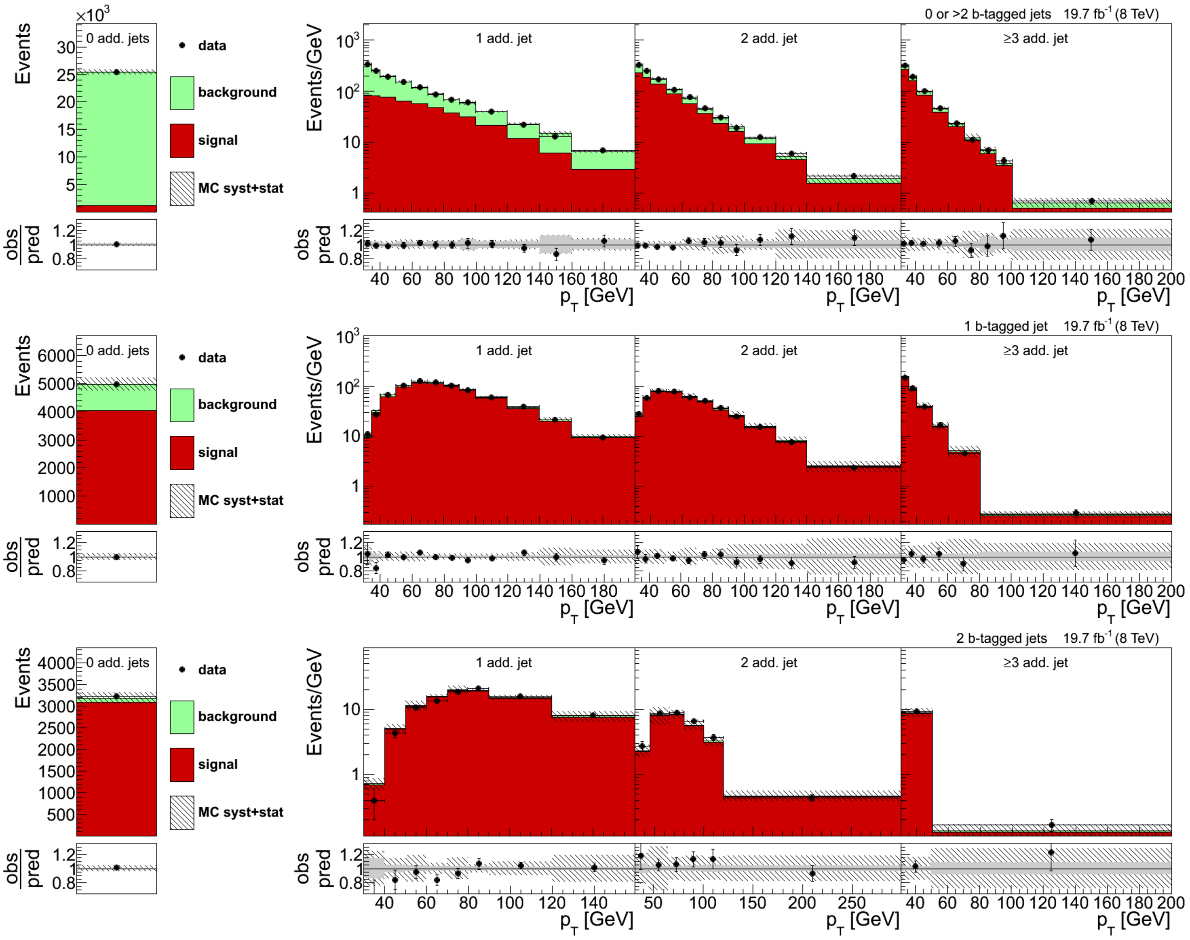

Figure 5.11: Fitted distributions. Left: total event yield for zero non-b-tagged jets (additional jets). Right: p_{T} of the least energetic additional jet in the event for events with one, two, and at least three additional jets. Shown are events with zero or more than two (top row), one (middle row), and two (bottom row) b-tagged jets at $\sqrt{s} = 8\,\mathrm{TeV}$. The hatched bands correspond to statistical and systematic uncertainties added in quadrature. The lower panels depict the ratio of observed and predicted yields. Here, the statistical uncertainty on the simulated yields is indicated by a gray shaded band.

5.4 Visible cross sections

The visible cross sections, $\sigma_{\mathrm{t\bar{t},vis}}$, are free parameters in the fit. The uncertainties Δ on $\sigma_{\mathrm{t\bar{t},vis}}$ are obtained using MINOS, the Profile Likelihood algorithm integrated in MINUIT by scanning the parameter space at the contour $-2\ln L_H = 1$. In this way, all correlations are taken into account in the total uncertainty.

The individual contributions to the total uncertainty are evaluated independently in a second step. For each parameter λ_m or a general set of parameters, $\vec{\lambda}_l$, $\vec{\lambda}_l$ are fixed to their best-fit values and the fit is repeated. In consequence, the total uncertainty, $\Delta(\neg\vec{\lambda}_l)$, does not depend on these parameters anymore. The difference in quadrature between Δ and $\Delta(\neg\vec{\lambda}_l)$ is interpreted as the contribution of the parameters $\vec{\lambda}_l$ to the total uncertainty.

The contributions of nuisance parameters that correspond to the same uncertainty source but for different $\sqrt{s}$ are evaluated simultaneously. In addition, the following uncertainty sources are combined: individual contributions to the JES uncertainty except for the JES: flavor component, individual components of the b-tagging uncertainties, and the normalization uncertainty for the contribution from DY processes in all b-jet categories. The resulting contributions to the total uncertainties are listed in Table 5.2. For a full breakdown of all nuisance parameters, see Appendix C.

The dominant uncertainties arise from trigger and lepton ID/isolation correction factors, while most modeling and b-tagging uncertainties are less significant and well constrained by the fit. The constraint on the JES uncertainties at $\sqrt{s} = 7\,\mathrm{TeV}$ is slightly smaller due to less statistics. The resulting visible $\mathrm{t\bar{t}}$ production cross sections are:

$$\sigma_{\mathrm{t\bar{t},vis}}(7\,\mathrm{TeV}) = 3.05 \pm^{0.11}_{0.10}\ \mathrm{pb\ and} \tag{5.17}$$

$$\sigma_{\mathrm{t\bar{t},vis}}(8\,\mathrm{TeV}) = 4.24 \pm^{0.16}_{0.14}\ \mathrm{pb.} \tag{5.18}$$

Source	Uncertainty [%]	
	7 TeV	8 TeV
trigger	1.3	1.2
lepton ID/isolation	1.5	1.5
lepton energy scale	0.1	0.1
jet energy scale	0.7	1.0
jet energy resolution	0.1	0.0
b-tag	0.5	0.6
mistag	0.2	0.1
pileup	0.2	0.3
single top background	0.9	0.6
DY background	1.3	1.2
$t\bar{t}$ background	0.1	0.1
$t\bar{t} + V$ background	0.0	0.1
diboson background	0.2	0.6
QCD/W+jets background	0.1	0.1
Q^2 scale	0.2	0.5
ME-PS matching	0.1	0.1
ME generator	0.3	0.3
hadronization	0.6	0.8
top p_T	0.2	0.3
color reconnection	0.1	0.2
underlying event	0.0	0.1
PDF	0.3	0.4
luminosity	2.2	2.6
statistics	1.2	0.6
total uncertainty on $\sigma_{\mathrm{t\bar{t}},\mathrm{vis}}$	$\pm^{3.5}_{3.4}$	$\pm^{3.7}_{3.4}$

Table 5.2: Summary of the individual groups of uncertainties to the systematic uncertainty on the visible $\mathrm{t\bar{t}}$ cross section measurements. From top to bottom: experimental, background, modeling, luminosity, and statistical uncertainties.

5.5 Extrapolation to the full phase space

The full-phase space cross sections for $\mathrm{t\bar{t}}$ production, $\sigma_{\mathrm{t\bar{t}}}$, are calculated according to Equation 5.2 using the lepton acceptance $A_{\mathrm{e}\mu}$. This factor is determined from MadGraph+pythia and depends on the theory model and the corresponding uncertainties as described in 5.2.2. Thus, $A_{\mathrm{e}\mu}$ is also parameterized as a function of all nuisance parameters. Their best-fit values are used to obtain the best estimate of $A_{\mathrm{e}\mu}$ which is employed to extract $\sigma_{\mathrm{t\bar{t}}}$.

While model uncertainties can be constrained by the data in the visible detector region, these constraints can not be applied to the unmeasured phase space. Therefore, additional uncertainties are assigned to $A_{e\mu}$. The sources relevant for MadGraph+pythia are the Q^2 and ME-PS matching scale variations, top p_T and PDF uncertainties. Each of the corresponding nuisance parameters λ_l is varied from the best fit value to ±1 and $\sigma_{t\bar{t}}$ is evaluated (see Equation 5.2). The resulting differences with respect to the nominal $\sigma_{t\bar{t}}$ are taken as additional extrapolation uncertainties. In general the extrapolation from the visible phase space to the full phase space does not introduce a significant increase in the total uncertainties, since only lepton kinematics enter $A_{e\mu}$. The dominant contribution comes from the top p_T modeling that directly propagates to the lepton p_T. The obtained uncertainties on $\sigma_{t\bar{t}}$ are listed in Table 5.3 and are added in quadrature to the uncertainties from the fit of $\sigma_{t\bar{t},\mathrm{vis}}$.

Source	Uncertainty [%]	
	7 TeV	8 TeV
total uncertainty on $\sigma_{t\bar{t},\mathrm{vis}}$	$\pm^{3.5}_{3.4}$	$\pm^{3.7}_{3.4}$
Q^2 scale (extrapol.)	$\mp^{0.0}_{0.4}$	$\pm^{0.2}_{0.1}$
ME-PS matching (extrapol.)	$\pm^{0.1}_{0.1}$	$\pm^{0.3}_{0.3}$
top p_T (extrapol.)	$\pm^{0.4}_{0.2}$	$\pm^{0.8}_{0.4}$
PDF (extrapol.)	$\mp^{0.2}_{0.1}$	$\pm^{0.2}_{0.1}$
total uncertainty on $\sigma_{t\bar{t}}$	$\pm^{3.6}_{3.4}$	$\pm^{3.8}_{3.5}$

Table 5.3: Breakdown of systematic uncertainties on the extrapolation to the full phase space $t\bar{t}$ production cross section.

The resulting inclusive cross $t\bar{t}$ sections at $\sqrt{s} = 7\,\mathrm{TeV}$ $\sigma_{t\bar{t}}(7\,\mathrm{TeV})$ and $\sqrt{s} = 8\,\mathrm{TeV}$ $\sigma_{t\bar{t}}(8\,\mathrm{TeV})$ are:

$$\sigma_{t\bar{t}}(7\,\mathrm{TeV}) = 174.4\ \pm^{6.3}_{5.9}\ \mathrm{pb\ and} \tag{5.19}$$

$$\sigma_{t\bar{t}}(8\,\mathrm{TeV}) = 245.7\ \pm^{9.3}_{8.6}\ \mathrm{pb.} \tag{5.20}$$

The measured values agree well with the predicted cross sections at NNLO+NNLL $\sigma^{\mathrm{pred}}_{t\bar{t}}(7\,\mathrm{TeV})$ and $\sigma^{\mathrm{pred}}_{t\bar{t}}(8\,\mathrm{TeV})$ for $m_t^{\mathrm{pole}} = 173.3\,\mathrm{GeV}$ [14]:

$$\sigma^{\mathrm{pred}}_{t\bar{t}}(7\,\mathrm{TeV}) = 172.0^{+4.4}_{-5.8}\,(\mathrm{scale}) \pm^{4.7}_{4.8}\ (\mathrm{PDF})\,\mathrm{pb\ and} \tag{5.21}$$

$$\sigma^{\mathrm{pred}}_{t\bar{t}}(8\,\mathrm{TeV}) = 245.8^{+6.2}_{-8.4}\,(\mathrm{scale}) \pm^{6.2}_{6.4}\ (\mathrm{PDF})\,\mathrm{pb.} \tag{5.22}$$

5.6 Cross-section ratio

The ratio $R_\sigma = \sigma_{t\bar{t}}(8\,\mathrm{TeV})/\sigma_{t\bar{t}}(7\,\mathrm{TeV})$ is determined from the measured inclusive $t\bar{t}$ production cross sections. The simultaneous fit returns the post-fit correlation coefficient $\rho_{7,8}$ between both fitted parameters. This coefficient gives direct access to the relative uncertainty on the ratio, Δ^F_R/R^2_σ, resulting from the fit in the visible phase space:

$$(\Delta^F_R)^2/R^2_\sigma = \left(\frac{\Delta^F_7}{\sigma_{t\bar{t}}(7\,\mathrm{TeV})}\right)^2 + \left(\frac{\Delta^F_8}{\sigma_{t\bar{t}}(8\,\mathrm{TeV})}\right)^2 - 2\cdot\rho_{7,8}\frac{\Delta^F_7\Delta^F_8}{\sigma_{t\bar{t}}(7\,\mathrm{TeV})\sigma_{t\bar{t}}(8\,\mathrm{TeV})}, \tag{5.23}$$

with Δ_7^F and Δ_8^F being the uncertainties on $\sigma_{\mathrm{t\bar{t},vis}}(7\,\mathrm{TeV})$ and $\sigma_{\mathrm{t\bar{t},vis}}(8\,\mathrm{TeV})$, respectively. Additional extrapolation uncertainties on the ratio are determined as described in Section 5.5 individually for each cross section, and then propagated to the ratio as fully correlated.

R_σ is determined to be

$$R_\sigma = 1.41 \pm^{0.06}_{0.06}\,, \tag{5.24}$$

in agreement with precise predictions computed with NNPDF2.1 at NNLO+NNLL [174]

$$R_\sigma^{\mathrm{pred}} = 1.430^{-0.001}_{-0.004}\,(\mathrm{scale}) \pm 0.004\,(\mathrm{PDF})^{-0.003}_{-0.003}\,(\alpha_\mathrm{S}). \tag{5.25}$$

5.7 Validation of the method

Possible biases of the simultaneous fit due to the underlying statistics model or the choice of selection requirements, such as the jet p_T threshold (30 GeV) or the b-tagging working point, are studied in the following.

5.7.1 Statistics model

The underlying assumptions on the statistics model are evaluated using *pseudo-experiments*, performed as follows.

For each pseudo experiment, new event yields for data (*pseudo-data*), the signal contribution, and the total background contribution are generated. Pseudo-data are generated taking the simulated event yields, μ_i, in each bin i as a reference, since they describe the data sufficiently. Using μ_i as a mean, a new Poisson-distributed random number is generated in each bin and employed instead of the measured data. New yields for the prediction are generated to mimic effects due to limited statistics of the simulation that affect the fit in two ways: fluctuations in the contributions from signal and background processes change the sum of predicted events in each bin; and fluctuations in the predicted signal yields change the values of the parameters that enter Equation 5.10 (ξ_i, $\epsilon_{e\mu}$). Therefore, new yields are generated for both, the contribution from signal and background processes, independently. For each, a bin-wise scaling factor f is determined that combines event weights and normalization. It can be obtained from the product of all event weights, $w_{i,j}$ per event j as $f = \sum_{j=1}^{N} w_{i,j}^2/\mu_i$, with N being the total number of simulated events. A new yield is generated based on Poisson statistics using μ_i/f as mean. The obtained value is scaled back with f and employed as simulated event yield. Based on the pseudo-data and the randomized contributions from signal and background processes, $\sigma_{\mathrm{t\bar{t},vis}}$ is extracted.

In total 20,000 of these pseudo-experiments are performed. For each of them, all nuisance parametes are fixed to 0, such that only statistical effects contribute to the total uncertainty. The difference between the prior cross section and the value obtained by the fit is divided by the corresponding statistical uncertainty. The resulting pull distributions can be seen in Figure 5.12 and show no bias for the extracted values, indicated by mean values compatible with 0. The widths of the pulls are close to 1. So even though the Poisson probability in Equation 5.4 neglects statistical fluctuations in the simulation, the fit underestimates the statistical uncertainty by only 6 and 8% for $\sqrt{s} = 7$ and 8 TeV, respectively. This effect is negligible compared to other uncertainties.

5.7.2 Requirements on jet p_T and b-tagging

The stability of the result is evaluated by repeating the measurement using different p_T thresholds (50 and 60 GeV) imposed on the jets and a different b-tag discriminator working point. The total uncertainty on the fitted cross section increases for higher jet p_T thresholds. Each result is normalized to the most precise one for the default threshold of 30 GeV. The relative increase of the total uncertainty represents a lower limit for the part of the uncertainty that is uncorrelated between the individual measurements. Therefore, it is used to quantify the compatibility of the extracted values as shown in Figure 5.13. No bias is observed. A possible bias due to the choice of the b-tag algorithm is estimated by categorizing the events using the medium instead of the tight b-tagging working point (see Section 4.3.2) and extracting $\sigma_{\mathrm{t\bar{t}}}$. The compatibility of the extracted values is estimated as aforementioned. In addition, the uncertainties due to the b-tagging are considered uncorrelated. Within the resulting total uncorrelated uncertainties, the extracted $\sigma_{\mathrm{t\bar{t}}}$ is stable at both $\sqrt{s}$.

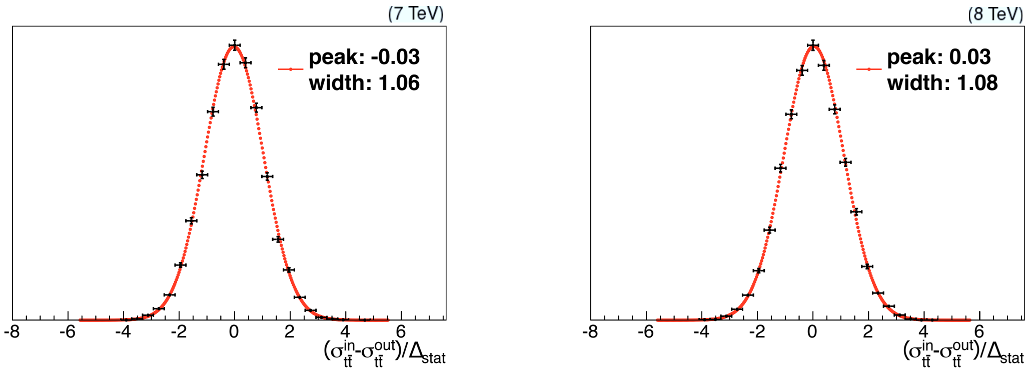

Figure 5.12: The left (right) panel shows the pull distribution for $\sigma_{\mathrm{t\bar{t},vis}}$ at $\sqrt{s} = 7$ (8) TeV as extracted from the fit. The difference between the $\sigma_{\mathrm{t\bar{t},vis}}$ hypothesis $\sigma^{\mathrm{in}}_{\mathrm{t\bar{t}}}$ and the extracted value $\sigma^{\mathrm{out}}_{\mathrm{t\bar{t}}}$ is divided by the statistical uncertainty on $\sigma^{\mathrm{out}}_{\mathrm{t\bar{t}}}$, Δ_{stat}.

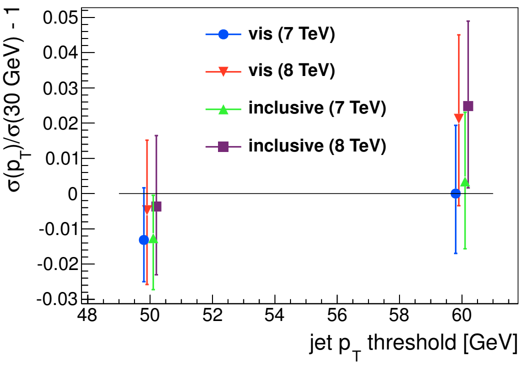

Figure 5.13: Dependence of the extracted $\sigma_{\mathrm{t\bar{t},vis}}$ ($\sigma_{\mathrm{t\bar{t}}}$) on the jet p_T threshold with respect to $\sigma_{\mathrm{t\bar{t},vis}}$ ($\sigma_{\mathrm{t\bar{t}}}$) obtained with a threshold of 30 GeV. The relative change of the total uncertainty is indicated by error bars.

5.8 Comparison to event-counting method

The $\mathrm{t\bar{t}}$ production cross sections are also measured using an event counting (C&C) method, which offers an estimation of the cross sections without assumptions on the underlying statistics model or the functional forms of systematic variations. Since this method is more sensitive to uncertainties from background contributions, a more stringent event selection is required. For this purpose, only events with at least 2 jets and at least one b jet are considered. The cross sections are determined from the number of selected events in data N^{data} and the expected contribution of events from background processes N^{BG} as:

$$\sigma_{\mathrm{t\bar{t},vis}} = \frac{N^{\mathrm{data}} - N^{\mathrm{BG}}}{L \cdot \epsilon_{\mathrm{add}}\epsilon_{\mathrm{e}\mu}} \tag{5.26}$$

with ϵ_{add} being the selection efficiency for the additional requirements, determined from the $\mathrm{t\bar{t}}$ signal simulation. Equation 5.26 is evaluated individually for all systematic uncertainties and differences with respect to the nominal result are added in quadrature to obtain the total uncertainty on $\sigma_{\mathrm{t\bar{t},vis}}$. The visible cross section is extrapolated to the full phase space using the same acceptance $A_{\mathrm{e}\mu}$ as for the fit result (see Section 5.5).

The $\mathrm{t\bar{t}}$ production cross sections obtained with this approach are:

$$\sigma^{\mathrm{C\&C}}_{\mathrm{t\bar{t},vis}}(7\,\mathrm{TeV}) = 3.04 \pm^{0.18}_{0.17}\ \mathrm{pb}, \tag{5.27}$$

$$\sigma^{\mathrm{C\&C}}_{\mathrm{t\bar{t},vis}}(8\,\mathrm{TeV}) = 4.28 \pm^{0.25}_{0.22}\ \mathrm{pb}, \tag{5.28}$$

$$\sigma^{\mathrm{C\&C}}_{\mathrm{t\bar{t}}}(7\,\mathrm{TeV}) = 173.8 \pm^{11}_{10}\ \mathrm{pb}, \tag{5.29}$$

$$\sigma^{\mathrm{C\&C}}_{\mathrm{t\bar{t}}}(8\,\mathrm{TeV}) = 248.0 \pm^{15}_{13}\ \mathrm{pb}. \tag{5.30}$$

The results obtained with the C&C method are significantly less precise but agree well with the fitted cross section values. The contributions of individual uncertainties to the total uncertainty on $\sigma_{\mathrm{t\bar{t}}}$ are listed in Table 5.4 and are compared to the precision achieved with the fit method. Dominant contributions from detector effects arise from variations of the luminosity, the JES, and the b-tagging scale factors. From the modeling uncertainties, mainly ME generator comparison, hadronization modeling, PDF and ME-PS matching scale variations contribute. In particular these uncertainties that affect the jet and b jet multiplicities are significantly reduced with the fit method.

The event counting analysis could be improved by optimizing the b-tagging working point in terms of both purity and reduction of systematic uncertainties. However, contributions from background processes would increase and the uncertainties from the jet modeling would remain dominant, such that the total uncertainty would not reach the precision of the fitted $\sigma_{\mathrm{t\bar{t}}}$.

The simultaneous fit of the $\sigma_{\mathrm{t\bar{t}}}$ and systematic uncertainties represents the most precise determination of $\sigma_{\mathrm{t\bar{t}}}$ performed by the CMS Collaboration, and yields a competitive precision compared to the measurement recently published by the ATLAS Collaboration [12].

Source	Uncertainty (fit)[%]		Uncertainty (C&C)[%]	
	7 TeV	8 TeV	7 TeV	8 TeV
trigger	1.3	1.2	1.3	1.3
lepton ID/isolation	1.5	1.5	1.5	1.6
lepton energy scale	0.1	0.1	0.2	0.2
jet energy scale	0.7	1.0	2.2	2.1
jet energy resolution	0.1	0.0	0.1	0.0
b-tag	0.5	0.6	2.7	2.4
mistag	0.2	0.1	0.6	0.8
pileup	0.2	0.3	0.2	0.4
single top background	0.9	0.6	0.8	1.3
DY background	1.3	1.2	0.0	0.2
$t\bar{t}$ background	0.1	0.1	0.1	0.1
$t\bar{t}+V$ background	0.0	0.1	0.0	0.1
diboson background	0.2	0.6	0.0	0.1
QCD/W+jets background	0.1	0.1	0.0	0.0
Q^2 scale	0.2	0.5	0.7	0.5
ME-PS matching	0.1	0.1	1.3	0.8
ME generator	0.3	0.3	2.0	2.0
hadronization	0.6	0.8	1.6	1.3
top p_T	0.2	0.3	0.6	0.5
color reconnection	0.1	0.2	0.5	0.5
underlying event	0.0	0.1	0.4	0.4
PDF	0.3	0.4	0.8	0.9
luminosity	2.2	2.6	2.2	2.7
statistics	1.2	0.6	2.3	1.3
total uncertainty on $\sigma_{\mathrm{t\bar{t}},\mathrm{vis}}$	$\pm^{3.5}_{3.4}$	$\pm^{3.7}_{3.4}$	$\pm^{6.0}_{5.5}$	$\pm^{5.9}_{5.2}$
Q^2 scale (extrapol.)	$\mp^{0.0}_{0.4}$	$\pm^{0.2}_{0.1}$	$\mp^{0.0}_{0.4}$	$\pm^{0.2}_{0.1}$
ME-PS matching (extrapol.)	$\pm^{0.1}_{0.1}$	$\pm^{0.3}_{0.3}$	$\pm^{0.1}_{0.1}$	$\pm^{0.3}_{0.3}$
top p_{T} (extrapol.)	$\pm^{0.4}_{0.2}$	$\pm^{0.8}_{0.4}$	$\pm^{0.4}_{0.2}$	$\pm^{0.8}_{0.4}$
PDF (extrapol.)	$\mp^{0.2}_{0.1}$	$\pm^{0.2}_{0.1}$	$\mp^{0.2}_{0.1}$	$\pm^{0.2}_{0.1}$
total uncertainty on $\sigma_{\mathrm{t\bar{t}}}$	$\pm^{3.6}_{3.4}$	$\pm^{3.8}_{3.5}$	$\pm^{6.0}_{5.5}$	$\pm^{6.0}_{5.2}$

Table 5.4: Contributions from individual sources of uncertainties to the measured total $\mathrm{t\bar{t}}$ production cross sections at $\sqrt{s} = 7\,\mathrm{TeV}$ and $\sqrt{s} = 8\,\mathrm{TeV}$ using the fit method (left columns) and the event counting method (right columns).

Chapter 6

Extraction of the Top-Quark Mass

The choice of the top-quark mass value in a certain scheme affects the predicted production cross sections for $\mathrm{t\bar{t}}$ pairs as well as the kinematics of their decay products. Section 6.1 is dedicated to the extraction of the top-quark pole mass m_t^{pole} from $\sigma_{\mathrm{t\bar{t}}}$. A determination of m_t^{MC} and studies to extract a well-defined value for m_t^{pole} from the kinematics of decay products are presented in Section 6.2.

6.1 Determination of m_t from $\sigma_{\mathrm{t\bar{t}}}$

The inclusive $\mathrm{t\bar{t}}$ production cross sections at $\sqrt{s} = 7$ and $8\,\text{TeV}$, precisely determined in Chapter 5 are employed to extract m_t^{pole}. The extraction is performed by a joint-likelihood approach confronting the measured cross sections with their predicted values for each $\sqrt{s}$ and is described in Section 6.1.1. The results for m_t^{pole} at $\sqrt{s} = 7\,\text{TeV}$ and $\sqrt{s} = 8\,\text{TeV}$ are combined in Section 6.1.2.

6.1.1 Extraction Technique

The predicted $\mathrm{t\bar{t}}$ production cross section, $\sigma_{\mathrm{t\bar{t}}}^{\text{pred}}$, and the measured cross section, $\sigma_{\mathrm{t\bar{t}}}$, depend on the choice of the top-quark mass value. For the prediction, the dependence is more pronounced and affects the production rate directly, whereas for the measurement, it enters mainly through small acceptance effects.

The mass dependence of the measured value of $\sigma_{\mathrm{t\bar{t}}}$ is evaluated by employing two signal MC samples with $m_t^{\text{MC}} = 166.5\,\text{GeV}$ and $m_t^{\text{MC}} = 178.5\,\text{GeV}$ in addition to the nominal simulation with $m_t^{\text{MC}} = 172.5\,\text{GeV}$. The $\mathrm{t\bar{t}}$ cross-section measurement, as described in Chapter 5, is repeated for each additional mass hypothesis. For each of them, variations in the distributions employed for the fit due to all detector related uncertainties, uncertainties from hadronization modeling, and PDF are re-evaluated. The simulations required to assess the remaining modeling uncertainties are only generated for the nominal m_t^{MC}. In these cases (Q^2 and ME-PS matching scale, ME generator, CR and UE tunes), the relative uncertainty estimated for the nominal mass is propagated to the other mass points. The uncertainty due to the top-p_{T} modeling is based on a measurement performed for $m_t^{\text{MC}} = 172.5\,\text{GeV}$. Therefore, the reweighting procedure applied to the simulation to match the measured spectrum is not valid for other m_t^{MC} values. To account for this, the relative variations are extrapolated form the nominal mass point, but the corresponding nuisance parameter is left free in the fit. This is expressed in terms of a floating prior as defined in Chapter 5.2.

The three cross-section values obtained for m_t^{MC} =165.5, 172.5, and 178.5 GeV are fitted with an exponential function to obtain a continuous dependence of $\sigma_{\mathrm{t\bar{t}}}$ on m_t^{MC} as:

$$\sigma_{\mathrm{t\bar{t}}}^{\mathrm{meas}}(8\,\mathrm{TeV}, m_t^{\mathrm{MC}}) = \exp\left(-0.267617 \cdot (m_t^{\mathrm{MC}}/\,\mathrm{GeV} - 176.729)\right) + 242.6\,\mathrm{pb} \quad (6.1)$$

$$\sigma_{\mathrm{t\bar{t}}}^{\mathrm{meas}}(7\,\mathrm{TeV}, m_t^{\mathrm{MC}}) = \exp\left(-0.130183 \cdot (m_t^{\mathrm{MC}}/\,\mathrm{GeV} - 184.100)\right) + 169.9\,\mathrm{pb}. \quad (6.2)$$

An exponential dependence[1] is chosen since the acceptance $A_{\mathrm{e}\mu}$ is expected to saturate for large m_t^{MC} values with respect to the beam energy, at which the $\mathrm{t\bar{t}}$ pair is produced without additional momentum. For lower m_t^{MC} or higher beam energies, the top quarks acquire more momentum in z direction and are produced with larger rapidities. These momenta are propagated to the decay products of the top quarks. The p_{T} of the leptons from the $\mathrm{t\bar{t}}$ decay decreases with m_t^{MC}, as shown in Figure 6.1, while the leptons are produced with larger η. Both effects lead to a decrease of the acceptance. A corresponding increase of $A_{\mathrm{e}\mu}$ can be observed for larger m_t^{MC} values. In consequence, the dependence of $\sigma_{\mathrm{t\bar{t}}}$ on the choice of m_t^{MC} is more pronounced the smaller the ratio $m_t^{\mathrm{MC}}/\sqrt{s}$ becomes.

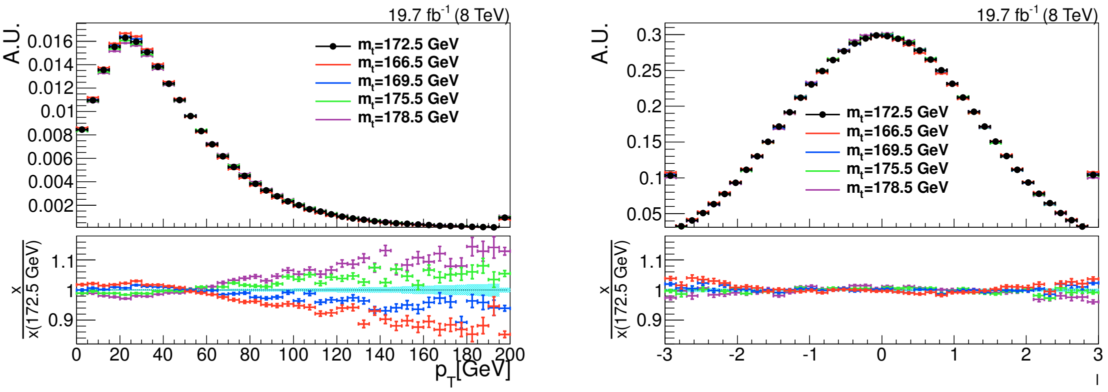

Figure 6.1: Predicted dependence of the generated lepton p_{T} (left) and η (right) on the m_t^{MC} hypothesis. All distributions are normalized and compared to the prediction for $m_t^{\mathrm{MC}} = 172.5\,\mathrm{GeV}$. Leptons p_{T} or η larger (lower) than the displayed range are included in the last (first) bins.

The measured dependence of $\sigma_{\mathrm{t\bar{t}}}$ on m_t^{MC} is expressed in terms of a likelihood constructed from $\sigma_{\mathrm{t\bar{t}}}^{\mathrm{meas}}(m_t^{\mathrm{MC}})$ and its uncertainty. The relative total uncertainties increasing or decreasing the cross section $\sigma_{\mathrm{t\bar{t}}}^{\mathrm{meas}}$, $\Delta_{\mathrm{meas},\pm}$, are almost constant for all mass hypotheses. In order to express the likelihood constructed from $\sigma_{\mathrm{t\bar{t}}}^{\mathrm{meas}}(m_t^{\mathrm{MC}})$ in terms of m_t^{pole}, an additional relative uncertainty $\Delta_{\mathrm{def}}(m_t^{\mathrm{MC}})$ is assigned accounting for the difference between m_t^{pole} and m_t^{MC}, estimated to be about 1 GeV. It is calculated from the fitted dependence as:

$$\Delta_{\mathrm{def},\pm}(m_t^{\mathrm{MC}}) = \frac{|\sigma_{\mathrm{t\bar{t}}}^{\mathrm{meas}}(m_t^{\mathrm{MC}} \mp 1\,\mathrm{GeV}) - \sigma_{\mathrm{t\bar{t}}}^{\mathrm{meas}}(m_t^{\mathrm{MC}})|}{\sigma_{\mathrm{t\bar{t}}}^{\mathrm{meas}}(m_t^{\mathrm{MC}})} \quad (6.3)$$

and added in quadrature to $\Delta_{\mathrm{meas},\pm}$. Then the final uncertainties on the measured dependence result

$$\tilde{\Delta}_{\mathrm{meas},\pm}^2 = \Delta_{\mathrm{meas},\pm}^2 + \Delta_{\mathrm{def},\pm}^2. \quad (6.4)$$

---

[1] An alternative choice of a second-order polynomial for the dependence of $\sigma_{\mathrm{t\bar{t}}}^{\mathrm{meas}}$ on m_t^{MC} has no effect on the final result.

The asymmetric uncertainties on $\sigma_{\mathrm{t\bar{t}}}^{\mathrm{meas}}$ are expressed in terms of an asymmetric Gaussian $G_a(x, y, w_+, w_-)$:

$$G_a(x, y, w_+, w_-) = \frac{(x-y)^2}{2c \cdot x} \text{ with } c = \begin{cases} w_+ \ , & x - y > 0 \\ w_- \ , & x - y \leq 0 \end{cases} \tag{6.5}$$

and the final likelihood for the measured dependence $L_{\mathrm{meas}}(m_t^{\mathrm{pole}}, \sigma_{\mathrm{t\bar{t}}})$ becomes

$$L_{\mathrm{meas}}(m_t^{\mathrm{pole}}, \sigma_{\mathrm{t\bar{t}}}) = exp\left[-0.5 \cdot G_a\left(\sigma_{\mathrm{t\bar{t}}}^{\mathrm{meas}}(m_t^{\mathrm{MC}} = m_t^{\mathrm{pole}}), \sigma_{\mathrm{t\bar{t}}}, \tilde{\Delta}_{\mathrm{meas},+}, \tilde{\Delta}_{\mathrm{meas},-}\right)\right]. \tag{6.6}$$

The predicted dependence of $\sigma_{\mathrm{t\bar{t}}}$ on m_t^{pole} at NNLO+NNLL is determined with TOP++ employing for PDF sets setting $\alpha_S(M_Z) = 0.118 \pm 0.001$: NNPDF3.0 [175], CT14 [176], and MMHT2014 [177], with M_Z being the Z-boson mass. For the ABM12 [178] PDF set, α_S is set to the value given the PDF set. The value of m_t^{pole} in the calculation is varied in 1 GeV steps between 166.5 GeV and 178.5 GeV. The resulting 13 central values are fitted with a sixth-order polynomial to obtain a continuous dependence on m_t^{pole}.

The relative uncertainties are constant with respect to different mass hypotheses. In addition to variations due to the choice of renormalization and factorization scales, PDF, and α_S, an uncertainty of 1.79% (7 TeV) and 1.72% (8 TeV) is assigned to the predicted cross section values to account for the uncertainty on the LHC beam energy [12]. Analogue to Equation 6.6, a likelihood $\hat{L}_{\mathrm{pred}}(m_t^{\mathrm{pole}}, \sigma_{\mathrm{t\bar{t}}})$ is defined, including the beam-energy uncertainty, PDF, and α_S variations summed in quadrature to a relative uncertainty, $\Delta_{p,\pm}$:

$$\hat{L}_{\mathrm{pred}}(m_t^{\mathrm{pole}}, \sigma_{\mathrm{t\bar{t}}}) = exp\left[-0.5 \cdot G_a\left(\sigma_{\mathrm{t\bar{t}}}^{\mathrm{pred}}(m_t^{\mathrm{pole}}), \sigma_{\mathrm{t\bar{t}}}, \Delta_{\mathrm{p},+}, \Delta_{\mathrm{p},-}\right)\right] \tag{6.7}$$

Given that no particular probability distribution is known that is adequate to model the confidence interval obtained from variations of renormalization and factorization scales, the corresponding uncertainty on the prediction is approximated using a box prior. Following [11], this prior is convoluted with $\hat{L}_{\mathrm{pred}}$ as

$$L_{\mathrm{pred}}(m_t, \sigma_{\mathrm{t\bar{t}}}) = \frac{1}{C(m_t^{\mathrm{pole}})}\left(\mathrm{erf}\left[\frac{\sigma_{\mathrm{t\bar{t}}}^{(h)}(m_t^{\mathrm{pole}}) - \sigma_{\mathrm{t\bar{t}}}}{\sqrt{2}\Delta_{p,+}}\right] - \mathrm{erf}\left[\frac{\sigma_{\mathrm{t\bar{t}}}^{(l)}(m_t^{\mathrm{pole}}) - \sigma_{\mathrm{t\bar{t}}}}{\sqrt{2}\Delta_{p,-}}\right]\right). \tag{6.8}$$

Here, $\sigma_{\mathrm{t\bar{t}}}^{(h)}(m_t^{\mathrm{pole}})$ and $\sigma_{\mathrm{t\bar{t}}}^{(l)}(m_t^{\mathrm{pole}})$ denote the upper and lower predicted cross section values, respectively, from independent variations of renormalization and factorization scales by a factor of 2. The normalization factor $C(m_t^{\mathrm{pole}})$ is given by the maximum value of $L_{\mathrm{pred}}(m_t^{\mathrm{pole}}, \sigma_{\mathrm{t\bar{t}}})$ for a free $\sigma_{\mathrm{t\bar{t}}}$ and a fixed m_t^{pole}. It only differs from 1 if the contributions of PDF, α_S, and the beam energy to the total uncertainty dominate significantly over the uncertainties due to variations of the renormalization and factorization scales.

The value of m_t^{pole} is extracted from the product of the likelihood for the measured and predicted dependence $L_{joint} = L_{\mathrm{pred}} \cdot L_{\mathrm{meas}}$. Its maximum corresponds to the most probable m_t^{pole}. The total uncertainty on m_t^{pole} is determined from the maximum spread of the $L_{joint} = exp(-0.5)$ contour in m_t^{pole}.

The measured m_t^{pole} and the likelihoods for the measured and predicted dependence of $\sigma_{\mathrm{t\bar{t}}}$ on m_t^{pole} are shown in Figure 6.2 for the NNPDF3.0 PDF set. The dependence of the measured cross section on m_t^{pole} is mild, but more pronounced for $\sqrt{s} = 8$ TeV.

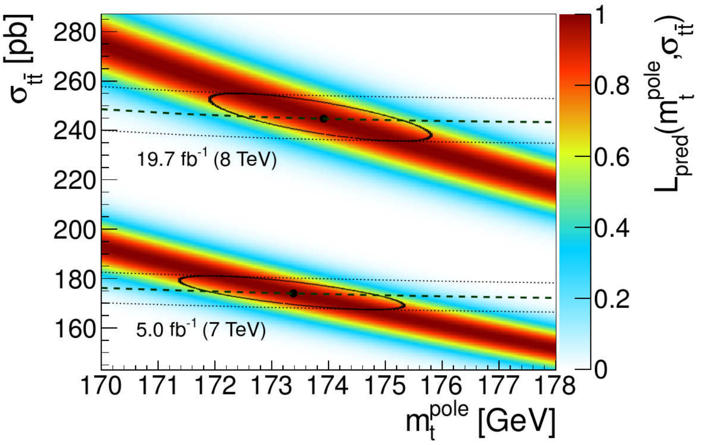

Figure 6.2: Likelihood for the predicted and measured dependence of the $\mathrm{t\bar{t}}$ production cross section, $\sigma_{\mathrm{t\bar{t}}}$, on the top-quark pole mass, m_t^{pole}, for $\sqrt{s} = 7\,\mathrm{TeV}$ (bottom) and $8\,\mathrm{TeV}$ (top). The prediction is calculated with TOP++ employing the NNPDF3.0 PDF set. The measured dependencies with their 1σ-uncertainties are represented by the dashed lines. The extracted pole mass values are indicated by black symbols, their total 1σ-uncertainty by a black contour.

The procedure is repeated for each PDF set. Uncertainties are evaluated at 68% CL. For CT14, the total PDF uncertainty is provided at 90% CL and scaled accordingly. The resulting values for m_t^{pole} are listed in Table 6.1. A fully consistent extraction using ABM12 is not possible since the resulting m_t^{pole} of 165.5 GeV is smaller than the probed range, 166.5-178.5 GeV, and is in the steeply falling part of $\sigma_{\mathrm{t\bar{t}}}^{\mathrm{meas}}(m_t^{\mathrm{pole}})$ at $\sqrt{s} = 8\,\mathrm{TeV}$.

	$m_t^{\mathrm{pole}}(7\,\mathrm{TeV})$	$m_t^{\mathrm{pole}}(8\,\mathrm{TeV})$
NNPDF3.0	$173.4 \pm^{2.0}_{2.0}$ GeV	$173.9 \pm^{1.9}_{2.0}$ GeV
MMHT2014	$173.7 \pm^{2.0}_{2.1}$ GeV	$174.2 \pm^{1.9}_{2.2}$ GeV
CT14	$173.9 \pm^{2.3}_{2.4}$ GeV	$174.3 \pm^{2.2}_{2.4}$ GeV

Table 6.1: Top quark pole mass at NNLO+NNLL extracted by confronting the measured $\mathrm{t\bar{t}}$ production cross section at $\sqrt{s} = 7\,\mathrm{TeV}$ and $\sqrt{s} = 8\,\mathrm{TeV}$ with predictions employing different PDF sets.

6.1.2 Combination of m_t at $\sqrt{s} = 7$ and $8\,\mathrm{TeV}$

The results for m_t^{pole} obtained at $\sqrt{s} = 7$ and $8\,\mathrm{TeV}$ are combined for each PDF set using a weighted mean defined as:

$$< m_t^{\mathrm{pole}} >= \left(\Delta_{u,7}^{-2} + \Delta_{u,8}^{-2}\right)^{-1} \cdot \left(\frac{m_t^{\mathrm{pole}}(7\,\mathrm{TeV})}{\Delta_{u,7}^2} + \frac{m_t^{\mathrm{pole}}(8\,\mathrm{TeV})}{\Delta_{u,8}^2} \right) \tag{6.9}$$

with $\Delta_{u,7}$ ($\Delta_{u,8}$) being the uncorrelated parts of the total uncertainty on m_t^{pole} at $\sqrt{s} = 7$ (8) TeV, determined as follows.

The uncertainties on the measured $\sigma_{t\bar{t}}$ comprise the uncertainty on $\sigma_{t\bar{t},\text{vis}}$ in the visible kinematic range Δ^{vis}, for which the correlation coefficient $\rho_{7,8}$ is obtained from the fit, and the fully correlated extrapolation uncertainties. With $\rho_{7,8} = 0.30$, the uncorrelated part of Δ^{vis} is removed by scaling $\Delta^{\text{vis}} \to \rho_{7,8}\Delta^{\text{vis}}$. The extrapolation of $\sigma_{t\bar{t},\text{vis}}$ to $\sigma_{t\bar{t}}$ is performed by adding the corresponding uncertainties in quadrature and the extraction of m_t^{pole} is repeated. The resulting uncertainty on m_t^{pole}, Δ_c, only includes fully correlated uncertainties, since the uncertainties on the prediction are also assumed to be fully correlated. The uncorrelated part Δ_u of the total uncertainty, Δ_{tot}, can therefore be determined as:

$$\Delta_u^2 = \Delta_{\text{tot}}^2 - \Delta_c{}^2 \tag{6.10}$$

The weighted mean of m_t^{pole} $< m_t^{\text{pole}} >$ is calculated using Equation 6.9. The contribution of $\Delta_{u,7}$ and $\Delta_{u,8}$ to its uncertainty is determined as:

$$\Delta_{u,\text{comb}}^2 = \left(\Delta_{u,7}^{-2} + \Delta_{u,8}^{-2}\right)^{-1} . \tag{6.11}$$

The fully correlated contribution is determined by varying $m_t^{\text{pole}}(7\,\text{TeV})$ and $m_t^{\text{pole}}(8\,\text{TeV})$ simultaneously within the fully correlated uncertainty. The resulting combined values for the top quark pole mass are listed in Table 6.2. The combined m_t^{pole} agree well for different PDF sets. Their precision of 1%-1.3% is similar to a recent determination from normalized differential $t\bar{t}$ production cross sections predicted at NLO accuracy (1.3%) [75], and supersedes the precision achieved for the extraction from the inclusive $t\bar{t}$ production cross section (1.5%) [12] using calculations at NNLO.

	$< m_t^{\text{pole}} >$
NNPDF3.0	$173.6 \pm^{1.7}_{1.8}$ GeV
MMHT2014	$173.9 \pm^{1.8}_{1.9}$ GeV
CT14	$174.1 \pm^{2.1}_{2.2}$ GeV

Table 6.2: Combined top quark pole mass at NNLO+NNLL extracted by confronting the measured $t\bar{t}$ production cross section with predictions employing different PDF sets.

6.2 Determination of m_t from the lepton-b-jet invariant mass distribution

Besides the total $t\bar{t}$ production cross section, additional information contained in differential cross sections can be used to determine m_t if an observable is chosen that is particularly sensitive to m_t and, in the best case, insensitive to certain systematic uncertainties.

Such an observable is the invariant mass distribution of the lepton and the b jet ($\mathrm{m_{lb}}$) in dileptonic $t\bar{t}$ events [17]. Calculations at NLO for $t\bar{t}$ production and decay are available [18, 19]. The shape of the $\mathrm{m_{lb}}$ distribution is affected by the choice of m_t. It is in principle under good theoretical control over the entire range that is relevant for measurements of m_t, but the way higher-order effects are included in the measurement could be crucial [9, 179].

In the following, an analysis of the $\mathrm{m_{lb}}$ observable and a determination of m_t from its shape is presented, using $t\bar{t}$ candidate events in the $e\mu$ channel from the data taken at $\sqrt{s} = 8\,\mathrm{TeV}$. The event selection is described in Section 6.2.1. The observable $\mathrm{m_{lb}}$ is defined in Section 6.2.2. A direct measurement of m_t^{MC} is performed by confronting the measured shape to predictions using MC simulation as described in Section 6.2.4. In Section 6.2.5, a generic approach for an alternative top-quark mass measurement is presented, comparing the measured $\mathrm{m_{lb}}$ distribution to fixed-order QCD calculations at LO and at NLO.

6.2.1 Event selection

The extraction of the top-quark mass from the $\mathrm{m_{lb}}$ shape requires a very clean signal with minimal contribution from background processes, since those contributions decrease the sensitivity of the distribution to the top-quark mass. Therefore, in addition to the trigger criteria and the dilepton selection described in Chapter 4, at least two jets, and one b jet are required. The loose working point for the b-tagging algorithm is employed, see Section 4.3.2. The additional criteria reduce the total predicted contribution from background processes to 7%, while keeping about 29,300 $\mathrm{t\bar{t}}$ signal events for analysis. As shown in Figure 6.3, the kinematics of the selected lepton candidates as well as of the leading b jet are well described by the simulation.

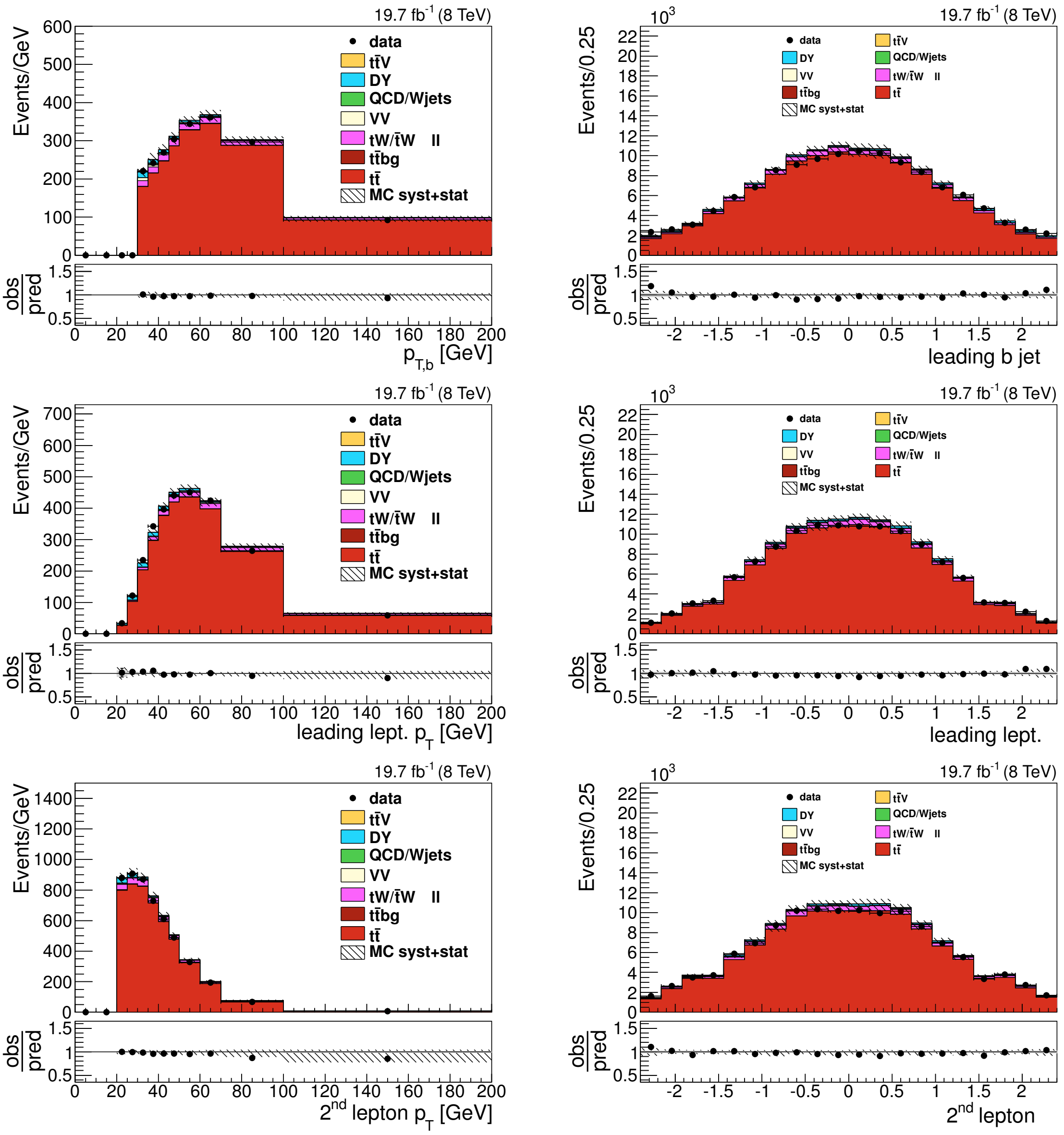

Figure 6.3: Transverse momentum (left column) and pseudorapidity (right column) of the leading b jet (first row), the leading lepton (second row), and the second leading lepton (third row). The hatched bands correspond to statistical and systematic uncertainties added in quadrature. The lower panels depict the ratio of observed and predicted yields. Here, the small contribution to the uncertainty from MC statistics is indicated by a gray shaded band.

6.2.2 Definition of the $\mathrm{m_{lb}}$ observable

The top-quark decay chain considered in this analysis is $t \to Wb$ followed by $W \to l\nu$. At LO and neglecting lepton and b-quark masses, one finds

$$\mathrm{m}_{\mathrm{lb}}^2 = \frac{m_t^2 - m_W^2}{2}\left(1 - \cos\theta_{lb}\right), \tag{6.12}$$

where m_W is the mass of the W boson and θ_{lb} is the opening angle between the lepton and the b-quark in the W-boson rest frame. This relation already illustrates that the $\mathrm{m_{lb}}$ distribution has an endpoint at

$$\max(\mathrm{m_{lb}}) \approx \sqrt{m_t^2 - m_W^2}. \tag{6.13}$$

For a top-quark mass of 173 GeV, $\max(\mathrm{m_{lb}})$ is around 153 GeV. The LO distribution is diluted by higher-order effects, but remains sensitive to m_t.

Experimental effects such as the limited detector acceptance and the finite resolution in the reconstruction of the lepton and jet four-momenta further decrease this sensitivity. In addition, the reconstructed jets cannot be associated to a particular top quark without dedicated reconstruction algorithms. For this analysis, a simple algorithmic approach for reconstructing $\mathrm{m_{lb}}$ is sufficient. The permutation $\mathrm{m_{lb}^{min}}$ is chosen that minimizes the value of $\mathrm{m_{lb}}$ in each event when pairing the leading b jet with the leading or second-leading lepton (e or μ) candidate[2]. The resulting distribution provides a good sensitivity to the choice of m_t^{MC}, especially for $\mathrm{m_{lb}^{min}} \approx 150$ GeV, as shown in Figure 6.4. For m_t^{MC} =172.5 GeV, expected and observed event yields agree well.

In addition, a predicted quantity $\mathrm{m_{lb,pred}^{min}}$ is defined based on generator information. The leading b quark and both leptons (e, μ or τ) from the W-boson decay are required to be in the visible phase space, defined as $p_{\mathrm{T}} > 20$ GeV (leptons) or $p_{\mathrm{T}} > 30$ GeV (b quark) and $|\eta| < 2.4$. Leptons and the leading b quark are paired according to the same algorithm used for $\mathrm{m_{lb}^{min}}$. The fraction of correct pairings of b quark and lepton to the corresponding top quark is studied using MadGraph+pythia and is found to be 72%.

6.2.3 Extraction technique and systematic uncertainties

The value of m_t^{MC} is determined by comparison of the measured and the expected normalized $\mathrm{m_{lb}^{min}}$ distributions, including contributions from the signal and background processes. The normalization factor n_{pred} (n_{obs}) is derived from the integral of the expected (observed) $\mathrm{m_{lb}^{min}}$ distribution. The observed yields, $N_{\mathrm{obs},i}$, are confronted with their expectation $N_{\mathrm{pred},i}$ in bin i of the distribution for different values of m_t^{MC}. For this purpose, an estimator $\chi^2(m_t^{\mathrm{MC}}, i)$ is defined as:

$$\chi^2(m_t^{\mathrm{MC}}, i) = \frac{\left(N_{\mathrm{pred},i}(m_t^{\mathrm{MC}})/n_{\mathrm{pred}} - N_{\mathrm{obs},i}/n_{\mathrm{obs}}\right)^2}{(\Delta_{\mathrm{pred},i}/n_{\mathrm{pred}})^2 + (\Delta_{\mathrm{obs},i}/n_{\mathrm{obs}})^2}, \tag{6.14}$$

with $\Delta_{\mathrm{pred},i}$ and $\Delta_{\mathrm{obs},i}$ being the statistical uncertainties of the expected and observed yields, respectively.

---

[2] Alternative definitions were studied and found to provide no gain in sensitivity and precision with respect to m_t.

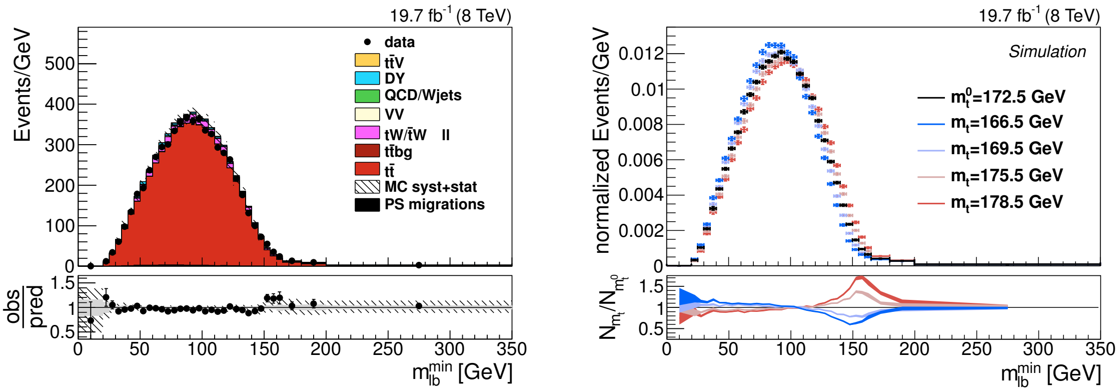

Figure 6.4: Left: Reconstructed $\mathrm{m}_{\mathrm{lb}}^{\mathrm{min}}$ for $m_t^{\mathrm{MC}} = 172.5\,\mathrm{GeV}$. The hatched band corresponds to the statistical and systematic uncertainties added in quadrature. The lower panel depicts the ratio of observed and predicted yields. Here, the uncertainty from MC statistics is indicated by a gray shaded band. Right: Dependence of the normalized $\mathrm{m}_{\mathrm{lb}}^{\mathrm{min}}$ distribution on the choice of m_t^{MC} normalized to the total number of selected events. The lower panel shows the relative difference of the shape for each m_t^{MC} with respect to $m_t^{\mathrm{MC}} = 172.5\,\mathrm{GeV}$.

The yields $N_{\mathrm{pred},i}(m_t^{\mathrm{MC}})$ are evaluated for $m_t^{\mathrm{MC}} = 166.5$, 169.5, 171.5, 172.5, 173.5, 175.5, and 178.5 GeV using dedicated simulations. In order to derive a continuous dependence on m_t^{MC}, the resulting yields are fitted with second-order polynomials, which describe this dependence well. The fitted curves for each bin are shown in Appendix D. A global estimator $\chi^2(m_t^{\mathrm{MC}})$ is derived by summing $\chi^2(m_t^{\mathrm{MC}}, i)$ over all bins i. The top-quark mass is determined from its minimum χ^2_{min}. The statistical uncertainty is obtained by applying the criterion $\chi^2(m_t^{\mathrm{MC}}) = \chi^2_{\mathrm{min}} + 1$.

The same sources of systematic uncertainties discussed in Section 5.2 are considered in this analysis. The impact of each source on m_t^{MC} is evaluated by varying the corresponding parameter, and determining the expected event yield as a function of $\mathrm{m}_{\mathrm{lb}}^{\mathrm{min}}$. The corresponding value of m_t^{MC} is extracted and the difference to the nominal result is taken as systematic uncertainty. For variations of the UE modeling and the ME-PS matching scale, these deviations are smaller than the statistical uncertainty on m_t^{MC} due to fluctuations in the simulation. Therefore, these statistical uncertainties are taken as systematic uncertainty, instead. The variations of m_t^{MC} with respect to individual components of the JES: flavor group describing gluon, c-, b-, and light-quark response are added linearly to account for the correlation among them. The remaining contributions to the total uncertainty on m_t^{MC} are added in quadrature.

In addition, systematic uncertainties related to the extraction procedure are studied and discussed in the following. These are assumptions on the statistical model used to define $\chi^2(m_t^{\mathrm{MC}})$, the m_t-dependence of the contribution from tW processes, and the parameterization of the predicted dependence as a function of m_t^{MC}.

Assumptions on the statistical model

For the definition of $\chi^2(m_t^{\mathrm{MC}})$ two assumptions are made: (a) the statistical uncertainties have Gaussian form and (b) all bins are uncorrelated. The assumption (a) might bias m_t^{MC} through bins with low statistics. The assumption (b) is true for all bins except one, which is correlated with the remaining ones through the normalization requirement. The effect of these assumptions can be quantified with pseudo-experiments. These are performed for three initial mass hypotheses $m_t^{in} = 169.5$, 172.5, and 175.5 GeV. Poisson-distributed pseudo-data are generated in each bin using $N_{\mathrm{pred},i}(m_t^{in})$ as the central value. Fluctuations of the predicted yields are simulated for background and signal contributions independently, following the approach described in Section 5.7.1. For each of in total $3 \cdot 10,000$ pseudo-experiments, the pull is calculated. The resulting pull distributions are fitted with a Gaussian, as shown in Figure 6.5. For all m_t^{in}, the peak positions are consistent with 0 indicating a bias-free measurement. Also the statistical uncertainty extracted by the criterion $\chi^2_{\mathrm{min}} + 1$ is well modeled since the pull widths are compatible with 1. Therefore, the simplifications in the definition of $\chi^2(m_t^{\mathrm{MC}})$ do not affect the extracted top-quark mass value.

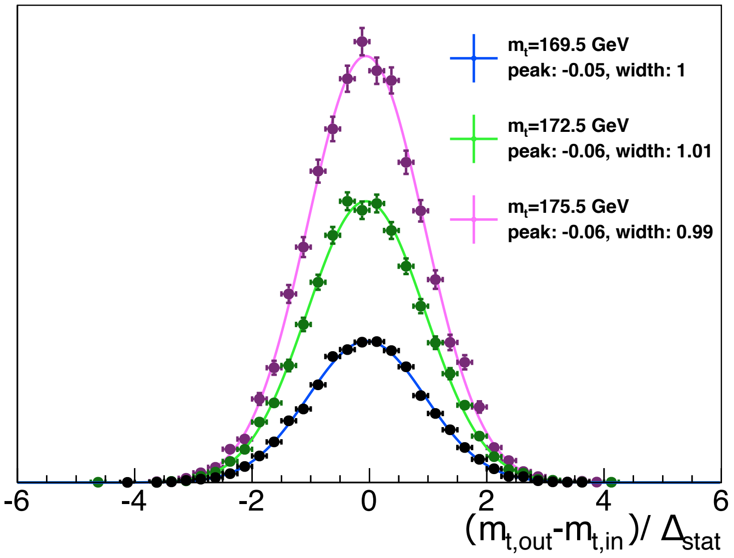

Figure 6.5: Pull distribution for the extraction of m_t^{MC} from the $\mathrm{m}_{\mathrm{lb}}^{\mathrm{min}}$ distribution evaluated for 3 different hypothesis of m_t^{MC}. The difference between hypothesis m_t^{in} and extracted value m_t^{out} is divided by the statistical uncertainty of m_t^{out}, Δ_{stat}.

Contribution from tW processes

The expected contribution from tW processes also depends on the top-quark mass. However, only variations of the $\mathrm{t\bar{t}}$ signal contribution are considered in the m_t^{MC}-dependence of the $\mathrm{m}_{\mathrm{lb}}^{\mathrm{min}}$ shape. The simulation of tW events is not available for all seven m_t^{MC} hypotheses and therefore only the simulated MC sample with m_t^{MC} fixed to 172.5 GeV is employed. The effect of this approximation on the final result is studied by comparing

5 scenarios using simulated $\mathrm{t\bar{t}}$ and tW events generated with $m_t^{\mathrm{MC}} = 166.5$, 172.5, and 178.5 GeV. In each case, the $\mathrm{m}_{\mathrm{lb}}^{\mathrm{min}}$ shape is evaluated for a different choice of m_t^{MC} in the simulation of $\mathrm{t\bar{t}}$ signal and tW processes, indicated as $\mathrm{t\bar{t}}(m_t^{\mathrm{MC}})$ or $\mathrm{tW}(m_t^{\mathrm{MC}})$, respectively. The following scenarios are considered:

0 $\mathrm{t\bar{t}}$(172.5 GeV) and tW(172.5 GeV)
1 $\mathrm{t\bar{t}}$(166.5 GeV) and tW(166.5 GeV)
2 $\mathrm{t\bar{t}}$(166.5 GeV) and tW(172.5 GeV)
3 $\mathrm{t\bar{t}}$(178.5 GeV) and tW(172.5 GeV)
4 $\mathrm{t\bar{t}}$(178.5 GeV) and tW(178.5 GeV)

The resulting normalized $\mathrm{m}_{\mathrm{lb}}^{\mathrm{min}}$ distributions are compared to scenario **0**, as presented in Figure 6.6. Consistent variations of m_t^{MC} in the tW and $\mathrm{t\bar{t}}$ simulation (**1** and **4**) lead to a slightly increased sensitivity of the distribution to m_t^{MC} and would thus increase the statistical precision of the extracted m_t. An upper limit on a possible bias can be estimated by comparing the maximum relative deviations of consistent and inconsistent variations. These are below 10% in the sensitive region with $\mathrm{m}_{\mathrm{lb}}^{\mathrm{min}} \approx 150$ GeV and hence correspond to a maximum bias of 0.1 GeV per 1 GeV difference to $m_t^{\mathrm{MC}} = 172.5$ GeV which is assigned as an additional systematic uncertainty (**tW**(m_t)).

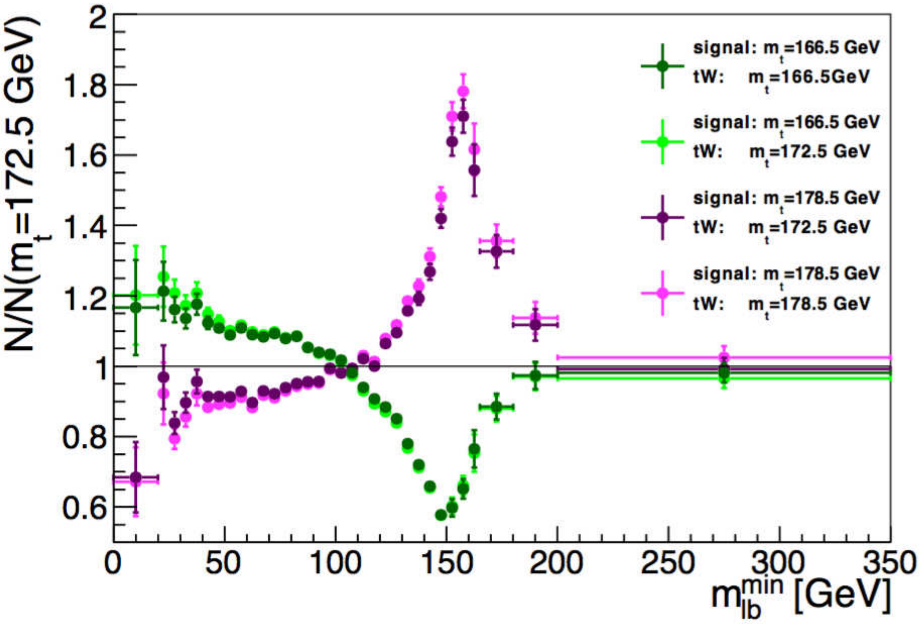

Figure 6.6: Relative variation of the $\mathrm{m}_{\mathrm{lb}}^{\mathrm{min}}$ shape for different top-mass hypothesis with respect to a hypothesis of $m_t = 172.5$ GeV. The value of m_t is varied independently for the $\mathrm{t\bar{t}}$ signal and the tW predictions.

Parametrization of the m_t^{MC} dependence

Second-order polynomials describe the dependence of the predicted yields in each bin of the $\mathrm{m}_{\mathrm{lb}}^{\mathrm{min}}$ distribution well. However, a possible impact of the choice of the functional form is studied. The bin-wise fits are performed for third-order polynomials up to fifth-order polynomials. For each, the extraction procedure is repeated and the maximum deviation from the nominal result for m_t^{MC} of 70 MeV is taken as **parametrization** uncertainty.

In addition, the dependence of the extracted m_t^{MC} on the number of m_t^{MC} hypothesis used to derive the parameterization is studied. For this purpose, 3 mass points are used instead of 7 to derive the parameterization: a central point with $m_t^{\mathrm{MC}} = 172.5\,\mathrm{GeV}$, and the most significant variations $m_t^{\mathrm{MC}} = 166.5\,\mathrm{GeV}$ and $m_t^{\mathrm{MC}} = 178.5\,\mathrm{GeV}$. Only a small shift of +60 MeV of the extracted m_t^{MC} value is observed. In the following, 7 m_t^{MC} hypotheses are employed for the $\mathrm{t\bar{t}}$ signal simulation.

Source	Δm_t^{MC} [GeV]
trigger	< 0.01
lepton ID/isolation	$^{+0.02}_{-0.03}$
lepton energy scale	$^{+0.12}_{-0.11}$
jet energy scale	$^{+0.42}_{-0.44}$
jet energy resolution	$^{+0.05}_{-0.07}$
b-tag	$^{-0.10}_{+0.13}$
mistag	$^{-0.15}_{+0.15}$
pileup	$^{-0.09}_{+0.09}$
background processes	$^{-0.11}_{+0.11}$
Q^2 scale	$^{+0.48}_{-0.66}$
ME-PS matching	$^{+0.13}_{-0.25}$
ME generator	$^{+0.15}_{-0.00}$
hadronization	$^{+0.68}_{-0.27}$
top p_T	$^{+0.64}_{-0.00}$
color reconnection	$^{-0.00}_{+0.22}$
underlying event	$^{-0.14}_{+0.14}$
PDF	$^{+0.05}_{-0.07}$
luminosity	< 0.01
stat	$^{+0.31}_{-0.32}$
parametrization	$^{-0.07}_{+0.07}$
$\mathrm{tW}(m_t)$	$^{-0.03}_{+0.03}$
total syst.+stat.	$^{+1.25}_{-1.00}$

Table 6.3: Breakdown of systematic uncertainties on the top-quark MC mass value, obtained by confronting the shape of the $\mathrm{m_{lb}^{min}}$ distribution to predictions by MadGraph+pythia.

6.2.4 Determination of m_t^{MC} from the $\mathrm{m}_{\mathrm{lb}}^{\mathrm{min}}$ shape

The measured shape of the $\mathrm{m}_{\mathrm{lb}}^{\mathrm{min}}$ distribution is compared to the prediction, comprising contributions from background processes and the $\mathrm{t\bar{t}}$ signal modeled by MadGraph+pythia, as presented in Figure 6.7. The data show the most compatibility with the expected shape for $m_t^{\mathrm{MC}} = 172.5\,\mathrm{GeV}$, while deviations from this value of $\pm 6\,\mathrm{GeV}$ are disfavored. The minimization of the global $\chi^2(m_t^{\mathrm{MC}})$ results in a top-quark MC mass value of

$$m_t^{\mathrm{MC}} = 172.8\ ^{+1.3}_{-1.0}\,\mathrm{GeV}, \tag{6.15}$$

consistent with the world average [8]. The total uncertainty is larger than the one in measurements based on semileptonic $\mathrm{t\bar{t}}$ decays, where an in-situ JES calibration is performed [69]. However, this analysis has partially complementary uncertainties and provides a result more precise than other measurements in the dilepton channel [180,181]. All contributions to the total uncertainty are listed in Table 6.3. The dominant uncertainties arise from the JES and the hadronization modeling. Furthermore, variations of top p_{T} and Q^2 scale have a large effect on the total uncertainty. Negligible contributions come from variations affecting the normalization of the prediction, e.g. from the luminosity or trigger uncertainties.

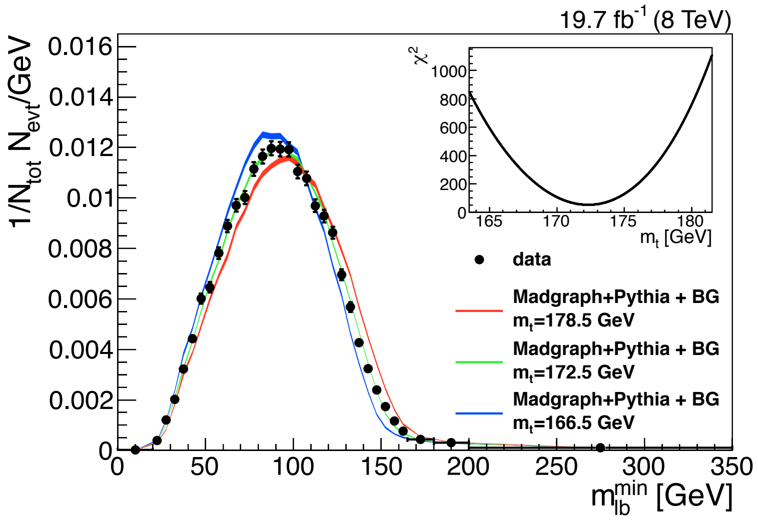

Figure 6.7: Normalized selected event yields presented as a function of $\mathrm{m}_{\mathrm{lb}}^{\mathrm{min}}$. The closed symbols represent data points and the error bars their statistical uncertainties. The predicted yields are obtained with a top-quark MC mass hypothesis of $m_t = 178.5\,\mathrm{GeV}$ (red band), $m_t = 172.5\,\mathrm{GeV}$ (green band), and $m_t = 166.5\,\mathrm{GeV}$ (blue band). The width of the bands indicate the statistical uncertainties on the prediction. The inset shows the χ^2 distribution as a function of m_t as determined from the comparison of data and predictions.

6.2.5 Folding: comparison to fixed-order calculations

In the following, a technique is introduced which allows to use fixed-order calculations (in particular MCFM) to determine the top-quark mass, by comparison with experimentally measured distributions. In general, these calculations provide the possibility to extract the top quark mass in a well-defined scheme. However, the predicted distributions can not be compared directly to the reconstructed quantities. The *folding* approach presented in this thesis allows to *fold* a predicted observable to its reconstructed counterpart, e.g. the $\mathrm{t\bar{t}}$ production cross section as a function of $\mathrm{m_{lb,pred}^{min}}$ to the event yields as a function of $\mathrm{m_{lb}^{min}}$. The folded prediction can then be compared to the data without the need of a full detector simulation.

For this purpose, a response matrix M is defined as

$$\vec{N}_{reco} = \mathcal{L} \cdot M\vec{\sigma}. \tag{6.16}$$

The event yields or differential cross sections in each bin of $\mathrm{m_{lb}^{min}}$ or $\mathrm{m_{lb,pred}^{min}}$ are represented by entries in $\vec{N}_{reco}$ and $\vec{\sigma}$, respectively. The response matrix comprises resolution effects through non-diagonal entries. Bin-wise selection efficiencies and acceptance corrections are included in the normalization of each column. The matrix is determined from the MadGraph+pythia signal simulation. For each simulated event, $\mathrm{m_{lb,pred}^{min}}$ is calculated and associated to a certain bin i. If the event passes all reconstruction requirements, $\mathrm{m_{lb}^{min}}$ is determined to be within bin j. The response matrix is calculated as

$$M_{ij} = \frac{1}{c_i + \tilde{\epsilon}_i} \sum_k w_{i,j,k}, \tag{6.17}$$

with $w_{i,j,k}$ being the weight assigned to event k due to correction factors discussed in Chapter 4. The matrix is normalized with $c_i = \sum_{j,k} w_{i,j,k}$ and $\tilde{\epsilon}_i$. The latter term implements the reconstruction efficiency and acceptance effects by summing all weights of events generated in bin i, that do not pass the selection requirements. The resulting response matrix for $\mathrm{m_{lb}^{min}}$ is shown in Figure 6.8. Dominant diagonal elements indicate a strong correlation between the generated and reconstructed observables. Thus, the sensitivity of $\mathrm{m_{lb}^{min}}$ to the top quark mass is not significantly decreased by the limited detector resolution. The intermediate leptonic τ decays from $\mathrm{W} \to \tau + \nu \to \mathrm{e}/\mu + 2\nu$ are considered signal for the reconstruction of $\mathrm{m_{lb}^{min}}$, while $\mathrm{m_{lb,pred}^{min}}$ is defined for *prompt* leptons from the $\mathrm{W} \to \mathrm{e}/\mu/\tau$ decay. The dominant diagonal elements in M demonstrate that this fact does not lead to a significantly softer reconstructed $\mathrm{m_{lb}^{min}}$ distribution. Nevertheless, even a pronounced bias would be corrected for by the folding technique.

The limited number of generated events leads to statistical uncertainties on each element M_{ij}. These are estimated using a binomial approximation, since the calculation of M_{ij} employs statistically correlated terms as:

$$(\Delta M_{ij})_{\mathrm{stat}} = \sqrt{\frac{M_{ij}(1 - M_{ij})}{\sum_k w_{i,j,k}}}. \tag{6.18}$$

These statistical uncertainties decrease with increasing simulated event rates (cross sections) as a function of $\mathrm{m_{lb}^{min}}$ ($\mathrm{m_{lb,pred}^{min}}$) and are propagated to the folded distribution.

Systematic uncertainties related to the detector response and the signal modeling by MadGraph+pythia enter the response matrix. For each uncertainty source and choice of m_t^{MC}, a new response matrix is derived. In cases where systematic variations can not be performed due to missing simulation for m_t^{MC} values other than 172.5 GeV, relative uncertainties are propagated from the response matrix for $m_t^{\mathrm{MC}} = 172.5\,\mathrm{GeV}$.

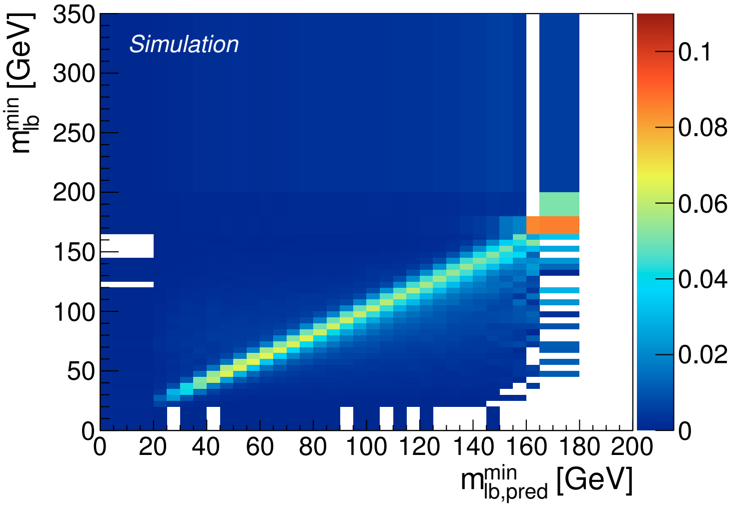

Figure 6.8: Response matrix for $\mathrm{m}_{\mathrm{lb}}^{\mathrm{min}}$, quantifying detector resolution and event reconstruction effects as defined in Equation 6.17. The matrix relates the predicted event rate as a function of $\mathrm{m}_{\mathrm{lb,pred}}^{\mathrm{min}}$ to the reconstructed event rate as a function of $\mathrm{m}_{\mathrm{lb}}^{\mathrm{min}}$. Bins without entries are left white.

This applies to variations of the Q^2 and matching scales, the ME generator, CR and UE tunes.

The resulting set of response matrices allows to fold a predicted $\mathrm{t\bar{t}}$ production cross section as a function of $\mathrm{m}_{\mathrm{lb,pred}}^{\mathrm{min}}$ and compare the resulting shape directly to the data, once contributions from background processes are added. The requirements on the visible phase space in the definition of $\mathrm{m}_{\mathrm{lb,pred}}^{\mathrm{min}}$ (see Section 6.2.2) reduce the impact of acceptance corrections.

Alternatively, an *unfolding* of the measured event yields to measured differential cross-sections can be performed. Within the unfolding, the response matrix M is inverted. This inversion can be ill-posed. Even though, ill-posed problems can be solved with *regularization* techniques [182], the statistical fluctuations in M^{-1} typically demand a coarser binning of the unfolded distributions [162] in comparison to the one used for m_{lb} here, which leads to a decrease in sensitivity to m_t. Furthermore, unfolding introduces statistical correlations between the bins of the unfolded distribution. These correlations must be taken into account in the estimator used to perform the extraction, since statistical uncertainties on the measurement are typically not negligible. Thus, the folding technique represents a robust, precise, and statistically well-defined method to extract m_t.

However, the definition of $\mathrm{m}_{\mathrm{lb,pred}}^{\mathrm{min}}$ used in MadGraph+pythia to derive the response matrices and in the prediction, in this case mcfm, must coincide. In addition, the m_t^{MC}-dependence of the response matrices might lead to a bias when extracting m_t in a well-defined scheme. These issues would also apply to the case of an unfolding approach and are discussed in the following.

Calculation of $\mathbf{m_{lb,pred}^{min}}$ in MCFM

The response matrices, as described above, are derived using MadGraph+pythia. The decay of the $\mathrm{t\bar{t}}$ pairs is simulated with MadSpin, which implements LO predictions. In a second step, real emissions are modeled with pythia. Therefore, the b quark and leptons can be considered either before or after this step (*before* or *after radiation*). In mcfm, the production and decay of $\mathrm{t\bar{t}}$ pairs can be predicted with LO or NLO accuracy. The NWA allows to separate both amplitudes, such that calculations at NLO (LO) for the production can be combined with calculations at LO (NLO) for the decay. In particular, the b quark momentum is affected by different choices for the decay.

Diagrams for the top-quark decay that are implemented in MadGraph+pythia and mcfm are schematically compared in Figure 6.9. The most consistent definition of $\mathrm{m_{lb,pred}^{min}}$ is achieved by considering the leptons and quarks given by calculations at LO for the decay in mcfm and their counterparts in MadGraph+pythia before radiation (Figure 6.9a). The corresponding mcfm routines are modified accordingly and adapted to apply the visible phase space requirements given in Section 6.2.2. For each top-quark mass hypothesis considered in MadGraph+pythia, the $\mathrm{t\bar{t}}$ production cross section as a function of $\mathrm{m_{lb,pred}^{min}}$ is calculated. Concerning the production, LO and NLO calculations are employed to extract the top-quark mass m_t^{LO} and m_t^{NLO}, respectively. The predictions are obtained using the MSTW2008 [183] PDF set at LO (NLO), with $\alpha_S(M_Z) = 0.1394$ (0.1202), and setting the b-quark mass to 4.75 GeV. Renormalization and factorization scales are set to m_t^{pole}. The full configuration of mcfm is listed in Appendix D.

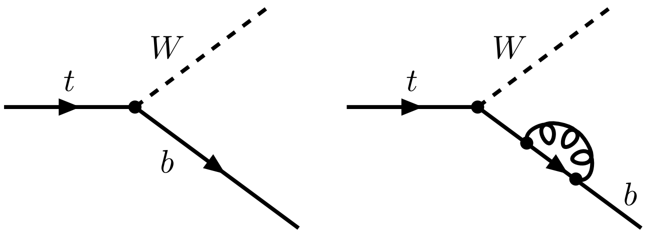

(a) LO (b) virtual correction

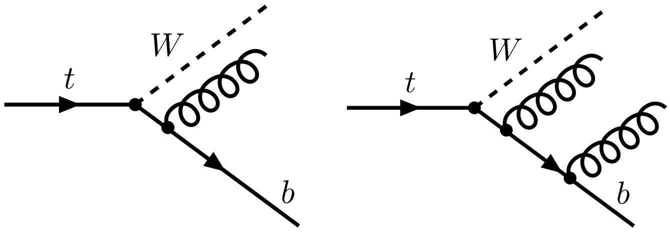

(c) one real emission (d) two real emissions

Figure 6.9: Feynman diagrams for the top quark decay at LO (a), an example of a virtual (b) and a real (c) correction to the decay at NLO. Figure (d) shows two real emissions. The corrections (a), (b), and (c) are implemented in mcfm. MadGraph includes (a), while (c) and (d) are modeled by the parton shower in pythia.

Dependence of the response matrix on $m_t^{\mathbf{MC}}$

For each m_t^{pole} hypothesis used in MCFM, the corresponding response matrix derived for m_t^{MC}, $M(m_t^{\text{MC}} = m_t^{\text{pole}})$, is used for the folding. However, m_t^{pole} and m_t^{MC} are not equal. Therefore, this procedure can introduce a bias if the response matrix depends strongly on m_t^{MC}. This possible bias is studied with MadGraph+pythia by comparing the initial and extracted values of m_t^{MC}. An artificial mismatch is introduced between m_t^{MC} used for the predicted $\mathrm{m}_{\mathrm{lb,pred}}^{\mathrm{min}}$ shape and the folding matrix. The nominal $\mathrm{m}_{\mathrm{lb,pred}}^{\mathrm{min}}$ distribution predicted with $m_t^{\text{MC}} = 172.5\,\text{GeV}$ is folded with response matrices $M(m_t^{\text{MC}})$ corresponding to $m_t^{\text{MC}} = 166.5$, 172.5, and 178.5 GeV. The resulting normalized event yields as a function of $\mathrm{m}_{\mathrm{lb}}^{\mathrm{min}}$ are presented in Figure 6.10.

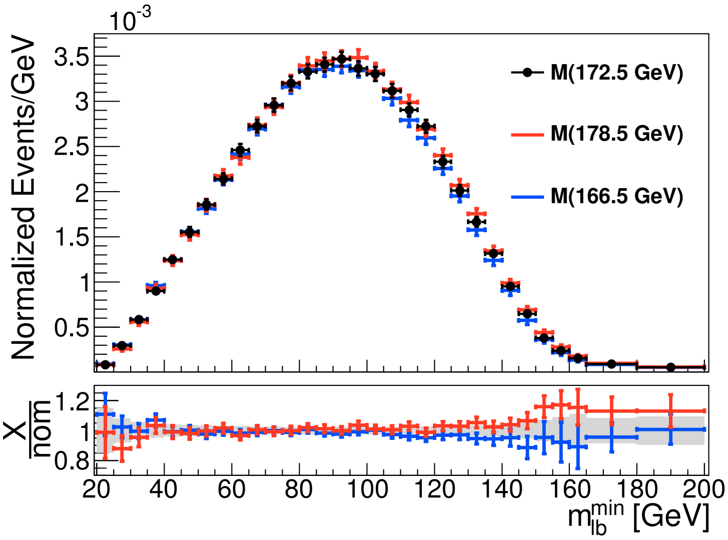

Figure 6.10: Folded and normalized $\mathrm{m}_{\mathrm{lb,pred}}^{\mathrm{min}}$ distribution as predicted by MadGraph+pythia for $m_t^{\text{MC}} = 172.5\,\text{GeV}$. The folding is performed with the response matrix M corresponding to $m_t^{\text{MC}} = 172.5\,\text{GeV}$ (nominal), $m_t^{\text{MC}} = 178.5\,\text{GeV}$, or $m_t^{\text{MC}} = 166.5\,\text{GeV}$. The statistical uncertainties are indicated with error bars. The lower panel shows the ratio of all distributions with respect to the nominal one. For the latter, statistical uncertainties are indicated with a shaded band.

The mismatch of ±6 GeV leads to small variations in the folded distributions. Their effect on the extracted top-quark mass is quantified by using these distributions instead of the one measured in data and performing the extraction of m_t^{MC} as described in Section 6.2.3. A bias of 200 MeV per 1 GeV mismatch is observed. Consequently, an additional systematic uncertainty (**$\boldsymbol{m_t}$ definition**) of 200 MeV is assigned to the folding procedure, since the difference between m_t^{pole} and m_t^{MC} is estimated to be of the order of 1 GeV.

Extracted top-quark mass and systematic uncertainties

The total uncertainty of the top-quark mass extracted from MCFM is composed of experimental uncertainties that affect the response matrix, systematic uncertainties related to the folding and extraction procedure, and theoretical uncertainties affecting the MCFM calculation. The latter comprise the PDF uncertainty (**PDF$_{\mathbf{mcfm}}$**) calculated at 68% CL according to the prescriptions of the MSTW2008 group. The value of α_S is varied using dedicated PDF sets [184] and differences to the central result are considered as additional uncertainty (**$\boldsymbol{\alpha_S}$**). The renormalization and factorization scales are varied independently by a factor of 2 up and down. The maximum deviation in each bin of $\mathrm{m}_{\mathrm{lb,pred}}^{\mathrm{min}}$ is taken as a systematic uncertainty (**scale$_{\mathbf{mcfm}}$**). The mass of the b quark is varied by ±0.25 GeV, resulting in an uncertainty (**b-quark mass**) on the extracted top-quark mass. Due to lacking statistics in the corresponding simulation, the response matrices for variations of CR and UE models suffer large fluctuations. Thus, these uncertainties are taken from the corresponding values obtained for m_t^{MC} measured using MadGraph+pythia.

The resulting top-quark masses extracted from the mcfm prediction employing calculations at (N)LO for the $\mathrm{t\bar{t}}$ production and at LO for the top-quark decay are

$$\begin{aligned} m_t^{\mathrm{LO}} &= 171.8^{+1.1}_{-1.0}\,\mathrm{GeV} \text{ and} && (6.19)\\ m_t^{\mathrm{NLO}} &= 171.5^{+1.1}_{-1.0}\,\mathrm{GeV}. && (6.20)\end{aligned}$$

A breakdown of the systematic uncertainties is provided in Table 6.4. The impact of top-p_{T} and PDF uncertainties on the mcfm-based result is slightly reduced in comparison to the mass determination based on MadGraph+pythia, since both affect only the simulation of the detector response, and not the shape of the predicted cross section as a function of $\mathrm{m}_{\mathrm{lb,pred}}^{\mathrm{min}}$. Both, m_t^{LO} and m_t^{NLO} agree within a few 100 MeV. The m_t extracted from the $\mathrm{m}_{\mathrm{lb}}^{\mathrm{min}}$ shape is mostly independent of the production mechanism. Hence, an extension of the studies presented here regarding the treatment of the $\mathrm{t\bar{t}}$ decay would be beneficial. This could be achieved by defining $\mathrm{m}_{\mathrm{lb,pred}}^{\mathrm{min}}$ in terms of a b jet instead of a b quark. In consequence, the method could be applied to predictions that do not separate the amplitudes for production and decay and take into account effects of a finite top-quark width. The corresponding calculations have been performed including the subsequent W-boson decays to leptons and studies show that uncertainties due to variations of renormalization and factorization scale seem to be underestimated when using the NWA [179]. Therefore, the uncertainties on m_t^{LO} and m_t^{NLO} should be interpreted as a lower limit. Nevertheless, these predictions are not publicly available in a form that is applicable to an experimental analysis.

	Δm_t [GeV]	
Source	LO	NLO
trigger	< 0.01	< 0.01
lepton ID/isolation	$^{+0.02}_{-0.02}$	$^{+0.02}_{-0.02}$
lepton energy scale	$^{+0.15}_{-0.10}$	$^{+0.14}_{-0.10}$
jet energy scale	$^{+0.42}_{-0.44}$	$^{+0.42}_{-0.45}$
jet energy resolution	$^{+0.05}_{-0.09}$	$^{+0.05}_{-0.08}$
b-tag	$^{-0.10}_{+0.14}$	$^{-0.10}_{+0.14}$
mistag	$^{-0.19}_{+0.21}$	$^{-0.17}_{+0.18}$
pileup	$^{-0.09}_{+0.09}$	$^{-0.08}_{+0.08}$
background processes	$^{-0.19}_{+0.19}$	$^{-0.15}_{+0.15}$
Q^2 scale	$^{+0.30}_{-0.54}$	$^{+0.31}_{-0.58}$
ME-PS matching	$^{+0.12}_{-0.21}$	$^{+0.06}_{-0.31}$
ME generator	$^{+0.40}_{-0.00}$	$^{+0.40}_{-0.00}$
hadronization	$^{+0.51}_{-0.27}$	$^{+0.51}_{-0.26}$
top p_T	$^{+0.24}_{-0.00}$	$^{+0.24}_{-0.00}$
color reconnection	$^{-0.00}_{+0.22}$	$^{-0.00}_{+0.22}$
underlying event	$^{-0.14}_{+0.14}$	$^{-0.14}_{+0.14}$
PDF	$^{+0.20}_{-0.00}$	$^{+0.27}_{-0.00}$
luminosity	< 0.01	< 0.01
stat	$^{+0.39}_{-0.39}$	$^{+0.39}_{-0.39}$
parametrization	$^{-0.07}_{+0.07}$	$^{-0.07}_{+0.07}$
tW(m_t)	$^{+0.10}_{-0.10}$	$^{+0.10}_{-0.10}$
m_t definition	$^{+0.20}_{-0.20}$	$^{+0.20}_{-0.20}$
scale$_{\text{MCFM}}$	$^{+0.01}_{-0.06}$	$^{-0.06}_{+0.04}$
PDF$_{\text{MCFM}}$	$^{-0.01}_{+0.01}$	$^{-0.02}_{+0.03}$
α_S	< 0.01	< 0.01
b-quark mass	< 0.01	< 0.01
total syst.+stat.	$^{+1.10}_{-0.98}$	$^{+1.10}_{-1.00}$

Table 6.4: Breakdown of systematic uncertainties on the top-quark mass values extracted using MCFM. The calculations are performed at LO and NLO for the production of $t\bar{t}$ pairs. The decay is calculated at LO in both cases.

Chapter 7

Calibration of the Top-Quark Monte-Carlo Mass

The precision of the extracted value of m_t^{MC} from the $\mathrm{m}_{\mathrm{lb}}^{\mathrm{min}}$ shape is mostly limited by the uncertainties on the JES, the hadronization modeling, the top p_{T} modeling and Q^2 scale. These variations are strongly constrained when fitted simultaneously with the $\mathrm{t\bar{t}}$ production cross sections, as described in Chapter 5. In consequence, an increased precision can be expected when combining both approaches. For this purpose, the fit technique used to extract $\sigma_{\mathrm{t\bar{t}}}$ is adapted to determine the m_t^{MC} parameter simultaneously. The modifications are described in Section 7.1. Based on the extracted $\sigma_{\mathrm{t\bar{t}}}$, both m_t^{pole} and $m_t^{\overline{\mathrm{MS}}}$ are determined in Section 7.2. The correlations between the extracted m_t^{MC} and $\sigma_{\mathrm{t\bar{t}}}$ can be assessed precisely allowing to compare the measured m_t^{pole} and $m_t^{\overline{\mathrm{MS}}}$ values consistently to m_t^{MC} as described in Section 7.3. Subsequently, m_t^{MC} is calibrated experimentally in terms of a top-quark mass in a theoretically well defined scheme.

7.1 Simultaneous fit of $\sigma_{\mathrm{t\bar{t}}}$ and m_t^{MC}

With the simultaneous fit of the systematic uncertainties and the $\mathrm{t\bar{t}}$ production cross sections at $\sqrt{s} = 7$ and 8 TeV, a precise determination of $\sigma_{\mathrm{t\bar{t}}}$ is possible, as discussed in Chapter 5. The fit, performed in 12 categories of b-tagged and non b-tagged (additional) jets, employs the additional jet p_{T} spectra to constrain modeling and detector uncertainties.

The fit is extended to m_t^{MC} by introducing m_t^{MC} as an additional free nuisance parameter. Three m_t^{MC} hypotheses are chosen to determine the variations of the fit distributions with respect to m_t^{MC}: $m_t^{\mathrm{MC}} = 172.5\,\mathrm{GeV}$ as the nominal value and $m_t^{\mathrm{MC}} = 166.5\,\mathrm{GeV}$ (178.5 GeV) as the lower (upper) variations. The m_t^{MC}-dependence of the contributions from tW processes is fully taken into account. For this purpose, dedicated simulations were produced privately for the aforementioned m_t^{MC} values at $\sqrt{s} = 7\,\mathrm{TeV}$ (details are given in Section 2.5).

The jet-p_{T} spectra used for the fit of $\sigma_{\mathrm{t\bar{t}}}$ have only small sensitivity on m_t^{MC}. The sensitivity of the predicted event yields as a function of $\mathrm{m}_{\mathrm{lb}}^{\mathrm{min}}$ provides significant constraints on m_t^{MC}, but less constraints on jet-related nuisance parameters. Thus, the $\mathrm{m}_{\mathrm{lb}}^{\mathrm{min}}$ shape is employed instead of jet-p_{T} spectra in 4 out of 12 categories with 1 and 2 b jets and 1 or 2 additional jets. In consequence, both m_t^{MC} and $\sigma_{\mathrm{t\bar{t}}}$ can be determined precisely. The resulting distributions for different m_t^{MC} hypotheses are shown in Figures 7.1 (7 TeV) and 7.2 (8 TeV). The sensitivity to m_t^{MC} is most pronounced at high values of $\mathrm{m}_{\mathrm{lb}}^{\mathrm{min}}$. In addition, a slight dependence of the jet-p_{T} spectra on m_t^{MC} can be observed.

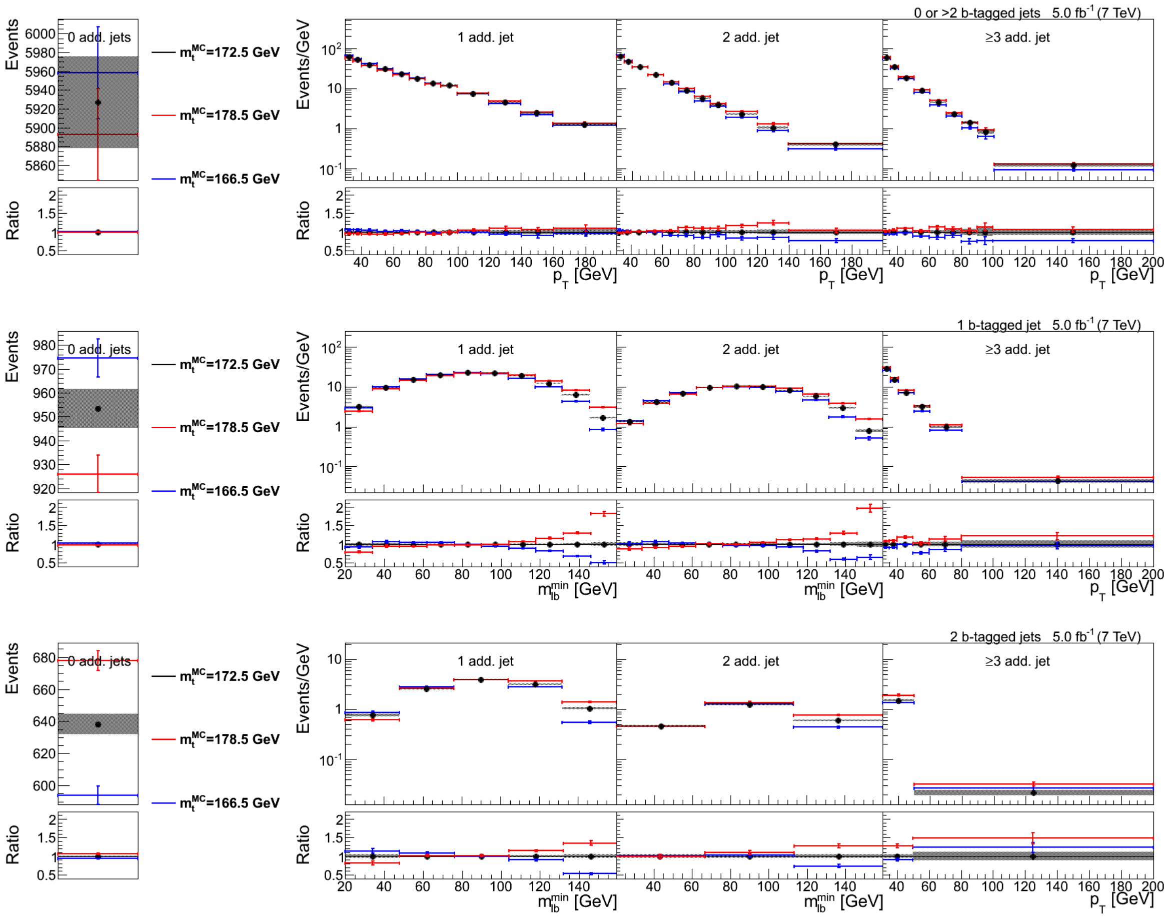

Figure 7.1: Sum of predicted signal and background event yields for 3 values of the top-quark MC mass, m_t^{MC}. Left: total event yield for zero non-b-tagged jets (additional jets). Right: p_{T} of the least energetic additional jet in the event or invariant mass of the lepton-b-jet pair $\mathrm{m}_{\mathrm{lb}}^{\mathrm{min}}$ for events with one, two, and at least three additional jets. Shown are events with zero or more than two (top row), one (middle row), and two (bottom row) b-tagged jets at $\sqrt{s} = 7\,\mathrm{TeV}$. The lower panels depict the ratio of the expected yields to the expectation for m_t^{MC} =172.5 GeV. The statistical uncertainties are indicated by error bars and shaded bands.

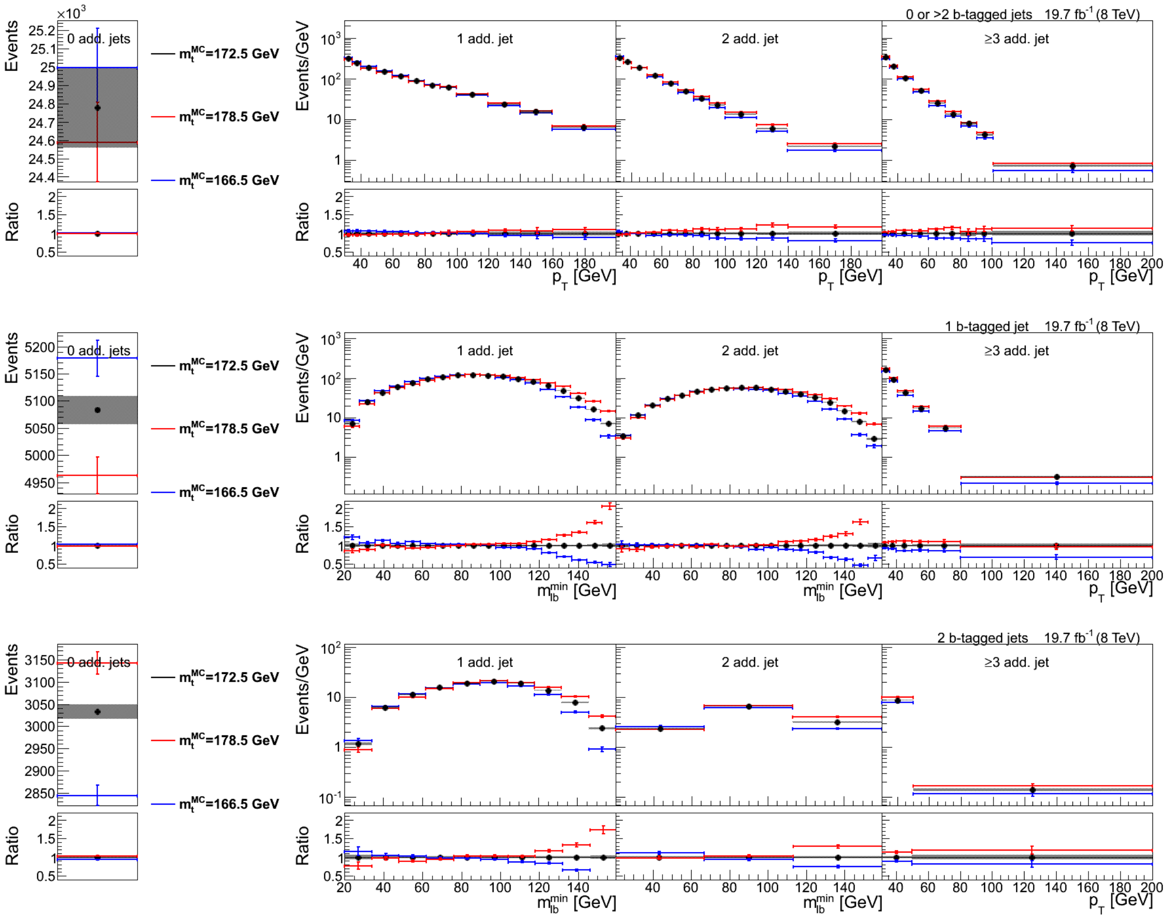

Figure 7.2: Sum of predicted signal and background event yields for 3 values of the top-quark MC mass, m_t^{MC}. Left: total event yield for zero non-b-tagged jets (additional jets). Right: p_{T} of the least energetic additional jet in the event or invariant mass of the lepton-b-jet pair $\mathrm{m}_{\mathrm{lb}}^{\mathrm{min}}$ for events with one, two, and at least three additional jets. Shown are events with zero or more than two (top row), one (middle row), and two (bottom row) b-tagged jets at $\sqrt{s} = 8\,\mathrm{TeV}$. The lower panels depict the ratio of the expected yields to the expectation for m_t^{MC} =172.5 GeV. The statistical uncertainties are indicated by error bars and shaded bands.

The statistical model used in the fit of m_t^{MC} and $\sigma_{\mathrm{t\bar{t}}}$ is validated using 30000 pseudo-experiments. Each is performed, as described in Section 5.7.1, by generating new poisson-distributed event yields in each bin of the fit distributions for data and MC, taking into account the corresponding statistical uncertainties. The resulting pull distributions for $\sigma_{\mathrm{t\bar{t}}}$ and m_t^{MC} are studied. The former are similar to the ones discussed in Section 5.7.1 and indicate a bias-free measurement of $\sigma_{\mathrm{t\bar{t}}}$. The pull distribution for m_t^{MC} can be seen in Figure 7.3. Here, the central value shows no bias, while a slight underestimation of the statistical uncertainty is indicated by a width of 1.09. This underestimation is mainly caused by neglecting the effect of MC statistics in the likelihood function employed in the fit. For m_t^{MC}, the statistical uncertainty of 0.30 GeV in not negligible, in contrast to the statistical uncertainty on $\sigma_{\mathrm{t\bar{t}}}$. Hence, the observed underestimation of 9% is accounted for by increasing the statistical uncertainty on m_t^{MC} by a factor of 1.1 to 0.33 GeV. For this purpose, an additional uncertainty (**MC stat**) of 0.14 GeV is added in quadrature to the total uncertainty on the extracted m_t^{MC} value.

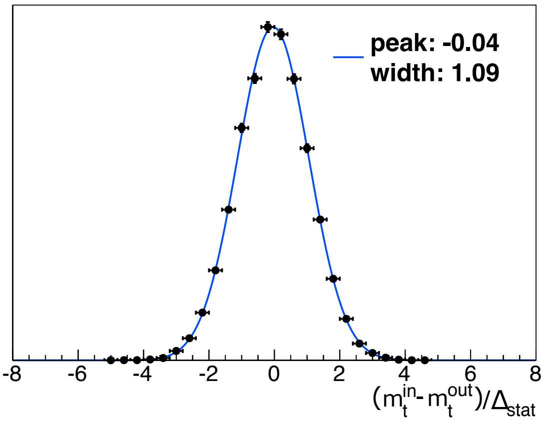

Figure 7.3: Pull distribution for m_t^{MC}. Difference between the m_t^{MC} hypothesis, m_t^{in}, and the extracted value, m_t^{out}, divided by the statistical uncertainty on m_t^{out}, Δ_{stat}.

7.1.1 Simultaneously measured m_t^{MC} and $\sigma_{\mathrm{t\bar{t}}}$

The visible cross section is determined by the simultaneous fit and extrapolated to the full phase space, as described in Section 5.5. The same sources of systematic uncertainties and correlations, described in Section 5.2, are considered. The resulting t$\bar{\mathrm{t}}$ production cross sections in the visible and the full phase space are

$$\begin{aligned}
\sigma_{\mathrm{t\bar{t},vis}}(7\,\mathrm{TeV}) &= 3.01 \pm^{0.11}_{0.10}\ \mathrm{pb} && (7.1)\\
\sigma_{\mathrm{t\bar{t}}}(7\,\mathrm{TeV}) &= 172.5 \pm^{6.2}_{5.9}\ \mathrm{pb} && (7.2)\\
\sigma_{\mathrm{t\bar{t},vis}}(8\,\mathrm{TeV}) &= 4.20 \pm^{0.15}_{0.14}\ \mathrm{pb} && (7.3)\\
\sigma_{\mathrm{t\bar{t}}}(8\,\mathrm{TeV}) &= 243.9 \pm^{9.3}_{8.5}\ \mathrm{pb}. && (7.4)
\end{aligned}$$

The extracted values for $\sigma_{\mathrm{t\bar{t}}}$ and their uncertainties are consistent with the ones determined in Chapter 5. The main advantage is that the measured $\sigma_{\mathrm{t\bar{t}}}$ are independent of the

m_t^{MC} parameter within their uncertainties. Also individual contributions to the total uncertainty remain stable and are summarized in Table 7.1. A detailed list of all parameters and correlations is given in Appendix E.

The sensitivity of the fit to m_t^{MC} is mainly given by the shape of the $\mathrm{m}_{\mathrm{lb}}^{\mathrm{min}}$ distribution. For illustration, this distribution is shown in Figure 7.4 before and after the fit, containing all events after the dilepton selection with at least one b jet. In addition to uncertainties due to all systematic variations, also a variation of the m_t^{MC} parameter of ±6 GeV is indicated. Both are significantly constrained by the fit. The post-fit uncertainties in each bin are calculated as described in Section 5.3.

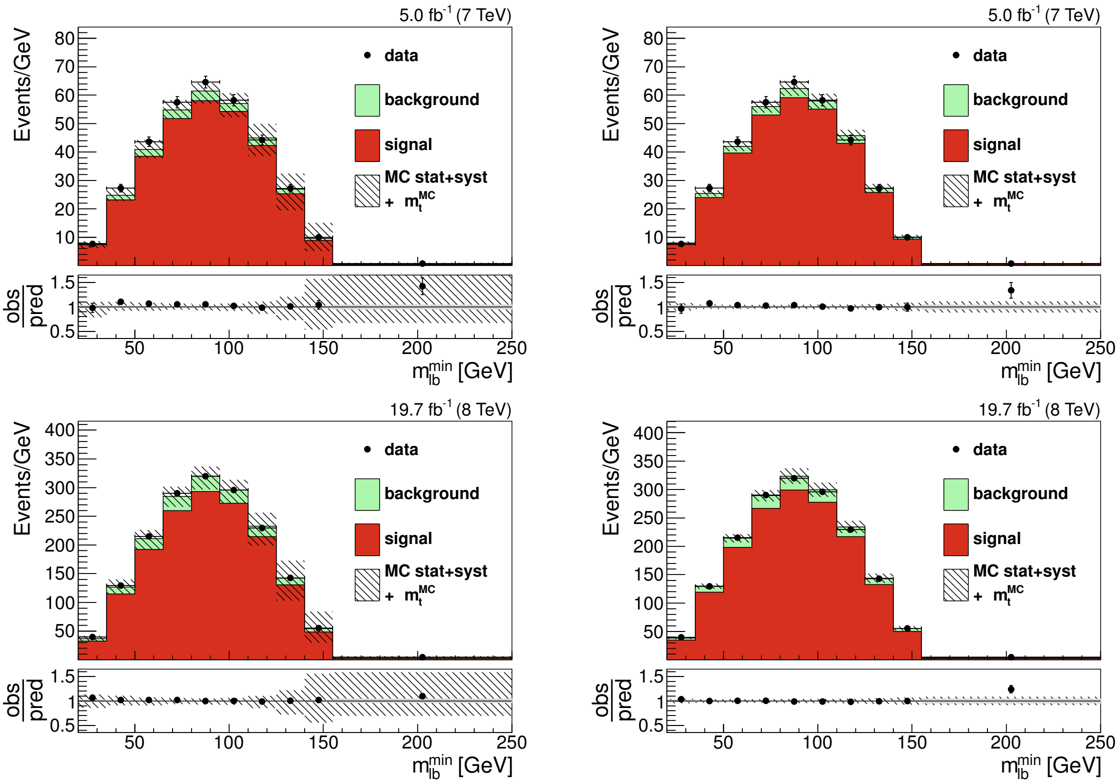

Figure 7.4: Lepton candidate and b jet invariant mass distribution $\mathrm{m}_{\mathrm{lb}}^{\mathrm{min}}$ before the fit (left) and after the fit (right) at $\sqrt{s} = 7\,\mathrm{TeV}$ (top) and $\sqrt{s} = 8\,\mathrm{TeV}$ (bottom). The hatched bands correspond to statistical and systematic uncertainties added in quadrature. In addition, a variation of m_t^{MC} by ±6 GeV is included. The ratios of observed and predicted event yields are shown in the lower panel. Here, the shaded gray band represents the statistical uncertainty on the MC prediction.

Two additional uncertainties on m_t^{MC} are accounted for based on the studies on the $\mathrm{m}_{\mathrm{lb}}^{\mathrm{min}}$ distribution presented in Chapter 6.2: first, the **parametrization** uncertainty on m_t^{MC} of 70 MeV is assigned, estimated by comparing different functional forms for the parameterization of the predicted event yields as a function of m_t^{MC}. Second, the possible bias on the extracted m_t^{MC} due to employing 3 instead of 7 m_t^{MC} hypotheses to derive this parametrization (**number of $\boldsymbol{m_t^{\mathrm{MC}}}$ hypothesis**) has been studied and was found to be below 60 MeV. Even though partially included in the parametrization uncertainty, the full 60 MeV are added in quadrature to the total uncertainty on m_t^{MC}.

For the extracted m_t^{MC}, correlations between $\sqrt{s} = 7$ and 8 TeV with respect to the sources of systematic uncertainties on the JES are crucial. Most of these uncertainties are treated as uncorrelated. In contrast to the extracted $\sigma_{t\bar{t}}$, lower correlations not necessarily result in larger uncertainties. In order to estimate this effect in a conservative way, the fit is repeated, treating all sources of the JES uncertainty as fully correlated between $\sqrt{s} = 7$ and 8 TeV. The difference (**JES correlations**) in the extracted m_t^{MC} is +200 MeV and is added in quadrature to the total uncertainty.

All contributions to the total uncertainty on m_t^{MC} are listed in Table 7.1. A detailed list of all individual parameters is given in Appendix E, where the pulls for each parameter are also listed. For each uncertainty, the absolute value of its pull is below or compatible with 1.

The resulting top-quark MC mass is:

$$m_t^{\mathrm{MC}} = 172.73 \pm^{0.71}_{0.68} \text{ GeV}. \tag{7.5}$$

The measured m_t^{MC} is in agreement with the value determined in Chapter 6, and with the world-average [8]. The relative precision of the extracted m_t^{MC} is 0.41%. Thus, it is the most precise single measurement of m_t^{MC} in the dileptonic decay channel, and has a similar precision as the most recent combination of measurements of m_t^{MC} from the CMS experiment, with a relative uncertainty of 0.38% [185]. In addition, it has the advantage of well-known correlations between the measured cross sections and m_t^{MC}. These correlations are small since the dominant sources of uncertainties that affect $\sigma_{t\bar{t}}$ arise from variations of normalization parameters such as the luminosity and lepton reconstruction efficiencies with a negligible effect on m_t^{MC}. The corresponding correlation coefficients are:

- 0.02 for m_t^{MC} and $\sigma_{t\bar{t}}(7\,\mathrm{TeV})$
- 0.10 for m_t^{MC} and $\sigma_{t\bar{t}}(8\,\mathrm{TeV})$
- 0.29 for $\sigma_{t\bar{t}}(7\,\mathrm{TeV})$ and $\sigma_{t\bar{t}}(8\,\mathrm{TeV})$

For illustration, a likelihood for the measured m_t^{MC} and $\sigma_{t\bar{t}}$ values including their correlations is shown in Figure 7.5. Here, the small correlation between $\sigma_{t\bar{t}}(8\,\mathrm{TeV})$ and m_t^{MC} is indicated by a slight tilt of the ellipse.

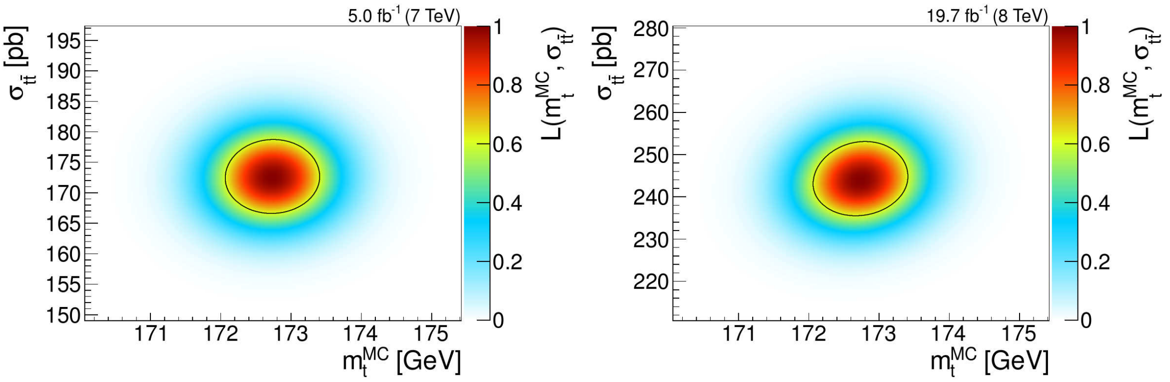

Figure 7.5: Likelihood L for the top-quark MC mass, m_t^{MC}, and the $t\bar{t}$ production cross section, $\sigma_{t\bar{t}}$, measured at $\sqrt{s} = 7\,\mathrm{TeV}$ (left) and $\sqrt{s} = 8\,\mathrm{TeV}$ (right). The contours corresponding to the 1 sigma uncertainty are indicated by the black lines.

Source	Uncertainty on $\sigma_{\mathrm{t\bar{t}}}$ [%]		Uncertainty on m_t^{MC} [GeV]
	7 TeV	8 TeV	
trigger	1.3	1.2	0.01
lepton ID/isolation	1.5	1.5	0.02
lepton energy scale	0.1	0.1	0.11
jet energy scale	0.7	0.6	0.24
jet energy resolution	0.1	0.1	0.06
b-tag	0.5	0.4	0.22
mistag	0.2	0.4	0.05
pileup	0.3	0.2	0.09
tW background	0.8	0.5	0.16
DY background	1.4	1.2	0.05
$t\bar{t}$ background	0.1	0.1	0.02
$t\bar{t}+V$ background	0.1	0.1	0.02
diboson background	0.3	0.7	0.05
QCD/W+jets background	0.1	0.1	0.02
Q^2 scale	0.3	0.3	0.11
ME-PS matching	0.1	0.1	0.03
ME generator	0.4	0.3	0.04
hadronization	0.4	0.7	0.35
top p_T	0.1	0.3	0.26
color reconnection	0.1	0.2	0.05
underlying event	0.1	0.1	0.09
PDF	0.4	0.5	0.10
luminosity	2.2	2.6	0.03
statistics	1.2	0.6	0.30
total uncertainty (visible)	$\pm^{3.6}_{3.4}$	$\pm^{3.6}_{3.4}$	-
Q^2 scale (extrapol.)	$\mp^{0.0}_{0.4}$	$\pm^{0.2}_{0.1}$	-
ME-PS matching (extrapol.)	$\pm^{0.1}_{0.1}$	$\pm^{0.3}_{0.3}$	-
top p_{T} (extrapol.)	$\pm^{0.4}_{0.2}$	$\pm^{0.8}_{0.4}$	-
PDF (extrapol.)	$\pm^{0.1}_{0.2}$	$\pm^{0.1}_{0.2}$	-
MC stat	-	-	0.14
parametrization	-	-	0.07
number of m_t^{MC} hypothesis	-	-	0.06
JES correlations	-	-	+0.20
m_t^{MC} unc. on $\sigma_{\mathrm{t\bar{t}}}$	±0.1	±0.4	-
$\sigma_{\mathrm{t\bar{t}}}$ unc. on m_t^{MC}	-	-	0.07
total uncertainty	$\pm^{3.6}_{3.4}$	$\pm^{3.8}_{3.5}$	$\pm^{0.71}_{0.68}$

Table 7.1: Contributions from individual sources of uncertainties to the total uncertainty on the measured visible, $\sigma_{\mathrm{t\bar{t},vis}}$, and total $\mathrm{t\bar{t}}$ production cross sections, $\sigma_{\mathrm{t\bar{t}}}$, at $\sqrt{s} = 8\,\mathrm{TeV}$ and $\sqrt{s} = 7\,\mathrm{TeV}$ and to the simultaneously fitted top-quark MC mass, m_t^{MC}. The contribution from m_t^{MC} ($\sigma_{\mathrm{t\bar{t}}}$) on the total uncertainty on $\sigma_{\mathrm{t\bar{t}}}$ (m_t^{MC}) is indicated as "m_t^{MC} unc. on $\sigma_{\mathrm{t\bar{t}}}$" ("$\sigma_{\mathrm{t\bar{t}}}$ unc. on m_t^{MC}").

7.2 Determination of m_t^{pole} and $m_t^{\overline{\mathrm{MS}}}$

With m_t^{MC} and $\sigma_{\mathrm{t\bar{t}}}$ extracted simultaneously, m_t^{pole} or $m_t^{\overline{\mathrm{MS}}}$ (generalized as m_t) can be determined directly from the top-quark mass value for which the predicted and measured cross sections coincide. The uncertainties on the extracted values are evaluated using the likelihood $L_{\mathrm{pred}}(\sigma_{\mathrm{t\bar{t}}}, m_t)$ for the predicted dependence of $\sigma_{\mathrm{t\bar{t}}}$ on m_t as introduced in Section 6.1. This likelihood includes uncertainties due to variations of PDF eigenvectors, α_S, and the LHC beam-energy. These are expressed as Gaussian probability distributions, convoluted with a box prior for variations of renormalization and factorization scales. The predicted dependence on $\sigma_{\mathrm{t\bar{t}}}$ on m_t^{pole} is determined with TOP++. The dependence on $m_t^{\overline{\mathrm{MS}}}$ is determined using HATHOR. For the predictions, different PDF sets are employed. The value of $\alpha_S(M_Z)$ is set to 0.118 ± 0.001. For ABM12, α_S is set to the value given by the PDF set. Uncertainties due to variations of CT14 eigenvectors are scaled from 90% to 68% CL.

The measured $\sigma_{\mathrm{t\bar{t}}}$ is expressed in terms of a likelihood function, constant in m_t^{pole} and $m_t^{\overline{\mathrm{MS}}}$. It is constructed from the measured cross section, $\sigma_{\mathrm{t\bar{t}}}^{\mathrm{meas}}$, and its total relative uncertainties yielding higher ($\Delta_{\mathrm{meas},+}$) or lower ($\Delta_{\mathrm{meas},-}$) $\sigma_{\mathrm{t\bar{t}}}$:

$$L_{\mathrm{meas}}(\sigma_{\mathrm{t\bar{t}}}) = exp\left[-0.5 \cdot G_a\left(\sigma_{\mathrm{t\bar{t}}}^{\mathrm{meas}}, \sigma_{\mathrm{t\bar{t}}}, \Delta_{\mathrm{meas},+}, \Delta_{\mathrm{meas},-}\right)\right] \quad \forall \;\; m_t, \tag{7.6}$$

with G_a describing a Gaussian exponent with asymmetric tails as defined in Equation 6.5. The uncertainty on the extracted m_t value is derived from the maximum and minimum m_t value of the contour given by the combined likelihood

$$L_{\mathrm{pred}}(\sigma_{\mathrm{t\bar{t}}}, m_t) \cdot L_{\mathrm{meas}}(\sigma_{\mathrm{t\bar{t}}}) = \exp\left(-0.5\right). \tag{7.7}$$

The extraction of m_t is performed by comparing calculations at different orders of perturbative QCD and different PDF sets.

For the determination of $m_t^{\overline{\mathrm{MS}}}$, calculations at LO, NLO, and NNLO QCD are confronted with the measured $\sigma_{\mathrm{t\bar{t}}}$. For the extraction of m_t^{pole}, predictions with LO+LL, NLO+NLL, and NNLO+NNLL accuracy are used in all cases. The PDF set is fixed to NNPDF3.0, evaluated at NNLO, and $\alpha_S(M_Z)$ is set to 0.118 ± 0.001. The results are illustrated in Figure 7.6.

The use of the running mass $m_t^{\overline{\mathrm{MS}}}$ in the calculation of the $\sigma_{\mathrm{t\bar{t}}}$ improves the convergence of the QCD perturbative series when higher orders are consistently included [186]. Therefore, also the extracted values of m_t exhibit a more rapid convergence in the $\overline{\mathrm{MS}}$ than in the pole mass scheme. This can be interpreted as follows: higher orders beyond NNLO in the calculation of $\sigma_{\mathrm{t\bar{t}}}$ would not change the extracted $m_t^{\overline{\mathrm{MS}}}$ value significantly, while larger corrections to the extracted m_t^{pole} can be expected. These can be estimated by a conversion of the $\overline{\mathrm{MS}}$ mass to the pole mass. The relation between pole and $\overline{\mathrm{MS}}$ mass is known to 4-loop accuracy [66], while the calculation of $\sigma_{\mathrm{t\bar{t}}}$ includes self-energy corrections up to 2 loops. This can result in a large difference between the m_t^{pole} extracted from $\sigma_{\mathrm{t\bar{t}}}$ (obtained by using predictions up to NNLO+NNLL accuracy), and the value of m_t^{pole} obtained from $m_t^{\overline{\mathrm{MS}}}$ by the conversion (that employs corrections up to 4 loops in QCD). The converted value is referred to as $m_t^{\mathrm{p,conv}}$ in the following. The dependence of $m_t^{\mathrm{p,conv}}$ on the accuracy of the conversion was studied up to 3 loops in Ref. [9]. Here, the conversion is performed at 4-loop accuracy.

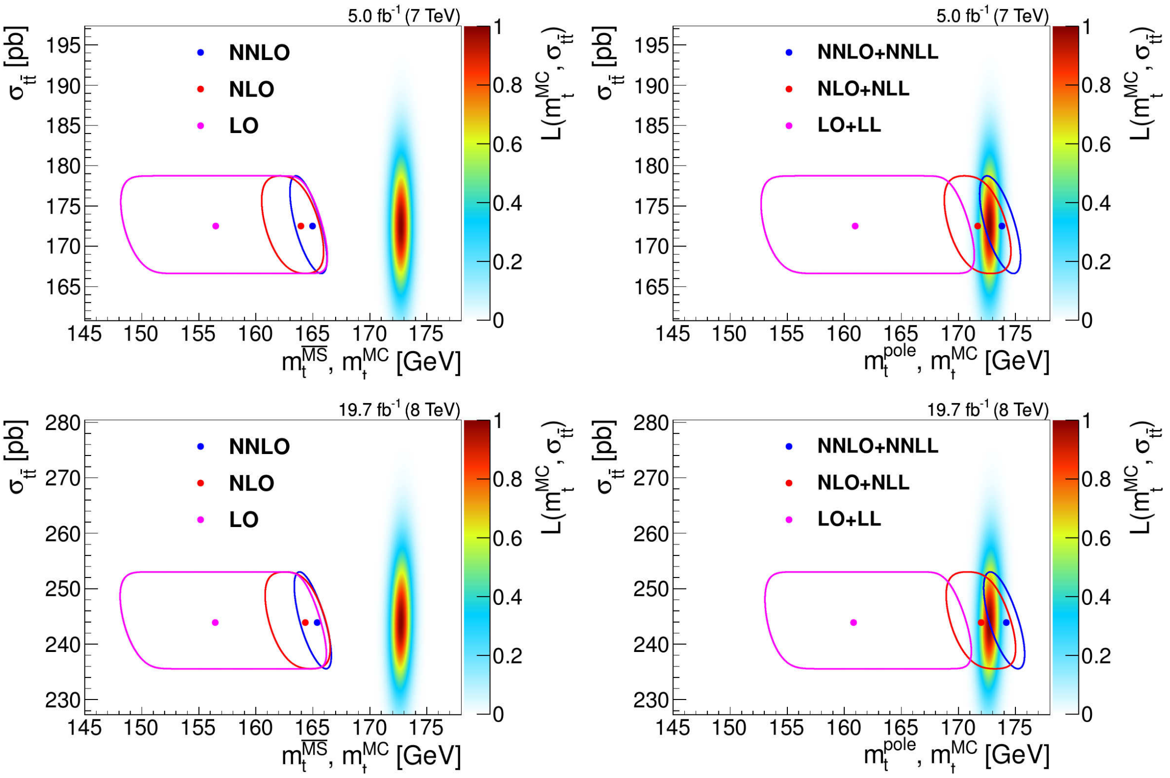

Figure 7.6: Likelihood L representing the top-quark MC mass, m_t^{MC}, and the $\mathrm{t\bar{t}}$ production cross section, $\sigma_{\mathrm{t\bar{t}}}$, measured at $\sqrt{s} = 7\,\mathrm{TeV}$ (top) and $\sqrt{s} = 8\,\mathrm{TeV}$ (bottom) compared to the extracted values for the top-quark $\overline{\mathrm{MS}}$ mass, $m_t^{\overline{\mathrm{MS}}}$, (left) and the top-quark pole mass, m_t^{pole}, (right) employing calculations at different orders of perturbative QCD and using the PDF set NNPDF3.0 at NNLO QCD. The extracted values are indicated by colored symbols and their uncertainties by colored lines.

The conversion is performed in an iterative procedure: it starts with a hypothesis for $m_t^{\mathrm{p,conv}}$. The hypothesis is used to obtain $\alpha_S^{(6)}(m_t^{\overline{\mathrm{MS}}})$ for 6 active flavors from $\alpha_S^{(5)}(M_Z)$ with 5 active flavors[1]. The decoupling scale is chosen to be $2 \cdot m_t^{\mathrm{p,conv}}$. Using $\alpha_S^{(6)}(m_t^{\overline{\mathrm{MS}}})$, $m_t^{\overline{\mathrm{MS}}}$ is converted to $m_t^{\mathrm{p,conv}}$ with 4-loop accuracy. The procedure is repeated until $m_t^{\mathrm{p,conv}}$ is stable within 10 MeV. The necessary calculations are performed with the program CRunDec [187, 188]. The program includes the conversion for α_S to 4 loops [189, 190] and from $m_t^{\overline{\mathrm{MS}}}$ to m_t^{pole} up to 3 loops [191–201]. The additional 4-loop correction is implemented and validated by numerical comparison with Ref. [66]. The conversion also depends on α_S. Thus, correlations between the uncertainty due to variations of $\alpha_S(M_Z)$ on the extracted $m_t^{\overline{\mathrm{MS}}}$, Δ_{α_S}, and on the conversion, $\Delta_{\alpha_S,\mathrm{conv}}$, need to be taken into account. For this purpose, Δ_{α_S} is determined by removing the corresponding uncertainty from the prediction of $\sigma_{\mathrm{t\bar{t}}}$. The extraction of $m_t^{\overline{\mathrm{MS}}}$ is repeated. The resulting reduction of the total uncertainty in quadrature corresponds to Δ_{α_S}. Using all PDF sets considered, the maximum value of Δ_{α_S} is found to be 0.43%. Variations of $\alpha_S^{(5)}(M_Z) = 0.118 \pm 0.001$ in the conversion result in $\Delta_{\alpha_S,\mathrm{conv}}$ below 0.06%. The combined correlated uncertainty is given as $\Delta_{\alpha_S} + \Delta_{\alpha_S,\mathrm{conv}}$. It is used to derive an expression, $\Delta_{\alpha_S,\mathrm{corr}}$, setting an upper limit on the additional uncertainty due to these correlations:

$$\Delta_{\alpha_S,\mathrm{corr}} > \sqrt{(\Delta_{\alpha_S} + \Delta_{\alpha_S,\mathrm{conv}})^2 - (\Delta_{\alpha_S})^2}, \tag{7.8}$$

where $\Delta_{\alpha_S,\mathrm{corr}}$, set to 0.25%, is added in quadrature to the total uncertainty of each $m_t^{\mathrm{p,conv}}$.

The results for the directly extracted m_t^{pole} and $m_t^{\overline{\mathrm{MS}}}$ at $\sqrt{s} = 7$ and 8 TeV are combined using the weighted mean technique described in Section 6.1.2, splitting the total uncertainty into fully correlated and fully uncorrelated contributions. The same technique is employed for all combinations in this chapter. Furthermore, the combined $m_t^{\overline{\mathrm{MS}}}$ are converted to the pole mass $m_t^{\mathrm{p,conv}}$. The numerical values are listed in Table 7.2.

	m_t^{pole} [GeV]	$m_t^{\overline{\mathrm{MS}}}$ [GeV]	$m_t^{\mathrm{p,conv}}$ [GeV]
LO(+LL)	$160.9\pm^{10.3}_{8.0}$	$156.5\pm^{9.7}_{8.3}$	$166.0\pm^{10.3}_{8.8}$
NLO(+NLL)	$171.9\pm^{3.0}_{3.0}$	$164.2\pm^{2.1}_{3.4}$	$174.0\pm^{2.3}_{3.6}$
NNLO(+NNLL)	$174.0\pm^{1.4}_{1.7}$	$165.2\pm^{1.1}_{1.7}$	$175.1\pm^{1.3}_{1.9}$

Table 7.2: First two columns: combined results from $\sqrt{s} = 7$ and 8 TeV for the directly measured top-quark pole mass, m_t^{pole}, and $\overline{\mathrm{MS}}$ mass, $m_t^{\overline{\mathrm{MS}}}$, at different orders of perturbative QCD, extracted by confronting the measured $\mathrm{t\bar{t}}$ production cross section with the prediction using the NNPDF3.0 PDF set. For the extraction of the pole mass LL, NLL, and NNLL resummation is employed. Last column: top-quark pole mass, $m_t^{\mathrm{p,conv}}$, converted from the measured $m_t^{\overline{\mathrm{MS}}}$ using QCD calculations at 4-loop accuracy.

The converted $m_t^{\mathrm{p,conv}}$ is consistently higher than m_t^{pole} and shows a better convergence when higher order in the perturbative series are accounted for in the calculation of $\sigma_{\mathrm{t\bar{t}}}$. At NNLO, the difference is about 1 GeV, however still sizable. The difference between $m_t^{\overline{\mathrm{MS}}}$ and m_t^{pole} at LO is caused only by the resummation of LL, since LO calculations cannot fix the mass scheme.

---

[1] At scales of $\mathcal{O}(2m_t^{\mathrm{pole}})$, the running of α_S receives contributions from all 6 quark flavors. At scales well below, only quarks with mass below the scale contribute.

In the following the $m_t^{\overline{\mathrm{MS}}}$ (m_t^{pole}) are determined by comparison of the measured and the predicted $\sigma_{\mathrm{t\bar{t}}}$ calculated at NNLO (+NNLL) using different PDF sets. The results for $\sqrt{s} = 7\,\mathrm{TeV}$ and $\sqrt{s} = 8\,\mathrm{TeV}$ are listed in Table 7.3. For each PDF set, the extracted values at $\sqrt{s} = 7\,\mathrm{TeV}$ and $\sqrt{s} = 8\,\mathrm{TeV}$ are consistent.

	m_t^{pole} [GeV]		$m_t^{\overline{\mathrm{MS}}}$ [GeV]	
	7 TeV	8 TeV	7 TeV	8 TeV
ABM12	$166.2\pm^{1.8}_{2.0}$	$167.1\pm^{1.7}_{2.1}$	$158.0\pm^{1.4}_{2.1}$	$158.9\pm^{1.4}_{2.1}$
NNPDF3.0	$173.8\pm^{1.6}_{2.0}$	$174.2\pm^{1.6}_{2.0}$	$165.0\pm^{1.3}_{2.0}$	$165.4\pm^{1.2}_{2.0}$
MMHT2014	$174.1\pm^{1.7}_{2.1}$	$174.4\pm^{1.7}_{2.1}$	$165.3\pm^{1.3}_{2.2}$	$165.6\pm^{1.2}_{2.2}$
CT14	$174.2\pm^{2.1}_{2.2}$	$174.5\pm^{2.0}_{2.2}$	$165.4\pm^{1.8}_{2.2}$	$165.7\pm^{1.7}_{2.2}$

Table 7.3: Top-quark pole mass, m_t^{pole}, at NNLO+NNLL and the $\overline{\mathrm{MS}}$ mass, $m_t^{\overline{\mathrm{MS}}}$, at NNLO, extracted by confronting the measured $\mathrm{t\bar{t}}$ production cross section at $\sqrt{s} = 7\,\mathrm{TeV}$ and $\sqrt{s} = 8\,\mathrm{TeV}$ with predictions employing different PDF sets.

The values of m_t^{pole} and $m_t^{\overline{\mathrm{MS}}}$ obtained at $\sqrt{s} = 7$ and $8\,\mathrm{TeV}$ are combined and $m_t^{\overline{\mathrm{MS}}}$ is used to calculate $m_t^{\mathrm{p,conv}}$. The results are listed in Table 7.4.

	m_t^{pole} [GeV]	$m_t^{\overline{\mathrm{MS}}}$ [GeV]	$m_t^{\mathrm{p,conv}}$ [GeV]
ABM12	$166.6\pm^{1.6}_{1.9}$	$158.4\pm^{1.2}_{1.9}$	$168.0\pm^{1.3}_{2.1}$
NNPDF3.0	$174.0\pm^{1.4}_{1.7}$	$165.2\pm^{1.1}_{1.7}$	$175.1\pm^{1.2}_{1.9}$
MMHT2014	$174.3\pm^{1.4}_{1.8}$	$165.4\pm^{1.1}_{1.9}$	$175.3\pm^{1.3}_{2.1}$
CT14	$174.4\pm^{1.8}_{2.0}$	$165.5\pm^{1.5}_{2.0}$	$175.4\pm^{1.7}_{2.2}$

Table 7.4: First two columns: combined results from $\sqrt{s} = 7\,\mathrm{TeV}$ and $\sqrt{s} = 8\,\mathrm{TeV}$ for the top-quark pole mass, m_t^{pole}, at NNLO+NNLL and the $\overline{\mathrm{MS}}$ mass, $m_t^{\overline{\mathrm{MS}}}$, at NNLO, extracted by confronting the measured $\mathrm{t\bar{t}}$ production cross section at $\sqrt{s} = 7$ and $8\,\mathrm{TeV}$ with predictions employing different PDF sets. Last column: top-quark pole mass converted from the measured $m_t^{\overline{\mathrm{MS}}}$ using QCD calculations at 4-loop accuracy.

The measured m_t^{pole} and $m_t^{\overline{\mathrm{MS}}}$ agree well for different PDF sets with the exception of ABM12. This set provides a lower gluon density and α_S in comparison to other PDF sets. Therefore, the predicted $\sigma_{\mathrm{t\bar{t}}}$ is smaller, yielding smaller values for m_t^{pole} and $m_t^{\overline{\mathrm{MS}}}$. The total uncertainty on the extracted m_t^{pole} ranges from 0.8% to 1.1%, decreased with respect to the results presented in Section 6.1.1, since no assumptions on the m_t^{MC} dependence of the extracted $\sigma_{\mathrm{t\bar{t}}}$ need to be made. The achieved precision supersedes all published m_t^{pole} measurements [12, 75]. The measured $m_t^{\overline{\mathrm{MS}}}$ benefits from the steeper dependence of $\sigma_{\mathrm{t\bar{t}}}$ on $m_t^{\overline{\mathrm{MS}}}$ leading to total uncertainties between $\pm^{0.7}_{1.0}\%$ and $\pm^{0.9}_{1.2}\%$. The results presented here represent the most precise determination of $m_t^{\overline{\mathrm{MS}}}$, with a significant better precision compared to a previous direct measurement of $m_t^{\overline{\mathrm{MS}}}$ with a precision of 3.1% [13]. The values of $m_t^{\mathrm{p,conv}}$ calculated at 4-loop accuracy from $m_t^{\overline{\mathrm{MS}}}$ are about $1\,\mathrm{GeV}$ higher than the directly measured m_t^{pole} at NNLO+NNLL, consistently for all PDF sets.

7.3 Calibration of m_t^{MC}

The extracted values for $m_t^{\overline{\mathrm{MS}}}$ and m_t^{pole}, and the calculated $m_t^{\mathrm{p,conv}}$ are compared to the simultaneously measured m_t^{MC}. The latter is calibrated to the theoretically well-defined top-quark mass definitions $m_t^{\overline{\mathrm{MS}}}$, m_t^{pole}, and $m_t^{\mathrm{p,conv}}$ (all referred to as m_t in the following). For this purpose, correlations between the m_t values at $\sqrt{s} = 7$ and 8 TeV have to be taken into account as well as correlations between the extracted m_t^{MC} and $\sigma_{\mathrm{t\bar{t}}}$. An upper limit on the correlation coefficient between $\sigma_{\mathrm{t\bar{t}}}$ and m_t^{MC}, $\rho(\sigma_{\mathrm{t\bar{t}}}, m_t^{\mathrm{MC}})$, is estimated from the correlation coefficient $\rho(\sigma_{\mathrm{t\bar{t}},\mathrm{vis}}, m_t^{\mathrm{MC}})$ given by the fit. The extrapolation uncertainties on $\sigma_{\mathrm{t\bar{t}}}$ and the additional uncertainties on m_t^{MC} (see lower part of Table 7.1) are treated as uncorrelated. In consequence, the coefficient $\rho(\sigma_{\mathrm{t\bar{t}},\mathrm{vis}}, m_t^{\mathrm{MC}})$ can be used as an upper limit for $\rho(\sigma_{\mathrm{t\bar{t}}}, m_t^{\mathrm{MC}})$.

The value of $\rho(\sigma_{\mathrm{t\bar{t}},\mathrm{vis}}, m_t^{\mathrm{MC}})$ is different for $\sigma_{\mathrm{t\bar{t}}}(8\,\mathrm{TeV})$ and $\sigma_{\mathrm{t\bar{t}}}(7\,\mathrm{TeV})$. Thus, the difference between m_t and m_t^{MC} is determined in a first step through comparison of the corresponding central values independently at $\sqrt{s} = 7$ and 8 TeV. For the calculation of the uncertainties, the total uncertainty on the extracted m_t is split into two contributions: an uncertainty due to the predicted $\sigma_{\mathrm{t\bar{t}}}$, Δ_{pred}, and an uncertainty due to the measured $\sigma_{\mathrm{t\bar{t}}}$, Δ_{meas}. Each contribution is determined by extracting m_t with the other one set to zero. The total uncertainty on the difference $m_t - m_t^{\mathrm{MC}}$, Δ_{calib}, is calculated with error propagation:

$$\Delta^2_{\mathrm{calib}} = \Delta^2_{\mathrm{pred}} + \Delta^2_{\mathrm{meas}} + \Delta^2_{m_t^{\mathrm{MC}}} + 2\rho(\sigma_{\mathrm{t\bar{t}},\mathrm{vis}}, m_t^{\mathrm{MC}}) \cdot \Delta_{\mathrm{meas}} \cdot \Delta_{m_t^{\mathrm{MC}}}, \tag{7.9}$$

with $\Delta_{m_t^{\mathrm{MC}}}$ being the uncertainty on the measured m_t^{MC} value. Asymmetric uncertainties are evaluated taking into account that an increase of the measured $\sigma_{\mathrm{t\bar{t}}}$ results in a decreasing m_t.

The extracted differences between m_t and m_t^{MC} at $\sqrt{s} = 7$ and 8 TeV are combined in a second step. The resulting calibrations for the m_t^{MC} parameter, evaluated using different PDF sets, are listed in Table 7.5 and represent the first fully consistent precise measurements of the difference between m_t and m_t^{MC}. At NNLO(+NNLL) all PDF sets, with the exception of ABM12, yield compatible calibration results and agree well with an estimated difference between m_t^{pole} and m_t^{MC} of the order of 1 GeV [10] or below [73]. However, this difference increases to more than 2 GeV when higher orders are accounted for in $m_t^{\mathrm{p,conv}}$, while the absolute difference decreases for the ABM12 PDF set.

	$m_t^{\mathrm{pole}} - m_t^{\mathrm{MC}}$ [GeV]	$m_t^{\overline{\mathrm{MS}}} - m_t^{\mathrm{MC}}$ [GeV]	$m_t^{\mathrm{p,conv}} - m_t^{\mathrm{MC}}$ [GeV]
ABM12	$-6.1\pm^{1.7}_{2.0}$	$-14.3\pm^{1.4}_{2.0}$	$-4.7\pm^{1.5}_{2.2}$
NNPDF3.0	$1.3\pm^{1.6}_{1.9}$	$-7.6\pm^{1.3}_{1.9}$	$2.4\pm^{1.5}_{2.0}$
MMHT2014	$1.5\pm^{1.6}_{2.0}$	$-7.3\pm^{1.3}_{2.1}$	$2.6\pm^{1.5}_{2.2}$
CT14	$1.6\pm^{1.9}_{2.1}$	$-7.2\pm^{1.7}_{2.1}$	$2.7\pm^{1.8}_{2.3}$

Table 7.5: Difference between the measured top-quark MC mass, m_t^{MC}, and the top-quark pole mass, m_t^{pole}, at NNLO+NNLL (left column), between m_t^{MC} and the $\overline{\mathrm{MS}}$ mass, $m_t^{\overline{\mathrm{MS}}}$, at NNLO (middle column) as well as between the top-quark pole mass converted from the $\overline{\mathrm{MS}}$ mass, $m_t^{\mathrm{p,conv}}$, and m_t^{MC} (right column) for different PDF sets.

Chapter 8

Summary and Conclusions

The work presented in this thesis focuses on precision measurements of the $\mathrm{t\bar{t}}$ production cross section and detailed studies on the top quark mass, both as the parameter implemented in MC simulation and in theoretically well-defined schemes, and the experimental relation of these mass parameters. The measurements are performed in the dilepton $\mathrm{t\bar{t}}$ decay channel. The full set of pp collision data collected during 2011 and 2012 by the CMS experiment at a center-of-mass energy of $\sqrt{s} = 7$ and 8 TeV is analyzed, which amounts to an integrated luminosity of $5\,\mathrm{fb}^{-1}$ and $20\,\mathrm{fb}^{-1}$, respectively.

Compared to previous precision measurements of the $\mathrm{t\bar{t}}$ production cross sections [12, 15, 16], the analyses presented here bring the following improvements: the full data sample recorded by the CMS experiment in the years 2011-2012 is analyzed and, more relevant, an improved cross section extraction method has been developed. The cross sections are extracted in a simultaneous binned likelihood fit, which employs a combination of a template fit of multi-differential distributions and a parameterization of the $\mathrm{t\bar{t}}$ signal component based on the expected event topology. The fit is performed simultaneously at $\sqrt{s} = 7$ and 8 TeV, with emphasis on a consistent treatment of correlations between systematic uncertainties. The cross sections are measured in the visible phase space, defined by requirements on the transverse momentum and the pseudorapidity of the charged leptons from the $\mathrm{t\bar{t}}$ decay in the final state. In addition, the visible cross sections are extrapolated to the full phase space yielding:

$$\sigma_{\mathrm{t\bar{t}}}(7\,\mathrm{TeV}) = 174.4\ \pm^{6.3}_{5.9}\ \mathrm{pb\ and} \tag{8.1}$$

$$\sigma_{\mathrm{t\bar{t}}}(8\,\mathrm{TeV}) = 245.7\ \pm^{9.3}_{8.6}\ \mathrm{pb}, \tag{8.2}$$

assuming a top-quark MC mass of 172.5 GeV. The total $\mathrm{t\bar{t}}$ production cross sections are consistent with SM predictions calculated at NNLO+NNLL. With total uncertainties of 3.6% (7 TeV) and 3.8% (8 TeV), the results of this thesis constitute the most precise measurements of $\sigma_{\mathrm{t\bar{t}}}$ performed with the CMS detector so far, and are competitive with recent results published by the ATLAS Collaboration.

These precise results are used to determine the top-quark pole mass, by comparing them to their predicted values at NNLO+NNLL QCD, using a joint-likelihood approach and several state-of-the-art PDF sets. The top-quark pole mass at NNLO+NNLL is measured to be

$$m_t^{\mathrm{pole}} = 173.6\ \pm^{1.7}_{1.8}\ \mathrm{GeV}, \tag{8.3}$$

using the NNPDF3.0 PDF set. This result improves the precision of previous measurements by the LHC and Tevatron experiments with uncertainties between 2.2 GeV [75] and 5 GeV [13]. Both the $\mathrm{t\bar{t}}$ production cross sections and the top-quark pole mass determined in this thesis, are published in Ref. [202] and being documented in a journal publication of the CMS Collaboration.

Moreover, the top-quark MC mass, m_t^{MC}, is measured from the shape of the invariant mass distribution $\mathrm{m}_{\mathrm{lb}}^{\mathrm{min}}$ of the final-state lepton (electron or muon) candidates and the b jet at $\sqrt{s} = 8\,\mathrm{TeV}$. The method employs a bin-wise estimator for the compatibility of the prediction for a certain m_t^{MC} and the data. The resulting value of

$$m_t^{\mathrm{MC}} = 172.8\ ^{+1.3}_{-1.0}\,\mathrm{GeV} \tag{8.4}$$

is consistent with the world-average and is the most precise measurement of this parameter in the dilepton channel.

An innovative folding technique is introduced to determine the top-quark mass from fixed-order calculations. The observable $\mathrm{m}_{\mathrm{lb,pred}}^{\mathrm{min}}$ is defined analogue to $\mathrm{m}_{\mathrm{lb}}^{\mathrm{min}}$ based on the generated leptons and b quarks. A matrix describing the detector response to relate $\mathrm{m}_{\mathrm{lb}}^{\mathrm{min}}$ to $\mathrm{m}_{\mathrm{lb,pred}}^{\mathrm{min}}$ is derived from simulation. It is applied to the predicted differential $\mathrm{t\bar{t}}$ production cross-section as a function of $\mathrm{m}_{\mathrm{lb,pred}}^{\mathrm{min}}$. The calculations are performed at NLO and LO for the production of $\mathrm{t\bar{t}}$ pairs with MCFM. Their decay is predicted with LO accuracy. The predictions are folded and the resulting distributions are compared to the shape of the measured $\mathrm{m}_{\mathrm{lb}}^{\mathrm{min}}$ distribution. The top-quark mass is extracted at LO (m_t^{LO}) or NLO (m_t^{NLO}) accuracy as

$$m_t^{\mathrm{LO}} = 171.8^{+1.1}_{-1.0}\,\mathrm{GeV} \tag{8.5}$$

$$m_t^{\mathrm{NLO}} = 171.5^{+1.1}_{-1.0}\,\mathrm{GeV}. \tag{8.6}$$

These results as well as the extraction of m_t^{MC} from the $\mathrm{m}_{\mathrm{lb}}^{\mathrm{min}}$ distribution are published in Ref. [203].

Finally, the analyses presented above are combined: the $\mathrm{m}_{\mathrm{lb}}^{\mathrm{min}}$ distribution is included in the cross section fit to determine the top-quark MC mass and the $\mathrm{t\bar{t}}$ production cross sections at $\sqrt{s} = 7$ and $8\,\mathrm{TeV}$ simultaneously. The relative uncertainties on $\sigma_{\mathrm{t\bar{t}}}$ remain unchanged due to this procedure and the total $\mathrm{t\bar{t}}$ production cross sections yield:

$$\sigma_{\mathrm{t\bar{t}}}(7\,\mathrm{TeV}) = 172.5\pm^{6.2}_{5.9}\ \mathrm{pb\ and} \tag{8.7}$$

$$\sigma_{\mathrm{t\bar{t}}}(8\,\mathrm{TeV}) = 243.9\pm^{9.3}_{8.5}\ \mathrm{pb}. \tag{8.8}$$

These results are the first measurements of $\sigma_{\mathrm{t\bar{t}}}$ independent of assumptions on the value of the top-quark mass. The simultaneously determined top-quark MC mass is:

$$m_t^{\mathrm{MC}} = 172.73\pm^{0.71}_{0.68}\ \mathrm{GeV}, \tag{8.9}$$

representing the most precise single measurement of this parameter in dileptonic $\mathrm{t\bar{t}}$ events, with the further advantage of well-known correlations to the measured cross sections. The extracted $\sigma_{\mathrm{t\bar{t}}}$ are used to determine the top quark pole and $\overline{\mathrm{MS}}$ mass through comparison with predictions using different PDF sets. The resulting values represent the most precise results for m_t^{pole} at NNLO+NNLL and $m_t^{\overline{\mathrm{MS}}}$ at NNLO with

$$m_t^{\mathrm{pole}} = 174.0\pm^{1.4}_{1.7}\ \mathrm{GeV\ and} \tag{8.10}$$

$$m_t^{\overline{\mathrm{MS}}} = 165.2\pm^{1.1}_{1.7}\ \mathrm{GeV}, \tag{8.11}$$

using the NNPDF3.0 PDF set. Their behavior with respect to different orders of perturbative QCD employed in the prediction of $\sigma_{\mathrm{t\bar{t}}}$ is studied. The measured values of m_t

exhibit a better convergence in the $\overline{\mathrm{MS}}$ than in the pole mass scheme. The extracted $m_t^{\overline{\mathrm{MS}}}$ is converted to the pole mass, $m_t^{\mathrm{p,conv}}$, using their relation at 4-loop QCD and compared to m_t^{pole}. For all PDF sets, $m_t^{\mathrm{p,conv}}$ is about 1 GeV higher than m_t^{pole}.

The m_t^{MC} parameter is calibrated consistently to the top-quark pole or $\overline{\mathrm{MS}}$ mass for different PDF sets, yielding

$$\begin{aligned} m_t^{\mathrm{pole}} - m_t^{\mathrm{MC}} &= 1.3 \pm^{1.6}_{1.9} \text{ GeV,} && (8.12)\\ m_t^{\mathrm{p,conv}} - m_t^{\mathrm{MC}} &= 2.4 \pm^{1.5}_{2.0} \text{ GeV, and} && (8.13)\\ m_t^{\overline{\mathrm{MS}}} - m_t^{\mathrm{MC}} &= -7.6 \pm^{1.3}_{1.9} \text{ GeV} && (8.14) \end{aligned}$$

for the NNPDF3.0 PDF set. This calibration is the first consistent measurement of the relation between the top-quark MC mass and mass parameters in theoretically well-defined schemes. The measured relation between m_t^{MC} and m_t^{pole} is consistent with theoretical estimates. A slight trend towards larger differences is observed for $m_t^{\mathrm{p,conv}}$, although it is not significant taking into account the uncertainties. For the ABM12 PDF set, the difference between $m_t^{\mathrm{p,conv}}$ and m_t^{MC} is

$$m_t^{\mathrm{p,conv}} - m_t^{\mathrm{MC}} = -4.7 \pm^{1.5}_{2.2} \text{ GeV} \qquad (8.15)$$

and smaller in absolute value than between m_t^{pole} and m_t^{MC}.

The precision of all measurements presented here are either limited by systematic uncertainties ($\sigma_{\mathrm{t\bar{t}}}$, m_t^{MC}) on the measurement or by uncertainties on the predicted cross sections (m_t^{pole}, $m_t^{\overline{\mathrm{MS}}}$). Even though the statistical uncertainty on the measurements is not dominant, an increasing production rate for $\mathrm{t\bar{t}}$ pairs at higher center-of-mass energies during LHC Run 2 could lead to a further reduction of uncertainties. The cross section for $\mathrm{t\bar{t}}$ production increases faster with the center-of-mass energy than the production rate of the dominant background processes [161]. Therefore, the purity of the selected data sample will be superior to the candidate events used here, assuming similar event selection requirements. The LHC experiments have started to collect data from pp collisions at $\sqrt{s} = 13\,\mathrm{TeV}$ and first measurements of the $\mathrm{t\bar{t}}$ production cross section at $\sqrt{s} = 13\,\mathrm{TeV}$ have been performed [161, 204]. These are still limited by large statistical and systematic uncertainties. Within these uncertainties, no deviations from the SM can be observed. However, with increasing luminosity, not only the statistical uncertainties will decrease, also the constraints on systematic uncertainties from the data will become stronger, either in simultaneous fits or dedicated determinations of data-driven corrections. As an additional aspect, the precision of the predicted $\mathrm{t\bar{t}}$ production cross section increases with the center-of-mass energy [14]. In particular, the contribution from the PDF uncertainty is reduced since the average momentum fraction needed to produce a $\mathrm{t\bar{t}}$ pair decreases to values where the PDFs are better known. Therefore, an improved precision can be achieved in the extraction of the top-quark mass from measurements of $\sigma_{\mathrm{t\bar{t}}}$ at $\sqrt{s} = 13\,\mathrm{TeV}$ or higher. Moreover, deviations of the measured $\mathrm{t\bar{t}}$ production cross sections from their predictions provide sensitivity to physics beyond the SM, and were already sucessfully used to set limits on several models [12, 202], complementing direct searches for new physics.

In the longer term, a very precise determination of a top-quark mass in a well-defined scheme could be achieved at a future linear e^+e^- collider. The mass could be determined together with the strong coupling in a threshold scan at center-of-mass energies around $2 \cdot m_t^{\mathrm{pole}}$. The expected uncertainty of this measurement is about 100 MeV [77], making an extraction of $m_t^{\overline{\mathrm{MS}}}$ preferable.

Bibliography

[1] ATLAS Collaboration, "Observation of a new particle in the search for the Standard Model Higgs boson with the ATLAS detector at the LHC," *Phys. Lett. B*, vol. 716, pp. 1–29, 2012.

[2] CMS Collaboration, "Observation of a new boson at a mass of 125 GeV with the CMS experiment at the LHC," *Phys. Lett. B*, vol. 716, pp. 30–61, 2012.

[3] CDF Collaboration, "Observation of top quark production in $\overline{p}p$ collisions with the collider detector at fermilab," *Phys. Rev. Lett.*, vol. 74, pp. 2626–2631, Apr 1995.

[4] D0 Collaboration, "Observation of the top quark," *Phys. Rev. Lett.*, vol. 74, pp. 2632–2637, Apr 1995.

[5] A. B. Galtieri, F. Margaroli, and I. Volobouev, "Precision measurements of the top quark mass from the Tevatron in the pre-LHC era," *Rept. Prog. Phys.*, vol. 75, p. 056201, 2012.

[6] S. Alekhin, A. Djouadi, and S. Moch, "The top quark and Higgs boson masses and the stability of the electroweak vacuum," *Phys. Lett. B*, vol. 716, pp. 214–219, 2012.

[7] G. Degrassi, S. Di Vita, J. Elias-Miro, J. R. Espinosa, G. F. Giudice, *et al.*, "Higgs mass and vacuum stability in the Standard Model at NNLO," *JHEP*, vol. 1208, p. 098, 2012.

[8] ATLAS, CDF, CMS, D0, "First combination of Tevatron and LHC measurements of the top-quark mass," *arXiv:1403.4427*, 2014.

[9] S. Moch, S. Weinzierl, S. Alekhin, J. Blumlein, L. de la Cruz, *et al.*, "High precision fundamental constants at the TeV scale," *arXiv:1405.4781*, 2014.

[10] A. Buckley, J. Butterworth, S. Gieseke, D. Grellscheid, S. Hoche, *et al.*, "General-purpose event generators for LHC physics," *Phys. Rept.*, vol. 504, pp. 145–233, 2011.

[11] CMS Collaboration, "Determination of the top-quark pole mass and strong coupling constant from the $t\bar{t}$ production cross section in pp collisions at $\sqrt{s} = 7$ TeV," *Phys. Lett. B*, vol. 728, pp. 496–517, 2014.

[12] ATLAS Collaboration, "Measurement of the $t\bar{t}$ production cross-section using $e\mu$ events with b-tagged jets in pp collisions at $\sqrt{s} = 7$ and 8 TeV with the ATLAS detector," *Eur. Phys. J. C*, vol. 74, no. 10, p. 3109, 2014.

[13] D0 Collaboration, "Determination of the pole and masses of the top quark from the cross section," *Phys. Lett. B*, vol. 703, no. 4, pp. 422 – 427, 2011.

[14] M. Czakon, P. Fiedler, and A. Mitov, "Total Top-Quark Pair-Production Cross Section at Hadron Colliders Through $O(\alpha_S^4)$," *Phys. Rev. Lett.*, vol. 110, p. 252004, 2013.

[15] CMS Collaboration, "Measurement of the $t\bar{t}$ production cross section in the dilepton channel in pp collisions at $\sqrt{s} = 8$ TeV," *JHEP*, vol. 02, p. 024, 2014. [Erratum: JHEP02,102(2014)].

[16] CMS Collaboration, "Measurement of the $t\bar{t}$ production cross section in the dilepton channel in pp collisions at $\sqrt{s} = 7$ TeV," *JHEP*, vol. 11, p. 067, 2012.

[17] M. Beneke, I. Efthymiopoulos, M. L. Mangano, J. Womersley, A. Ahmadov, *et al.*, "Top quark physics," *arXiv:hep-ph/0003033*, 2000.

[18] K. Melnikov and M. Schulze, "NLO QCD corrections to top quark pair production and decay at hadron colliders," *JHEP*, vol. 0908, p. 049, 2009.

[19] J. M. Campbell and R. K. Ellis, "Top-quark processes at NLO in production and decay," *arXiv:1204.1513*, 2012.

[20] J. M. Campbell and R. Ellis, "MCFM for the Tevatron and the LHC," *Nucl. Phys. Proc. Suppl.*, vol. 205-206, pp. 10–15, 2010.

[21] A. W. Thomas and W. Weise, *The Structure of the Nucleon.* Wiley-VCH, 2000.

[22] G. tHooft, "Renormalization and gauge invariance," *Progress of Theoretical Physics Supplement*, vol. 170, pp. 56–71, 2007.

[23] G. tHooft and M. Veltman, "Regularization and Renormalization of Gauge Fields," *Nucl. Phys.*, vol. B44, pp. 189–213, 1972.

[24] MissMJ, "Standard model of elementary particles — Wikipedia, the free encyclopedia," 2014. online: `http://commons.wikimedia.org/wiki/File:Standard_Model_of_Elementary_Particles.svg`, [accessed November 2014], Own work by uploader, PBS NOVA, Fermilab, Office of Science, United States Department of Energy, Particle Data Group.

[25] M. Kobayashi and T. Maskawa, "CP Violation in the Renormalizable Theory of Weak Interaction," *Prog. Theor. Phys.*, vol. 49, pp. 652–657, 1973.

[26] J. H. Christenson, J. W. Cronin, V. L. Fitch, and R. Turlay, "Evidence for the 2π decay of the k_2^0 meson," *Phys. Rev. Lett.*, vol. 13, pp. 138–140, Jul 1964.

[27] KTeV, "Observation of direct CP violation in $K_{S,L} \to \pi\pi$ decays," *Phys. Rev. Lett.*, vol. 83, pp. 22–27, 1999.

[28] CMS Collaboration, "Measurement of the t-channel single-top-quark production cross section and of the $\mid V_{tb} \mid$ CKM matrix element in pp collisions at $\sqrt{s}$= 8 TeV," *JHEP*, vol. 1406, p. 090, 2014.

[29] S. Weinberg, "A model of leptons," *Phys. Rev. Lett.*, vol. 19, pp. 1264–1266, Nov 1967.

[30] S. L. Glashow, "Partial-symmetries of weak interactions," *Nucl. Phys.*, vol. 22, no. 4, pp. 579 – 588, 1961.

[31] H1 Collaboration, "Measurement and QCD analysis of neutral and charged current cross-sections at HERA," *Eur. Phys. J. C*, vol. 30, pp. 1–32, 2003.

[32] ZEUS, H1, "Combination of Measurements of Inclusive Deep Inelastic $e^{\pm}p$ Scattering Cross Sections and QCD Analysis of HERA Data," *arXiv:1506.06042*, 2015.

[33] P. W. Higgs, "Broken symmetries and the masses of gauge bosons," *Phys. Rev. Lett.*, vol. 13, pp. 508–509, Oct 1964.

[34] Particle Data Group, "Review of particle physics: status of higgs boson physics," *Chin. Phys. C*, vol. 38, p. 090001, 2014.

[35] H1 and ZEUS Collaboration, "Combined Measurement and QCD Analysis of the Inclusive $e^{\pm}p$ Scattering Cross Sections at HERA," *JHEP*, vol. 1001, p. 109, 2010.

[36] NuTeV Collaboration, "Precise measurement of neutrino and anti-neutrino differential cross sections," *Phys. Rev. D*, vol. 74, p. 012008, 2006.

[37] CMS Collaboration, "Measurement of the muon charge asymmetry in inclusive $pp \to W + X$ production at $\sqrt{s} = 7$ TeV and an improved determination of light parton distribution functions," *Phys. Rev. D*, vol. 90, p. 032004, Aug 2014.

[38] V. Gribov and L. Lipatov, "Deep inelastic scattering in perturbation theory," *Sov. J. Nucl. Phys*, vol. 15, p. 438, 1972.

[39] G. Curci, W. Furmanski, and R. Petronzio, "Evolution of parton densities beyond leading order: The non-singlet case," *Nucl. Phys. B*, vol. 175, no. 1, pp. 27 – 92, 1980.

[40] W. Furmanski and R. Petronzio, "Singlet parton densities beyond leading order," *Phys. Lett. B*, vol. 97, no. 3–4, pp. 437 – 442, 1980.

[41] G. Altarelli and G. Parisi, "Asymptotic freedom in parton language," *Nucl. Phys. B*, vol. 126, no. 2, pp. 298 – 318, 1977.

[42] S. Moch, J. Vermaseren, and A. Vogt, "The Three loop splitting functions in QCD: The Nonsinglet case," *Nucl. Phys. B*, vol. 688, pp. 101–134, 2004.

[43] A. Vogt, S. Moch, and J. Vermaseren, "The Three-loop splitting functions in QCD: The Singlet case," *Nucl. Phys. B*, vol. 691, pp. 129–181, 2004.

[44] K. Lipka, "Recent results from HERA and their impact for LHC," *Eur. Phys. J. Conf.*, vol. 28, p. 02008, 2012.

[45] S. D. Drell and T.-M. Yan, "Massive lepton-pair production in hadron-hadron collisions at high energies," *Phys. Rev. Lett.*, vol. 25, pp. 316–320, Aug 1970.

[46] J. M. Campbell, J. W. Huston, and W. J. Stirling, "Hard Interactions of Quarks and Gluons: A Primer for LHC Physics," *Rept. Prog. Phys.*, vol. 70, p. 89, 2007.

[47] D0 Collaboration, "Observation of the Top Quark," *Phys. Rev. Lett.*, vol. 74, pp. 2632–2637, Apr 1995.

[48] U. Langenfeld, S. Moch, and P. Uwer, "Measuring the running top-quark mass," *Phys. Rev. D*, vol. 80, p. 054009, 2009.

[49] R. S. Chivukula, "Electroweak symmetry breaking," *Journal of Physics: Conference Series*, vol. 37, no. 1, p. 28, 2006.

[50] A. De Simone, O. Matsedonskyi, R. Rattazzi, and A. Wulzer, "A First Top Partner Hunter's Guide," *JHEP*, vol. 1304, p. 004, 2013.

[51] W. Bernreuther, "Top quark physics at the LHC," *J. Phys. G*, vol. 35, p. 083001, 2008.

[52] W. J. Stirling, "Progress in Parton Distribution Functions and implications for LHC," *arXiv:0812.2341*, 2008.

[53] F. Cascioli, S. Kallweit, P. Maierhöfer, and S. Pozzorini, ""a unified nlo description of top-pair and associated wt production"," *Eur. Phys. J. C*, vol. 74, no. 3, 2014.

[54] C. D. White, S. Frixione, E. Laenen, and F. Maltoni, "Isolating Wt production at the LHC," *JHEP*, vol. 0911, p. 074, 2009.

[55] S. Frixione, E. Laenen, P. Motylinski, B. R. Webber, and C. D. White, "Single-top hadroproduction in association with a W boson," *JHEP*, vol. 0807, p. 029, 2008.

[56] T. M. Tait, "The tW^- mode of single top production," *Phys. Rev. D*, vol. 61, p. 034001, 2000.

[57] S. Moch, "Precision determination of the top-quark mass," *PoS*, vol. LL2014, p. 054, 2014.

[58] I. I. Y. Bigi, M. A. Shifman, and N. Uraltsev, "Aspects of heavy quark theory," *Ann. Rev. Nucl. Part. Sci.*, vol. 47, pp. 591–661, 1997.

[59] M. C. Smith and S. S. Willenbrock, "Top quark pole mass," *Phys. Rev. Lett.*, vol. 79, pp. 3825–3828, 1997.

[60] M. Beneke, "Renormalons," *Phys. Rept.*, vol. 317, pp. 1–142, 1999.

[61] M. Beneke and V. Braun, "Naive nonabelianization and resummation of fermion bubble chains," *Phys. Lett. B*, vol. 348, no. 3–4, pp. 513 – 520, 1995.

[62] P. Ball, M. Beneke, and V. M. Braun, "Resummation of (beta0 alpha-s)**n corrections in QCD: Techniques and applications to the tau hadronic width and the heavy quark pole mass," *Nucl. Phys. B*, vol. 452, pp. 563–625, 1995.

[63] K. Philippides and A. Sirlin, "Leading vacuum polarization contributions to the relation between pole and running masses," *Nucl. Phys. B*, vol. 450, pp. 3–20, 1995.

[64] M. Beneke and V. M. Braun, “Heavy quark effective theory beyond perturbation theory: Renormalons, the pole mass and the residual mass term,” *Nucl. Phys. B*, vol. 426, pp. 301–343, 1994.

[65] I. I. Y. Bigi, M. A. Shifman, N. G. Uraltsev, and A. I. Vainshtein, “The Pole mass of the heavy quark. Perturbation theory and beyond,” *Phys. Rev. D*, vol. 50, pp. 2234–2246, 1994.

[66] P. Marquard, A. V. Smirnov, V. A. Smirnov, and M. Steinhauser, “Quark mass relations to four-loop order in perturbative qcd,” *Phys. Rev. Lett.*, vol. 114, p. 142002, Apr 2015.

[67] A. H. Hoang and I. W. Stewart, “Top Mass Measurements from Jets and the Tevatron Top-Quark Mass,” *Nucl. Phys. Proc. Suppl.*, vol. 185, pp. 220–226, 2008.

[68] A. H. Hoang, A. Jain, I. Scimemi, and I. W. Stewart, “R-evolution: Improving perturbative QCD,” *Phys. Rev. D*, vol. 82, p. 011501, 2010.

[69] CMS Collaboration, “Measurement of the top-quark mass in $t\bar{t}$ events with lepton+jets final states in pp collisions at $\sqrt{s} = 8$ TeV,” CMS-PAS-TOP-14-001, CERN, Geneva, 2014.

[70] ATLAS Collaboration, “Measurement of the top quark mass in the $t\bar{t} \to$ lepton+jets and $t\bar{t} \to$ dilepton channels using $\sqrt{s} = 7$ TeV ATLAS data,” *Eur. Phys. J. C*, vol. 75, no. 7, p. 330, 2015.

[71] D0 Collaboration, “Precision measurement of the top-quark mass in lepton+jets final states,” *Phys. Rev. Lett.*, vol. 113, p. 032002, 2014.

[72] CDF Collaboration, “Precision Top-Quark Mass Measurements at CDF,” *Phys. Rev. Lett.*, vol. 109, p. 152003, 2012.

[73] M. Mangano, “Interpreting the top quark mass: theoretical and MC aspects,” 2013. online: `https://indico.desy.de/getFile.py/access?contribId=30&sessionId=9&resId=0&materialId=slides&confId=7095`, [accessed August 2015], TOP 2013 Durbach, Sept 14-19 2013 (presentation).

[74] S. Alioli, P. Fernandez, J. Fuster, A. Irles, S.-O. Moch, P. Uwer, and M. Vos, “A new observable to measure the top-quark mass at hadron colliders,” *Eur. Phys. J. C*, vol. 73, p. 2438, 2013.

[75] ATLAS Collaboration, “Determination of the top-quark pole mass using $t\bar{t}$ + 1-jet events collected with the ATLAS experiment in 7 TeV pp collisions,” *arXiv:1507.01769*, 2015.

[76] CMS Collaboration, “Measurement of masses in the $t\bar{t}$ system by kinematic endpoints in pp collisions at $\sqrt{s} = 7$ TeV,” *Eur. Phys. J. C*, vol. 73, p. 2494, 2013.

[77] K. Seidel, F. Simon, M. Tesar, and S. Poss, “Top quark mass measurements at and above threshold at CLIC,” *Eur. Phys. J. C*, vol. 73, p. 2530, 2013.

[78] A. H. Hoang and M. Stahlhofen, "The Top-Antitop Threshold at the ILC: NNLL QCD Uncertainties," *JHEP*, vol. 05, p. 121, 2014.

[79] M. Beneke, Y. Kiyo, P. Marquard, A. Penin, J. Piclum, and M. Steinhauser, "Next-to-next-to-next-to-leading order QCD prediction for the top anti-top S-wave pair production cross section near threshold in e+ e- annihilation," *arXiv:1506.06864*, 2015.

[80] Bärnreuther, Peter and Czakon, Michal and Mitov, Alexander, "Percent Level Precision Physics at the Tevatron: First Genuine NNLO QCD Corrections to $q\bar{q} \to t\bar{t} + X$," *Phys. Rev. Lett.*, vol. 109, p. 132001, 2012.

[81] M. Czakon and A. Mitov, "NNLO corrections to top-pair production at hadron colliders: the all-fermionic scattering channels," *JHEP*, vol. 1212, p. 054, 2012.

[82] M. Czakon and A. Mitov, "NNLO corrections to top pair production at hadron colliders: the quark-gluon reaction," *JHEP*, vol. 1301, p. 080, 2013.

[83] M. Beneke, P. Falgari, S. Klein, and C. Schwinn, "Hadronic top-quark pair production with NNLL threshold resummation," *Nucl. Phys. B*, vol. 855, pp. 695–741, 2012.

[84] M. Cacciari, M. Czakon, M. Mangano, A. Mitov, and P. Nason, "Top-pair production at hadron colliders with next-to-next-to-leading logarithmic soft-gluon resummation," *Phys. Lett. B*, vol. 710, pp. 612–622, 2012.

[85] M. Czakon and A. Mitov, "Top++: A Program for the Calculation of the Top-Pair Cross-Section at Hadron Colliders," *Comput. Phys. Commun.*, vol. 185, p. 2930, 2014.

[86] M. Aliev, H. Lacker, U. Langenfeld, S. Moch, P. Uwer, *et al.*, "HATHOR: HAdronic Top and Heavy quarks crOss section calculatoR," *Comput. Phys. Commun.*, vol. 182, pp. 1034–1046, 2011.

[87] P. Kant, O. Kind, T. Kintscher, T. Lohse, T. Martini, *et al.*, "HatHor for single top-quark production: Updated predictions and uncertainty estimates for single top-quark production in hadronic collisions," *Comput. Phys. Commun.*, vol. 191, pp. 74–89, 2015.

[88] J. H. Kuhn, A. Scharf, and P. Uwer, "Electroweak corrections to top-quark pair production in quark-antiquark annihilation," *Eur. Phys. J. C*, vol. 45, pp. 139–150, 2006.

[89] J. H. Kuhn, A. Scharf, and P. Uwer, "Electroweak effects in top-quark pair production at hadron colliders," *Eur. Phys. J. C*, vol. 51, pp. 37–53, 2007.

[90] J. H. Kühn, A. Scharf, and P. Uwer, "Weak Interactions in Top-Quark Pair Production at Hadron Colliders: An Update," *Phys. Rev. D*, vol. 91, no. 1, p. 014020, 2015.

[91] N. Kidonakis, "Differential and total cross sections for top pair and single top production," *Proceedings, 20th International Workshop on Deep-Inelastic Scattering and Related Subjects (DIS 2012)*, pp. 831–834, 2012.

[92] N. Kidonakis, "Two-loop soft anomalous dimensions for single top quark associated production with a W- or H-," *Phys. Rev. D*, vol. 82, p. 054018, 2010.

[93] M. Guzzi, K. Lipka, and S.-O. Moch, "Top-quark pair production at hadron colliders: differential cross section and phenomenological applications with DiffTop," *JHEP*, vol. 1501, p. 082, 2015.

[94] S. Frixione, P. Nason, and B. R. Webber, "Matching NLO QCD and parton showers in heavy flavor production," *JHEP*, vol. 0308, p. 007, 2003.

[95] S. Alioli, K. Hamilton, P. Nason, C. Oleari, and E. Re, "Jet pair production in POWHEG," *JHEP*, vol. 1104, p. 081, 2011.

[96] R. Frederix, S. Frixione, F. Maltoni, and T. Stelzer, "Automation of next-to-leading order computations in QCD: The FKS subtraction," *JHEP*, vol. 0910, p. 003, 2009.

[97] M. Czakon, P. Fiedler, and A. Mitov, "Resolving the tevatron top quark forward-backward asymmetry puzzle: Fully differential next-to-next-to-leading-order calculation," *Phys. Rev. Lett.*, vol. 115, p. 052001, Jul 2015.

[98] N. Kidonakis, "High order corrections and subleading logarithms for top quark production," *Phys. Rev. D*, vol. 64, p. 014009, 2001.

[99] N. Kidonakis, E. Laenen, S. Moch, and R. Vogt, "Sudakov resummation and finite order expansions of heavy quark hadroproduction cross-sections," *Phys. Rev. D*, vol. 64, p. 114001, 2001.

[100] N. Kidonakis, "A Unified approach to NNLO soft and virtual corrections in electroweak, Higgs, QCD, and SUSY processes," *Int. J. Mod. Phys. A*, vol. 19, pp. 1793–1821, 2004.

[101] N. Kidonakis and R. Vogt, "Next-to-next-to-leading order soft gluon corrections in top quark hadroproduction," *Phys. Rev. D*, vol. 68, p. 114014, 2003.

[102] N. Kidonakis, "Next-to-next-to-next-to-leading-order soft-gluon corrections in hard-scattering processes near threshold," *Phys. Rev. D*, vol. 73, p. 034001, 2006.

[103] N. Kidonakis and R. Vogt, "The Theoretical top quark cross section at the Tevatron and the LHC," *Phys. Rev. D*, vol. 78, p. 074005, 2008.

[104] N. Kidonakis, "Next-to-next-to-leading soft-gluon corrections for the top quark cross section and transverse momentum distribution," *Phys. Rev. D*, vol. 82, p. 114030, 2010.

[105] M. Czakon, A. Mitov, and G. F. Sterman, "Threshold Resummation for Top-Pair Hadroproduction to Next-to-Next-to-Leading Log," *Phys. Rev. D*, vol. 80, p. 074017, 2009.

[106] W. Bernreuther and Z.-G. Si, "Distributions and correlations for top quark pair production and decay at the Tevatron and LHC.," *Nucl. Phys. B*, vol. 837, pp. 90–121, 2010.

[107] T. Sjostrand, S. Mrenna, and P. Z. Skands, "PYTHIA 6.4 Physics and Manual," *JHEP*, vol. 0605, p. 026, 2006.

[108] R. Field, "Min-Bias and the Underlying Event at the LHC," *Acta Phys. Polon.*, vol. B42, pp. 2631–2656, 2011.

[109] CMS Collaboration, "Study of the underlying event at forward rapidity in pp collisions at $\sqrt{s} = 0.9$, 2.76, and 7 TeV," *JHEP*, vol. 072, p. 1304, 2013.

[110] J. Pumplin, D. R. Stump, J. Huston, H. L. Lai, P. M. Nadolsky, and W. K. Tung, "New generation of parton distributions with uncertainties from global QCD analysis," *JHEP*, vol. 07, p. 012, 2002.

[111] P. Z. Skands, "Tuning Monte Carlo Generators: The Perugia Tunes," *Phys. Rev. D*, vol. 82, p. 074018, 2010.

[112] S. Jadach, Z. Was, R. Decker, and J. H. Kuhn, "The tau decay library TAUOLA: Version 2.4," *Comput. Phys. Commun.*, vol. 76, pp. 361–380, 1993.

[113] J. Alwall, M. Herquet, F. Maltoni, O. Mattelaer, and T. Stelzer, "MadGraph 5 : Going Beyond," *JHEP*, vol. 1106, p. 128, 2011.

[114] S. Frixione, E. Laenen, P. Motylinski, and B. R. Webber, "Angular correlations of lepton pairs from vector boson and top quark decays in Monte Carlo simulations," *JHEP*, vol. 0704, p. 081, 2007.

[115] S. Mrenna and P. Richardson, "Matching matrix elements and parton showers with HERWIG and PYTHIA," *JHEP*, vol. 05, p. 040, 2004.

[116] P. Nason, "A New method for combining NLO QCD with shower Monte Carlo algorithms," *JHEP*, vol. 0411, p. 040, 2004.

[117] S. Frixione, P. Nason, and C. Oleari, "Matching NLO QCD computations with Parton Shower simulations: the POWHEG method," *JHEP*, vol. 0711, p. 070, 2007.

[118] S. Alioli, P. Nason, C. Oleari, and E. Re, "NLO single-top production matched with shower in POWHEG: s- and t-channel contributions," *JHEP*, vol. 09, p. 111, 2009. [Erratum: JHEP02,011(2010)].

[119] S. Alioli, P. Nason, C. Oleari, and E. Re, "A general framework for implementing NLO calculations in shower Monte Carlo programs: the POWHEG BOX," *JHEP*, vol. 1006, p. 043, 2010.

[120] E. Re, "Single-top Wt-channel production matched with parton showers using the POWHEG method," *Eur. Phys. J. C*, vol. 71, p. 1547, 2011.

[121] J. M. Campbell and R. K. Ellis, "$t\bar{t}W^{\pm}$ production and decay at NLO," *JHEP*, vol. 1207, p. 052, 2012.

[122] M. Garzelli, A. Kardos, C. Papadopoulos, and Z. Trócsányi, " $t\bar{t}$ $W^{\pm}$ and $t\bar{t}$ Z Hadroproduction at NLO accuracy in QCD with Parton Shower and Hadronization effects," *JHEP*, vol. 1211, p. 056, 2012.

[123] Y. Li and F. Petriello, "Combining QCD and electroweak corrections to dilepton production in FEWZ," *Phys. Rev. D*, vol. 86, p. 094034, 2012.

[124] S. A. et al., "Geant4—a simulation toolkit," *Nuclear Instruments and Methods in Physics Research Section A: Accelerators, Spectrometers, Detectors and Associated Equipment*, vol. 506, no. 3, pp. 250 – 303, 2003.

[125] J. e. a. Allison, "Geant4 developments and applications," *IEEE Transactions on Nuclear Science*, vol. 53, pp. 270–278, Feb 2006.

[126] O. S. Brüning, P. Collier, P. Lebrun, S. Myers, R. Ostojic, J. Poole, and P. Proudlock, *LHC Design Report*. Geneva: CERN, 2004.

[127] CMS Collaboration, "Delivered luminosity versus time for 2010, 2011, 2012 (p-p data only)," 2012. online: `https://twiki.cern.ch/twiki/bin/view/CMSPublic/LumiPublicResults`, [accessed April 2015].

[128] CMS Collaboration, *CMS Physics: Technical Design Report Volume 1: Detector Performance and Software*. Technical Design Report CMS, Geneva: CERN, 2006.

[129] "CMS Detector Drawings." online: `http://cmsinfo.web.cern.ch/cmsinfo/Media/Images/Detector/Detector%20Drawings/index.html`, [accessed Mai 2015].

[130] CMS Collaboration, "Alignment of the cms silicon tracker during commissioning with cosmic rays," *JINST*, vol. 5, no. 03, p. T03009, 2010.

[131] CMS Collaboration, "The CMS experiment at the CERN LHC," *JINST*, vol. 3, no. 08, p. S08004, 2008.

[132] CMS Collaboration, "Performance of the cms hadron calorimeter with cosmic ray muons and lhc beam data," *JINST*, vol. 5, no. 03, p. T03012, 2010.

[133] CMS Collaboration, *The CMS muon project: Technical Design Report*. Technical Design Report CMS, Geneva: CERN, 1997.

[134] CMS Collaboration, "Absolute Calibration of the Luminosity Measurement at CMS: Winter 2012 Update," CMS-PAS-SMP-12-008, CERN, Geneva, 2012.

[135] CMS Collaboration, "CMS Luminosity Based on Pixel Cluster Counting - Summer 2013 Update," CMS-PAS-LUM-13-001, CERN, Geneva, 2013.

[136] S. van der Meer, "Calibration of the effective beam height in the ISR," CERN-ISR-PO-68-31. ISR-PO-68-31, CERN, Geneva, 1968.

[137] CMS Collaboration, "Zero bias and HF-based minimum bias triggering for pp collisions at 14 TeV in CMS," CMS-PAS-QCD-07-002, CERN, Geneva, 2008.

[138] CERN, “CMS Media,” 2012. online: `http://cmsinfo.web.cern.ch/cmsinfo/Media`, [accessed March 2012].

[139] K. Rose, “Deterministic annealing for clustering, compression, classification, regression, and related optimization problems,” *Proceedings of the IEEE*, vol. 86, pp. 2210–2239, Nov 1998.

[140] CMS Collaboration, “Description and performance of track and primary-vertex reconstruction with the CMS tracker,” *JINST*, vol. 9, no. 10, p. P10009, 2014.

[141] CMS Collaboration, “Measurement of the inelastic proton–proton cross section,” *Phys. Lett. B*, vol. 722, no. 1–3, pp. 5 – 27, 2013.

[142] CMS Collaboration, “Inelastic proton-proton cross section measurements in CMS at $\sqrt{s} = 7$ TeV,” in *Proceedings, 20th International Workshop on Deep-Inelastic Scattering and Related Subjects (DIS 2012)*, pp. 781–784, 2012.

[143] M. Hildreth, “Strategies for Modeling Extreme Luminosities in the CMS Simulation,” 2014. online: `https://indico.cern.ch/event/279530/session/4/contribution/15/attachments/511927/706536/Hildreth_CMS_Pileup_v2.pdf`, [accessed August 2015], LHC detector simulations: status, needs and prospects (presentation).

[144] CMS Collaboration, “Particle-Flow Event Reconstruction in CMS and Performance for Jets, Taus, and MET,” CMS-PAS-PFT-09-001, CERN, 2009. Geneva, Apr 2009.

[145] CMS Collaboration, “Commissioning of the Particle-Flow reconstruction in Minimum-Bias and Jet Events from pp Collisions at 7 TeV,” CMS-PAS-PFT-10-002, CERN, Geneva, 2010.

[146] CMS Collaboration, “Measurement of the inclusive jet cross section in pp collisions at $\sqrt{s} = 2.76$ TeV,” CMS-PAS-SMP-14-017, CERN, Geneva, 2015.

[147] CMS Collaboration, “Performance of electron reconstruction and selection with the CMS detector in proton-proton collisions at $\sqrt{s} = 8$ TeV,” *JINST*, vol. 10, no. 06, p. P06005, 2015.

[148] CMS Collaboration, “Search for neutral Higgs bosons decaying to tau pairs in pp collisions at $\sqrt{s} = 7$ TeV,” *Phys. Lett. B*, vol. 713, no. 2, pp. 68 – 90, 2012.

[149] C. Diez Pardos and J. Kieseler, “Dilepton trigger and lepton identification efficiencies for the top quark pair production cross section measurement at 8 TeV in the dilepton decay channel,” 2014. CMS AN-2012/389 [CMS internal note].

[150] CMS Collaboration, “Muon ID and Isolation Efficiencies in 2012 RunAB,” CMS DP-2012/025, CERN, Geneva, 2012.

[151] A. Bodek, A. van Dyne, J. Y. Han, W. Sakumoto, and A. Strelnikov, “Extracting Muon Momentum Scale Corrections for Hadron Collider Experiments,” *Eur. Phys. J. C*, vol. 72, p. 2194, 2012.

[152] M. Cacciari, G. P. Salam, and G. Soyez, "The Anti-k(t) jet clustering algorithm," *JHEP*, vol. 0804, p. 063, 2008.

[153] H. Kirschenmann, *Jet Energy Scale Corrections and their Impact on Measurements of the Top-Quark Mass at CMS.* PhD thesis, U. Hamburg, Dept. Phys., 2014.

[154] CMS Collaboration, "Determination of Jet Energy Calibration and Transverse Momentum Resolution in CMS," *JINST*, vol. 6, p. P11002, 2011.

[155] K. Goebel, J. Haller, J. Ott, and H. Stadie, "Jet Transverse Momentum Resolution Measurement using Dijet Events at $\sqrt{s} = 8$ TeV," 2014. CMS AN-2013/416 [CMS internal note].

[156] CMS Collaboration, "Identification of b-quark jets with the CMS experiment," *JINST*, vol. 8, p. P04013, 2013.

[157] T. D. Collaboration, "B-tagging graphic," 2009. online: `http://www-d0.fnal.gov/Run2Physics/top/singletop_observation/b_tagging_graphic.png`, [accessed August 2015].

[158] CMS Collaboration, "Performance of b tagging at $\sqrt{s} = 8$ TeV in multijet, $t\bar{t}$ and boosted topology events," CMS-PAS-BTV-13-001, CERN, Geneva, 2013.

[159] U. Heintz, "Algorithm to adjust the b-tagging efficiency in simulated events," 2013. online: `https://twiki.cern.ch/twiki/pub/CMS/BTagSFUtil/btagSF.pdf`, [accessed August 2015].

[160] CMS Collaboration, "Double Muon Trigger efficiency in 2012 data," CMS-DP-2014/038, CERN, Geneva, 2014.

[161] CMS Collaboration, "Measurement of the top quark pair production cross section in proton-proton collisions at $\sqrt{s} = 13$ TeV with the CMS detector," CMS-PAS-TOP-15-003, CERN, Geneva, 2015.

[162] CMS Collaboration, "Measurement of the Differential Cross Section for Top Quark Pair Production in pp Collisions at $\sqrt{s} = 8$ TeV," *arXiv:1505.04480*, 2015.

[163] CMS Collaboration, "Measurement of the Jet Multiplicity in dileptonic Top Quark Pair Events at 8 TeV," CMS-PAS-TOP-12-041, CERN, Geneva, 2013.

[164] CMS Collaboration, "First measurement of the differential cross section for $t\bar{t}$ production in the dilepton final state at $\sqrt{s} = 13$ TeV," CMS-PAS-TOP-15-010, CERN, Geneva, 2015.

[165] CMS Collaboration, "Observation of the associated production of a single top quark and a W boson in pp collisions at $\sqrt{s}$ =8 TeV," *Phys. Rev. Lett.*, vol. 112, no. 23, p. 231802, 2014.

[166] CMS Collaboration, "Search for the associated production of the Higgs boson with a top-quark pair," *JHEP*, vol. 09, p. 087, 2014. [Erratum: JHEP10,106(2014)].

[167] Particle Data Group, "Review of Particle Physics," *Chin. Phys. C*, vol. 38, p. 090001, 2014.

[168] ATLAS Collaboration, "Measurement of the cross section for top-quark pair production in *pp* collisions at $\sqrt{s} = 7$ TeV with the ATLAS detector using final states with two high-pt leptons," *JHEP*, vol. 05, p. 059, 2012.

[169] CMS Collaboration, "Search for the standard model Higgs boson produced in association with a top-quark pair in pp collisions at the LHC," *JHEP*, vol. 1305, p. 145, 2013.

[170] ALEPH, "Study of the fragmentation of b quarks into B mesons at the Z peak," *Phys. Lett. B*, vol. 512, pp. 30–48, 2001.

[171] DELPHI, "A study of the b-quark fragmentation function with the DELPHI detector at LEP I and an averaged distribution obtained at the Z Pole," *Eur. Phys. J. C*, vol. 71, p. 1557, 2011.

[172] J. Gao, M. Guzzi, J. Huston, H.-L. Lai, Z. Li, P. Nadolsky, J. Pumplin, D. Stump, and C.-P. Yuan, ""CT10 next-to-next-to-leading order global analysis of QCD"," *Phys. Rev. D*, vol. 89, p. 033009, Feb 2014.

[173] F. James and M. Roos, "Minuit – A System for Function Minimization and Analysis of the Parameter Errors and Correlations," *Comp. Phys. Comm.*, vol. 10, p. 343, 1975.

[174] M. L. Mangano and J. Rojo, "Cross Section Ratios between different CM energies at the LHC: opportunities for precision measurements and BSM sensitivity," *JHEP*, vol. 1208, p. 010, 2012.

[175] NNPDF, "Parton distributions for the LHC Run II," *JHEP*, vol. 04, p. 040, 2015.

[176] S. Dulat, T. J. Hou, J. Gao, M. Guzzi, J. Huston, P. Nadolsky, J. Pumplin, C. Schmidt, D. Stump, and C. P. Yuan, "The CT14 Global Analysis of Quantum Chromodynamics," *arXiv:1506.07443*, 2015.

[177] L. A. Harland-Lang, A. D. Martin, P. Motylinski, and R. S. Thorne, "Parton distributions in the LHC era: MMHT 2014 PDFs," *Eur. Phys. J. C*, vol. 75, no. 5, p. 204, 2015.

[178] S. Alekhin, J. Blumlein, and S. Moch, "The ABM parton distributions tuned to LHC data," *Phys. Rev. D*, vol. 89, no. 5, p. 054028, 2014.

[179] G. Heinrich, A. Maier, R. Nisius, J. Schlenk, and J. Winter, "NLO QCD corrections to $W^+W^-b\bar{b}$ production with leptonic decays in the light of top quark mass and asymmetry measurements," *JHEP*, vol. 06, p. 158, 2014.

[180] CMS Collaboration, "Measurement of the Top Quark Mass in Dilepton $t\bar{t}$ Decays at $\sqrt{s} = 8$ TeV," CMS-PAS-TOP-14-010, CERN, Geneva, 2014.

[181] ATLAS Collaboration, "Measurement of the Top Quark Mass in Dileptonic Top Quark Pair Decays with $\sqrt{s} = 7$ TeV ATLAS Data," ATLAS-CONF-2013-077, CERN, Geneva, Jul 2013.

[182] Behnke, Olaf and Kröninger, Kevin and Schott, Gregory and Schörner-Sadenius, Thomas, *Data Analysis in High Energy Physics: A Practical Guide to Statistical Methods*. Wiley-VCH, 2013.

[183] A. D. Martin, W. J. Stirling, R. S. Thorne, and G. Watt, "Parton distributions for the LHC," *Eur. Phys. J. C*, vol. 63, pp. 189–285, 2009.

[184] A. D. Martin, W. J. Stirling, R. S. Thorne, and G. Watt, "Uncertainties on alpha(S) in global PDF analyses and implications for predicted hadronic cross sections," *Eur. Phys. J. C*, vol. 64, pp. 653–680, 2009.

[185] CMS Collaboration, "Combination of the CMS top-quark mass measurements from Run 1 of the LHC," CMS-PAS-TOP-14-015, CERN, Geneva, 2014.

[186] A. H. Hoang, A. Jain, I. Scimemi, and I. W. Stewart, "Infrared renormalization-group flow for heavy-quark masses," *Phys. Rev. Lett.*, vol. 101, p. 151602, Oct 2008.

[187] K. G. Chetyrkin, J. H. Kuhn, and M. Steinhauser, "RunDec: A Mathematica package for running and decoupling of the strong coupling and quark masses," *Comput. Phys. Commun.*, vol. 133, pp. 43–65, 2000.

[188] B. Schmidt and M. Steinhauser, "CRunDec: a C++ package for running and decoupling of the strong coupling and quark masses," *Comput. Phys. Commun.*, vol. 183, pp. 1845–1848, 2012.

[189] K. G. Chetyrkin, J. H. Kuhn, and C. Sturm, "QCD decoupling at four loops," *Nucl. Phys. B*, vol. 744, pp. 121–135, 2006.

[190] Y. Schroder and M. Steinhauser, "Four-loop decoupling relations for the strong coupling," *JHEP*, vol. 01, p. 051, 2006.

[191] N. Gray, D. J. Broadhurst, W. Grafe, and K. Schilcher, "Three Loop Relation of Quark (Modified) Ms and Pole Masses," *Z. Phys. C*, vol. 48, pp. 673–680, 1990.

[192] K. Melnikov and T. v. Ritbergen, "The Three loop relation between the MS-bar and the pole quark masses," *Phys. Lett. B*, vol. 482, pp. 99–108, 2000.

[193] P. Marquard, L. Mihaila, J. H. Piclum, and M. Steinhauser, "Relation between the pole and the minimally subtracted mass in dimensional regularization and dimensional reduction to three-loop order," *Nucl. Phys. B*, vol. 773, pp. 1–18, 2007.

[194] R. Tarrach, "The pole mass in perturbative QCD," *Nucl. Phys. B*, vol. 183, no. 3, pp. 384 – 396, 1981.

[195] K. G. Chetyrkin and M. Steinhauser, "Short distance mass of a heavy quark at order α_s^3," *Phys. Rev. Lett.*, vol. 83, pp. 4001–4004, 1999.

[196] K. G. Chetyrkin and M. Steinhauser, "The Relation between the MS-bar and the on-shell quark mass at order alpha(s)**3," *Nucl. Phys. B*, vol. 573, pp. 617–651, 2000.

[197] R. Hempfling and B. A. Kniehl, "Relation between the fermion pole mass and msbar yukawa coupling in the standard model," *Phys. Rev. D*, vol. 51, pp. 1386–1394, Feb 1995.

[198] F. Jegerlehner and M. Yu. Kalmykov, "O(alpha alpha(s)) correction to the pole mass of the t quark within the standard model," *Nucl. Phys. B*, vol. 676, pp. 365–389, 2004.

[199] M. Faisst, J. H. Kuhn, and O. Veretin, "Pole versus MS mass definitions in the electroweak theory," *Phys. Lett. B*, vol. 589, pp. 35–38, 2004.

[200] S. P. Martin, "Fermion self-energies and pole masses at two-loop order in a general renormalizable theory with massless gauge bosons," *Phys. Rev. D*, vol. 72, p. 096008, 2005.

[201] D. Eiras and M. Steinhauser, "Two-loop O(alpha alpha(s)) corrections to the on-shell fermion propagator in the standard model," *JHEP*, vol. 02, p. 010, 2006.

[202] CMS Collaboration, "Measurement of the $t\bar{t}$ production cross section in the $e\mu$ channel in pp collisions at 7 and 8 TeV," CMS-PAS-TOP-13-004, CERN, Geneva, 2015.

[203] CMS Collaboration, "Determination of the top-quark mass from the m(lb) distribution in dileptonic $t\bar{t}$ events at $\sqrt{s} = 8$ TeV," CMS-PAS-TOP-14-014, CERN, Geneva, 2014.

[204] ATLAS Collaboration, "Measurement of the $t\bar{t}$ production cross-section in pp collisions at $\sqrt{s} = 13$ TeV using $e\mu$ events with b-tagged jets," ATLAS-CONF-2015-033, CERN, Geneva, Jul 2015.

Appendix A

Monte Carlo Parameters

This section lists the parameters employed to configure the MC generators used for the production of the signal and tW simulation (MadGraph and powheg). Variations of parameters are not explicitly indicated.

For contributions from tW processes, MC samples are produced with powheg specifically for the analyses presented here.

Madgraph run card configuration

```
#*********************************************************************
#                       MadGraph/MadEvent                            *
#                  http://madgraph.hep.uiuc.edu                      *
#                                                                    *
#                        run_card.dat                                *
#                                                                    *
#  This file is used to set the parameters of the run.               *
#                                                                    *
#  Some notation/conventions:                                        *
#                                                                    *
#   Lines starting with a ’# ’ are info or comments                  *
#                                                                    *
#   mind the format:   value    = variable     ! comment             *
#*********************************************************************
#
#*******************
# Running parameters
#*******************
#
#*********************************************************************
# Tag name for the run (one word)                                    *
#*********************************************************************
  tag_1     = run_tag ! name of the run
#*********************************************************************
# Run to generate the grid pack                                      *
#*********************************************************************
  .true.     = gridpack  !True = setting up the grid pack
#*********************************************************************
# Number of events and rnd seed                                      *
# Warning: Do not generate more than 1M events in a single run       *
# If you want to run Pythia, avoid more than 50k events in a run.    *
#*********************************************************************
```

```
  10000 = nevents ! Number of unweighted events requested
      0       = iseed   ! rnd seed (0=assigned automatically=default))
#*********************************************************************
# Collider type and energy                                           *
# lpp: 0=No PDF, 1=proton, -1=antiproton, 2=photon from proton,      *
#                                         3=photon from electron     *
#*********************************************************************
        1     = lpp1    ! beam 1 type
        1     = lpp2    ! beam 2 type
     3500     = ebeam1  ! beam 1 total energy in GeV
     3500     = ebeam2  ! beam 2 total energy in GeV
#*********************************************************************
# Beam polarization from -100 (left-handed) to 100 (right-handed)    *
#*********************************************************************
        0     = polbeam1 ! beam polarization for beam 1
        0     = polbeam2 ! beam polarization for beam 2
#*********************************************************************
# PDF CHOICE: this automatically fixes also alpha_s and its evol.    *
#*********************************************************************
 'cteq6l1'    = pdlabel     ! PDF set
#*********************************************************************
# Renormalization and factorization scales                           *
#*********************************************************************
 F        = fixed_ren_scale  ! if .true. use fixed ren scale
 F        = fixed_fac_scale  ! if .true. use fixed fac scale
 91.1880  = scale            ! fixed ren scale
 91.1880  = dsqrt_q2fact1    ! fixed fact scale for pdf1
 91.1880  = dsqrt_q2fact2    ! fixed fact scale for pdf2
 1        = scalefact        ! scale factor for event-by-event scales
#*********************************************************************
# Matching - Warning! ickkw > 1 is still beta
#*********************************************************************
 1        = ickkw            ! 0 no matching, 1 MLM, 2 CKKW matching
 1        = highestmult      ! for ickkw=2, highest mult group
 1        = ktscheme         ! for ickkw=1, 1 Durham kT, 2 Pythia pTE
 1        = alpsfact         ! scale factor for QCD emission vx
 F        = chcluster        ! cluster only according to channel diag
 F        = pdfwgt           ! for ickkw=1, perform pdf reweighting
 5        = asrwgtflavor     ! highest quark flavor for a_s reweight
#*********************************************************************
# Automatic ptj and mjj cuts if xqcut > 0
# (turn off for VBF and single top processes)
#**********************************************************
   T  = auto_ptj_mjj  ! Automatic setting of ptj and mjj
#**********************************************************
#
#**********************************
# BW cutoff (M+/-bwcutoff*Gamma)
#**********************************
  15  = bwcutoff      ! (M+/-bwcutoff*Gamma)
```

```
#**********************************************************
# Apply pt/E/eta/dr/mij cuts on decay products or not
# (note that etmiss/ptll/ptheavy/ht/sorted cuts always apply)
#**********************************************************
   F  = cut_decays    ! Cut decay products
#*************************************************************
# Number of helicities to sum per event (0 = all helicities)
# 0 gives more stable result, but longer run time (needed for
# long decay chains e.g.).
# Use >=2 if most helicities contribute, e.g. pure QCD.
#*************************************************************
   0  = nhel          ! Number of helicities used per event
#*******************
# Standard Cuts
#*******************
#
#*********************************************************************
# Minimum and maximum pt's (for max, -1 means no cut)               *
#*********************************************************************
 20  = ptj       ! minimum pt for the jets
 20  = ptb       ! minimum pt for the b
 10  = pta       ! minimum pt for the photons
 10  = ptl       ! minimum pt for the charged leptons
  0  = misset    ! minimum missing Et (sum of neutrino's momenta)
  0  = ptheavy   ! minimum pt for one heavy final state
 1.0 = ptonium   ! minimum pt for the quarkonium states
 -1  = ptjmax    ! maximum pt for the jets
 -1  = ptbmax    ! maximum pt for the b
 -1  = ptamax    ! maximum pt for the photons
 -1  = ptlmax    ! maximum pt for the charged leptons
 -1  = missetmax ! maximum missing Et (sum of neutrino's momenta)
#*********************************************************************
# Minimum and maximum E's (in the lab frame)                        *
#*********************************************************************
  0  = ej     ! minimum E for the jets
  0  = eb     ! minimum E for the b
  0  = ea     ! minimum E for the photons
  0  = el     ! minimum E for the charged leptons
 -1   = ejmax ! maximum E for the jets
 -1   = ebmax ! maximum E for the b
 -1   = eamax ! maximum E for the photons
 -1   = elmax ! maximum E for the charged leptons
#*********************************************************************
# Maximum and minimum absolute rapidity (for max, -1 means no cut)   *
#*********************************************************************
   5  = etaj    ! max rap for the jets
   5  = etab    ! max rap for the b
 2.5  = etaa    ! max rap for the photons
 2.5  = etal    ! max rap for the charged leptons
 0.6  = etaonium ! max rap for the quarkonium states
```

```
   0  = etajmin ! min rap for the jets
   0  = etabmin ! min rap for the b
   0  = etaamin ! min rap for the photons
   0  = etalmin ! main rap for the charged leptons
#*********************************************************************
# Minimum and maximum DeltaR distance                                *
#*********************************************************************
 0.001 = drjj    ! min distance between jets
 0.01   = drbb    ! min distance between b's
 0.4 = drll    ! min distance between leptons
 0.4 = draa    ! min distance between gammas
 0.01   = drbj    ! min distance between b and jet
 0.4 = draj    ! min distance between gamma and jet
 0.4 = drjl    ! min distance between jet and lepton
 0.4   = drab    ! min distance between gamma and b
 0.4   = drbl    ! min distance between b and lepton
 0.4 = dral    ! min distance between gamma and lepton
 1d2  = drjjmax ! max distance between jets
 -1  = drbbmax ! max distance between b's
 -1  = drllmax ! max distance between leptons
 -1  = draamax ! max distance between gammas
 -1  = drbjmax ! max distance between b and jet
 -1  = drajmax ! max distance between gamma and jet
 -1  = drjlmax ! max distance between jet and lepton
 -1  = drabmax ! max distance between gamma and b
 -1  = drblmax ! max distance between b and lepton
 -1  = dralmax ! maxdistance between gamma and lepton
#*********************************************************************
# Minimum and maximum invariant mass for pairs                       *
#*********************************************************************
 0   = mmjj    ! min invariant mass of a jet pair
 0   = mmbb    ! min invariant mass of a b pair
 0   = mmaa    ! min invariant mass of gamma gamma pair
 0   = mmll    ! min invariant mass of l+l- (same flavour) lepton pair
 -1  = mmjjmax ! max invariant mass of a jet pair
 -1  = mmbbmax ! max invariant mass of a b pair
 -1  = mmaamax ! max invariant mass of gamma gamma pair
 -1  = mmllmax ! max invariant mass of l+l- (same flavour) lepton pair
#*********************************************************************
# Minimum and maximum invariant mass for all letpons                 *
#*********************************************************************
 0   = mmnl    ! min invariant mass for all letpons (l+- and vl)
 -1  = mmnlmax ! max invariant mass for all letpons (l+- and vl)
#*********************************************************************
# Minimum and maximum pt for 4-momenta sum of leptons                *
#*********************************************************************
 0   = ptllmin  ! Minimum pt for 4-momenta sum of leptons(l and vl)
 -1  = ptllmax  ! Maximum pt for 4-momenta sum of leptons(l and vl)
#*********************************************************************
# Inclusive cuts                                                     *
```

```
#*********************************************************************
 0  = xptj ! minimum pt for at least one jet
 0  = xptb ! minimum pt for at least one b
 0  = xpta ! minimum pt for at least one photon
 0  = xptl ! minimum pt for at least one charged lepton
#*********************************************************************
# Control the pt's of the jets sorted by pt                          *
#*********************************************************************
 0   = ptj1min ! minimum pt for the leading jet in pt
 0   = ptj2min ! minimum pt for the second jet in pt
 0   = ptj3min ! minimum pt for the third jet in pt
 0   = ptj4min ! minimum pt for the fourth jet in pt
 -1  = ptj1max ! maximum pt for the leading jet in pt
 -1  = ptj2max ! maximum pt for the second jet in pt
 -1  = ptj3max ! maximum pt for the third jet in pt
 -1  = ptj4max ! maximum pt for the fourth jet in pt
 0   = cutuse  ! reject event if fails any (0) / all (1) jet pt cuts
#*********************************************************************
# Control the pt's of leptons sorted by pt                           *
#*********************************************************************
 0   = ptl1min ! minimum pt for the leading lepton in pt
 0   = ptl2min ! minimum pt for the second lepton in pt
 0   = ptl3min ! minimum pt for the third lepton in pt
 0   = ptl4min ! minimum pt for the fourth lepton in pt
 -1  = ptl1max ! maximum pt for the leading lepton in pt
 -1  = ptl2max ! maximum pt for the second lepton in pt
 -1  = ptl3max ! maximum pt for the third lepton in pt
 -1  = ptl4max ! maximum pt for the fourth lepton in pt
#*********************************************************************
# Control the Ht(k)=Sum of k leading jets                            *
#*********************************************************************
 0   = htjmin ! minimum jet HT=Sum(jet pt)
 -1  = htjmax ! maximum jet HT=Sum(jet pt)
 0   = ihtmin  !inclusive Ht for all partons (including b)
 -1  = ihtmax  !inclusive Ht for all partons (including b)
 0   = ht2min ! minimum Ht for the two leading jets
 0   = ht3min ! minimum Ht for the three leading jets
 0   = ht4min ! minimum Ht for the four leading jets
 -1  = ht2max ! maximum Ht for the two leading jets
 -1  = ht3max ! maximum Ht for the three leading jets
 -1  = ht4max ! maximum Ht for the four leading jets
#*********************************************************************
# WBF cuts                                                           *
#*********************************************************************
 0   = xetamin ! minimum rapidity for two jets in the WBF case
 0   = deltaeta ! minimum rapidity for two jets in the WBF case
#*********************************************************************
# maximal pdg code for quark to be considered as a light jet         *
# (otherwise b cuts are applied)                                     *
#*********************************************************************
```

```
 5 = maxjetflavor    ! Maximum jet pdg code
#*********************************************************************
# Jet measure cuts                                                   *
#*********************************************************************
 20   = xqcut   ! minimum kt jet measure between partons
#*********************************************************************
```

Madgraph parameter card configuration

```
######################################################################
## PARAM_CARD AUTOMATICALY GENERATED BY MG5 FOLLOWING UFO MODEL   ####
######################################################################
##                                                                  ##
##  Width set on Auto will be computed following the information   ##
##        present in the decay.py files of the model. By default,  ##
##        this is only 1->2 decay modes.                            ##
##                                                                  ##
######################################################################

###################################
## INFORMATION FOR MASS
###################################
Block mass
    5 4.800000e+00 # MB
    6 1.725000e+02 # MT
   15 1.777000e+00 # MTA
   23 9.118800e+01 # MZ
   25 1.200000e+02 # MH
## Dependent parameters, given by model restrictions.
## Those values should be edited following the
## analytical expression. MG5 ignores those values
## but they are important for interfacing the output of MG5
## to external program such as Pythia.
  1 0.000000 # d : 0.0
  2 0.000000 # u : 0.0
  3 0.000000 # s : 0.0
  4 0.000000 # c : 0.0
  11 0.000000 # e- : 0.0
  12 0.000000 # ve : 0.0
  13 0.000000 # mu- : 0.0
  14 0.000000 # vm : 0.0
  16 0.000000 # vt : 0.0
  21 0.000000 # g : 0.0
  22 0.000000 # a : 0.0
  24 80.419002 # w+ : cmath.sqrt(MZ__exp__2/2. +
                #cmath.sqrt(MZ__exp__4/4. -
                #(aEW*cmath.pi*MZ__exp__2)/(Gf*sqrt__2)))

###################################
```

```
## INFORMATION FOR SMINPUTS
###################################
Block sminputs
    1 1.325070e+02 # aEWM1
    2 1.166390e-05 # Gf
    3 1.180000e-01 # aS

###################################
## INFORMATION FOR YUKAWA
###################################
Block yukawa
    5 4.700000e+00 # ymb
    6 1.730000e+02 # ymt
   15 1.777000e+00 # ymtau

###################################
## INFORMATION FOR DECAY
###################################
DECAY   6 1.491500e+00 # WT
DECAY  23 2.441404e+00 # WZ
DECAY  24 2.047600e+00 # WW
DECAY  25 5.753088e-03 # WH
## Dependent parameters, given by model restrictions.
## Those values should be edited following the
## analytical expression. MG5 ignores those values
## but they are important for interfacing the output of MG5
## to external program such as Pythia.
DECAY  1 0.000000 # d : 0.0
DECAY  2 0.000000 # u : 0.0
DECAY  3 0.000000 # s : 0.0
DECAY  4 0.000000 # c : 0.0
DECAY  5 0.000000 # b : 0.0
DECAY  11 0.000000 # e- : 0.0
DECAY  12 0.000000 # ve : 0.0
DECAY  13 0.000000 # mu- : 0.0
DECAY  14 0.000000 # vm : 0.0
DECAY  15 0.000000 # ta- : 0.0
DECAY  16 0.000000 # vt : 0.0
DECAY  21 0.000000 # g : 0.0
DECAY  22 0.000000 # a : 0.0
```

Madgraph process card configuration

```
#************************************************************
#*                        MadGraph 5                        *
#*                                                          *
#*                *                       *                 *
#*                  *        * *        *                   *
#*                    * * * * 5 * * * *                     *
```

```
#*                  *        * *        *                   *
#*                *                       *                 *
#*                                                          *
#*                                                          *
#*         VERSION 1.5.11                2013-06-21         *
#*                                                          *
#*    The MadGraph Development Team - Please visit us at    *
#*    https://server06.fynu.ucl.ac.be/projects/madgraph     *
#*                                                          *
#************************************************************
#*                                                          *
#*               Command File for MadGraph 5                *
#*                                                          *
#*     run as ./bin/mg5  filename                           *
#*                                                          *
#************************************************************

set group_subprocesses Auto
set ignore_six_quark_processes False
set gauge unitary
set complex_mass_scheme False
import model sm
define p = g u c d s u~ c~ d~ s~
define j = g u c d s u~ c~ d~ s~
define l+ = e+ mu+
define l- = e- mu-
define vl = ve vm vt
define vl~ = ve~ vm~ vt~
# Define multiparticle labels
define p = g u c d s u~ c~ d~ s~ b b~
define j = p
define l+ = e+ mu+ ta+
define l- = e- mu- ta-
define vl = ve vm vt
define vl~ = ve~ vm~ vt~
define lept = l+ l- vl vl~
# Specify process(es) to run
generate p p > t t~ @0
add process p p > t t~ j @1
add process p p > t t~ j j @2
add process p p > t t~ j j j @3
# Processes to MadEvent directory
output -f
```

MadSpin configuration (inclusive)

```
set seed 123456
set load_me True
set load_weights True
```

```
set compile_me False
set store_me False
set store_weights False
set max_calculators 1

import unweighted_events.lhe.gz
define ww = w+ w-
define bb = b b~
decay t > w+ b , w+ > all all
decay t~ > w- b~ , w- > all all
launch
```

MadSpin configuration (dilepton)

```
set seed 123456
set load_me True
set load_weights True
set compile_me False
set store_me False
set store_weights False
set max_calculators 1

import unweighted_events.lhe.gz
define ww = w+ w-
define bb = b b~
decay t > w+ b , w+ > lept lept
decay t~ > w- b~ , w- > lept lept
launch
```

Powheg 2 configuration

```
! TTbar production parameters
!randomseed 352345 ! uncomment to set the random seed to a value of your choice.
                   ! It generates the call RM48IN(352345,0,0) (see the RM48 manual).
                   ! THIS MAY ONLY AFFECTS THE GENERATION OF POWHEG EVENTS!
                   ! If POWHEG is interfaced to a shower MC, refer to the shower MC
                   ! documentation to set its seed.

!Heavy flavour production parameters

numevts 36051    ! number of events to be generated
iseed   52936029       ! Start the random number generator with seed iseed
ih1   1        ! hadron 1
ih2   1        ! hadron 2
#ndns1 131      ! pdf for hadron 1 (hvqpdf numbering)
#ndns2 131      ! pdf for hadron 2
```

```
! To be set only if using LHA pdfs
lhans1 10050       ! pdf set for hadron 1 (LHA numbering)
lhans2 10050       ! pdf set for hadron 2 (LHA numbering)
! To be set only if using different pdf sets for the two incoming hadrons
! QCDLambda5  0.25 ! for not equal pdf sets
ebeam1 3500    ! energy of beam 1
ebeam2 3500    ! energy of beam 2
qmass  172.5     ! mass of heavy quark in GeV
facscfact 1    ! factorization scale factor: mufact=muref*facscfact
renscfact 1    ! renormalization scale factor: muren=muref*renscfact
#fixedscale 1    ! use ref. scale=qmass (default 0, use running scale)
hdamp 172.5

topdecaymode 22222   ! an integer of 5 digits that are either 0, or 2,
                     !     representing in
                     ! the order the maximum number of the following
                     !    particles(antiparticles)
                     ! in the final state: e  mu tau up charm
                     ! For example
                     ! 22222    All decays (up to 2 units of everything)
                     ! 20000    both top go into b l nu
                     !            (with the appropriate signs)
                     ! 10011    one top goes into electron (or positron),
                     !            the other into (any) hadro
                     !          or one top goes into charm, the other into up
                     ! 00022    Fully hadronic
                     ! 00002    Fully hadronic with two charms
                     ! 00011    Fully hadronic with a single charm
                     ! 00012    Fully hadronic with at least one charm

!semileptonic 1      ! uncomment if you want to filter out only semileptonic events.
                     ! For example,
                     ! with topdecaymode 10011 and semileptonic 1 you get only events
                     ! with one top g
                     ! to an electron or positron, and the other into any hadron.

! Parameters for the generation of spin correlations in t tbar decays
tdec/wmass 80.4  ! W mass for top decay
tdec/wwidth 2.141
tdec/bmass 4.8
tdec/twidth  1.31
tdec/elbranching 0.108
tdec/emass 0.00051
tdec/mumass 0.1057
tdec/taumass 1.777
tdec/dmass   0.100
tdec/umass   0.100
tdec/smass   0.200
tdec/cmass   1.5
tdec/sin2cabibbo 0.051
```

```
! Parameters to allow-disallow use of stored data
use-old-grid 1    ! if 1 use old grid if file pwggrids.dat is present
                  !    (# 1: regenerate)
use-old-ubound 1  ! if 1 use norm of upper bounding function stored in
                  !    pwgubound.dat, if present; #

ncall1 10000   ! number of calls for initializing the integration grid
itmx1 5        ! number of iterations for initializing the integration grid
ncall2 100000  ! number of calls for computing the integral and finding
               !    upper bound
itmx2 5        ! number of iterations for computing the integral and finding
               !    upper bound
foldcsi   1      ! number of folds on x integration
foldy   1      ! number of folds on y integration
foldphi 1      ! number of folds on phi integration
nubound 100000  ! number of bbarra calls to setup norm of upper bounding function
iymax 1        ! <= 10, normalization of upper bounding function in iunorm X
               !    iunorm square in y, log
ixmax 1        ! <= 10, normalization of upper bounding function in iunorm X
               !    iunorm square in y, log
xupbound 2      ! increase upper bound for radiation generation

pdfreweight 1       ! PDF reweighting
dampreweight 1      ! h_damp reweighting (mt/2, mt, mt*2)
storeinfo_rwgt 1    ! store weight information
withnegweights 0    ! default 0

lhrwgt_id 'c'
lhrwgt_descr 'muR=0.10000E+01 muF=0.10000E+01'
lhrwgt_group_name 'scale_variation'
lhrwgt_group_combine 'envelope'
```

Powheg 1 configuration (dilepton)

```
! ST-wtchannel production parameter

withdamp    1      ! (default 0, do not use) use Born-zero damping factor

numevts 1000000    ! number of events to be generated
ih1   1           ! hadron 1 (1 for protons, -1 for antiprotons)
ih2   1           ! hadron 2 (1 for protons, -1 for antiprotons)
ebeam1 3500d0     ! energy of beam 1
ebeam2 3500d0     ! energy of beam 2

! To be set only if using LHA pdfs
lhans1 10050      ! pdf set for hadron 1 (LHA numbering)
lhans2 10050      ! pdf set for hadron 2 (LHA numbering)
! To be set only if using different pdf sets for the two incoming hadrons
```

```
! QCDLambda5  0.25 ! for not equal pdf sets

! Parameters to allow or not the use of stored data
use-old-grid    1 ! if 1 use old grid if file pwggrids.dat is present
                  !  (<> 1 regenerate)
use-old-ubound  1 ! if 1 use norm of upper bounding function stored in
                  !  pwgubound.dat, if present; <>

ncall1 50000   ! number of calls for initializing the integration grid
itmx1    5     ! number of iterations for initializing the integration grid
ncall2 50000   ! number of calls for computing the integral and finding upper
               !  bound
itmx2    5     ! number of iterations for computing the integral and finding
               !  upper bound
foldcsi   1    ! number of folds on csi integration
foldy     1    ! number of folds on  y  integration
foldphi   1    ! number of folds on phi integration
nubound 50000  ! number of bbarra calls to setup norm of upper bounding
               !  function
icsimax  1     ! <= 100, number of csi subdivision when computing the upper
               !  bounds
iymax    1     ! <= 100, number of y subdivision when computing the upper
               !  bounds
xupbound 2d0   ! increase upper bound for radiation generation

! PROCESS SPECIFIC PARAMETERS
! production parameters
ttype -1          ! 1 for t, -1 for tbar

topmass      172.5
wmass        80.398
sthw2        0.23113
alphaem_inv  127.011989

CKM_Vud   0.9740
CKM_Vus   0.2225
CKM_Vub   0.000001
CKM_Vcd   0.2225
CKM_Vcs   0.9740
CKM_Vcb   0.000001
CKM_Vtd   0.000001
CKM_Vts   0.000001
CKM_Vtb   1.0

! decay parameters
topwidth  1.7
wwidth    2.141


topdecaymode 11100   ! decay mode: the 5 digits correspond to the following
```

```
                     ! top-decay channels (l,mu,tau,u,c)
                     ! 0 means close, 1 open
wdecaymode 11100   ! decay mode: the 5 digits correspond to the following
                     ! primary-w-decay channels (l,mu,tau,u,c)
                     ! 0 means close, 1 open

tdec/elbranching 0.108  ! W electronic branching fraction

lhfm/cmass 1.28
lhfm/bmass 4.16
lhfm/emass 0.000511
lhfm/mumass 0.1056
lhfm/taumass 1.777

! OPTIONAL PARAMETERS
#renscfact  1d0   ! (default 1d0) ren scale factor: muren  = muref * renscfact
#facscfact  1d0   ! (default 1d0) fac scale factor: mufact = muref * facscfact
#ptsupp     0d0   ! (default 0d0)  mass param for Born suppression factor
                   !  (generation cut) If < 0 su
#bornonly   0      ! (default 0) if 1 do Born only
#smartsig   0      ! (default 1) remember equal amplitudes (0 do not remember)
#withsubtr  0      ! (default 1) subtract real counterterms (0 do not subtract)
#ptsqmin    0.8    ! (default 0.8 GeV) minimum pt for generation of radiation
#charmthr   1.5    ! (default 1.5 GeV) charm treshold for gluon splitting
#bottomthr  5.0    ! (default 5.0 GeV) bottom treshold for gluon splitting
#testplots  1      ! (default 0, do not) do NLO and PWHG distributions
#hfact    100d0    ! (default no dumping factor) dump factor for high-pt
                   !     radiation: > 0 dumpfac=h**2
#testsuda  1       ! (default 0, do not test) test Sudakov form factor
#radregion 1       ! (default all regions) only generate radiation in the
                   !    selected singular region
#charmthrpdf  1.5  ! (default 1.5 GeV) pdf charm treshold
#bottomthrpdf 5.0  ! (default 5.0 GeV) pdf bottom treshold

iseed    54217137    ! initialize random number sequence
rand1    326544694   ! initialize random number sequence
rand2    0           ! initialize random number sequence

#iupperisr 1 ! (default 1) choice of ISR upper bounding functional form
#iupperfsr 2 ! (default 2) choice of FSR upper bounding functional form
```

Appendix B

Determination of Trigger Efficiencies

In this section the detailed lists of dilepton triggers (Tables B.1 and B.2) and monitoring triggers (Table B.3 and B.4) are presented.

HLT_Mu10_Ele10_CaloIdL_*
HLT_Mu8_Ele17_CaloIdL_*
HLT_Mu17_Ele8_CaloIdL*
HLT_Mu17_Ele8_CaloIdT_CaloIsoVL_v*
HLT_Mu8_Ele17_CaloIdT_CaloIsoVL_v*

Table B.1: List of dilepton HLT paths employed to record data at $\sqrt{s} = 7\,\mathrm{TeV}$.

HLT_Mu17_Ele8_CaloIdT_CaloIsoVL_TrkIdVL_TrkIsoVL_v*
HLT_Mu8_Ele17_CaloIdT_CaloIsoVL_TrkIdVL_TrkIsoVL_v*

Table B.2: List of dilepton HLT paths employed to record data at $\sqrt{s} = 8\,\mathrm{TeV}$.

HLT_CentralJet80_MET65_v*
HLT_DiJet60_MET45_v*
HLT_DiCentralJet20_MET80_v*
HLT_CentralJet80_MET80_v*
HLT_CentralJet80_MET95_v*
HLT_DiCentralJet20_BTagIP_MET65_v*
HLT_DiCentralJet20_MET100_HBHENoiseFiltered_v*
HLT_CentralJet80_MET110_v*
HLT_MET120_HBHENoiseFiltered_v*
HLT_MET120_HBHENoiseFiltered_v*
HLT_MET200_HBHENoiseFiltered_v*
HLT_MET200_HBHENoiseFiltered_v*

Table B.3: List of $\not{E}_T$ triggers employed as monitoring triggers for the determination of the dilepton trigger efficiency at $\sqrt{s} = 7\,\mathrm{TeV}$.

HLT_MET120_HBHENoiseCleaned_v*
HLT_PFHT350_PFMET100_v*
HLT_PFHT400_PFMET100_v*
HLT_MonoCentralPFJet80_PFMETnoMu95_NHEF0p95_v*
HLT_MET120_v*
HLT_MET80_Track50_dEdx3p6_v*
HLT_MET80_Track60_dEdx3p7_v*
HLT_MET200_v*
HLT_MET200_HBHENoiseCleaned_v*
HLT_MET300_v*
HLT_MET300_HBHENoiseCleaned_v*
HLT_PFMET150_v*
HLT_DiPFJet40_PFMETnoMu65_MJJ800VBF_AllJets_v*
HLT_DiPFJet40_PFMETnoMu65_MJJ600VBF_LeadingJets_v*
HLT_PFMET180_v*
HLT_Photon70_CaloIdXL_PFMET100_v*
HLT_MonoCentralPFJet80_PFMETnoMu95_NHEF0p95_v*
HLT_DiPFJet40_PFMETnoMu65_MJJ600VBF_LeadingJets_v*
HLT_PFMET150_v*
HLT_PFMET180_v*
HLT_Photon70_CaloIdXL_PFMET100_v*
HLT_PFHT350_PFMET100_v*
HLT_PFHT400_PFMET100_v*
HLT_DiPFJet40_PFMETnoMu65_MJJ800VBF_AllJets_v*
HLT_MonoCentralPFJet80_PFMETnoMu95_NHEF0p95_v*
HLT_MET80_Track50_dEdx3p6_v*
HLT_MET80_Track60_dEdx3p7_v*
HLT_Photon70_CaloIdXL_PFMET100_v*
HLT_PFHT350_PFMET100_v*
HLT_MET120_HBHENoiseCleaned_v*
HLT_DiPFJet40_PFMETnoMu65_MJJ600VBF_LeadingJets_v*
HLT_PFMET150_v*
HLT_MET120_v*
HLT_MET200_v*
HLT_MET200_HBHENoiseCleaned_v*
HLT_MET300_v*
HLT_MET300_HBHENoiseCleaned_v*
HLT_MET400_v*
HLT_MET400_HBHENoiseCleaned_v*
HLT_PFHT400_PFMET100_v*
HLT_PFMET180_v*
HLT_DiPFJet40_PFMETnoMu65_MJJ800VBF_AllJets_v*
HLT_MET80_v*
HLT_MET400_v*
HLT_MET400_HBHENoiseCleaned_v*
HLT_PFHT350_PFMET100_v*
HLT_PFHT400_PFMET100_v*
HLT_MonoCentralPFJet80_PFMETnoMu95_NHEF0p95_v*
HLT_DiPFJet40_PFMETnoMu65_MJJ600VBF_LeadingJets_v*

Table B.4: List of $\not{E}_T$ triggers employed as monitoring triggers for the determination of the dilepton trigger efficiency at $\sqrt{s} = 8\,\text{TeV}$.

Appendix C

Fitted Parameters and Correlations

Here, pulls and constraints of all individual nuisance parameters in the fit of $\sigma_{\mathrm{t\bar{t}}}$ described in Chapter 5 are presented. In addition, estimates of the contribution from individual parameters to the total uncertainty on the fitted $\sigma_{\mathrm{t\bar{t}}}$ are listed in Tables C.1 and C.2 at $\sqrt{s} = 7$ and 8 TeV, respectively. The full correlation matrix with $148 \otimes 148$ entries can be found at:
`http://www.desy.de/~kiesej/thesis_pub/cross_section_corr.pdf`

Name	Pull	Constr / σ	Contribution [%]
BTAGH_BFragmentation	0.1	0.8	∓0.07
BTAGH_DeltaR	0.02	0.8	∓0.05
BTAGH_GluonSplitting	-0.13	0.6	∓0.05
BTAGH_IFSR	0	1	±0.00
BTAGH_IP-bias	-0.42	0.9	∓0.01
BTAGH_JetAway	0.41	0.7	∓0.12
BTAGH_KT	0	1	∓0.00
BTAGH_LT-Bias	0	1	∓0.00
BTAGH_LT-Cb	0.6	0.9	∓0.00
BTAGH_LT-others	0.18	0.6	∓0.15
BTAGH_MuPt	-0.02	0.8	∓0.02
BTAGH_PS	0	1	±0.00
BTAGH_PT-l2c	-0.17	0.8	∓0.02
BTAGH_S8-ptrel	0.87	0.9	∓0.03
BTAGH_TCT	0	1	∓0.00
JES: High p_T Extra	-0.32	1	∓0.11
JES: Single pion ECAL	0.09	0.7	∓0.04
JES: Single pion HCAL	-0.2	0.9	∓0.16
Top p_T	0.36	0.3	∓0.32
B-hadron ν decay fraction	-0.01	1	±0.00
b-fragmentation tune	0.5	0.4	±0.54
MG+PY → PH+PY	0	1	±0.46
ME/PS matching	-0.14	0.3	±0.00
Q^2 scale	0.06	0.2	∓0.38
PDF10	0.08	0.9	±0.01
PDF11	-0.05	1	∓0.06
PDF12	-0.16	0.9	±0.13
PDF13	0.02	1	∓0.02
PDF14	-0.03	1	∓0.00
PDF15	0.01	1	±0.02

Name	Pull	Constr / σ	Contribution [%]
PDF16	0.11	0.9	∓0.06
PDF17	-0.06	0.9	±0.18
PDF18	0.03	1	±0.03
PDF19	-0.02	1	∓0.00
PDF1	0.06	1	±0.03
PDF20	0.08	1	±0.03
PDF21	-0.03	1	∓0.02
PDF22	-0.01	1	∓0.01
PDF23	0.02	1	±0.03
PDF24	-0.05	0.9	∓0.07
PDF25	-0.01	1	∓0.00
PDF26	0.03	1	∓0.00
PDF2	-0.02	1	∓0.00
PDF3	-0.04	1	∓0.07
PDF4	-0.11	0.9	±0.01
PDF5	0.06	1	±0.02
PDF6	0.04	0.9	±0.02
PDF7	0	1	±0.05
PDF8	0.01	1	∓0.00
PDF9	0	1	±0.01
Color reconnection	-0.24	0.3	±0.12
Underlying event	-0.13	0.4	±0.04
JES: Flavor	-0.02	0.8	±0.10
JES: Absolute Stat (7TeV)	-0.7	0.8	∓0.03
JES: Absolute Scale (7TeV)	-0.44	0.8	∓0.05
JES: Time (7TeV)	-0.55	1.1	∓0.11
JES: Relative JER EC1 (7TeV)	-0.16	1	∓0.05
JES: Relative JER EC2 (7TeV)	0	1	∓0.00
JES: Relative JER HF (7TeV)	0	1	∓0.00
JES: Relative p_T BB (7TeV)	-0.7	0.8	∓0.03
JES: Relative p_T EC1 (7TeV)	-0.38	1	∓0.11
JES: Relative p_T EC2 (7TeV)	0	1	∓0.00
JES: Relative p_T HF (7TeV)	0	1	∓0.00
JES: Relative Stat EC2 (7TeV)	0	1	∓0.00
JES: Relative Stat HF (7TeV)	0	1	∓0.00
JES: Pileup Data/MC (7TeV)	0.15	1	∓0.02
JES: Pileup Bias (7TeV)	0	1	∓0.00
JES: Intercalibration (7TeV)	0.03	0.9	∓0.01
JES: MPF (7TeV)	-0.7	0.8	∓0.03
JES: Pileup p_T BB (7TeV)	-1.36	0.8	∓0.37
JES: Pileup p_T EC (7TeV)	-0.71	0.7	∓0.17
JES: Pileup p_T HF (7TeV)	0	1	∓0.00
Jet energy resolution	0.42	0.9	∓0.07
Jet energy resolution (7TeV)	-0.12	1	∓0.02
Muon energy scale	-0.15	0.8	∓0.08
Muon energy scale (7TeV)	-0.07	1	∓0.06

Name	Pull	Constr / σ	Contribution [%]
Muon ID	0.04	1	∓0.82
Muon ID (7TeV)	0.04	1	∓0.40
Electron energy scale	-0.02	1	∓0.05
Electron energy scale (7TeV)	-0.04	1	∓0.03
Electron ID	0.06	1	∓1.02
Electron ID (7TeV)	0.04	1	∓0.50
BTAGH_Statistic (7TeV)	0.24	0.6	∓0.18
BTAGH_JES	0	0.9	∓0.01
BTAGH_JES (7TeV)	0	0.7	∓0.03
Mistag	-1.7	0.6	∓0.00
Mistag (7TeV)	-0.1	0.9	∓0.03
Trigger	0.04	1	∓1.04
Trigger (7TeV)	0.1	1	∓0.78
Pile-up	0	0.9	±0.09
Pile-up (7TeV)	-0.24	0.8	±0.21
Single top background	0.16	0.7	∓0.74
Single top background (7TeV)	0.82	1	∓0.59
Diboson background	0.75	0.8	±0.21
Diboson background (7TeV)	0.61	1	±0.08
$t\bar{t}$ background	0.01	1	∓0.08
$t\bar{t}$ background (7TeV)	0	1	∓0.04
BG_QCD/Wjets	-0.15	0.8	±0.02
BG_QCD/Wjets (7TeV)	0.14	1	±0.01
$t\bar{t}+V$ background	0.12	1	∓0.00
$t\bar{t}+V$ background (7TeV)	0	1	∓0.00
DY background (0 b-jets)	-0.1	0.4	±0.50
DY background (0 b-jets) (7TeV)	-0.19	0.7	±0.51
DY background (1 b-jets)	-0.23	1	∓0.01
DY background (1 b-jets) (7TeV)	0.07	1	∓0.03
DY background (2 b-jets)	0.01	1	∓0.01
DY background (2 b-jets) (7TeV)	0	1	∓0.01
Lumi (7TeV)	0.24	1	∓2.28
JES: Absolute Stat (8TeV)	0.25	0.9	±0.05
JES: Absolute Scale (8TeV)	0.23	0.9	±0.01
JES: Time (8TeV)	1.16	1.2	±0.04
JES: Relative JER EC1 (8TeV)	-0.03	1.3	∓0.00
JES: Relative JER EC2 (8TeV)	0	1	∓0.00
JES: Relative JER HF (8TeV)	0	1	∓0.00
JES: Relative p_T BB (8TeV)	0.23	0.5	±0.08
JES: Relative p_T EC1 (8TeV)	-0.89	1.5	±0.06
JES: Relative p_T EC2 (8TeV)	0	1	∓0.00
JES: Relative p_T HF (8TeV)	0	1	∓0.00
JES: Relative Stat EC2 (8TeV)	0	1	±0.00
JES: Relative Stat HF (8TeV)	0	1	∓0.00
JES: Pileup Data/MC (8TeV)	0.13	0.9	∓0.02
JES: Pileup Bias (8TeV)	0	1	∓0.00

Name	Pull	Constr / σ	Contribution [%]
JES: Intercalibration (8TeV)	0.07	1.1	∓0.00
JES: MPF (8TeV)	0.32	1	±0.15
JES: Pileup p_T BB (8TeV)	0.41	0.7	∓0.29
JES: Pileup p_T EC (8TeV)	0.54	0.6	∓0.09
JES: Pileup p_T HF (8TeV)	0	1	±0.00
Jet energy resolution (8TeV)	0.31	1	±0.03
Muon energy scale (8TeV)	-0.03	0.9	±0.00
Muon ID (8TeV)	-0.02	1	±0.00
Electron energy scale (8TeV)	0.03	1	±0.00
Electron ID (8TeV)	-0.01	1	±0.00
BTAGH_Statistic (8TeV)	1.1	0.6	∓0.05
BTAGH_JES (8TeV)	-0.01	0.9	∓0.00
Mistag (8TeV)	-0.33	0.8	±0.07
Trigger (8TeV)	-0.07	1	±0.00
Pile-up (8TeV)	0.28	0.9	∓0.05
Single top background (8TeV)	-0.74	0.9	±0.35
Diboson background (8TeV)	-0.25	0.9	±0.01
$t\bar{t}$ background (8TeV)	0	1	±0.00
BG_QCD/Wjets (8TeV)	-0.21	1	±0.00
$t\bar{t}+V$ background (8TeV)	0.06	1	∓0.00
DY background (0 b-jets) (8TeV)	0.14	0.7	∓0.35
DY background (1 b-jets) (8TeV)	-0.18	1	±0.02
DY background (2 b-jets) (8TeV)	0	1	±0.00
Lumi (8TeV)	-0.23	1	±0.01
Stat			∓1.24
Total vis			$\pm^{3.55}_{3.37}$
$\sigma_{t\bar{t}}$(7 TeV) vis			3.04 pb
Q^2 scale (extr)			$\mp^{0.02}_{0.40}$
ME/PS matching (extr)			$\pm^{0.06}_{0.15}$
PDF (extr)			$\pm^{0.20}_{0.14}$
Top p_T (extr)			$\pm^{0.43}_{0.24}$
Total			$\pm^{3.58}_{3.41}$
$\sigma_{t\bar{t}}$(7 TeV)			173.9 pb

Table C.1: Extracted cross-sections for $\sqrt{s} = 7\,\text{TeV}$ including a detailed list of contributions from all nuisance parameters to the total uncertainty. The pulls and constraints on parameters are normalized to the pre-fit ±1 sigma variation.

Name	Pull	Constr / σ	Contribution [%]
BTAGH_BFragmentation	0.1	0.8	∓0.02
BTAGH_DeltaR	0.02	0.8	∓0.08
BTAGH_GluonSplitting	-0.13	0.6	∓0.00
BTAGH_IFSR	0	1	±0.00
BTAGH_IP-bias	-0.42	0.9	∓0.01
BTAGH_JetAway	0.41	0.7	∓0.17
BTAGH_KT	0	1	∓0.00

Name	Pull	Constr / σ	Contribution [%]
BTAGH_LT-Bias	0	1	∓0.00
BTAGH_LT-Cb	0.6	0.9	±0.01
BTAGH_LT-others	0.18	0.6	∓0.08
BTAGH_MuPt	-0.02	0.8	∓0.02
BTAGH_PS	0	1	±0.00
BTAGH_PT-l2c	-0.17	0.8	∓0.01
BTAGH_S8-ptrel	0.87	0.9	±0.03
BTAGH_TCT	0	1	∓0.00
JES: High p_T Extra	-0.32	1	∓0.11
JES: Single pion ECAL	0.09	0.7	∓0.03
JES: Single pion HCAL	-0.2	0.9	∓0.31
Top p_T	0.36	0.3	∓0.37
B-hadron ν decay fraction	-0.01	1	±0.19
b-fragmentation tune	0.5	0.4	±0.69
MG+PY → PH+PY	0	1	±0.51
ME/PS matching	-0.14	0.3	±0.09
Q^2 scale	0.06	0.2	∓0.62
PDF10	0.08	0.9	±0.02
PDF11	-0.05	1	∓0.06
PDF12	-0.16	0.9	±0.24
PDF13	0.02	1	∓0.01
PDF14	-0.03	1	±0.01
PDF15	0.01	1	±0.03
PDF16	0.11	0.9	∓0.06
PDF17	-0.06	0.9	±0.20
PDF18	0.03	1	∓0.02
PDF19	-0.02	1	∓0.01
PDF1	0.06	1	±0.03
PDF20	0.08	1	∓0.00
PDF21	-0.03	1	∓0.03
PDF22	-0.01	1	∓0.01
PDF23	0.02	1	±0.02
PDF24	-0.05	0.9	∓0.06
PDF25	-0.01	1	∓0.00
PDF26	0.03	1	∓0.03
PDF2	-0.02	1	±0.00
PDF3	-0.04	1	∓0.07
PDF4	-0.11	0.9	±0.03
PDF5	0.06	1	±0.03
PDF6	0.04	0.9	±0.02
PDF7	0	1	±0.03
PDF8	0.01	1	∓0.01
PDF9	0	1	∓0.01
Color reconnection	-0.24	0.3	±0.16
Underlying event	-0.13	0.4	±0.05
JES: Flavor	-0.02	0.8	±0.20

Name	Pull	Constr / σ	Contribution [%]
JES: Absolute Stat (7TeV)	-0.7	0.8	±0.04
JES: Absolute Scale (7TeV)	-0.44	0.8	±0.04
JES: Time (7TeV)	-0.55	1.1	±0.01
JES: Relative JER EC1 (7TeV)	-0.16	1	±0.00
JES: Relative JER EC2 (7TeV)	0	1	∓0.00
JES: Relative JER HF (7TeV)	0	1	∓0.00
JES: Relative p_T BB (7TeV)	-0.7	0.8	±0.08
JES: Relative p_T EC1 (7TeV)	-0.38	1	±0.02
JES: Relative p_T EC2 (7TeV)	0	1	∓0.00
JES: Relative p_T HF (7TeV)	0	1	∓0.00
JES: Relative Stat EC2 (7TeV)	0	1	∓0.00
JES: Relative Stat HF (7TeV)	0	1	∓0.00
JES: Pileup Data/MC (7TeV)	0.15	1	±0.01
JES: Pileup Bias (7TeV)	0	1	∓0.00
JES: Intercalibration (7TeV)	0.03	0.9	±0.01
JES: MPF (7TeV)	-0.7	0.8	±0.04
JES: Pileup p_T BB (7TeV)	-1.36	0.8	∓0.05
JES: Pileup p_T EC (7TeV)	-0.71	0.7	±0.04
JES: Pileup p_T HF (7TeV)	0	1	∓0.00
Jet energy resolution	0.42	0.9	±0.01
Jet energy resolution (7TeV)	-0.12	1	∓0.02
Muon energy scale	-0.15	0.8	∓0.09
Muon energy scale (7TeV)	-0.07	1	∓0.00
Muon ID	0.04	1	∓0.89
Muon ID (7TeV)	0.04	1	∓0.02
Electron energy scale	-0.02	1	∓0.03
Electron energy scale (7TeV)	-0.04	1	±0.00
Electron ID	0.06	1	∓1.02
Electron ID (7TeV)	0.04	1	∓0.02
BTAGH_Statistic (7TeV)	0.24	0.6	∓0.07
BTAGH_JES	0	0.9	∓0.00
BTAGH_JES (7TeV)	0	0.7	∓0.01
Mistag	-1.7	0.6	∓0.12
Mistag (7TeV)	-0.1	0.9	∓0.01
Trigger	0.04	1	∓0.97
Trigger (7TeV)	0.1	1	∓0.04
Pile-up	0	0.9	±0.12
Pile-up (7TeV)	-0.24	0.8	±0.02
Single top background	0.16	0.7	∓0.57
Single top background (7TeV)	0.82	1	∓0.15
Diboson background	0.75	0.8	±0.44
Diboson background (7TeV)	0.61	1	∓0.16
$t\bar{t}$ background	0.01	1	∓0.08
$t\bar{t}$ background (7TeV)	0	1	±0.00
BG_QCD/Wjets	-0.15	0.8	±0.05
BG_QCD/Wjets (7TeV)	0.14	1	∓0.02

Name	Pull	Constr / σ	Contribution [%]
$t\bar{t}+V$ background	0.12	1	∓0.09
$t\bar{t}+V$ background (7TeV)	0	1	∓0.00
DY background (0 b-jets)	-0.1	0.4	±0.46
DY background (0 b-jets) (7TeV)	-0.19	0.7	∓0.33
DY background (1 b-jets)	-0.23	1	∓0.02
DY background (1 b-jets) (7TeV)	0.07	1	∓0.01
DY background (2 b-jets)	0.01	1	∓0.01
DY background (2 b-jets) (7TeV)	0	1	∓0.00
Lumi (7TeV)	0.24	1	∓0.10
JES: Absolute Stat (8TeV)	0.25	0.9	±0.03
JES: Absolute Scale (8TeV)	0.23	0.9	∓0.03
JES: Time (8TeV)	1.16	1.2	∓0.09
JES: Relative JER EC1 (8TeV)	-0.03	1.3	±0.01
JES: Relative JER EC2 (8TeV)	0	1	∓0.00
JES: Relative JER HF (8TeV)	0	1	∓0.00
JES: Relative p_T BB (8TeV)	0.23	0.5	±0.01
JES: Relative p_T EC1 (8TeV)	-0.89	1.5	∓0.02
JES: Relative p_T EC2 (8TeV)	0	1	∓0.00
JES: Relative p_T HF (8TeV)	0	1	∓0.00
JES: Relative Stat EC2 (8TeV)	0	1	±0.00
JES: Relative Stat HF (8TeV)	0	1	∓0.00
JES: Pileup Data/MC (8TeV)	0.13	0.9	∓0.10
JES: Pileup Bias (8TeV)	0	1	∓0.00
JES: Intercalibration (8TeV)	0.07	1.1	∓0.01
JES: MPF (8TeV)	0.32	1	±0.06
JES: Pileup p_T BB (8TeV)	0.41	0.7	∓0.71
JES: Pileup p_T EC (8TeV)	0.54	0.6	∓0.23
JES: Pileup p_T HF (8TeV)	0	1	±0.00
Jet energy resolution (8TeV)	0.31	1	±0.01
Muon energy scale (8TeV)	-0.03	0.9	∓0.04
Muon ID (8TeV)	-0.02	1	∓0.41
Electron energy scale (8TeV)	0.03	1	∓0.02
Electron ID (8TeV)	-0.01	1	∓0.47
BTAGH_Statistic (8TeV)	1.1	0.6	∓0.18
BTAGH_JES (8TeV)	-0.01	0.9	±0.00
Mistag (8TeV)	-0.33	0.8	±0.09
Trigger (8TeV)	-0.07	1	∓0.69
Pile-up (8TeV)	0.28	0.9	±0.21
Single top background (8TeV)	-0.74	0.9	∓0.05
Diboson background (8TeV)	-0.25	0.9	±0.35
$t\bar{t}$ background (8TeV)	0	1	∓0.04
BG_QCD/Wjets (8TeV)	-0.21	1	±0.04
$t\bar{t}+V$ background (8TeV)	0.06	1	∓0.04
DY background (0 b-jets) (8TeV)	0.14	0.7	±0.46
DY background (1 b-jets) (8TeV)	-0.18	1	±0.00
DY background (2 b-jets) (8TeV)	0	1	∓0.00

Name	Pull	Constr / σ	Contribution [%]
Lumi (8TeV)	-0.23	1	∓ 2.62
Stat			∓ 0.55
Total vis			$\pm^{3.67}_{3.43}$
$\sigma_{t\bar{t}}$(8 TeV) vis			4.24 pb
Q^2 scale (extr)			$\pm^{0.20}_{0.08}$
ME/PS matching (extr)			$\pm^{0.27}_{0.32}$
PDF (extr)			$\pm^{0.21}_{0.15}$
Top p_T (extr)			$\pm^{0.75}_{0.43}$
Total			$\pm^{3.76}_{3.48}$
$\sigma_{t\bar{t}}$(8 TeV)			245.6 pb

Table C.2: Extracted cross-sections for $\sqrt{s} = 8\,\text{TeV}$ including a detailed list of contributions from all nuisance parameters to the total uncertainty. The pulls and constraints on parameters are normalized to the pre-fit ±1 sigma variation.

Appendix D

Extraction of m_t from $\mathrm{m_{lb}}$

For the extraction of m_t^{MC} from the $\mathrm{m_{lb}^{min}}$ distribution, the variation due to m_t^{MC} of the predicted normalized event yields in each bin of the distribution is fitted with second-order polynomials, which describe he dependence well as shown in Figure D.1. The parameters of the functional form are mainly determined by the central, and the outermost m_t^{MC} points.

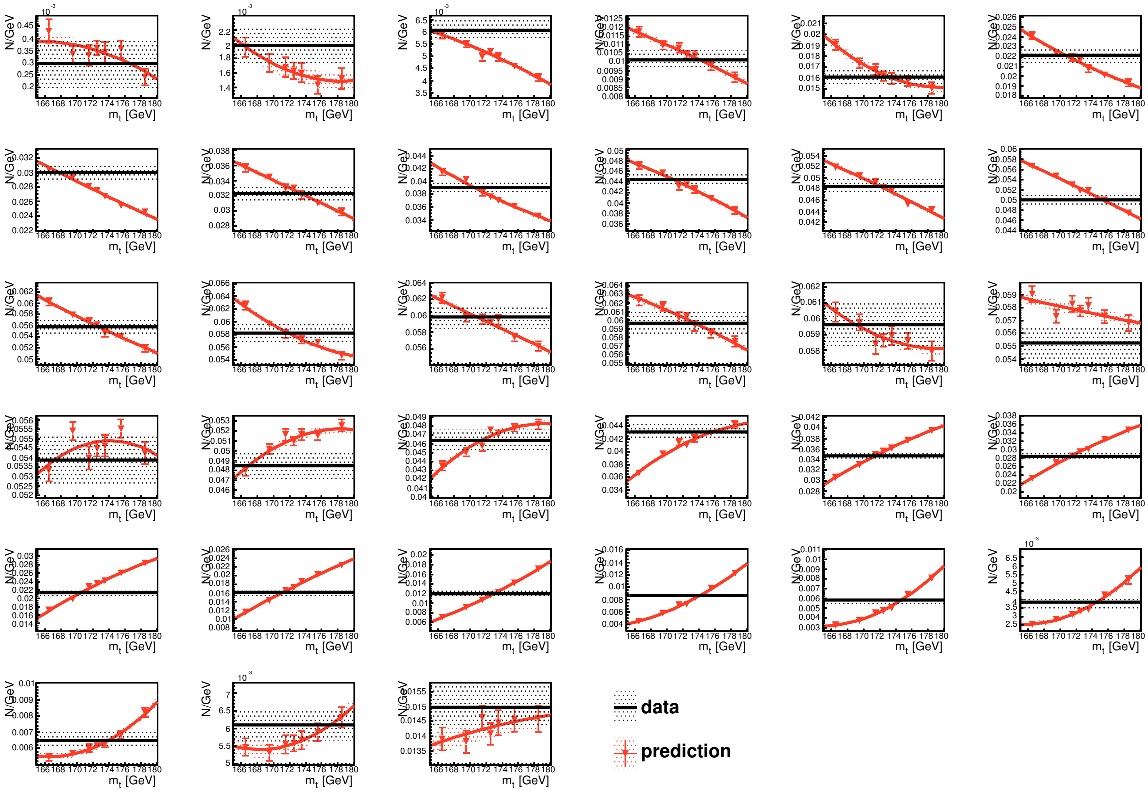

Figure D.1: Dependence on m_t^{MC} of the predicted and observed event yield in each bin of the normalized $\mathrm{m_{lb}^{min}}$ distribution, represented by triangles with error bars or a line with a shaded band, respectively. The error bars and the shaded bands correspond to the statistical uncertainties on the data and the simulation. The fit to the predicted dependence with second-order polynomials is shown as a red line. The uncertainty on the fitted curve is very small and indicated by a red shaded area.

The configuration of MCFM used to predict the $t\bar{t}$ production cross section as a function of $m_{lb,pred}^{min}$ is presented below. The parameters that are varied are explicitly given in Section 6.2 and indicated with “see text”.

```
                     MCFM configuration

'6.7'           [file version number]

[Flags to specify the mode in which MCFM is run]
-1              [nevtrequested]
.false.         [creatent]
.false.         [skipnt]
.false.         [dswhisto]
.false.         [creategrid]
.true.          [writetop]
.false.         [writedat]
.false.         [writegnu]
.true.          [writeroot]
.false.         [writepwg]

[General options to specify the process and execution]
141             [nproc]
(see text)      [part 'lord','real' or 'virt','tota']
runname         ['runstring']
8000            [sqrts in GeV]
+1              [ih1 =1 for proton and -1 for antiproton]
+1              [ih2 =1 for proton and -1 for antiproton]
126d0           [hmass]
(see text)      [scale:QCD scale choice]
(see text)      [facscale:QCD fac_scale choice]
'no'            [dynamicscale]
.false.         [zerowidth]
.false.         [removebr]
10              [itmx1, number of iterations for pre-conditioning]
2000000         [ncall1]
10              [itmx2, number of iterations for final run]
2000000         [ncall2]
1089            [ij]
.false.         [dryrun]
.true.          [Qflag]
.true.          [Gflag]

[Heavy quark masses]
(see text)      [top mass]
(see text)      [bottom mass]
1.5d0           [charm mass]

[Pdf selection]
(see text)

[Jet definition and event cuts]
```

```
0d0             [m34min]
14000d0         [m34max]
0d0             [m56min]
14000d0         [m56max]
.true.          [inclusive]
'ankt'          [algorithm]
0d0             [ptjet_min]
0d0             [|etajet|_min]
99d0            [|etajet|_max]
0.5d0           [Rcut_jet]
.true.          [makecuts]
20d0            [ptlepton_min]
2.4d0           [|etalepton|_max]
0d0,0d0         [|etalepton|_veto]
0d0             [ptmin_missing]
20d0            [ptlepton(2nd+)_min]
2.4d0           [|etalepton(2nd+)|_max]
0d0,0d0         [|etalepton(2nd+)|_veto]
0d0             [minimum (3,4) transverse mass]
0d0             [R(jet,lept)_min]
0d0             [R(lept,lept)_min]
0d0             [Delta_eta(jet,jet)_min]
.false.         [jets_opphem]
0               [lepbtwnjets_scheme]
0d0            [ptmin_bjet]
99d0            [etamax_bjet]

[Settings for photon processes]
.false.         [fragmentation included]
'BFGsetII'      [fragmentation set]
80d0            [fragmentation scale]
20d0            [ptmin_photon]
2.5d0           [etamax_photon]
10d0            [ptmin_photon(2nd)]
10d0            [ptmin_photon(3rd)]
0.7d0           [R(photon,lept)_min]
0.4d0           [R(photon,photon)_min]
0.4d0           [R(photon,jet)_min]
0.7d0           [cone size for isolation]
0.4d0           [epsilon_h, energy fraction for isolation]

[Anomalous couplings of the W and Z]
0.0d0           [Delta_g1(Z)]
0.0d0           [Delta_K(Z)]
0.0d0           [Delta_K(gamma)]
0.0d0           [Lambda(Z)]
0.0d0           [Lambda(gamma)]
0.0d0           [h1(Z)]
0.0d0           [h1(gamma)]
0.0d0           [h2(Z)]
```

```
0.0d0           [h2(gamma)]
0.0d0           [h3(Z)]
0.0d0           [h3(gamma)]
0.0d0           [h4(Z)]
0.0d0           [h4(gamma)]
2.0d0           [Form-factor scale, in TeV]

[Anomalous width of the Higgs]
1d0             [Gamma_H/Gamma_H(SM)]

[How to resume/save a run]
.false.         [readin]
.false.         [writeout]
''              [ingridfile]
''              [outgridfile]

[Technical parameters that should not normally be changed]
.false.         [debug]
.true.          [verbose]
.false.         [new_pspace]
.false.         [virtonly]
.false.         [realonly]
.true.          [spira]
.false.         [noglue]
.false.         [ggonly]
.false.         [gqonly]
.false.         [omitgg]
.false.         [vanillafiles]
1               [nmin]
2               [nmax]
.true.          [clustering]
.false.         [realwt]
0               [colourchoice]
1d-2            [rtsmin]
1d-4            [cutoff]
0.2d0           [aii]
0.2d0           [aif]
0.2d0           [afi]
1d0             [aff]
1d0             [bfi]
1d0             [bff]
```

Appendix E

Fitted Parameters and Correlations in the Fit of $\sigma_{\mathrm{t\bar{t}}}$ and m_t^{MC}

In this appendix, pulls and constraints of all individual parameters in the simultaneous fit of $\sigma_{\mathrm{t\bar{t}}}$ and m_t^{MC} described in Chapter 7 are listed. In addition, estimates of the contribution from individual parameters to the total uncertainty on the fitted $\sigma_{\mathrm{t\bar{t}}}$ and m_t^{MC} are listed in Tables E.1 and E.2 at $\sqrt{s} = 7$ and 8 TeV, respectively. The full correlation matrix with $149 \otimes 149$ entries can be found at:
`http://www.desy.de/~kiesej/thesis_pub/cross_section_mt_corr.pdf`

Name	Pull	Constr / σ	Contribution [%]
BTAGH_BFragmentation	-0.404	1.1	-0.085
BTAGH_DeltaR	0.214	0.9	0.006
BTAGH_GluonSplitting	-0.398	1	-0.081
BTAGH_IFSR	0	1	0.000
BTAGH_IP-bias	-0.009	1.1	0.014
BTAGH_JetAway	1.348	0.9	0.066
BTAGH_KT	0	1	0.000
BTAGH_LT-Bias	0	1	0.000
BTAGH_LT-Cb	0.506	1.1	-0.026
BTAGH_LT-others	0.557	1.5	-0.044
BTAGH_MuPt	0.057	1	-0.011
BTAGH_PS	0	1	0.000
BTAGH_PT-l2c	-0.244	1	-0.015
BTAGH_S8-ptrel	0.513	1.1	-0.034
BTAGH_TCT	0	1	0.000
JES: High p_T Extra	0.167	0.8	-0.104
JES: Single pion ECAL	0.07	0.7	-0.060
JES: Single pion HCAL	0.077	0.6	-0.131
Top p_T	0.307	0.4	0.065
B-hadron ν decay fraction	0.399	1.1	-0.119
b-fragmentation tune	0.495	0.4	0.364
MG+PY → PH+PY	0.02	0.2	0.427
ME/PS matching	-0.093	0.3	-0.056
Q^2 scale	0.143	0.2	-0.334
PDF10	0.08	1	0.020
PDF11	0.1	1.1	-0.033
PDF12	0.275	1	0.278
PDF13	0.001	0.2	-0.003

Name	Pull	Constr / σ	Contribution [%]
PDF14	0.058	1.1	0.012
PDF15	0.006	1.1	0.024
PDF16	0.102	1.1	-0.051
PDF17	0.148	1.1	0.194
PDF18	-0.044	1	-0.003
PDF19	0.011	1	0.000
PDF1	-0.016	1.1	0.022
PDF20	-0.028	1	0.010
PDF21	-0.027	1.1	-0.027
PDF22	0.002	0.3	-0.004
PDF23	-0.035	1.1	0.021
PDF24	0	0.1	-0.003
PDF25	0.009	1.1	-0.001
PDF26	0.044	1	-0.018
PDF2	0	0.1	0.002
PDF3	0.21	1.1	-0.046
PDF4	0.15	1.1	0.020
PDF5	0.092	1.1	0.025
PDF6	0.057	1.1	0.022
PDF7	-0.083	1	0.011
PDF8	0.049	1.1	0.002
PDF9	-0.019	1.1	-0.006
Color reconnection	-0.07	0.7	0.132
Underlying event	0.022	0.3	0.074
JES: Flavor	0.436	0.5	0.085
JES: Absolute Stat (7TeV)	-0.482	0.9	-0.025
JES: Absolute Scale (7TeV)	-0.445	1.2	-0.056
JES: Time (7TeV)	-1.04	1.6	-0.140
JES: Relative JER EC1 (7TeV)	-0.309	1.2	-0.036
JES: Relative JER EC2 (7TeV)	0	1	0.000
JES: Relative JER HF (7TeV)	0	1	0.000
JES: Relative p_T BB (7TeV)	-0.496	0.9	-0.048
JES: Relative p_T EC1 (7TeV)	-0.46	1.1	-0.102
JES: Relative p_T EC2 (7TeV)	0	1	0.000
JES: Relative p_T HF (7TeV)	0	1	0.000
JES: Relative Stat EC2 (7TeV)	0	1	0.000
JES: Relative Stat HF (7TeV)	0	1	0.000
JES: Pileup Data/MC (7TeV)	0.051	1.1	-0.020
JES: Pileup Bias (7TeV)	0	1	0.000
JES: Intercalibration (7TeV)	-0.019	1	-0.010
JES: MPF (7TeV)	-0.482	0.9	-0.025
JES: Pileup p_T BB (7TeV)	-1.43	0.7	-0.366
JES: Pileup p_T EC (7TeV)	-1.605	0.8	-0.123
JES: Pileup p_T HF (7TeV)	0	1	0.000
Jet energy resolution	-0.421	0.9	0.016
Jet energy resolution (7TeV)	-0.665	1.7	0.013

Name	Pull	Constr / σ	Contribution [%]
Muon energy scale	-0.083	0.8	-0.043
Muon energy scale (7TeV)	-0.065	1.1	-0.039
Muon ID	-0.029	1	-0.811
Muon ID (7TeV)	0.05	1	-0.401
Electron energy scale	-0.047	0.9	0.025
Electron energy scale (7TeV)	0.006	1	0.004
Electron ID	0.135	1	-1.046
Electron ID (7TeV)	0.047	1	-0.501
BTAGH_Statistic (7TeV)	0.019	1.3	-0.141
BTAGH_JES	-0.031	1	-0.009
BTAGH_JES (7TeV)	-0.077	1.1	-0.031
Mistag	-0.675	0.7	0.066
Mistag (7TeV)	0.15	0.9	-0.046
Trigger	0.05	1	-1.031
Trigger (7TeV)	0.107	1	-0.782
Pile-up	-0.059	1	0.043
Pile-up (7TeV)	-0.242	0.8	0.275
Single top background	0.324	0.6	-0.602
Single top background (7TeV)	1.019	0.9	-0.539
Diboson background	0.735	0.7	0.247
Diboson background (7TeV)	0.545	0.9	0.077
$t\bar{t}$ background	0.061	1	-0.074
$t\bar{t}$ background (7TeV)	0.025	1	-0.034
BG_QCD/Wjets	-0.104	0.8	0.032
BG_QCD/Wjets (7TeV)	0.179	1	-0.004
$t\bar{t} + V$ background	-0.006	1	-0.025
$t\bar{t} + V$ background (7TeV)	-0.296	1	-0.115
DY background (0 b-jets)	-0.082	0.4	0.496
DY background (0 b-jets) (7TeV)	-0.125	0.7	0.511
DY background (1 b-jets)	0.025	0.9	0.070
DY background (1 b-jets) (7TeV)	0.088	1	-0.015
DY background (2 b-jets)	0.021	1	-0.006
DY background (2 b-jets) (7TeV)	-0.007	1	-0.003
Lumi (7TeV)	0.279	1	-2.283
JES: Absolute Stat (8TeV)	0.119	0.6	0.020
JES: Absolute Scale (8TeV)	0.1	0.8	0.020
JES: Time (8TeV)	0.188	1.2	0.026
JES: Relative JER EC1 (8TeV)	0.002	0.2	-0.002
JES: Relative JER EC2 (8TeV)	0	1	0.000
JES: Relative JER HF (8TeV)	0	1	0.000
JES: Relative p_T BB (8TeV)	0.001	0.5	0.038
JES: Relative p_T EC1 (8TeV)	0.044	1.4	0.007
JES: Relative p_T EC2 (8TeV)	0	1	0.000
JES: Relative p_T HF (8TeV)	0	1	0.000
JES: Relative Stat EC2 (8TeV)	0	1	0.000
JES: Relative Stat HF (8TeV)	0	1	0.000

Name	Pull	Constr / σ	Contribution [%]
JES: Pileup Data/MC (8TeV)	0.226	0.8	-0.021
JES: Pileup Bias (8TeV)	0	1	0.000
JES: Intercalibration (8TeV)	-0.041	0.9	-0.007
JES: MPF (8TeV)	0.164	0.7	0.064
JES: Pileup p_T BB (8TeV)	0.408	0.5	-0.124
JES: Pileup p_T EC (8TeV)	0.748	0.6	-0.143
JES: Pileup p_T HF (8TeV)	0	1	0.000
Jet energy resolution (8TeV)	0.05	0.8	0.015
Muon energy scale (8TeV)	-0.008	0.8	0.008
Muon ID (8TeV)	-0.064	1	0.010
Electron energy scale (8TeV)	-0.028	0.9	0.008
Electron ID (8TeV)	0.018	1	-0.004
BTAGH_Statistic (8TeV)	0.835	0.6	-0.110
BTAGH_JES (8TeV)	-0.075	0.9	-0.017
Mistag (8TeV)	-0.738	0.9	0.076
Trigger (8TeV)	-0.069	1	0.008
Pile-up (8TeV)	-0.047	0.8	-0.028
Single top background (8TeV)	-0.863	0.9	0.363
Diboson background (8TeV)	-0.189	0.9	0.018
$t\bar{t}$ background (8TeV)	0.005	1	-0.002
BG_QCD/Wjets (8TeV)	-0.23	1	0.018
$t\bar{t}+V$ background (8TeV)	0.268	1	-0.009
DY background (0 b-jets) (8TeV)	0.085	0.7	-0.356
DY background (1 b-jets) (8TeV)	-0.076	1	0.047
DY background (2 b-jets) (8TeV)	0.017	1	0.000
Lumi (8TeV)	-0.225	1	0.024
Stat			1.245
Total vis			$\pm^{3.555}_{3.383}$
$\sigma_{t\bar{t}}$(7 TeV) vis			3.0134 pb
Q^2 scale (extr)			$\mp^{0.037}_{0.376}$
ME/PS matching (extr)			$\pm^{0.058}_{0.154}$
PDF (extr)			$\pm^{0.142}_{0.196}$
Top p_T (extr)			$\pm^{0.464}_{0.204}$
Total			$\pm^{3.589}_{3.419}$
$\sigma_{t\bar{t}}$(7 TeV)			172.51 pb

Table E.1: Extracted cross-sections for $\sqrt{s} = 7\,\text{TeV}$ including a detailed list of contributions from all nuisance parameters to the total uncertainty. The pulls and constraints on parameters are normalized to the pre-fit ±1 sigma variation. The parameter "TOP-MASS" corresponds to the deviation of m_t^{MC} from 172.5 GeV multiplied by 6.

Name	Pull	Constr / σ	Contribution [%]
BTAGH_BFragmentation	-0.404	1.1	-0.037
BTAGH_DeltaR	0.214	0.9	-0.027
BTAGH_GluonSplitting	-0.398	1	-0.072
BTAGH_IFSR	0	1	0.000

Name	Pull	Constr / σ	Contribution [%]
BTAGH_IP-bias	-0.009	1.1	−0.025
BTAGH_JetAway	1.348	0.9	−0.025
BTAGH_KT	0	1	0.000
BTAGH_LT-Bias	0	1	0.000
BTAGH_LT-Cb	0.506	1.1	−0.015
BTAGH_LT-others	0.557	1.5	−0.029
BTAGH_MuPt	0.057	1	−0.023
BTAGH_PS	0	1	0.000
BTAGH_PT-l2c	-0.244	1	−0.003
BTAGH_S8-ptrel	0.513	1.1	0.045
BTAGH_TCT	0	1	0.000
JES: High p_T Extra	0.167	0.8	−0.097
JES: Single pion ECAL	0.07	0.7	−0.063
JES: Single pion HCAL	0.077	0.6	−0.128
Top p_T	0.307	0.4	0.234
B-hadron ν decay fraction	0.399	1.1	0.499
b-fragmentation tune	0.495	0.4	0.455
MG+PY → PH+PY	0.02	0.2	0.353
ME/PS matching	-0.093	0.3	−0.001
Q^2 scale	0.143	0.2	−0.283
PDF10	0.08	1	0.022
PDF11	0.1	1.1	−0.004
PDF12	0.275	1	0.464
PDF13	0.001	0.2	−0.002
PDF14	0.058	1.1	0.032
PDF15	0.006	1.1	0.020
PDF16	0.102	1.1	−0.053
PDF17	0.148	1.1	0.213
PDF18	-0.044	1	−0.074
PDF19	0.011	1	0.000
PDF1	-0.016	1.1	0.000
PDF20	-0.028	1	−0.051
PDF21	-0.027	1.1	−0.034
PDF22	0.002	0.3	−0.006
PDF23	-0.035	1.1	0.008
PDF24	0	0.1	0.003
PDF25	0.009	1.1	0.005
PDF26	0.044	1	−0.057
PDF2	0	0.1	0.005
PDF3	0.21	1.1	−0.026
PDF4	0.15	1.1	0.050
PDF5	0.092	1.1	0.030
PDF6	0.057	1.1	0.019
PDF7	-0.083	1	−0.038
PDF8	0.049	1.1	−0.001
PDF9	-0.019	1.1	−0.036

Name	Pull	Constr / σ	Contribution [%]
Color reconnection	-0.07	0.7	0.167
Underlying event	0.022	0.3	0.057
JES: Flavor	0.436	0.5	0.085
JES: Absolute Stat (7TeV)	-0.482	0.9	0.038
JES: Absolute Scale (7TeV)	-0.445	1.2	0.028
JES: Time (7TeV)	-1.04	1.6	0.012
JES: Relative JER EC1 (7TeV)	-0.309	1.2	0.001
JES: Relative JER EC2 (7TeV)	0	1	0.000
JES: Relative JER HF (7TeV)	0	1	0.000
JES: Relative p_T BB (7TeV)	-0.496	0.9	0.057
JES: Relative p_T EC1 (7TeV)	-0.46	1.1	0.017
JES: Relative p_T EC2 (7TeV)	0	1	0.000
JES: Relative p_T HF (7TeV)	0	1	0.000
JES: Relative Stat EC2 (7TeV)	0	1	0.000
JES: Relative Stat HF (7TeV)	0	1	0.000
JES: Pileup Data/MC (7TeV)	0.051	1.1	0.008
JES: Pileup Bias (7TeV)	0	1	0.000
JES: Intercalibration (7TeV)	-0.019	1	0.001
JES: MPF (7TeV)	-0.482	0.9	0.038
JES: Pileup p_T BB (7TeV)	-1.43	0.7	-0.049
JES: Pileup p_T EC (7TeV)	-1.605	0.8	-0.009
JES: Pileup p_T HF (7TeV)	0	1	0.000
Jet energy resolution	-0.421	0.9	-0.059
Jet energy resolution (7TeV)	-0.665	1.7	-0.001
Muon energy scale	-0.083	0.8	-0.057
Muon energy scale (7TeV)	-0.065	1.1	-0.006
Muon ID	-0.029	1	-0.867
Muon ID (7TeV)	0.05	1	-0.015
Electron energy scale	-0.047	0.9	0.027
Electron energy scale (7TeV)	0.006	1	0.002
Electron ID	0.135	1	-1.048
Electron ID (7TeV)	0.047	1	-0.023
BTAGH_Statistic (7TeV)	0.019	1.3	0.050
BTAGH_JES	-0.031	1	-0.001
BTAGH_JES (7TeV)	-0.077	1.1	0.008
Mistag	-0.675	0.7	0.155
Mistag (7TeV)	0.15	0.9	0.047
Trigger	0.05	1	-0.954
Trigger (7TeV)	0.107	1	-0.033
Pile-up	-0.059	1	0.038
Pile-up (7TeV)	-0.242	0.8	0.046
Single top background	0.324	0.6	-0.415
Single top background (7TeV)	1.019	0.9	-0.101
Diboson background	0.735	0.7	0.540
Diboson background (7TeV)	0.545	0.9	-0.163
$t\bar{t}$ background	0.061	1	-0.082

Name	Pull	Constr / σ	Contribution [%]
$t\bar{t}$ background (7TeV)	0.025	1	0.002
BG_QCD/Wjets	-0.104	0.8	0.099
BG_QCD/Wjets (7TeV)	0.179	1	-0.020
$t\bar{t} + V$ background	-0.006	1	-0.010
$t\bar{t} + V$ background (7TeV)	-0.296	1	0.032
DY background (0 b-jets)	-0.082	0.4	0.431
DY background (0 b-jets) (7TeV)	-0.125	0.7	-0.333
DY background (1 b-jets)	0.025	0.9	0.153
DY background (1 b-jets) (7TeV)	0.088	1	-0.004
DY background (2 b-jets)	0.021	1	-0.009
DY background (2 b-jets) (7TeV)	-0.007	1	0.000
Lumi (7TeV)	0.279	1	-0.088
JES: Absolute Stat (8TeV)	0.119	0.6	0.000
JES: Absolute Scale (8TeV)	0.1	0.8	-0.007
JES: Time (8TeV)	0.188	1.2	0.006
JES: Relative JER EC1 (8TeV)	0.002	0.2	-0.002
JES: Relative JER EC2 (8TeV)	0	1	0.000
JES: Relative JER HF (8TeV)	0	1	0.000
JES: Relative p_T BB (8TeV)	0.001	0.5	-0.031
JES: Relative p_T EC1 (8TeV)	0.044	1.4	-0.041
JES: Relative p_T EC2 (8TeV)	0	1	0.000
JES: Relative p_T HF (8TeV)	0	1	0.000
JES: Relative Stat EC2 (8TeV)	0	1	0.000
JES: Relative Stat HF (8TeV)	0	1	0.000
JES: Pileup Data/MC (8TeV)	0.226	0.8	-0.065
JES: Pileup Bias (8TeV)	0	1	0.000
JES: Intercalibration (8TeV)	-0.041	0.9	-0.020
JES: MPF (8TeV)	0.164	0.7	0.021
JES: Pileup p_T BB (8TeV)	0.408	0.5	-0.376
JES: Pileup p_T EC (8TeV)	0.748	0.6	-0.267
JES: Pileup p_T HF (8TeV)	0	1	0.000
Jet energy resolution (8TeV)	0.05	0.8	0.007
Muon energy scale (8TeV)	-0.008	0.8	-0.024
Muon ID (8TeV)	-0.064	1	-0.404
Electron energy scale (8TeV)	-0.028	0.9	0.011
Electron ID (8TeV)	0.018	1	-0.484
BTAGH_Statistic (8TeV)	0.835	0.6	-0.137
BTAGH_JES (8TeV)	-0.075	0.9	-0.012
Mistag (8TeV)	-0.738	0.9	0.124
Trigger (8TeV)	-0.069	1	-0.683
Pile-up (8TeV)	-0.047	0.8	0.212
Single top background (8TeV)	-0.863	0.9	-0.037
Diboson background (8TeV)	-0.189	0.9	0.378
$t\bar{t}$ background (8TeV)	0.005	1	-0.041
BG_QCD/Wjets (8TeV)	-0.23	1	0.063
$t\bar{t} + V$ background (8TeV)	0.268	1	-0.082

Name	Pull	Constr / σ	Contribution [%]
DY background (0 b-jets) (8TeV)	0.085	0.7	0.459
DY background (1 b-jets) (8TeV)	-0.076	1	0.074
DY background (2 b-jets) (8TeV)	0.017	1	-0.005
Lumi (8TeV)	-0.225	1	-2.605
Stat			0.554
Total vis			$\pm^{3.621}_{3.404}$
$\sigma_{t\bar{t}}$(8 TeV) vis			4.1989 pb
Q^2 scale (extr)			$\pm^{0.185}_{0.094}$
ME/PS matching (extr)			$\pm^{0.253}_{0.335}$
PDF (extr)			$\pm^{0.147}_{0.206}$
Top p_T (extr)			$\pm^{0.825}_{0.361}$
Total			$\pm^{3.730}_{3.447}$
$\sigma_{t\bar{t}}$(8 TeV)			243.89 pb

Table E.2: Extracted cross-sections for $\sqrt{s} = 8\,\text{TeV}$ including a detailed list of contributions from all nuisance parameters to the total uncertainty. The pulls and constraints on parameters are normalized to the pre-fit ±1 sigma variation. The parameter "TOP-MASS" corresponds to the deviation of m_t^{MC} from 172.5 GeV multiplied by 6.

Name	Pull	Constr / σ	Contribution [%]
BTAGH_BFragmentation	-0.404	1.1	-0.002
BTAGH_DeltaR	0.214	0.9	0.004
BTAGH_GluonSplitting	-0.398	1	-0.080
BTAGH_IFSR	0	1	0.000
BTAGH_IP-bias	-0.009	1.1	-0.022
BTAGH_JetAway	1.348	0.9	0.026
BTAGH_KT	0	1	0.000
BTAGH_LT-Bias	0	1	0.000
BTAGH_LT-Cb	0.506	1.1	0.036
BTAGH_LT-others	0.557	1.5	-0.033
BTAGH_MuPt	0.057	1	-0.007
BTAGH_PS	0	1	0.000
BTAGH_PT-l2c	-0.244	1	-0.002
BTAGH_S8-ptrel	0.513	1.1	0.041
BTAGH_TCT	0	1	0.000
JES: High p_T Extra	0.167	0.8	0.001
JES: Single pion ECAL	0.07	0.7	-0.004
JES: Single pion HCAL	0.077	0.6	-0.038
Top p_T	0.307	0.4	0.143
B-hadron ν decay fraction	0.399	1.1	0.096
b-fragmentation tune	0.495	0.4	0.147
MG+PY → PH+PY	0.02	0.2	-0.019
ME/PS matching	-0.093	0.3	-0.032
Q^2 scale	0.143	0.2	-0.055
PDF10	0.08	1	0.001
PDF11	0.1	1.1	0.008

Name	Pull	Constr / σ	Contribution [%]
PDF12	0.275	1	0.048
PDF13	0.001	0.2	0.000
PDF14	0.058	1.1	0.005
PDF15	0.006	1.1	0.000
PDF16	0.102	1.1	0.001
PDF17	0.148	1.1	0.012
PDF18	-0.044	1	-0.014
PDF19	0.011	1	0.000
PDF1	-0.016	1.1	-0.005
PDF20	-0.028	1	-0.013
PDF21	-0.027	1.1	-0.002
PDF22	0.002	0.3	-0.001
PDF23	-0.035	1.1	-0.003
PDF24	0	0.1	0.001
PDF25	0.009	1.1	0.001
PDF26	0.044	1	-0.006
PDF2	0	0.1	0.001
PDF3	0.21	1.1	0.007
PDF4	0.15	1.1	0.010
PDF5	0.092	1.1	0.003
PDF6	0.057	1.1	0.002
PDF7	-0.083	1	-0.009
PDF8	0.049	1.1	0.002
PDF9	-0.019	1.1	-0.007
Color reconnection	-0.07	0.7	-0.032
Underlying event	0.022	0.3	-0.049
JES: Flavor	0.436	0.5	-0.108
JES: Absolute Stat (7TeV)	-0.482	0.9	-0.009
JES: Absolute Scale (7TeV)	-0.445	1.2	-0.013
JES: Time (7TeV)	-1.04	1.6	-0.001
JES: Relative JER EC1 (7TeV)	-0.309	1.2	-0.004
JES: Relative JER EC2 (7TeV)	0	1	0.000
JES: Relative JER HF (7TeV)	0	1	0.000
JES: Relative p_T BB (7TeV)	-0.496	0.9	-0.013
JES: Relative p_T EC1 (7TeV)	-0.46	1.1	-0.003
JES: Relative p_T EC2 (7TeV)	0	1	0.000
JES: Relative p_T HF (7TeV)	0	1	0.000
JES: Relative Stat EC2 (7TeV)	0	1	0.000
JES: Relative Stat HF (7TeV)	0	1	0.000
JES: Pileup Data/MC (7TeV)	0.051	1.1	0.002
JES: Pileup Bias (7TeV)	0	1	0.000
JES: Intercalibration (7TeV)	-0.019	1	0.001
JES: MPF (7TeV)	-0.482	0.9	-0.009
JES: Pileup p_T BB (7TeV)	-1.43	0.7	-0.005
JES: Pileup p_T EC (7TeV)	-1.605	0.8	0.007
JES: Pileup p_T HF (7TeV)	0	1	0.000

Name	Pull	Constr / σ	Contribution [%]
Jet energy resolution	-0.421	0.9	0.020
Jet energy resolution (7TeV)	-0.665	1.7	0.002
Muon energy scale	-0.083	0.8	-0.042
Muon energy scale (7TeV)	-0.065	1.1	-0.005
Muon ID	-0.029	1	-0.006
Muon ID (7TeV)	0.05	1	0.000
Electron energy scale	-0.047	0.9	-0.033
Electron energy scale (7TeV)	0.006	1	-0.002
Electron ID	0.135	1	0.002
Electron ID (7TeV)	0.047	1	0.000
BTAGH_Statistic (7TeV)	0.019	1.3	0.017
BTAGH_JES	-0.031	1	-0.002
BTAGH_JES (7TeV)	-0.077	1.1	0.002
Mistag	-0.675	0.7	-0.010
Mistag (7TeV)	0.15	0.9	-0.015
Trigger	0.05	1	-0.003
Trigger (7TeV)	0.107	1	-0.001
Pile-up	-0.059	1	-0.004
Pile-up (7TeV)	-0.242	0.8	0.013
Single top background	0.324	0.6	-0.072
Single top background (7TeV)	1.019	0.9	-0.017
Diboson background	0.735	0.7	-0.016
Diboson background (7TeV)	0.545	0.9	-0.001
$t\bar{t}$ background	0.061	1	-0.005
$t\bar{t}$ background (7TeV)	0.025	1	0.000
BG_QCD/Wjets	-0.104	0.8	0.005
BG_QCD/Wjets (7TeV)	0.179	1	0.000
$t\bar{t}+V$ background	-0.006	1	0.001
$t\bar{t}+V$ background (7TeV)	-0.296	1	0.005
DY background (0 b-jets)	-0.082	0.4	0.007
DY background (0 b-jets) (7TeV)	-0.125	0.7	0.003
DY background (1 b-jets)	0.025	0.9	0.008
DY background (1 b-jets) (7TeV)	0.088	1	-0.002
DY background (2 b-jets)	0.021	1	-0.001
DY background (2 b-jets) (7TeV)	-0.007	1	0.000
Lumi (7TeV)	0.279	1	-0.003
Xsec (7TeV)	-3.711	6.1	0.007
JES: Absolute Stat (8TeV)	0.119	0.6	-0.031
JES: Absolute Scale (8TeV)	0.1	0.8	-0.014
JES: Time (8TeV)	0.188	1.2	-0.014
JES: Relative JER EC1 (8TeV)	0.002	0.2	-0.001
JES: Relative JER EC2 (8TeV)	0	1	0.000
JES: Relative JER HF (8TeV)	0	1	0.000
JES: Relative p_T BB (8TeV)	0.001	0.5	-0.053
JES: Relative p_T EC1 (8TeV)	0.044	1.4	-0.025
JES: Relative p_T EC2 (8TeV)	0	1	0.000

Name	Pull	Constr / σ	Contribution [%]
JES: Relative p_T HF (8TeV)	0	1	0.000
JES: Relative Stat EC2 (8TeV)	0	1	0.000
JES: Relative Stat HF (8TeV)	0	1	0.000
JES: Pileup Data/MC (8TeV)	0.226	0.8	0.000
JES: Pileup Bias (8TeV)	0	1	0.000
JES: Intercalibration (8TeV)	-0.041	0.9	-0.006
JES: MPF (8TeV)	0.164	0.7	-0.063
JES: Pileup p_T BB (8TeV)	0.408	0.5	-0.012
JES: Pileup p_T EC (8TeV)	0.748	0.6	-0.033
JES: Pileup p_T HF (8TeV)	0	1	0.000
Jet energy resolution (8TeV)	0.05	0.8	0.011
Muon energy scale (8TeV)	-0.008	0.8	-0.017
Muon ID (8TeV)	-0.064	1	-0.002
Electron energy scale (8TeV)	-0.028	0.9	-0.014
Electron ID (8TeV)	0.018	1	0.001
BTAGH_Statistic (8TeV)	0.835	0.6	-0.047
BTAGH_JES (8TeV)	-0.075	0.9	-0.010
Mistag (8TeV)	-0.738	0.9	-0.010
Trigger (8TeV)	-0.069	1	-0.001
Pile-up (8TeV)	-0.047	0.8	-0.045
Single top background (8TeV)	-0.863	0.9	-0.007
Diboson background (8TeV)	-0.189	0.9	-0.006
$t\bar{t}$ background (8TeV)	0.005	1	-0.002
BG_QCD/Wjets (8TeV)	-0.23	1	0.002
$t\bar{t}+V$ background (8TeV)	0.268	1	0.002
DY background (0 b-jets) (8TeV)	0.085	0.7	-0.001
DY background (1 b-jets) (8TeV)	-0.076	1	0.006
DY background (2 b-jets) (8TeV)	0.017	1	-0.001
Lumi (8TeV)	-0.225	1	-0.001
Xsec (8TeV)	-7.784	8.8	0.037
Stat			0.158
Total			$\pm^{0.371}_{0.368}$
m_t^{MC}			172.733

Table E.3: Extracted top-quark MC mass, m_t^{MC}, including a detailed list of contributions from all nuisance parameters to the total uncertainty. The pulls and constraints on parameters are normalized to the pre-fit ±1 sigma variation.

List of Publications

The work during my PhD studies resulted in the following publications:

- J. Kieseler, K. Lipka, S. Moch, *Calibration of the Top-Quark Monte-Carlo Mass*, Submitted to PRL, arXiv:1511.00841
- CMS Collaboration, *Measurement of the $t\bar{t}$ production cross section in the $e\mu$ channel in pp collisions at $\sqrt{s}$ = 7 and 8 TeV*, CMS-PAS-TOP-13-004, 2015
- CMS Collaboration, *First measurement of the differential cross section for ttbar production in the dilepton final state at $\sqrt{s}$ = 13 TeV*, CMS-PAS-TOP-15-010, 2015
- CMS Collaboration, *Measurement of the top quark pair production cross section in proton-proton collisions at $\sqrt{s}$ =13 TeV*, Submitted to PRL, 2015, arXiv:1510.05302
- CMS Collaboration, *Measurement of t-tbar production with additional jet activity, including b quark jets, in the dilepton channel using pp collisions at $\sqrt{s} = 8$ TeV*, Submitted to EPJC, 2015, arXiv:1510.03072
- CMS Collaboration, *Measurement of the differential cross section for top quark pair production in pp collisions at $\sqrt{s}$ = 8 TeV*, EPJC 75 (2015) 542, 2015, arXiv:1505.04480
- CMS Collaboration, *Determination of the top-quark mass from the m(lb) distribution in dileptonic ttbar events at $\sqrt{s}$ = 8 TeV*, CMS-PAS-TOP-14014, 2014
- CMS Collaboration, *Search for the associated production of the Higgs boson with a top-quark pair* , JHEP 1409 (2014) 087, JHEP 1410 (2014) 106, arXiv:1408.1682
- CMS Collaboration, *Observation of the associated production of a single top quark and a W boson in pp collisions at $\sqrt{s}$ =8 TeV*, PRL 112 (2014) 23, 231802, 2014, arXiv:1401.2942
- J. Kieseler (for the CMS Collaboration), *Measurement of the jet multiplicity in dileptonic top-quark pair events at $\sqrt{s} = 8$ TeV*, 6th International Workshop on Top Quark Physics (TOP2013) Durbach, Germany, September 14-19, 2013
- CMS Collaboration, *Measurement of the $t\bar{t}$ production cross section in the dilepton channel in pp collisions at $\sqrt{s}$ = 8 TeV*, JHEP02 (2014) 024, 2014, arXiv:1312.7582
- J. Kieseler (for the CMS Collaboration), *Top Quark Pair Cross Section Measurements at CMS* , PoS DIS2013 (2013) 048, 2013
- J. Kieseler (for the CMS Collaboration), *Measurement of the $t\bar{t}$ production cross section in the dilepton channel in proton-proton collisions at $\sqrt{s} = 8$ TeV with the CMS experiment*, J.Phys.Conf.Ser. 452 (2013) 1, 012029, 2013

Eidesstattliche Versicherung

Hiermit erkläre ich an Eides statt, dass ich die vorliegende Dissertationsschrift selbst verfasst und keine anderen als die angegebenen Quellen und Hilfsmittel benutzt habe.

Hamburg, 21.09.2015

Jan Kieseler

Acknowledgments

I would like to thank my supervisor, Dr. Katerina Lipka, for offering me the opportunity to work within her group already during my diploma thesis and for giving me a lot of freedom to work independently - but also for giving clear directions at the same time and saying clear words every once in a while - also beyond the scope of this thesis.

My gratitude to Prof. Dr. Sven Moch, for very useful discussions and support, and also for evaluating my thesis efficiently and accurately. I would also like to thank my third referee, Prof. Dr. Zhiqing Zhang, for his very thorough and extraordinary fast evaluation.

Thanks also to Dr. Olaf Behnke, Prof. Dr. Elisabetta Gallo, and Prof. Dr. Caren Hagner for taking part in my disputation and for agreeing on a date on short notice. I would like to thank Olaf additionally for many inspirational discussions, in particular concerning statistics.

Many thanks to Maria for her invaluable and intense support and her constant willingness to help in every department - starting from my first steps with programming and the computing facilities in “the” office several years ago, up to discussions about almost everything as friends, nowadays.

Many thanks to Sebastian for push-starting the m_{lb} efforts and his help as convener.

I would like to thank everyone I shared an office with for making it pleasent to come there every morning: Monica with her extraordinary collection of tea, Marco for discussions about theoretical physics and guitar-equipment, and Roberval for his calmness while I was writing.

My gratitude to my other former and present colleagues, it was a pleasure working (and having lunch) with you: Johannes and Benjamin being interested in even the most technical programming aspects, Jasone always having a piece of chocolate and a smile in almost every situation, Eleni providing the complementary cookies and spotting even the tiniest missing sub-subscript, Ivan enjoying class-to-class conversion complications, Wolf probably solving them, Ali and Simon building yet another piece of hardware, Anya and Jenya being in either the one or the other office, and Gregor as the expert on administrative procedures. But it was also a pleasure discussing and working with the other more-or-less recent additions to the top group: Mykola, Christian C., Till, Alexander, Christian S., Kelly, and Gerrit.

Thanks to Samantha, Paolo, Francesco, and Ringaile for several conversations about physics and more.

Auch möchte ich meiner gesamten Familie danken - dafür, dass ihr mich unterstützt habt, wann immer ich es brauchte.

Besonders unterstützt während der Promotion – aber nicht nur in Bezug darauf – hast du mich, Carmen, so dass diese Arbeit im positiven Sinne eng mit dir verbunden ist. Danke!